

**PRODUCTION OF NANO CaCO₃
BY CARBONIZATION ROUTE**

**A Thesis Submitted to
the Graduate School of Engineering and Sciences of
İzmir Institute of Technology
in Partial Fulfillment of the Requirements for the Degree of**

DOCTOR OF PHILOSOPHY

in Chemical Engineering

**by
Murat MOLVA**

**June 2011
İZMİR**

We approve the thesis of **Murat MOLVA**

Assist. Prof. Ekrem ÖZDEMİR
Supervisor

Prof. Ahmet Emin EROĞLU
Committee Member

Assoc. Prof. Fikret İNAL
Committee Member

Prof. Gönül GÜNDÜZ
Committee Member

Prof. Mehmet POLAT
Committee Member

17 June 2011

Prof. Mehmet POLAT
Head of the Department of
of
Chemical Engineering

Prof. Durmuş Ali DEMİR
Dean of the Graduate School
Engineering and Sciences

ACKNOWLEDGEMENTS

I am heartily thankful to my supervisor, Dr. Ekrem ÖZDEMİR, whose encouragement, supervision, and support from the preliminary to the concluding level enabled me to develop an understanding of the subject. This thesis would not be possible without his help and I thank him from the bottom of my heart.

I thank my Committee Members, Dr. Ahmet E. EROĞLU, Dr. Fikret İNAL, Dr. Gönül GÜNDÜZ, and Dr. Mehmet POLAT for their comments and their suggestions to make this dissertation more valuable. I would also like to thank our research group, Dr. Sevgi KILIÇ OZDEMİR, Bora KANBAR, Yelda MEYVA, Şeniz E. BÖLÜKÇÜ, E. Aysu SAĞDIÇ, Görkem TOPRAK, and Mehmet AŞKIN for their valuable discussions during the lab works and for their friendships. I also appreciate İzmir Institute of Technology for giving me academic credentials and many friends.

Some of the preliminary results of the current dissertation were ended up with a research grant from The Scientific and Technological Research Council of Turkey (TUBITAK), and I appreciate it very much. I also appreciate the Center for Materials Research of İzmir Institute of Technology (İYTE-MAM) for SEM and XRD analyses. I also acknowledge Dow Chemical, İstanbul, Turkey, for supplying HYPOL2060 for the synthesis of polyurethane foams.

The families of Molva, Çınar, Okudur, and Tanrıkulu deserved all thanks for different period of my life, from childhood to my academic life. Also, special thanks are addressed to İmge and Ekim, as two of my special friends. They always walked along me during my entire academic carrier. Finally, and most importantly, words alone cannot express the thanks, I owe to my wife *Çelenk*. Her support, encouragement, quiet patience and unwavering love were undeniably the keystone upon which the past years of my life have been built. Her tolerance of my occasional moods during the doctoral period was a testament in itself of her unyielding loyalty and love. I also thank to my little lovely daughter, *İris Naz*. She was always next to me with her sweetness and her cheerful babyish smiles giving me strength for all time. *This dissertation was dedicated to my lovely daughter İris and her mother.*

ABSTRACT

PRODUCTION OF NANO CaCO₃ BY CARBONIZATION ROUTE

Calcium carbonate (CaCO₃) is one of the most abundant materials in nature and widely used as filling material in various industries in order to decrease the product costs and to improve some mechanical properties of the composite materials. Because commercial calcite sold in the market is in granular form, in micron size, and inhomogeneous size distribution, the required properties can only be obtained by the recrystallization method. However, because the crystallization is an ionic reaction, there is not a standard procedure to obtain calcite in nano size, monodisperse, and different morphologies. Therefore, the present study aims to investigate the ways of producing nano CaCO₃ by the carbonization route. In order to understand the progress in crystal formation, crystals were synthesized by the chemical method by slow or fast addition of reactant into the solution. A mini reactor was built in a Ca(OH)₂ solution for the carbonization method and reproducible results were obtained. During the precipitation reactions, pH and conductivity of the solutions were monitored. Particles were separated by centrifugation and dried at 103 °C in an oven overnight. Morphological characteristics of the precipitated CaCO₃ samples were analyzed by SEM, XRD and FTIR. On the basis of XRD and FTIR analyses, the main crystal form of the precipitated samples was found to be calcite. Colloidal stability tests revealed that these nano particles do form aggregates. It was shown that the crystallization occurs on the surfaces of both the undissolved Ca(OH)₂ particles and on the already grown CaCO₃ particles as nano calcite evidenced from the XRD patterns of the samples. It was also observed that, in the late stage of the crystallization, because the pH decreased, the morphology of the particles was affected, indicating that erosion took place on the surface due to ionization. The effects of the enzyme, carbonic anhydrase, polyurethane foam, and organic solvents such as methanol, ethanol, toluene, hexane and benzene were also studied. It was observed that, in the presence of solvents nano crystals can be synthesized in the form of calcite, which were mostly monodisperse particles.

ÖZET

KARBONİZASYON YÖNTEMİ İLE NANO CaCO₃ ÜRETİMİ

Kalsiyum karbonat (CaCO₃) doğada en fazla miktarda bulunan minerallerden biridir. Üretim maliyetlerini düşürmek ve kompozit malzemelerin bazı mekanik özelliklerini iyileştirmek amacıyla dolgu malzemesi olarak çeşitli endüstrilerde yaygın olarak kullanılmaktadır. Ticari olarak piyasada satılan kalsit granül formda, mikron boyutlarında ve homojen olmayan boyut dağılımında olduğu için, istenen özelliklerde kalsit üretebilmek sadece yeniden kristalizasyon metodlarıyla elde edilebilmektedir. Ancak, kristalizasyon bir iyonik reaksiyon olduğundan, nano boyutta, aynı boyut dağılımında ve değişik morfolojilerde kalsit elde edebilmek için standart bir prosedür henüz önerilmemiştir. Bu nedenle, bu çalışma karbonizasyon metodu ile nano boyutta kalsit üretiminin yollarını araştırmayı amaçlamaktadır. Kristal oluşumunu anlamak maksadıyla, kristaller kimyasal yöntem ile reaktantın çözeltiye yavaş ve hızlı ilave edilmesiyle sentezlenmiştir. Karbonizasyon metodu için, Ca(OH)₂ çözeltisi içinde bir mini reaktör oluşturulmuş ve tekrarlanabilir sonuçlar elde edilmiştir. Çökeltme reaksiyonu boyunca çözeltilerin pH ve iletkenlik değerleri izlenmiştir. Parçacıklar sentrifüj yöntemi ile çözeltiden ayrılmış ve 103 °C'de etüvde gece süresince bekletilmiştir. Elde edilen CaCO₃ taneciklerinin morfolojik özellikleri, SEM, XRD ve FTIR teknikleri ile analiz edilmiştir. XRD ve FTIR sonuçlarından oluşan taneciklerin kalsit formunda oldukları anlaşılmıştır. Kolloidal stabilite testleri bu nano parçacıkların topaklaşma eğiliminde olduklarına işaret etmektedir. Örneklerden elde edilen XRD grafiklerine göre kristalizasyonun hem çözünmemiş Ca(OH)₂ parçacıklarının yüzeyinde, hem de daha önceden oluşmuş CaCO₃ parçacıkları üzerinde meydana geldiği gösterilmiştir. Ayrıca, kristalizasyonun ileri aşamalarında pH düştüğünden dolayı, elde edilen taneciklerin yüzeyinin iyonizasyon kaynaklı erezyona uğradığı gözlenmiştir. Karbonik anhidraz enzimi, poliüretan, ve metanol, etanol, toluen, hekzan, ve benzen gibi organik çözücülerin etkileri de ayrıca çalışılmıştır. Çözücülerin varlığında, çoğunlukla homojen boyut dağılımında nano boyutta kalsit taneciklerinin sentezlenebildiği gözlenmiştir.

*Dedicated to love of my life;
İris Naz and Çelenk*

TABLE OF CONTENTS

LIST OF FIGURES	ix
LIST OF TABLES	xix
LIST OF SYMBOLS	xx
CHAPTER 1. INTRODUCTION	1
CHAPTER 2. LITERATURE REVIEW	6
2.1. Forms of Calcium Carbonate	6
2.2. Usage of CaCO ₃ as Filling Material	7
2.3. Production of CaCO ₃	11
2.4. Transport Processes in CaCO ₃ Crystallization	14
2.5. CaCO ₃ Crystallization Mechanisms	24
2.6. Important Turning Points in Nano CaCO ₃ Production	26
2.7. Factors Affecting CaCO ₃ Production	32
2.8. Effect of Additives	33
CHAPTER 3. INTERPARTICLE RELATIONS AND COLLOIDAL STABILITY OF CALCITE –WATER SYSTEM	36
3.1. Electrostatic Double Layer around Calcite Particles	36
3.2. Settling of Particles	41
3.3. Coagulation of Particles	43
CHAPTER 4. MATERIALS AND METHODS	47
4.1. Materials	47
4.2. CaCO ₃ Synthesis by Chemical Method	47
4.3. Dissolution of Ca(OH) ₂	49
4.4. CaCO ₃ Synthesis by Carbonization Method	50
4.5. Progress in CaCO ₃ Formation	51
4.6. Effect of Carbonic Anhydrase on CaCO ₃ Crystallization	54
4.7. Effect of Organic Solvents on CaCO ₃ Crystallization	57

4.8. Sample Characterization	60
4.8.1. SEM Analyses	60
4.8.2. XRD Analyses.....	60
4.8.3. FTIR Analyses.....	61
4.8.4. Particle Size Distribution Analyses.....	61
4.8.5. Zeta Potential Measurements	62
CHAPTER 5. RESULTS AND DISCUSSIONS	63
5.1. CaCO ₃ Synthesis by Chemical Method	63
5.2. Ca(OH) ₂ Dissolution	72
5.3. CaCO ₃ Synthesis by Carbonization Method	78
5.4. Progress in CaCO ₃ Crystallization	89
5.5. Colloidal Stability of Calcite –Water System	104
5.6. Effect of Free Carbonic Anhydrase on CaCO ₃ Crystallization.....	110
5.7. Effect of Polyurethane Foam on CaCO ₃ Production.....	114
5.8. Effect of Immobilized Carbonic Anhydrase on CaCO ₃ Production	117
5.9. Effect of Organic Solvents on CaCO ₃ Crystallization	128
CHAPTER 6. CONCLUSIONS	150
REFERENCES	152
APPENDICES	
APPENDIX A. MATHCAD PROGRAM CODE FOR THE CALCULATION OF COLLOIDAL STABILITY OF CALCITE-WATER SYTEM.....	164
APPENDIX B. ATHENA PROGRAM CODE FOR Ca(OH) ₂ DISSOLUTION	173

LIST OF FIGURES

<u>Figure</u>	<u>Page</u>
Figure 1.1. Tensile yield strength of polypropylene – calcite composite material	2
Figure 1.2. Commercial CaCO ₃ in markets.....	3
Figure 2.1. Lattice structure of calcite crystal (a) Calcite structure (b) Differences of calcite and aragonite structures (c) Lattices of the cubic system	7
Figure 2.2. Using CaCO ₃ as filling material (a) Low Density Polyethylene (LDPE) ³⁷ and (b) Polypropylene (PP).....	8
Figure 2.3. Production methods of CaCO ₃	11
Figure 2.4. Schematic of a typical reactor for CaCO ₃ production by carbonization method (1) jacketed reactor provided with a gas injection tube, (2) temperature probe, (3) conductivity cell, (4) conductivity meter, (5) computer with a data acquisition system (6) shaker, (7) peristaltic pump, (8) flow meter, (9) gas supply bottle,(10) jacketed feeding tank....	13
Figure 2.5. Production of CaCO ₃ by Chemical and Carbonization methods.....	14
Figure 2.6. Two film model for CO ₂ absorption in Ca(OH) ₂ slurry (C _{Bi} : Concentration of OH ⁻ ions at gas-liquid interface; C _B : Concentration of OH ⁻ ions in bulk liquid phase C _{BS} : saturation concentration of OH ⁻ ions in aqueous solution in equilibrium with Ca(OH) ₂ (solid)	17
Figure 2.7. Experimental rates of precipitation of vaterite obtained at pH values 9.0 and 10.0. Curves c and b represent the growth and nucleation contribution to the total rate of precipitation (curve a)	21
Figure 2.8. Proposed concentration profiles for species in the production of CaCO ₃	23
Figure 2.9. Schematic representation of classical and novel crystallization.....	24
Figure 2.10. The classical and novel CaCO ₃ crystallization mechanism suggested by Gebauer et al., (2008).	25
Figure 2.11. The different stages of template-controlled calcium carbonate formation.....	26

<u>Figure</u>	<u>Page</u>
Figure 2.12. CaCO ₃ production in micro membrane reactor (a) Schematic of the process 1, continuous phase vessel; 2, measuring pump; 3, membrane dispersion minireactor; 4, valve; 5, flow meter; 6, pressure gauges; 7, source of the mixed gas; 8, pH indicator; 9, temperature control bath. (b) Change of pH values with reaction time at the inlet and the outlet of the reactor. (c) TEM images of CaCO ₃ particles prepared by the minireactor.....	27
Figure 2.13. CaCO ₃ production under the influence of high gravity. 1, stirred tank; 2, pump; 3, valve; 4, rotor flowmeter; 5, distributor; 6, packed rotator; 7, outlet; 8, valve; 9, rotor flowmeter; 10, inlet.....	29
Figure 2.14. Absorption rate of CO ₂ and rate of precipitation process.....	30
Figure 2.15. The predicted variation of the calcite surface speciation as a function of pH with a schematic summary of the different surface terminations, and the predicted the most abundant surface speciation as a function of pH under conditions of calcite–water equilibrium ($P_{CO_2} = 5 \cdot 10^{-3.5}$ atm; $T = 25^\circ C$).	31
Figure 2.16. Growth rate (R) versus the inverse of the solution $[Ca^{++}]/[CO_3^{=}]$ ratio, r, for two different degrees of supersaturation with respect to calcite.....	32
Figure 3.1. Electrokinetic phenomena and electrical double layer (EDL) around a particle	37
Figure 3.2. DLVO Curve.....	40
Figure 4.1. Experimental set-up for chemical route (1) 20 ml of CaCl ₂ or Na ₂ CO ₃ injection solution (2) syringe pump (3) 250 ml of CaCl ₂ or Na ₂ CO ₃ stock solution (4) 5-neck jacketed reactor with magnetic bar (5) pH probe (6) conductivity probe (7) data logger (8) computer	48
Figure 4.2. Experimental set-up for CaCO ₃ carbonization	51
Figure 4.3. Experimental set-up for progress in CaCO ₃ formation.....	52
Figure 4.4. Experimental set-up for CaCO ₃ carbonization in a round bottom flask reactor	53
Figure 4.5. Experimental set-up for progress in CaCO ₃ formation in a 500 ml volumetric flask reactor.	54
Figure 4.6. Structures of the polyurethane prepolymer.....	55

<u>Figure</u>	<u>Page</u>
Figure 4.7. Enzyme immobilization by cross-linking within polyurethane foam.....	56
Figure 4.8. XRD patterns of all CaCO ₃ phases based on JCPDS. MHC: mono hydrate calcium carbonate; ACC: amorphous calcium carbonate.....	60
Figure 4.9. Infrared spectra of various CaCO ₃ phases.	61
Figure 5.1. (a) Fast addition of Na ₂ CO ₃ (94 mM) into CaCl ₂ solution (7.4 mM) (at a rate of 0.67 ml/min) (b) pH and conductivity change during fast addition (c) Slow addition of Na ₂ CO ₃ (94 mM) into CaCl ₂ solution (7.4 mM) (at a rate of 0.077 ml/min) (d) pH and conductivity change during slow addition. pH was adjusted to 11.5 by the addition of 5 ml of 250 mM NaOH solution.	64
Figure 5.2. SEM images of the precipitates obtained from addition of Na ₂ CO ₃ (94 mM) into CaCl ₂ solution (7.4 mM) (a) fast addition at a rate of 0.67 ml/min (b) slow addition at a rate of 0.077 ml/min.	65
Figure 5.3. Addition of (a) Na ₂ CO ₃ (76 mM) into CaCl ₂ solution (23 mM) at a rate of 0.67 ml/min, initial pH 9.35	66
Figure 5.4. SEM image of the precipitates obtained from addition of Na ₂ CO ₃ (76 mM) into CaCl ₂ solution (23 mM) at a rate of 0.67 ml/min.....	66
Figure 5.5. Addition of low (15 mM) and high (760 mM) concentrations of CaCl ₂ into Na ₂ CO ₃ solution (75 mM) at a rate of 0.077 ml/min (a) low CaCl ₂ concentration (b) high CaCl ₂ concentration (c) pH and conductivity change during low CaCl ₂ concentration (d) pH and conductivity change during high CaCl ₂ concentrations.....	67
Figure 5.6. SEM images of the precipitates obtained from addition of (a) low (15 mM) and (b) high (760 mM) concentrations of CaCl ₂ into Na ₂ CO ₃ solution (75 mM) at a rate of 0.077 ml/min. pH was adjusted to 11.5 by the addition of 5 ml of 250 mM NaOH solution.....	68
Figure 5.7. Calculated concentrations of Ca(OH) ₂ and HCO ₃ ⁻ and [Ca(OH) ₂] / [HCO ₃ ⁻] ratio. (a) slow addition of [HCO ₃ ⁻] (0.1 mL/sec) into 20 mM of [Ca(OH) ₂] (b) fast addition of [HCO ₃ ⁻] (1.0 mL/sec) into 20 mM of [Ca(OH) ₂] and (c) fast addition of [HCO ₃ ⁻] (1.0 mL/sec) into 40 mM of [Ca(OH) ₂].	69
Figure 5.8. pH change during the slow (0.1 mL/sec) and fast (1.0 mL/sec) addition of 100 mL of bicarbonate ions into 100 mL of 20 mM and 40 mM of Ca(OH) ₂ solution.	70

<u>Figure</u>	<u>Page</u>
Figure 5.9. SEM images of the precipitates obtained by adding into Ca(OH) ₂ solution (a) slow addition of bicarbonate ions at 0.1 ml/sec into 20 mM Ca(OH) ₂ solution (b) fast addition at 1.0 ml/sec into 20 mM Ca(OH) ₂ solution, and (c) fast addition at 1.0 ml/sec into 40 mM Ca(OH) ₂ solution.....	71
Figure 5.10. XRD patterns of the precipitates for the slow and fast addition of bicarbonate ions into 20 mM and 40 mM Ca(OH) ₂ solutions. (a) slow addition of bicarbonate ions at 0.1 ml/sec into 20 mM Ca(OH) ₂ solution (b) fast addition at 1.0 ml/sec into 20 mM Ca(OH) ₂ solution, and (c) fast addition at 1.0 ml/sec into 40 mM Ca(OH) ₂ solution.	72
Figure 5.11. Change in conductivity (mS/cm) for the incomplete dissolution of Ca(OH) ₂ and CaCO ₃ (T=25 °C) and comparison with the observation by Burns et al. (2005) (T =18 °C).	73
Figure 5.12. Change of pH and conductivity in the presence of various amounts of Ca(OH) ₂ (T = 25 °C).....	74
Figure 5.13. Change of size distribution with time during the dissociation of (a) 1 mM, (b) 5 mM, (c) 10 mM, and (d) 20 mM Ca(OH) ₂ (T= 25 °C ; stirring rate: 600 rpm).....	75
Figure 5.14. Change of mean size diameter for various concentrations of Ca(OH) ₂	76
Figure 5.15. Modeling of the dissolution of Ca(OH) ₂ for different concentrations.....	77
Figure 5.16. Modeling of concentrations of species during the dissolution of Ca(OH) ₂ in solution	77
Figure 5.17. Change of conductivity and pH in the presence of 10 mM Ca(OH) ₂ (stirring rate : 600 rpm) (diameter of glass tube for CO ₂ injection: 5 mm).....	79
Figure 5.18. Change of (a) pH and conductivity (b) deviation in pH and conductivity in the presence of 20 mM Ca(OH) ₂ (stirring rate : 600 rpm) (diameter of glass tube for CO ₂ injection: 5 mm).....	80
Figure 5.19. Change of pH and conductivity in the presence of extreme amounts of Ca(OH) ₂ on the precipitation of CO ₂ (stirring rate : 600 rpm; diameter of glass tube for CO ₂ injection: 10 mm; T = 25 °C)	81

<u>Figure</u>	<u>Page</u>
Figure 5.20. Change of pH and conductivity in presence of (a) 0.1 mM, (b) 50 mM (c) 200 mM (d) 500 mM $\text{Ca}(\text{OH})_2$ on the CaCO_3 precipitation (derivative curves).	82
Figure 5.21. Effect of extremely high amounts of $\text{Ca}(\text{OH})_2$ on the shape and the size of the PCC's.....	84
Figure 5.22. Change of pH and conductivity in the presence of various $\text{Ca}(\text{OH})_2$ amounts by CO_2 bubbling.....	84
Figure 5.23. Change of derivatives of the pH and conductivity in the presence of (a) 20 ml (b) 60 ml (c) 100 ml (d) 300 ml (e) 500 ml of $\text{Ca}(\text{OH})_2$ by CO_2 bubbling.	85
Figure 5.24. SEM images of the precipitate in the presence of various $\text{Ca}(\text{OH})_2$ concentrations by CO_2 bubbling.....	87
Figure 5.25. XRD patterns of the precipitate in the presence of various $\text{Ca}(\text{OH})_2$ concentrations by CO_2 bubbling (C: calcite)	88
Figure 5.26. pH and conductivity curves of the stepwise carbonization reaction with direct CO_2 injection. ($\text{Ca}(\text{OH})_2$: 30 mM; stirring: 600 rpm; $T=25\text{ }^\circ\text{C}$; reactor: 250 ml volumetric flask).....	89
Figure 5.27. SEM images of the precipitates obtained by the stepwise carbonization reaction with direct CO_2 injection. ($\text{Ca}(\text{OH})_2$: 30 mM; stirring: 600 rpm; $T=25\text{ }^\circ\text{C}$; reactor: 250 ml volumetric flask)	90
Figure 5.28. (a) FTIR spectra and (b) XRD patterns of the precipitates obtained by the stepwise carbonization reaction with direct CO_2 injection. ($\text{Ca}(\text{OH})_2$: 30 mM; stirring: 600 rpm; $T=25\text{ }^\circ\text{C}$; reactor: 250 ml volumetric flask)	91
Figure 5.29. pH and conductivity curves of the stepwise carbonization reaction with direct CO_2 injection. ($\text{Ca}(\text{OH})_2$: 5 mM; stirring: 600 rpm; $T=25\text{ }^\circ\text{C}$; reactor: 250 ml volumetric flask).....	93
Figure 5.30. SEM images of the precipitates obtained by the stepwise carbonization reaction with direct CO_2 injection. ($\text{Ca}(\text{OH})_2$: 5 mM; stirring: 600 rpm; $T=25\text{ }^\circ\text{C}$; reactor: 250 ml vol flask) (a) 5 min (b)10 min (c) 20 min (d) 30 min (e) 45 min (f) 85 min precipitation time	94

<u>Figure</u>	<u>Page</u>
Figure 5.31. Change of pH and conductivity of the slurry with time, showing effect of stirring rate under shear (Ca(OH)_2 : 10 mM; $T=25\text{ }^\circ\text{C}$; reactor: 250 ml volumetric flask).....	95
Figure 5.32. SEM images of the precipitates obtained from the stepwise carbonization at 600 rpm (a) 0 min (b) 10 min (c) 15 min (d) 45 min (e) 80 min (f) 24 h showing effect of stirring rate under shear (Ca(OH)_2 : 10 mM; $T=25\text{ }^\circ\text{C}$; reactor: 250 ml volumetric flask)	96
Figure 5.33. SEM images of the precipitates obtained from the stepwise carbonization at 800 rpm (a) 5 min (b) 15 min (c) 20 min (d) 23 min (e) 25 min (f) 30 min showing effect of stirring rate under shear (Ca(OH)_2 : 10 mM; $T=25\text{ }^\circ\text{C}$; reactor: 250 ml volumetric flask)	98
Figure 5.34. SEM images of the precipitates produced at various volumes (a) 600 ml (b) 300 ml (c) 100 ml of the slurry and fixed reaction time. (Ca(OH)_2 :30 mM; $T= 25\text{ }^\circ\text{C}$; reaction time: 20 min).....	100
Figure 5.35. Conversion of the precipitates produced at various volumes of slurry and fixed reaction time. (a) FTIR spectra, (b) XRD patterns (Ca(OH)_2 :30 mM; $T= 25\text{ }^\circ\text{C}$; reaction time: 20 min)	101
Figure 5.36. Final pH and conductivity values of the slurry under shear at various volume, fixed reaction time. (Ca(OH)_2 : 30 mM; stirring: 600 rpm; $T=25\text{ }^\circ\text{C}$; reactor: 500 ml volumetric flask, time: 30 min).	102
Figure 5.37. SEM images of the precipitates obtained from stepwise carbonization at various volume (a) 520 ml (b) 500 ml (c) 400 ml (d) 300 ml (e) 100 ml, at fixed reaction time. (Ca(OH)_2 : 30 mM; stirring: 600 rpm; $T=25\text{ }^\circ\text{C}$; reactor: 500 ml volumetric flask, time: 30 min)	103
Figure 5.38. Change of zeta potential distribution during stepwise carbonization reaction with direct CO_2 injection (Ca(OH)_2 : 30 mM; stirring: 600 rpm; $T=25\text{ }^\circ\text{C}$; reactor: 250 ml volumetric flask)	105
Figure 5.39. Total interaction energy curve (DLVO) for calcite particles in water in terms of kT (Joule) ($d= 100\text{ nm}$, $A_{\text{CWC}}=2.23 \times 10^{-20}\text{ J}$, $\psi_0=-14.92\text{ mV}$ at $\text{pH}=12$; $\psi_0 =-6.49\text{ mV}$ at $\text{pH}=7.5$; $\psi_0 = +11.42\text{ mV}$ at $\text{pH}=6.5$).....	105
Figure 5.40. Potential profile for calcite powder in pure water ($\psi_0=-14.92\text{ mV}$ at $\text{pH}=12$; $\psi_0 =-6.49\text{ mV}$ at $\text{pH}=7.5$; $\psi_0 = +11.42\text{ mV}$ at $\text{pH}=6.5$ $A_{\text{CWC}}=2.23 \times 10^{-20}$)	106

<u>Figure</u>	<u>Page</u>
Figure 5.41. Change in particle number concentration of nano calcite particles for rapid coagulation ($V_t=0$ kT; $C_{CaCO_3} = 30$ Mm; $N_o = 4.773 \cdot 10^{16}$).....	107
Figure 5.42. Change in particle number concentration of nano calcite particles for slow coagulation ($V_t=0$ kT; $C_{CaCO_3} = 30$ Mm; $N_o = 4.773 \cdot 10^{16}$).....	107
Figure 5.43. Change of particle size distribution (number intensity) during stepwise carbonization reaction with direct CO_2 injection ($Ca(OH)_2$: 30 mM; stirring: 600 rpm; $T=25$ °C; reactor: 250 ml volumetric flask).....	108
Figure 5.44. Change of particle size distribution (cumulative number) during stepwise carbonization reaction with direct CO_2 injection ($Ca(OH)_2$: 30 mM; stirring: 600 rpm; $T=25$ °C; reactor: 250 ml volumetric flask).....	109
Figure 5.45. Terminal settling velocity of nano Calcite particles in water.	110
Figure 5.46. pH and conductivity curves for the precipitation of CO_2 in the presence various amounts of free carbonic anhydrase and 20 mM $Ca(OH)_2$ (diameter of glass pipe : 5 mm).....	111
Figure 5.47. SEM images of the precipitated solids in the presence of various concentrations of free CA enzyme.....	113
Figure 5.48. XRD patterns of the crystals in the presence of various concentrations of free CA	114
Figure 5.49. SEM images of PU foam showing its porous structure PU foam and its hydrophilic surface	114
Figure 5.50. Change of pH and conductivity in the presence of various foam amounts (only foam, no CA)	115
Figure 5.51. SEM images of precipitated $CaCO_3$ crystals on the surface and (b) within the pore of the PU foam.....	115
Figure 5.52. SEM images of the precipitates obtained from the carbonization experiments in the presence of various amount of PU foam. (CA: 0.00 μ M; $Ca(OH)_2$:20 mM)	116
Figure 5.53. XRD patterns of the precipitates obtained from the carbonization experiments in the presence of various amount of PU foam. (CA: 0.00 μ M; $Ca(OH)_2$: 20 mM)	117

<u>Figure</u>	<u>Page</u>
Figure 5.54. Change of pH and conductivity in the presence of im-BCA (3.45 mg BCA / g HYPOL) with various amounts of PU foam (Ca(OH) ₂ : 20 mM)	118
Figure 5.55. SEM images of CaCO ₃ particles obtained in the presence of immobilized CA (3.45 mg BCA / g HYPOL) with various amounts of PU foam (Ca(OH) ₂ : 20 mM)	119
Figure 5.56. XRD patterns of CaCO ₃ particles obtained in the presence of immobilized CA (3.45 mg BCA / g HYPOL) with various amounts of PU foam (Ca(OH) ₂ : 20 mM)	120
Figure 5.57. Change of pH and conductivity with increasing BCA amount on PU foam (PU foam : 0.25 g)	120
Figure 5.58. SEM images of the precipitates obtained by various BCA amounts immobilized on PU foam (PU foam: 0.25 g).....	121
Figure 5.59. XRD patterns of the precipitates obtained by various BCA amounts immobilized on PU foam (PU foam : 0.25 g).....	122
Figure 5.60. Change of pH and conductivity with increasing BCA amount on PU foam (PU foam : 0.50 g)	122
Figure 5.61. SEM images of the precipitates obtained by various BCA amounts immobilized on PU foam (PU foam : 0.50 g).....	123
Figure 5.62. XRD patterns of the precipitates obtained by various BCA amounts immobilized on PU foam (PU foam : 0.50 g).....	124
Figure 5.63. Change of pH and conductivity with increasing BCA amount on PU foam (PU foam : 0.75 g)	124
Figure 5.64. SEM images of the precipitates obtained by various BCA amounts immobilized on PU foam (PU foam : 0.75 g).....	125
Figure 5.65. XRD patterns of the precipitates obtained by various BCA amounts immobilized on PU foam (PU foam : 0.75 g).....	126
Figure 5.66. SEM images of CaCO ₃ crystals (a) inside and (b) on the surface of a PU pore immobilized with CA.	126
Figure 5.67. Change of pH and conductivity during precipitation in the presence of additives. Amount of Ca(OH) ₂ :20 mM stirring: 800 rpm additives : 5 % (v/v)	129

<u>Figure</u>	<u>Page</u>
Figure 5.68. SEM images of the precipitates obtained by the modification of the additives. Amount of Ca(OH) ₂ :20 mM stirring: 800 rpm additives : 5 % (v/v)	130
Figure 5.69. XRD patterns of the precipitates obtained by the modification of the additives. Amount of Ca(OH) ₂ :20 mM stirring: 800 rpm additives : 5 % (v/v)	131
Figure 5.70. Change of pH and conductivity during precipitation in the presence of additives. Amount of Ca(OH) ₂ :20 mM stirring: 800 rpm additives : 20 % (v/v)	132
Figure 5.71. SEM images of the precipitates obtained by the modification of the additives. Amount of Ca(OH) ₂ :20 mM stirring: 800 rpm additives : 20 % (v/v)	133
Figure 5.72. XRD patterns of the precipitates obtained by the modification of the additives. Amount of Ca(OH) ₂ :20 mM stirring: 800 rpm additives : 20 % (v/v)	134
Figure 5.73. FTIR Spectra's of calcites which obtained in the presence of (a) methanol (b) ethanol (c) hexane (d) toluene (e) benzene: Amount of Ca(OH) ₂ :20 mM stirring: 800 rpm additives : 20 % (v/v).....	135
Figure 5.74. Vibrational modes of the molecules and their oscillation directions.....	136
Figure 5.75. Change of pH and conductivity during precipitation in the presence of additives. Amount of Ca(OH) ₂ :40 mM stirring: 800 rpm additives : 5 % (v/v)	137
Figure 5.76. SEM images of the precipitates obtained by the modification of the additives. Amount of Ca(OH) ₂ :40 mM stirring: 800 rpm additives : 5 % (v/v)	138
Figure 5.77. XRD patterns of the precipitates obtained by the modification of the additives. Amount of Ca(OH) ₂ :40 mM stirring: 800 rpm additives : 5 % (v/v)	139
Figure 5.78. Change of pH and conductivity during precipitation in the presence of additives. Amount of Ca(OH) ₂ :40 mM stirring: 800 rpm additives : 20 % (v/v)	139
Figure 5.79. SEM images of the precipitates obtained by the modification of the additives. Amount of Ca(OH) ₂ :40 mM stirring: 800 rpm additives : 20 % (v/v)	140

<u>Figure</u>	<u>Page</u>
Figure 5.80. XRD patterns of the precipitates obtained by the modification of the additives. Amount of Ca(OH) ₂ :40 mM stirring: 800 rpm additives : 20 % (v/v)	141
Figure 5.81. Change of pH and conductivity during precipitation in the presence of toluene. Amount of Ca(OH) ₂ :20 mM stirring: 800 rpm (from 0.2 S to 2.0 S in legend indicates from 0.2-fold to 2-fold of toluene solubility in water).	144
Figure 5.82. SEM images of the precipitates obtained from toluene solution. Amount of Ca(OH) ₂ :20 mM stirring: 800 rpm (from 0.2 S to 2.0 S in legend indicates from 0.2-fold to 2-fold of toluene solubility in water)..	146
Figure 5.83. Change of pH and conductivity during precipitation in the presence of toluene. Amount of Ca(OH) ₂ :40 mM stirring: 800 rpm (from 0.2 S to 1.0 S in legend indicates from 0.2-fold to 1-fold of toluene solubility in water).	147
Figure 5.84. SEM images of the precipitates obtained from toluene solution. Amount of Ca(OH) ₂ :40 mM stirring: 800 rpm (from 0.2 S to 1.0 S in legend indicates from 0.2 – fold to 1-fold of toluene solubility in water).	147
Figure 5.85. Change of pH and conductivity during precipitation in the presence of hexane. Amount of Ca(OH) ₂ :20 mM stirring: 800 rpm (from 0.2 S to 2.0 S in legend indicates from 0.2 – fold to 2-fold of hexane solubility in water).	148
Figure 5.86. SEM images of the precipitates obtained from hexane solution. Amount of Ca(OH) ₂ :20 mM stirring: 800 rpm (from 0.2 S to 2.0 S in legend indicates from 0.2 – fold to 2-fold of hexane solubility in water).	149

LIST OF TABLES

<u>Table</u>		<u>Page</u>
Table 2.1.	CaCO ₃ as filler material in recent studies	9
Table 2.2.	Reactions and reaction rate constants for the CaCO ₃ precipitation	22
Table 4.1.	Matrix of the CaCO ₃ production in the presence of polyurethane foam and Carbonic Anhydrase and their sample codes	57
Table 4.2.	Physicochemical properties of additives.....	57
Table 4.3.	Variables and their ranges in experiments with sample codes.	59
Table 5.1.	Evaluation of the precipitates obtained by the CO ₂ bubbling.....	88
Table 5.2.	Evaluation of the PCC's obtained by free Carbonic Anhydrase	112
Table 5.3.	Size of the crystals obtained by biomimetic reactions by immobilized CA	127
Table 5.4.	Evaluation of the PCC's obtained by organic solvent sets	143

LIST OF SYMBOLS

A	Surface area of $\text{Ca}(\text{OH})_2$	$\text{m}^2 \text{g}^{-1}$
A_{ij}	Hamaker constant for particles i and j	J
A_{11}	Hamaker constant of calcite in water	J
A_{33}	Hamaker constant for water	J
A_t	Effective Hamaker constant of calcite - water colloidal dispersion	J
A_p	Cross-sectional area of the particle	m^2
a	Activity for Ca^{++} and OH^- ions	mol L^{-1}
a	Acceleration of the particle	m sec^{-2}
a	Gas-liquid surface area	$\text{m}^2 \text{m}^{-3}$
B	Dimensionless thermodynamic parameter	
C^*_A	Concentration of CO_2 at the gas-liquid interface	mol L^{-1}
C_{AL}	Concentration of CO_2 at the bulk liquid	mol L^{-1}
C_B	Concentration of OH^- ions in bulk liquid phase	mol L^{-1}
C_B^{bulk}	OH^- concentration in the bulk liquid	mol L^{-1}
C_{BS}	Saturation concentration of OH^- ions in aqueous solution in equilibrium with $\text{Ca}(\text{OH})_2$	mol L^{-1}
C_D	Dimensionless drag coefficient	
C_i	Concentration of the ion, i	mol L^{-1}
C_0	Concentration of electrolyte (1 mM for water)	
d	Diameter of particles	nm
D	Diffusion coefficient of charged particles given by Stoke's Einstein Equation	
D_A	Diffusivity of CO_2 in the liquid phase	$\text{cm}^{-2} \text{sec}$
D_B	Diffusivity of OH^- in the liquid phase	$\text{cm}^{-2} \text{sec}$
d_p	Particle diameter	μm
F	Faraday constant	$96484.5 \text{ C mol}^{-1}$
F_b	Buoyant force	$\text{kg.m}^{-1}\text{sec}^{-2}$
F_d	Drag force	$\text{kg.m}^{-1}\text{sec}^{-2}$
F_g	Gravitational force ($\text{kg.m}^{-1}\text{sec}^{-2}$),	
F_{net}	Net force on the particle settling	$\text{kg.m}^{-1}\text{sec}^{-2}$

g	Acceleration of particle due to gravity	9.81 m sec^{-2}
H	Henry's Constant	$\text{mol m}^{-3} \text{ Pa}^{-1}$
H	Length of distance separating two particles	nm
IAP	Ionic activity product	$(\text{mol m}^{-3})^2$
I	Ionic activity of the solution	$(\text{mol m}^{-3})^2$
J	Critical nucleation rate	m^3/s or m^2/s
K_G	Coefficient of average linear velocity of crystallization	$\mu\text{m/s}$
K_j	Nucleation rate constant	$\text{m}^{-3} \text{ sec}^{-3}$
K_{sp}	Dissolution constant	
k_b	Backward rate constant of a reaction	$\text{M m}^{-2} \text{ sec}^{-1}$ or sec^{-1} or $\text{M}^{-1} \text{ sec}^{-1}$
k_B	Boltzmann's constant	J K^{-1}
k_f	Forward rate constant of a reaction	$\text{M m}^{-2} \text{ sec}^{-1}$ or sec^{-1} or $\text{M}^{-1} \text{ sec}^{-1}$
k_g	Mass transfer coefficient in the gas film	
k_i	Forward rate constant of i_{th} reaction	$\text{M m}^{-2} \text{ sec}^{-1}$ or sec^{-1} or $\text{M}^{-1} \text{ sec}^{-1}$
k_{-i}	Backward rate constant of i_{th} reaction	$\text{M m}^{-2} \text{ sec}^{-1}$ or sec^{-1} or $\text{M}^{-1} \text{ sec}^{-1}$
k_j	Temperature dependent - kinetic parameter ($\text{m}^3 \text{ s}^{-1}$ for homogeneous nucleation or $\text{m}^2 \text{ s}^{-1}$ for 2D nucleation)	$\text{m}^3 \text{ s}^{-1}$ or $\text{m}^2 \text{ s}^{-1}$
k_L	Liquid side mass transfer coefficient	cm sec^{-1}
m_p	Mass of the particle	g
n	Number of ions	
N	Absorption rate of CO_2	$\text{mole sec}^{-1} \text{ cm}^{-2}$
N_∞	Total number of particles per unit volume of fluid	
$N_{\infty(s)}$	Total number of the particles for slow coagulation	
$N_{\infty(s)}(0)$	Initial number of the particles for slow coagulation	
N_{jj}	Number of collisions per unit time per unit volume between two particles	

n_i	Number concentrations of particles with volume v_i	cm^{-3}
n_j	Number concentrations of particles with volume v_j	cm^{-3}
n_k	Number density of particles of volume v_k as a result of Brownian motion	number nm^{-2}
P_g	Partial pressures of CO_2 in the gas phase	atm
P_{gi}	Partial pressures of CO_2 at the gas-liquid interface	atm
R	Particles' radius	nm
R	Dissolution rate of $\text{Ca}(\text{OH})_2$	
R	Ideal gas constant	$\text{Jmol}^{-1}\text{K}^{-1}$
Re	Reynolds number	
r	Initial crystal growth rate	nm sec^{-1}
S	Saturation rate	
T	Temperature	K or $^{\circ}\text{C}$
t	Coagulation time	sec
W^*	Critical work for nucleation	J
W	Coagulation rate	
V	Volume of the solution	L
V_{el}	Repulsive interaction energy between particles	kT
V_p	Volume of the spherical particle	m^3
$V(r)$	Interaction energy due to the force between the centers of two particles separated by a distance r	kT
V_{vdW}	Attractive interaction energy between particles	kT
v	Molecular volume	$\text{m}^3 \text{mole}^{-1}$
v_p	Velocity of the particle	m sec^{-1}
v_i	Volume of the particle i	nm^3
v_j	Volume of the particle j	nm^3
z	Valency of electrolyte	
γ_i	Activity coefficient for the ion, i	
[]	Ion concentration	mM
β	Collision frequency function	
ϵ	Relative permittivity of water (78.5)	
ϵ_0	Relative permittivity of vacuum	$8.854 \times 10^{-12} \text{ C}^2 \text{ J}^{-1} \text{ m}^{-1}$

ΔG	Gibbs free energy in terms	J mol^{-1}
$i + j = k$	Over all collisions	
κ	Reciprocal thickness of double layer	m^{-1}
μ_f	Viscosity of the fluid	$\text{kg m}^{-1} \text{sec}^{-1}$
ρ_p	Density of the particle	kg m^{-3}
ρ_f	Density of the fluid	kg m^{-3}
σ	Interfacial tension	N m^{-1}
$\psi(x)$	Potential of the particle in solution at a point X between the plates	volts
ψ_1	Surface potential of particle 1	volts
ψ_2	Surface potential of particle 2	volts

CHAPTER 1

INTRODUCTION

Calcium carbonate (CaCO_3) has been used as filling material in various industries including paper, ink, plastics, electronics, optics, ceramics, metallurgy, pharmaceuticals, and etc.¹⁻⁵. Currently, more than 80% of the fillers used in thermoplastics are based on calcium carbonate minerals⁶⁻⁸. Using filling materials significantly reduce the product cost, and in most cases, improve the physical properties of the composite materials.

Annual CaCO_3 production in the world was reported as 72 million tons in 2007⁹. It was predicted that, production of CaCO_3 will reach up to 108.5 million tons by 2015¹⁰. Asia-Pacific represents the largest regional market for CaCO_3 worldwide. China has the largest production capacity of more than 70% of the total in Asia. Annual production of CaCO_3 in China has grown from 5.2 million tons in 2002 to 11.9 million tons in 2007 and predicted to reach 20 million tons by 2015.⁹ Turkey has 40 % of world CaCO_3 reserves¹¹. Niğde, Çanakkale, Bayramiç, Biga, Ezine, Balıkesir, Trakya, Bursa, İzmir, Muğla are the major locations for CaCO_3 reserves. Although Turkey has important amounts of world reserves, the production and exportation capacity of refined CaCO_3 are very limited.

Calcium carbonate has three different anhydrous polymorphs such as calcite, aragonite, and vaterite. Calcite is the most stable form of the CaCO_3 at standard conditions. Aragonite and vaterite are not stable, but they transform into the stable calcite¹². CaCO_3 has also other hydrous forms such as calcium carbonate monohydrate, calcium carbonate hexahydrate, and amorphous calcium carbonate (ACC)¹³⁻¹⁷.

Calcite has been used extensively in polymeric composites. It was observed that using filling material enhanced some of the physical and mechanical properties of the polymeric composites. For example, the tensile yield strength of polypropylene (PP)-calcite composite material was decreased as the volume fraction of calcite increased.¹⁸ As shown in Figure 1.1 the tensile yield strength was decreased significantly for the large particles.³⁹ Such effect is less pronounced when the particle size was smaller. Especially, CaCO_3 particles of 10 nm in size did not decrease the tensile yield strength,

but, on the contrary, improved the tensile yield strength. Therefore, production of calcite in nano sizes is highly important.

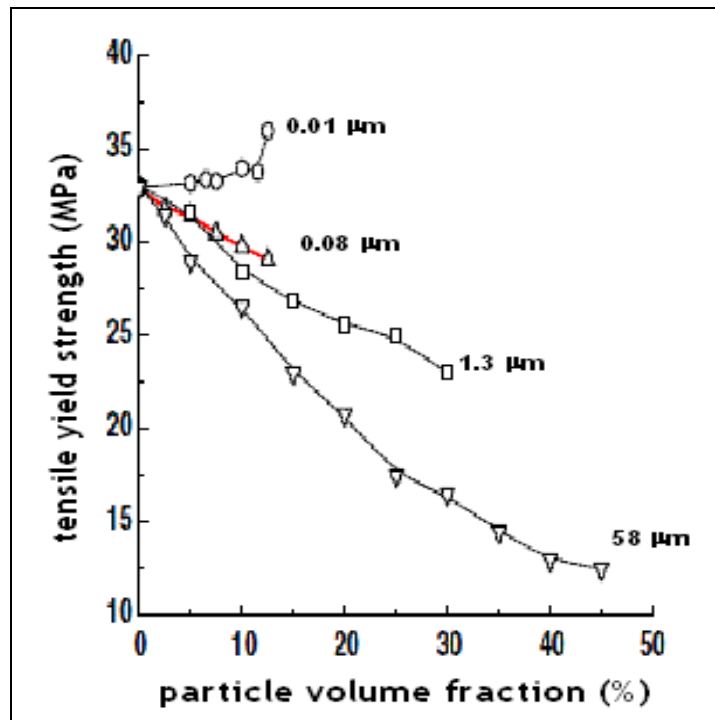


Figure 1.1. Tensile yield strength of polypropylene – calcite composite material³⁹

It could be possible to produce CaCO_3 from minerals of natural sources by crushing, grinding, and sieving processes. The CaCO_3 produced from the grinding process is called Ground Calcium Carbonate (GCC). However, the costs for crushing and milling processes are high. Also, as can be seen in Figure 1.2, calcite produced from natural sources won't be in desired quality and purity. The GCC in micron sized and they have inhomogeneous size distribution¹⁹. Therefore, production of nano calcite can be achieved by recrystallization; such that the mineral CaCO_3 is converted to calcium oxide (CaO) by calcination, hydrated to calcium hydroxide ($\text{Ca}(\text{OH})_2$) and recrystallized by carbon dioxide (CO_2). Since the raw materials are cheap and readily available in nature, the production capacity by recrystallization in industrial scale can supply the market demands²⁰.

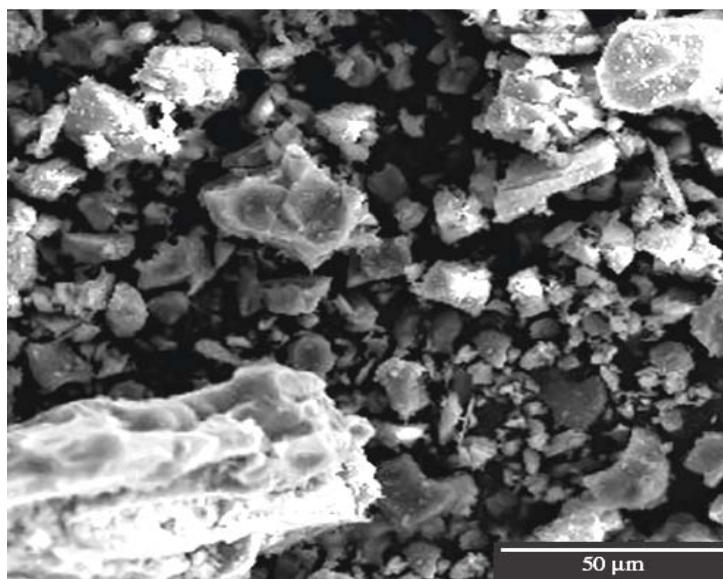


Figure 1.2. Commercial CaCO_3 in markets²¹

There are mainly two methods for recrystallization in aqueous solution; chemical method and carbonization method. The chemical method utilizes calcium chloride (CaCl_2) as the calcium source and sodium carbonate (Na_2CO_3) as the carbonate source. The carbonization method, on the other hand utilizes $\text{Ca}(\text{OH})_2$ as the calcium source and CO_2 as the carbonate source. Chemical method has been employed extensively in laboratory conditions in order to study the parameters that affect the crystallization. For example, effects of supersaturation, temperature, pH, stirring rate, the addition rate of feeds, the effect of any organic or inorganic additives on crystallization and on the kinetic rates, were studied²²⁻²⁷. In this method, interesting figures such as flower-like, tulip-like, sculpture-like morphologies were obtained. However, the particles produced by the chemical method were shown to be larger than three micron (μm). Therefore, it is difficult to produce nano calcite by the chemical method especially in the industrial scale. Therefore, the carbonization method can only be employed for the production of nano calcite in the industrial scale. Although the reactions of CaCO_3 formation are well known and frequently studied, the resulting products are not generally in the desired size (less than $1 \mu\text{m}$), homogeneous size distribution, and different morphologies. The reason could be: “the theoretical models do not represent the experimental conditions, or the experimental conditions do not obey the theoretical models”. For example, there are very large differences between the nucleation rate and crystal growth rate in solution. Since the crystallization is an ionic reaction, the crystal growth rate can not be easily controlled, and thus, it is difficult to

obtain particles in nano sizes, homogeneous size distribution, and different morphologies. In order to produce nano calcite with the desired properties, different approaches should be developed.

Mechanistic studies on classical crystallization claim that the nucleation step is required before crystal growth¹³. However, novel crystallization mechanisms require a prenucleation process in which ions will form stable cluster particles²⁸. These clusters are charged particles in equilibrium with their ions and they can grow or collide to produce amorphous CaCO₃ nuclei. In a recent study, crystallization on a polymeric template was revealed²⁵. A 1 to 3 nm of clusters were identified by cryo-TEM image analysis. These clusters collide on the template or attached to the already grown amorphous CaCO₃ particles to produce larger particles of about 30 nm. This process continues yielding larger particles. These particles are initially in amorphous form and reorganize into the new crystalline form. To be able to produce nano particles, the progress in crystal formation need to be analyzed and the growth of the particles needs to be inhibited at certain conditions. Unfortunately, there are not such sharp conditions specified in the current literature to produce particles in nano sizes, homogenous size distribution and different morphologies²⁹.

It was reported that the precipitation rate of calcite was depended on the slow reaction of CO₂ dissolution in aqueous solution^{30,31}. The stoichiometry of overall reaction for the calcite precipitation requires that one molecule of CO₂ should be released for each CaCO₃ molecule deposited on the surface and 2 molecules of HCO₃⁻ were consumed^{30,31}. It was claimed that the CaCO₃ crystallization rate could be enhanced by using Carbonic Anhydrase (CA) enzyme, catalyzing the hydration of CO₂ in aqueous solution. However, this idea was debated by Zhang and Grattoni, (1998)³² indicating that CA could have reduced the energy barrier of forming new nuclei of CaCO₃ which provided additional sites for crystallization. The authors³³ responded that their claim was valid. The effect of CA enzyme on CaCO₃ crystallization and nano calcite production need to be clarified.

There are two components in crystal growth rate; one is nucleation rate, and the other is the growth rate. Supersaturation, temperature, pH, interfacial tension, etc. may play a major role in crystallization rate and crystal morphology. Because solvents and other organic and inorganic additives may alter crystal morphology and particle size, the effect of some organic solvents on the particle size and morphology need to be identified.

In order to be able to produce nano calcite with narrow size distribution and different morphologies, the objectives of the present dissertation are:

- (1) to investigate the progress in CaCO_3 crystallization,
- (2) to investigate the effect of Carbonic Anhydrase on the particle size and morphology of CaCO_3 ,
- (3) to investigate the effect of various solvents such as methanol, ethanol, hexane, toluene and benzene on the particle size and morphology of CaCO_3

CHAPTER 2

LITERATURE REVIEW

2.1. Forms of Calcium Carbonate

Calcium carbonate is one of the most abundant minerals in nature. About 4 % of the Earth's crust is CaCO_3 . CaCO_3 has hydrated and anhydrous forms. There are three different anhydrous polymorphs which are calcite, aragonite, and vaterite. The hydrous polymorphs of CaCO_3 are, in the order of increasing solubility, calcium carbonate monohydrate, calcium carbonate hexahydrate, and amorphous calcium carbonate¹³⁻¹⁷. Calcite is formed in rhombohedral, trigonal, hexagonal and scalenohedral crystalline forms. Aragonite is formed in needle-like, orthorhombic, and dipyramidal shapes. Vaterite is formed in spherical, orthorhombic, hexagonal, dihexagonal, and dipyramidal morphologies. Figure 2.1 shows the lattice structure of each anhydrous forms^{15,34}. Calcite has a trigonal structure with two molecules per unit cell. The calcium ions and the carbon atoms of the carbonate ions all lie on the trigonal axis and the orientations of the two carbonate ions are staggered relative to each other so that there is a centre of symmetry¹⁴. Calcite is the most stable form of the CaCO_3 at standard conditions. Aragonite and vaterite are not stable, but they can transform into the stable calcite¹². Calcite and aragonite have very similar crystal structures and the calcium ions are located almost in the same lattice position in (0 0 1) layers alternating with the layers of carbonate ions^{35,36}. Synthetic scalenohedral calcite is generally produced through a batch carbonization method. The rhombohedral morphology, bounded by the (1 0 4) form, is usually precipitated by using chemical solution method, but rarely by the mentioned carbonization method as the industrial process³⁶.

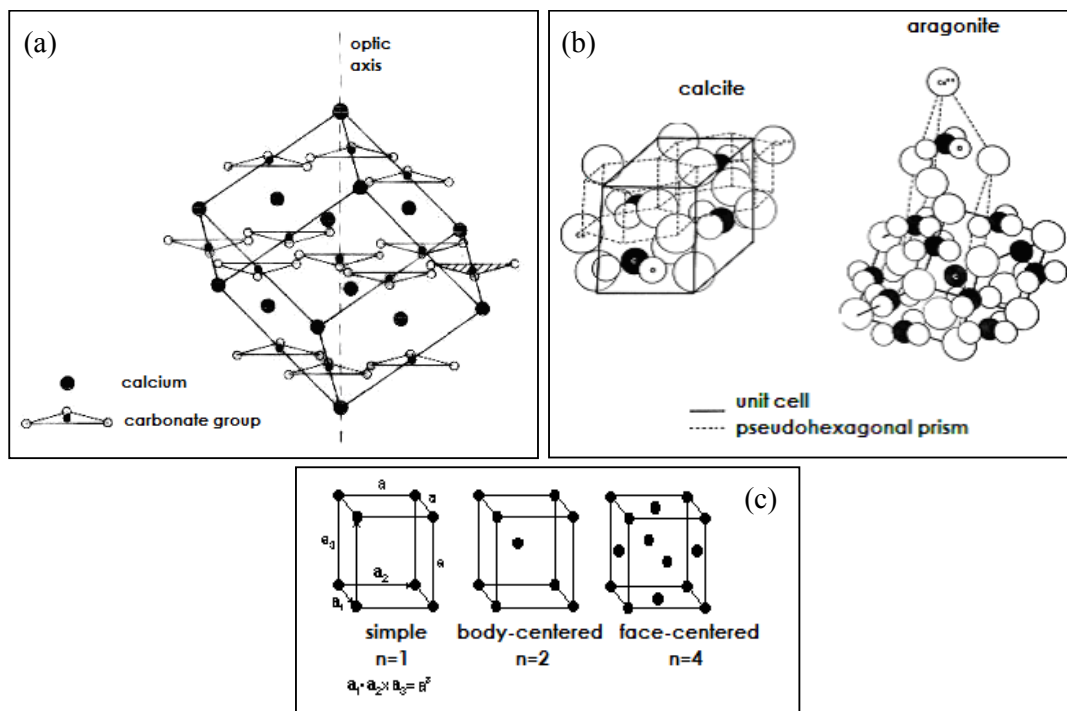


Figure 2.1. Lattice structure of calcite crystal (a) Calcite structure (b) Differences of calcite and aragonite structures (c) Lattices of the cubic system^{15,34}

2.2. Usage of CaCO_3 as Filling Material

Calcium carbonate has been used as filling materials especially in paper, ink, polymeric composites, paints, pigments, ceramic and cement industries¹⁻⁵. Mostly calcite crystals were used for the production of polymeric composites. Figure 2.2a shows low density polyethylene (LDPE)–calcite nano composite polymeric material where a 20% of 5 μm -size CaCO_3 particles were mixed with the LDPE. In this case, the tensile strength of the composite was increased two fold³⁷. Figure 2.2b shows the polypropylene (PP)-calcite polymeric composite material, where 80 nm of CaCO_3 particles were mixed with the PP. In this case, the impact resistance of the composite was increased approximately 5 fold³⁸. On the other hand, when CaCO_3 with particle size of 10 nm or lower was used, the mechanical properties of the polymeric composite were noticeably enhanced as shown in Figure 1.1. In general, Table 2.1 summarizes the recent studies on the different types of polymeric composite materials using CaCO_3 as filling material. In the table, enhancements in various properties of the composite materials were also indicated. As can be seen in the table, the improvements in the physical properties were significant when the nano sized CaCO_3 particles were used.

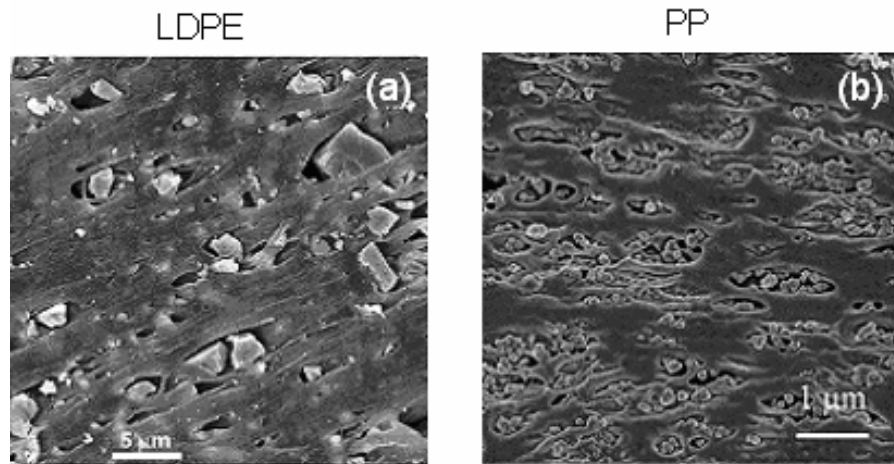


Figure 2.2. Using CaCO_3 as filling material (a) Low Density Polyethylene (LDPE)³⁷ and (b) Polypropylene (PP)^{18,37,38}.

Nanoparticles have been categorized as advanced materials³⁹. Recently, a large number of researches have been conducted on the synthesis, characterization, and properties of nanoparticles. However, there are serious doubts about the large scale production of nano-particles in industry in cost effective methods. In order to produce a high volume of CaCO_3 , research has accelerated for the last decades. The world consumption rate of some inorganic filling materials used in polymeric composite materials such as CaCO_3 , silica (SiO_2), titanium dioxide (TiO_2), and clay were predicted to be 10^9 tons/year³⁹ in 2015. Therefore, the importance of production of nano- CaCO_3 in large quantities was well understood^{18,20,40-48}.

Table 2.1. CaCO₃ as filler material in recent studies

Polymeric material	CaCO₃ (µm)	Observed significant effect	Ref .
Acrylonitrile-butadiene-styrene (ABS) terpolymer	14 – 40 2.5 – 6.5	<ul style="list-style-type: none"> • Increase in toughness and strength of the composite 	49
Acrylonitrile-butadiene-styrene (ABS) copolymer	0.04 –1.4	<ul style="list-style-type: none"> • Decrease in melting flow of the composite with the increase in the amount of filling material (only 10 % increase in melting flow with respect to unfilled material). 	50
High density polyethylene (HDPE)	0.44 0.7 3.5	<ul style="list-style-type: none"> • Significant increase in hardness and toughness • 16-fold increase in impact energy (from 50 J/m to 800 J/m). • 50 % increase in Young modulus and impact energy 	51
Polybenzoxazine	1.5- 20	<ul style="list-style-type: none"> • Increase in elastic modulus values 	18
HDPE Low density polyethylene (LDPE) Linear low density polyethylene (LLDPE) Carboxylic Polyethylene	1.1	<ul style="list-style-type: none"> • Increase in tensile stress and yield stress • Increase in elongation at break • Increase in complex melt viscosity 	52
HDPE	0.07	<ul style="list-style-type: none"> • 10 % increase in Yield stress • 35 % increase in Young modulus • 500 % increase in elongation at break 	53
Polyethylene film	3 - 5	<ul style="list-style-type: none"> • Formation of crystal phase at polyethylene surface and increase in mechanical strength 	54
Polyaspartic acid (PAsp) Polyglutamic acid (PGlu) Polyacrylic acid (PA-Asp)	>1 calcite >1 aragonite >1 vaterite	<ul style="list-style-type: none"> • Increase in mechanical strength and thermal properties of crystal structure 	55
Polyester amide (PEA)	0.1 - 0.12 calcite silicon oxide	<ul style="list-style-type: none"> • Significant enhancement in both mechanical properties and hydrolysis of the polymer 	56
Polystyrene (PS)	0.04-0.08	<ul style="list-style-type: none"> • A very tight encapsulation between polystyrene and the calcite 	45
Polystyrene	0.03 - 0.1	<ul style="list-style-type: none"> • Increase in Young's modulus and creep resistance • Improvement in polymerization activity • Improvement in tensile strength with filler material 	57

(Cont. on next page)

Table 2.1. (Cont)

Polymeric material	CaCO₃ (μm)	Observed significant effect	Ref
2-hidroxiethyl metakralet (HEMA) Methyl metakralet (MMA) Ethylene glycol dimetakralet (EGDMA) 2-hidroxy-2-methyle-1-phenylpropane	0.05 -0.15 calcite 0.38 – 1.25 aragonite	<ul style="list-style-type: none"> • Significant increase in shear stress and compressive strength depending on the use of calcite • Decrease in mechanical strength depending on the growth of particle size • 4-fold increase in shear stress and 10-fold increase in compressive strength depending on the use of aragonite. 	58
Poly vinyl acetate (PVA)	2.2 - 2.7	<ul style="list-style-type: none"> • After modification of the calcite with stearic acid, improvement in mechanical properties. Increase in tensile strength. • Improvement of tensile breaking stress and tensile strength. • Increase in elongation at break because of homogeneous particle distribution 	59
Poly(vinylidene fluoride) (PVDF)	> 1	<ul style="list-style-type: none"> • Except the melting temperature, improved thermal characteristics in all • Improvement of crystallization • Production of more homogeneous, highly flexible and durable products 	2
Polyethylene co-vinyl acetate film	5 - 10	<ul style="list-style-type: none"> • Decrease in permeability of the film • Decrease in the value of reflection 	60
Polypropylene (PP)	0.11 - 2.13	<ul style="list-style-type: none"> • 3-fold increase in viscosity • 1.5-fold increase in tensile strength 	61
Polypropylene (PP)	0.04	<ul style="list-style-type: none"> • Increase in Young's modulus and tensile strength 	62
Polypropylene	0.021	<ul style="list-style-type: none"> • Significant increase in Young's modulus and tensile strength with the installation of high amounts of filler 	18
Polyvinyl chloride (PVC)	2.3	<ul style="list-style-type: none"> • Significant increase in tensile strength and Young's modulus 	18
PVC	0.1	<ul style="list-style-type: none"> • Approximately 24 % increase in potency factor Approximately 150 % increase in elongation at break • Approximately 10 % increase in tensile strength 	42

2.3. Production of CaCO₃

There are mainly two crystallization methods on the synthesis of CaCO₃ in literature^{16,20,39,63}. These are chemical method and carbonization method as shown in Figure 2.3. In chemical method, for example, the solutions of calcium chloride (CaCl₂) and sodium carbonate (Na₂CO₃) are mixed with known amounts and stirring rates. Because both salts are fully dissolved in water, CaCO₃ crystallizes by the direct reaction between calcium (Ca⁺⁺) and carbonate (CO₃⁼) ions in the aqueous phase^{64,65}. Chemical method is an easy method at the laboratory conditions because the parameters can easily be controlled. For example, effects of supersaturation, the addition rates of the feeds, temperature, pH, stirring rate, any organic or inorganic additives on the crystal morphology can be determined by the chemical method. Also, most kinetic studies were conducted by the chemical method²²⁻²⁷. The particle size produced by the chemical method is more than micron size and, interesting figures such as flower-like, tulip-like, sculpture-like morphologies can be obtained. The chemical method has also been frequently used in biomimetic studies for the understanding of the occurrence of the inorganic structures as the biological templates, and there have been numerous publications in the literature on the topic^{13,22,34,66,67}. Unfortunately, nano CaCO₃ production could not be possible by the chemical method especially in industrial scale.

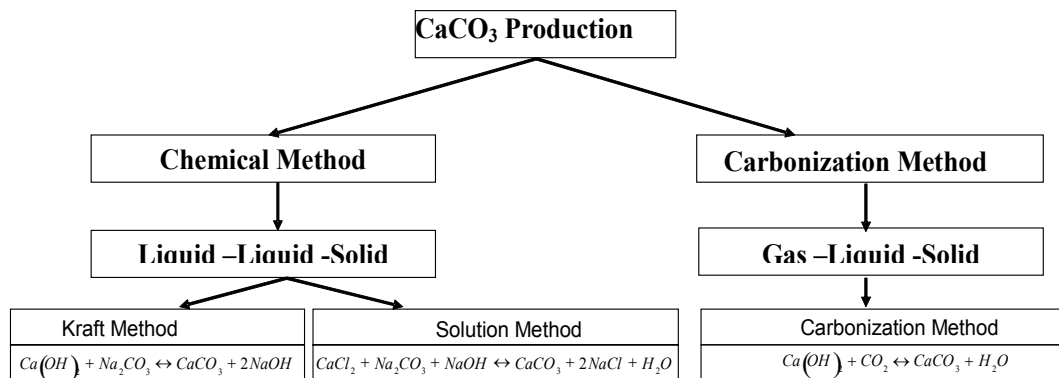


Figure 2.3. Production methods of CaCO₃

In carbonization route, Ca(OH)₂ is used as Ca⁺⁺ ion source and CO₂ is used as CO₃⁼ ion source in the aqueous solution^{20,40,41,43,63,68,69}. The carbonization method is the most suitable method for the production of CaCO₃ in the industrial scale. Because the

raw materials are abundant and cheap, the production of calcite by the carbonization method satisfies the market needs. Although the production of CaCO_3 by carbonization method has been studied in the literature; somehow, a standard procedure for the production of nano CaCO_3 could not be suggested. The production of CaCO_3 is generally based on the introduction of gaseous CO_2 into the $\text{Ca}(\text{OH})_2$ solution in a semi-batch reactor^{20,40}. For example, a schematic of the crystallization reactor has been used by Carmona et al. (2003)^{16,20,40,63,68} as given in Figure 2.4. The reactor was filled with deionized (DI) water and then CO_2 injection was started through the water. The pH and conductivity were set to a constant value for the crystallization. When $\text{Ca}(\text{OH})_2$ slurry was fed to the reactor with the pump, the crystallization was started. Reaching the set values took time and during this initial adjustments, the conductivity values were sometimes overshoot, sometimes decreased to a value and then increased back to the set values and, different explanations were given for each situations^{16,40,63,68}. After the $\text{Ca}(\text{OH})_2$ pump was stopped, CO_2 injection was continued in order to complete the crystallization. At the time, pH and conductivity values were shown to decrease. When the conductivity was zero or pH decreased to 7.0, the crystallization reaction was interrupted, samples were withdrawn and analyzed¹⁶. However, in our opinion, some technical errors were made in their experiments such that crystallization solution is composed of active nuclei and growing particles which would result in larger particles with various morphologies. When the pumping of $\text{Ca}(\text{OH})_2$ solution was stopped and CO_2 was continued to flow, pH in reactor was shown to decrease sharply. When pH decreases, the solubility of both $\text{Ca}(\text{OH})_2$ and CaCO_3 increases. On the other hand, the surface charge of the CaCO_3 crystals would transform from negative to positive⁷⁰. Therefore, it would be possible to obtain chain like and aggregated CaCO_3 crystals in various morphologies^{16,40,63,68}. Fortunately, larger particles with sizes of more than 3 μm were produced. Also, homogeneous size distribution could not be obtained.

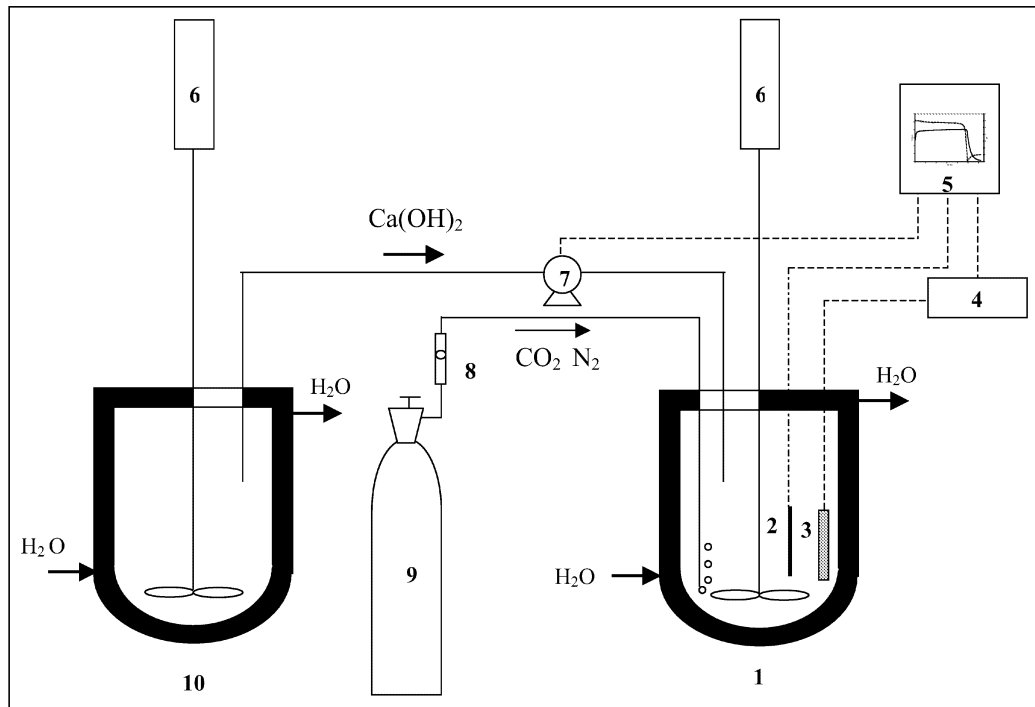


Figure 2.4. Schematic of a typical reactor for CaCO_3 production by carbonization method^{16,20,43} (1) jacketed reactor provided with a gas injection tube, (2) temperature probe, (3) conductivity cell, (4) conductivity meter, (5) computer with a data acquisition system (6) shaker, (7) peristaltic pump, (8) flow meter, (9) gas supply bottle, (10) jacketed feeding tank.

Typical CaCO_3 particles which were produced by chemical and carbonization methods were given in Figure 2.5. As shown in the figure, granular calcite and needle like aragonite were produced at low and higher temperatures, respectively, by the chemical method⁶⁵. The sizes of the crystals were significantly large, more than $3 \mu\text{m}$. In carbonization method, rhombohedral calcite particles were produced at low electrical conductivity values in the solution. When the conductivity values were increased, rhombo scalenohedral and scalenohedral calcite crystals were synthesized. When the conductivity values were too high, only scalenohedral calcite crystals were produced¹⁶. Unfortunately, the sizes of these particles were still larger than $1 \mu\text{m}$.

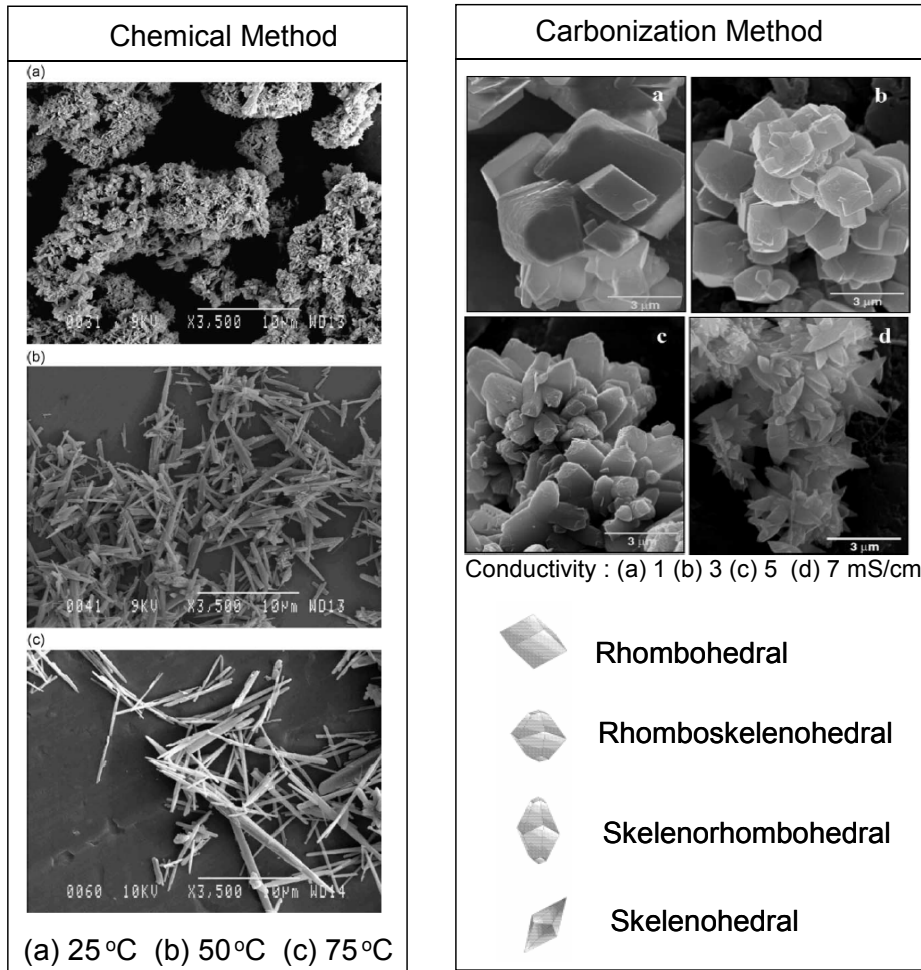
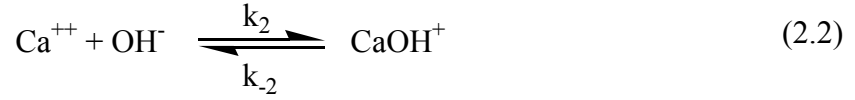
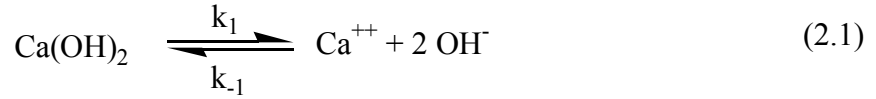


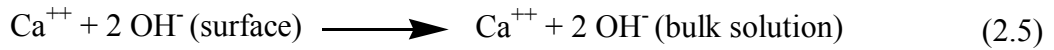
Figure 2.5. Production of CaCO_3 by Chemical and Carbonization methods^{16,65}.

2.4. Transport Processes in CaCO_3 Crystallization

There are mainly three processes in CaCO_3 crystallization. These are the dissolution of Ca(OH)_2 , CO_2 absorption, and CaCO_3 crystallization. The first step in CaCO_3 crystallization is the Ca(OH)_2 dissolution as shown in Eq(2.1). The complexation of Ca^{++} with OH^- ions in solution is given by Eq(2.2). The ionization of water is also considered in Eq(2.3).



Two methods were reported for the dissolution kinetics of Ca(OH)_2 . These are a rotating disk with a chunk of Ca(OH)_2 slab and Ca(OH)_2 powder. Wang et al. (1998)⁷¹, studied the dissolution mechanism of Ca(OH)_2 by the rotating disk method and reported that while the Ca^{++} ions were dissolved into the solution, OH^- ions were left on the surface as shown in Eq (2.4). The OH^- ions were released from the surface when attacked by the free Ca^{++} ions in the solution as shown in Eq (2.5).



The dissolution of Ca(OH)_2 in powder form was studied by Johannsen and Rademacher (1999)⁷² indicating that the particle size, and, therefore the surface area are the main factors in Ca(OH)_2 dissolution. They suggested a kinetic rate equation for the Ca(OH)_2 dissolution as shown in (2.6) and reported a forward rate constant, k_f of $1.6 \times 10^{-4} \text{ M m}^2\text{s}^{-1}$ and backward rate constant, k_b of $55.0 \text{ M}^2 \text{ m}^2\text{s}^{-1}$.

$$R = \frac{1}{A} \frac{d[\text{Ca}^{++}]}{dt} = k_f - k_b \cdot (a)_{\text{Ca}^{++}} \cdot (a^2)_{\text{OH}^-} \quad (2.6)$$

where R is the dissolution rate of Ca(OH)_2 , A is the surface area, and a is the activity for Ca^{++} and OH^- ions which is defined as $a = \gamma_i \cdot C_i$; for which γ_i is activity coefficient for the ion, i , given as

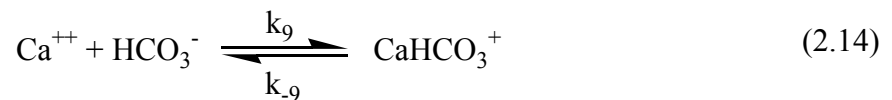
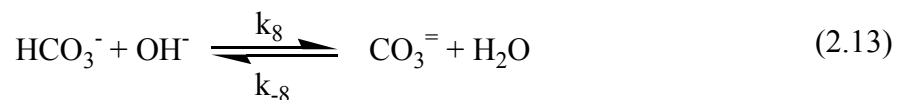
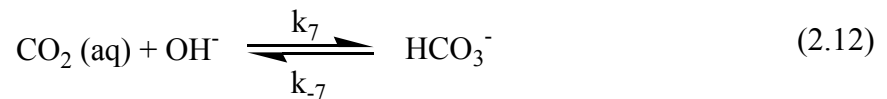
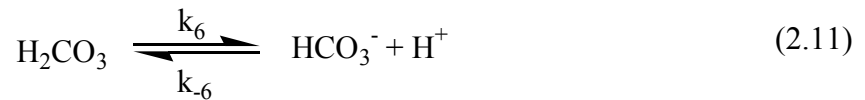
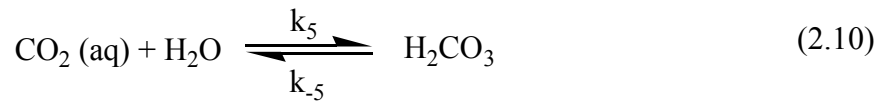
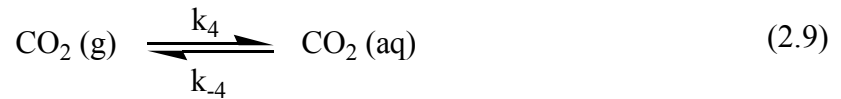
$$\log \gamma_i = -Az_i^2 \left(\frac{\sqrt{I}}{1 + \sqrt{I}} - 0.3I \right) \quad (2.7)$$

where A is a constant, and I is the ionic strength of the solution given as

$$I = \frac{1}{2} \sum c_i \cdot z_i^2 \quad (2.8)$$

It was shown that the dissolution of Ca(OH)_2 was increased linearly with its concentration up to about 18 - 25 mM which is the saturation concentration for Ca(OH)_2 ⁷³. However, the dissolution of Ca(OH)_2 was 20% lower than its theoretical solubility values, especially at higher concentrations. Burns and Juckhuk (2005)⁷³, also reported a 24 % of reduction in dissociation of Ca(OH)_2 from its theoretical values indicating that there would be incomplete dissolution of Ca(OH)_2 in aqueous solution. Unfortunately, the incomplete dissolution of Ca(OH)_2 on the CaCO_3 crystal size, size distribution, and crystal morphologies have not clearly been shown in the current literature.

The second step in CaCO_3 crystallization is the CO_2 absorption. In this case, the CO_2 should undergo a number of transformations, such as the transport from gas phase into the liquid phase through a gas-liquid interface, (Eq (2.9)), hydration by water (Eq (2.10)), ionization (Eq (2.11)), carbonate formation (Eq (2.13)), and complexation (Eq (2.14))⁷⁴. Among these, the hydration of CO_2 (Eq (2.10)) is the slowest step. When the pH is higher than 10, Eq (2.12) dominates. When the pH is less than 8, Eq (2.12) is negligible.



Reactive absorption of CO₂ in suspension of lime has been studied extensively⁷⁵⁻⁷⁹. The CO₂ absorption in a slurry of Ca(OH)₂ can be modeled with a two film model as shown in Figure 2.6.

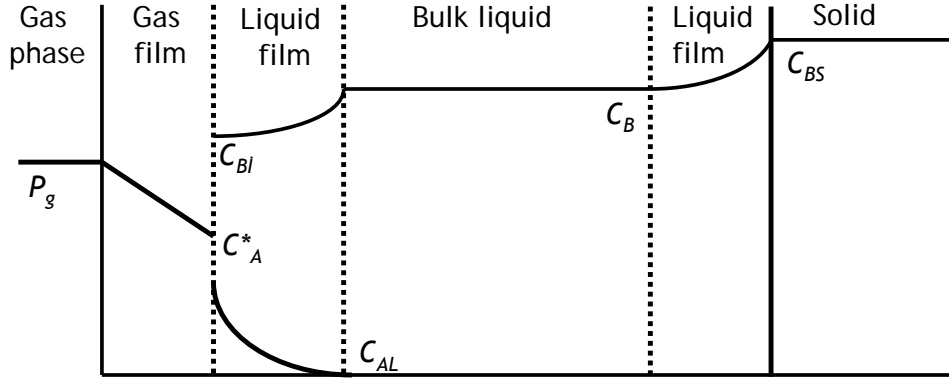


Figure 2.6. Two film model for CO₂ absorption in Ca(OH)₂ slurry (C_{Bi} : Concentration of OH⁻ ions at gas-liquid interface; C_B : Concentration of OH⁻ ions in bulk liquid phase C_{BS} : saturation concentration of OH⁻ ions in aqueous solution in equilibrium with Ca(OH)₂ (solid)⁴³).

Here, the transport rate of CO₂ through the gas film can be given as^{43,75}

$$N = k_g a (P_g - P_{gi}) \quad (2.15)$$

where N is the absorption rate of CO₂, k_g is mass transfer coefficient in the gas film, a is the gas-liquid surface area, P_g and P_{gi} are partial pressures of CO₂ in the gas phase and at the gas-liquid interface, respectively. The transport rate can also be expressed in terms of liquid side concentrations such that

$$N = k_L a (C_A^* - C_{AL}) \quad (2.16)$$

where k_L is the liquid side mass transfer coefficient, C_A^* and C_{AL} are the concentrations of CO₂ at the gas-liquid interface and the bulk liquid, respectively. It was assumed that, the bulk liquid is well agitated so that, there are no concentration gradients in the bulk liquid.

The concentrations at the gas-liquid interface can be related to each other by the Henry's Constant (H)

$$P_{Ai} = H C_A^* \quad (2.17)$$

The absorption of CO₂ in the liquid film will be enhanced considerably due to the reaction of CO₂ with the OH⁻ ions. The enhancement factor will be dependent on the liquid side mass transfer coefficient (k_L) in the absence of chemical reaction, [OH⁻] concentration, the diffusivities of CO₂ and OH⁻ ions in the liquid phase (D_A and D_B), and the rate constant (k_2) for the reaction between CO₂ and OH⁻. Therefore, when the OH⁻ concentration gradient between the bulk liquid and gas-liquid interface is none or negligible, the CO₂ transfer rate can be given as⁷⁵

$$N = C_A^* a \sqrt{D_A k_2 C_B^{bulk}} \quad (2.18)$$

where C_B^{bulk} is the [OH⁻] concentration in the bulk liquid. Here, the following conditions must be satisfied when the chemical reactions take place within the liquid film.

$$\frac{\sqrt{D_A k_2 C_B^{bulk}}}{k_L} \gg 1 \quad (2.19)$$

$$\frac{\sqrt{D_A k_2 C_B^{bulk}}}{k_L} \ll \frac{C_B^{bulk}}{z C_A^*} \sqrt{\frac{D_B}{D_A}} \quad (2.20)$$

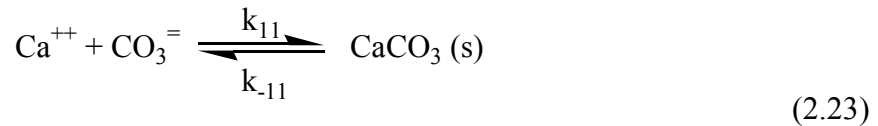
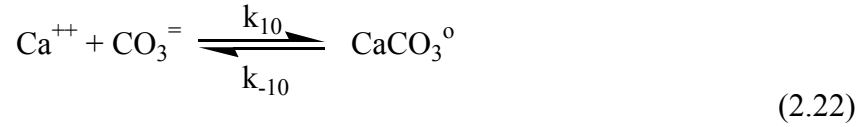
If the conditions presented in Eq(2.19) and Eq(2.20) were not satisfied, this means that the part of the chemical reaction between CO₂ and OH⁻ are carried out at the liquid film, and the other part in the bulk solution. In this case, the CO₂ mass transfer rate could be related to:

$$N = C_A^* a \sqrt{D_A k_2 C_B^{bulk} + k_L^2} \quad (2.21)$$

It is clear that the CO₂ absorption rate is proportional to CO₂ concentration (C_A^*) at the gas-liquid interface, which is related to the partial pressure of CO₂ in the gas phase by the Henry's Constant, the bulk concentration of OH⁻ (C_B^{bulk}) in solution, the reaction rate constant (k_2), the liquid side mass transfer coefficient (k_L), and the interfacial area (a) between the gas and liquid phases. Therefore, the CO₂ transfer rate

can be thought to be affected mostly by the interfacial surface area, OH⁻ concentrations and CO₂ partial pressures.

The third step in CaCO₃ crystallization is the nucleation and precipitation of CaCO₃. The reactions can be given as



The driving force for the formation of CaCO₃ in the saturated solution can be explained thermodynamically by the Gibbs free energy given as

$$-\Delta G = \eta RT \ln S \quad (2.24)$$

Here, ΔG is the Gibbs free energy in terms of the dissolution of the solid phase (J/mol); R is the ideal gas constant (J/mol.K); T is the temperature (K); and S is the saturation rate. The saturation rate for CaCO₃ can be given as

$$S = \left(\frac{IAP}{K_{sp}} \right)^{\frac{1}{\eta}} = \left(\frac{[\text{Ca}^{2+}][\text{CO}_3^{2-}]}{K_{sp}} \right)^{\frac{1}{2}} \quad (2.25)$$

Here, IAP is the ionic activity product, K_{sp} is the dissolution constant and its value is defined under standard conditions. However, the concentrations of Ca⁺⁺ and CO₃⁼ ions would not be in equal ratios as occurred during the dissolution of pure CaCO₃ in an aqueous solution. Therefore, these concentrations need to be calculated accounting the Eq (2.1)-(2.3), Eq (2.9)-(2.14), and Eq (2.22)-(2.23) or the actual concentrations need to be evaluated by the developed software programs such as MINTEQC and PREEQC, etc.^{16,78}

Nucleation rate increases proportionally with the super saturation, S . The critical nucleation rate is given by Eq (2.26) in terms of m^3/s or m^2/s .

$$J = k_2 S^2 \exp\left(\frac{-W^*}{k_B T}\right) = k_j S^2 \exp\left(\frac{-B}{\ln^2 S^2}\right) \quad (2.26)$$

Here, W^* is the critical work for nucleation in Joule, k_B is the Boltzmann's constant ($1.3806 \cdot 10^{-23}$ Joule K^{-1}); B is the dimensionless thermodynamic parameter, and k_j is the temperature dependent - kinetic parameter which also depends on the type of nucleation (for homogeneous nucleation m^3/s or for 2D nucleation m^2/s).

After critical nuclei were created or they were introduced directly to the media, a continuous crystal growth will occur in a sequential series of steps. The crystal formation rate generally follows a parabolic trend with saturation

$$G = K_G (S - 1)^2 \quad (2.27)$$

Here, K_G is coefficient of average linear velocity of crystallization ($\mu\text{m}/\text{s}$).

The initial crystal growth rate (\dot{r}) can be transformed into the linear form²⁶

$$\dot{r} = \frac{K_j V \sigma v}{kT} \cdot \frac{S}{\ln S} \cdot \exp\left(-\frac{B}{\ln^2 S}\right) + K_G (S - 1)^2 \quad (2.28)$$

where, K_j is nucleation rate constant, V is the volume of the solution, v is molecular volume and σ is interfacial tension.

Here, the crystal growth rate has two components; one is the nucleation rate, while the other is the growth rate. Spanos and Koutsoukos, (1998)²⁶ reported the experimental and theoretical growth rate for CaCO_3 in the form of vaterite as shown in Figure 2.7. As can be seen in the figure, the crystal growth rate by size is proportional to the saturation level of the solution. When saturation increases, both the crystallization

rate, as well as particle size will increase. It can be inferred from the figure that the particle could be controlled at low saturation levels.

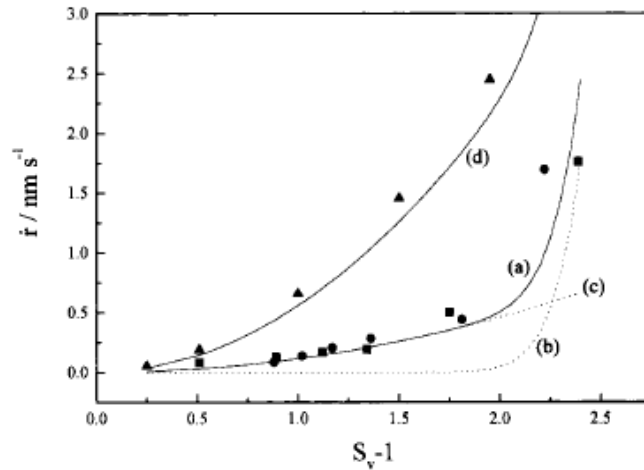


Figure 2.7. Experimental rates of precipitation of vaterite obtained at pH values 9.0 and 10.0. Curves c and b represent the growth and nucleation contribution to the total rate of precipitation (curve a)²⁶.

The selected reaction rates and equilibrium constants corresponding to the chemical reactions occurred in the CaCO_3 crystallization are given in Table 2.2. As shown in the table, the slow reactions in CaCO_3 crystallization could be the dissolution of Ca(OH)_2 , the hydration of CO_2 , and the nucleation and crystallization rates of CaCO_3 . Here, the dissolution of Ca(OH)_2 and the formation of CaCO_3 were reported as fast reactions compared to the hydration of CO_2 ^{16,40,80}. The hydration of CO_2 could be the rate determining step of the crystallization and might be enhanced by using CA enzyme.

Table 2.2. Reactions and reaction rate constants for the CaCO₃ precipitation

		Reaction	Rate Constants				Equilibrium Constants		Ref.
			Forward	Unit	Backward	Unit		Unit	
Dissolution of Ca(OH) ₂	1	$\text{Ca(OH)}_2 \xrightleftharpoons[k_{-1}]{k_1} \text{Ca}^{++} + 2 \text{OH}^-$	1.6×10^{-4}	$\text{M.m}^{-2}.\text{s}^{-1}$	55	$\text{M}^{-2}.\text{m}^{-2}.\text{s}^{-1}$	2.91×10^{-6}	M	72
	2	$\text{Ca}^{++} + \text{OH}^- \xrightleftharpoons[k_{-2}]{k_2} \text{CaOH}^+$					19.3		78
	3	$\text{H}^+ + \text{OH}^- \xrightleftharpoons[k_{-3}]{k_3} \text{H}_2\text{O}$					6.76×10^{13}		81
CO ₂ Absorption	4	$\text{CO}_2(\text{g}) \xrightleftharpoons[k_{-4}]{k_4} \text{CO}_2(\text{aq})$					2.98×10^{-2}	M.bar^{-1}	82
	5	$\text{CO}_2(\text{aq}) + \text{H}_2\text{O} \xrightleftharpoons[k_{-5}]{k_5} \text{H}_2\text{CO}_3$	4.68×10^{-2}	s^{-1}	40.7	s^{-1}	1.15×10^{-3}		81
	6	$\text{H}_2\text{CO}_3 \xrightleftharpoons[k_{-6}]{k_6} \text{HCO}_3^- + \text{H}^+$	1.0×10^7	s^{-1}	5.0×10^{10}	$\text{M}^{-1}.\text{s}^{-1}$	2.0×10^{-4}	M	83
	7	$\text{CO}_2(\text{aq}) + \text{OH}^- \xrightleftharpoons[k_{-7}]{k_7} \text{HCO}_3^-$	1.24×10^4	$\text{M}^{-1}.\text{s}^{-1}$	3.86×10^{-4}	s^{-1}	3.21×10^7	M^{-1}	81
	8	$\text{HCO}_3^- + \text{OH}^- \xrightleftharpoons[k_{-8}]{k_8} \text{CO}_3^{=} + \text{H}_2\text{O}$							
	9	$\text{Ca}^{++} + \text{HCO}_3^- \xrightleftharpoons[k_{-9}]{k_9} \text{CaHCO}_3^+$					13.7		78
CaCO ₃ Formation	10	$\text{Ca}^{++} + \text{CO}_3^{=} \xrightleftharpoons[k_{-10}]{k_{10}} \text{CaCO}_3^0$	2.0	$\text{M}^{-1}.\text{s}^{-1}$	1.0×10^{-3}	s^{-1}	2.0×10^3	M^{-1}	83
	11	$\text{Ca}^{++} + \text{CO}_3^{=} \xrightleftharpoons[k_{-11}]{k_{11}} \text{CaCO}_3(\text{s})$					3.02×10^8		84

The possible concentration profiles for the species in CaCO_3 crystallization by the carbonization method were given by Lin et al., (2006)⁴³ as shown in Figure 2.8. The concentration profiles for the Ca^{++} and OH^- ions from the dissolution of $\text{Ca}(\text{OH})_2$ are shown on the right side of the figure. Here, the diffusion of Ca^{++} and OH^- ions in the liquid film around the dispersed $\text{Ca}(\text{OH})_2$ solid particles were shown. As expected the OH^- ion concentration is higher than Ca^{++} ion concentration. On the left hand side, the diffusion of CO_2 through a gas film was shown. Here, the CO_2 dissolves in the gas-liquid interface. During this process, the CO_2 reacts with the OH^- ions at the interface and their concentrations decrease simultaneously. As a result, the concentration of $\text{CO}_3^{=}$ ions increase in the liquid film. At the same time, Ca^{++} and $\text{CO}_3^{=}$ ions form CaCO_3^0 nuclei and their concentrations decrease in the solution. In the middle, growth of a CaCO_3 crystal particle is seen. Here, the CaCO_3 nuclei cause the growth of CaCO_3 particle and the Ca^{++} and $\text{CO}_3^{=}$ ions were not shown. In this model, both $\text{Ca}(\text{OH})_2$ and CaCO_3 solid particles were present in the solution. However, the effect of $\text{Ca}(\text{OH})_2$ on the CaCO_3 particle size, size distribution and morphology were not identified.

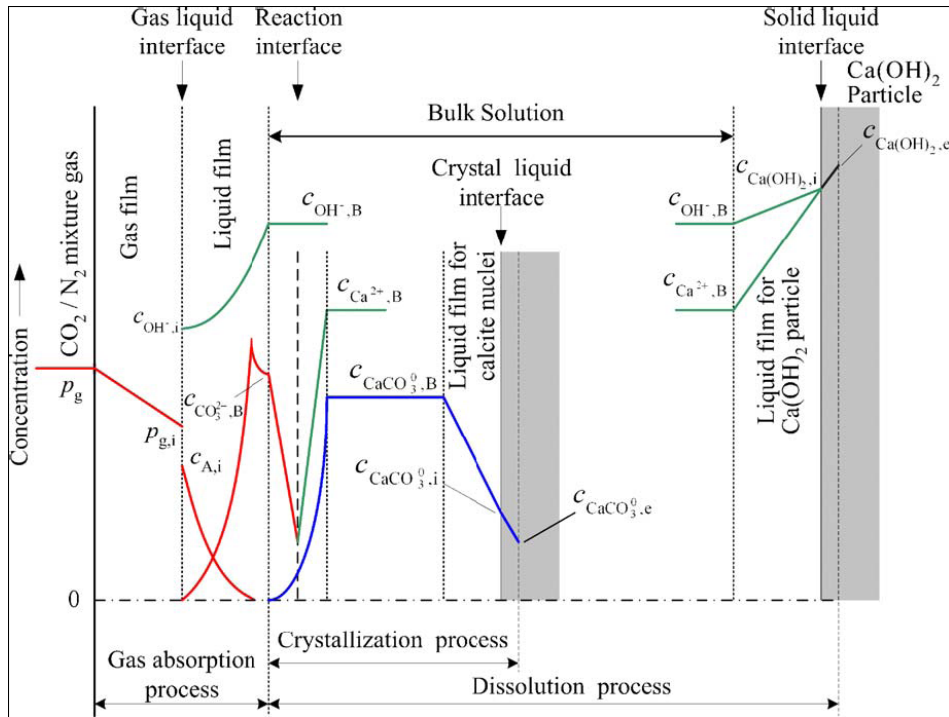


Figure 2.8. Proposed concentration profiles for species in the production of CaCO_3 ⁴³.

2.5. CaCO₃ Crystallization Mechanisms

CaCO₃ crystallization mechanism has been studied extensively with respect to nucleation rate and the crystal growth because it was taken as the model to many other crystallization processes. Therefore, there are a large number of publications on the CaCO₃ crystallization in literature. Classical models developed so far was replaced by new (novel) models, especially for the last 2-3 years, published by two *Science* articles in 2008 and 2009^{25,28}. However, there are still uncertainties in crystallization mechanisms. Figure 2.9 shows the classical and novel crystallization⁸⁵. As shown in the figure, some nucleation clusters will form from the complexation of Ca⁺⁺ and CO₃⁼ ions in solution and grow to sizes larger than 3 nm to form primary nanoparticles known as the nucleus. The single crystals will grow from these primary nanoparticles by amplification. The primary nanoparticles can also arrange to form an iso-oriented crystal, where the nanocrystalline building units can crystallographically lock in and fuse to form a single crystal. If the primary nanoparticles get covered by a polymer or other additive before they undergo a mesoscale assembly, they can form a mesocrystal. Mesocrystals can even form from pure nanoparticles. There is also the possibility that amorphous particles are formed, which can transform to more complicated morphologies. As can be seen from the classical crystallization theory, there should first form nuclei and then grow to form stable crystals.

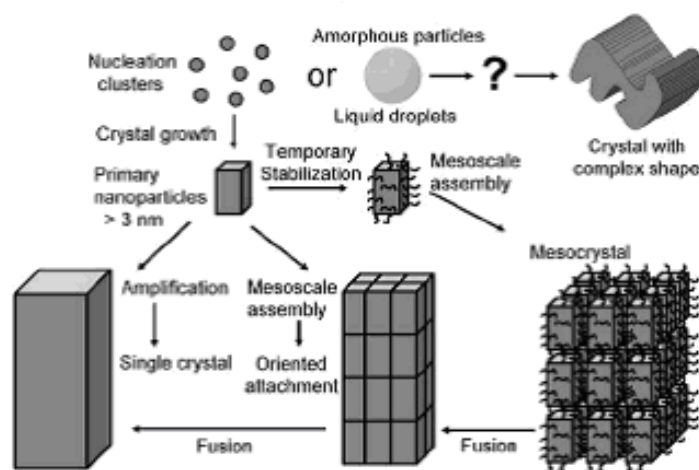


Figure 2.9. Schematic representation of classical and novel crystallization¹³.

Based on a new model suggested by Gebauer et al. (2008)²⁸, stable CaCO_3 clusters will form from Ca^{++} and $\text{CO}_3^{=}$ ions in solution as shown in Figure 2.10. These ions and clusters are in equilibrium, which is pH dependent.



The number of ions, n , in a cluster remains unknown. They indicated that the hydrodynamic diameter of a cluster is about 2 nm, and at this size, about 70 of Ca^{++} and $\text{CO}_3^{=}$ ions would be combined in a single cluster on average. These clusters detected during pre-nucleation step almost disappeared or became invisible after the nucleation step, indicating that the nucleation took place through the cluster aggregation, forming amorphous CaCO_3 particles. They also suggested that the calcite, vaterite, or aragonite are produced from the different form of the amorphous phases such as ACC I for calcite and ACC II for vaterite, but, the ACC form for aragonite was unclear. The nucleation phenomena of different ACC phases were also unknown. It is clear that stable clusters would form during the CaCO_3 crystallization even in the absence of nucleation, and an amorphous structure will form before the crystallization²⁸.

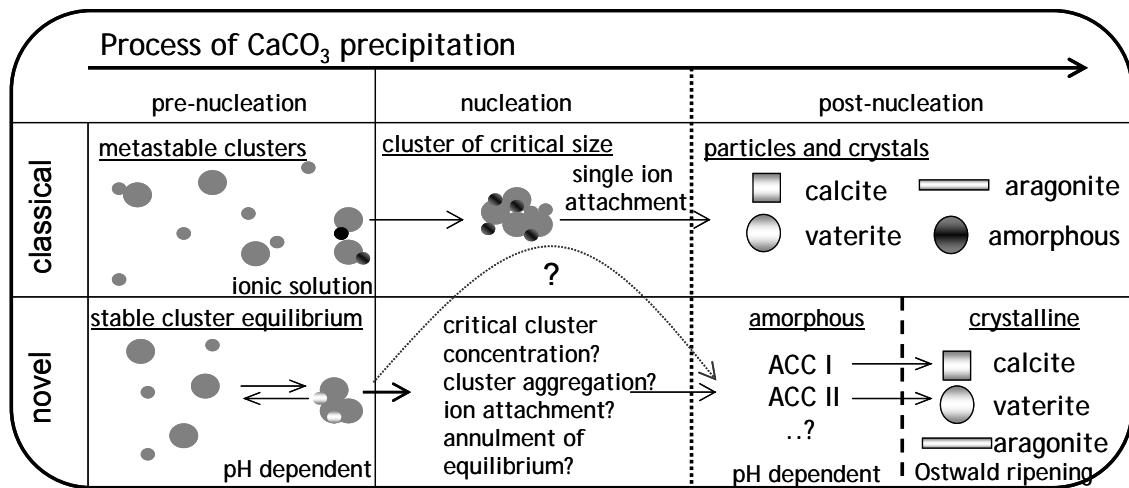


Figure 2.10. The classical and novel CaCO_3 crystallization mechanism suggested by Gebauer et al. (2008)²⁸.

In a study by Pouget et al. (2009)²⁵, a template-controlled CaCO_3 crystal formation mechanism and their possible sizes were reported as shown in Figure 2.11. In their model, about 0.6 to 1.1 nm of stable clusters were formed from Ca^{++} and $\text{CO}_3^{=}$

ions. Aggregation of these clusters in solution was resulted in nucleation of ACC nanoparticles with an average particle size of about 30 nm. These particles were associated with the surface of the organic matrix as the template and started to grow. With the participation of new ions and clusters, approximately 70-300 nm amorphous particles were emerged. Arrangement of ions in the amorphous phase was resulted in the development of crystal formation. While the particles grow, a crystallization zone stabilized by the template would be created. Thus, the growth and formation of a particle greater than 500 nm were completed. Here, it was claimed that the nanoparticles were in equilibrium with ions and clusters in solution, and therefore the formation of large particles would occur as a result of the dissolution and the re-precipitation of these particles²⁵. It is possible that the size of nano particles would be the result of an equilibrium state.

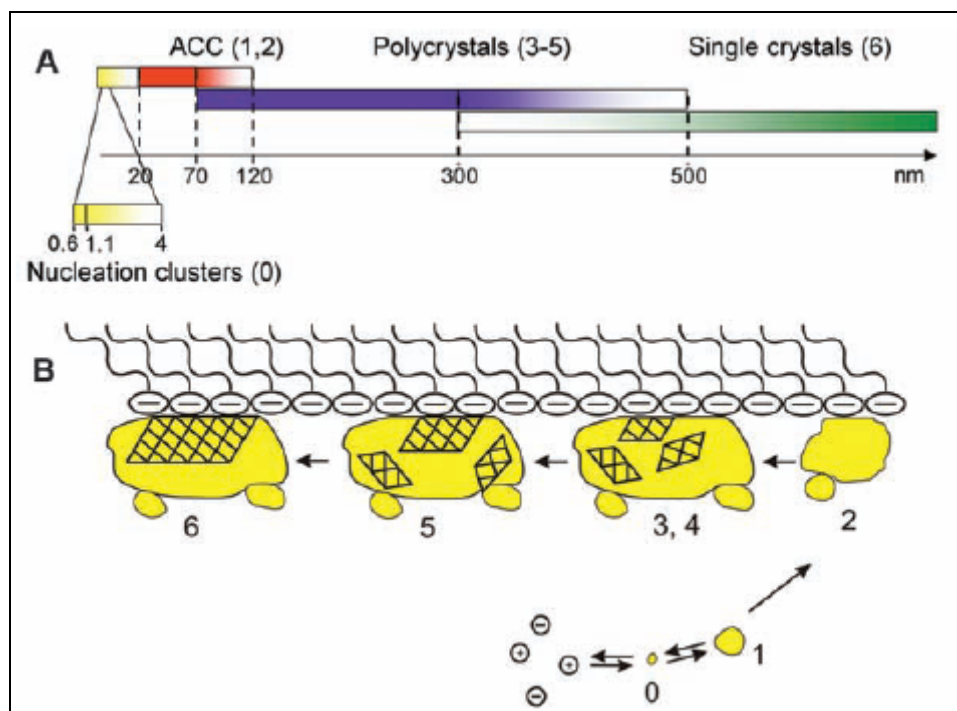


Figure 2.11. The different stages of template-controlled calcium carbonate formation²⁵.

2.6. Important Turning Points in Nano CaCO₃ Production

There are special configurations in literature that nano CaCO₃ particles were synthesized. For instance, it was argued that the CO₂ absorption rate would have a significant effect on the CaCO₃ crystallization. Wu et al., (2007)⁸⁶ therefore suggested that a micropore membrane could be used to enhance the CO₂ absorption. They placed a

microporous membrane with a 10 μm pore size at the bottom of a column reactor having 7 cm in diameter and 20 cm in height and they injected the CO_2 through these micropores into the $\text{Ca}(\text{OH})_2$ solution. Because the diameter of the gas bubbles were so small, they could manage to effectively distribute the CO_2 in the solution and achieve to produce CaCO_3 particles with sizes less than 200 nm.

In a similar study, the same group repeated the same success producing about 100 nm of CaCO_3 particles by using a membrane reactor⁸⁰ as shown in Figure 2.12. In their set-up, the $\text{Ca}(\text{OH})_2$ solution was circulated by a pump between the membrane mini reactor and the constant stirring tank. They measured the pH values in the stirring tank and after the membrane mini reactor in order to understand the completion of the crystallization. While pH was decreasing at the exit of the membrane mini reactor, the pH was still high in the stirring vessel. Especially, the difference was significant during the completion of the crystallization. It could be possible that while the CaCO_3 clusters were formed in the membrane mini reactor, stabilization would be achieved in the stirring tank so that nano CaCO_3 could be produced.

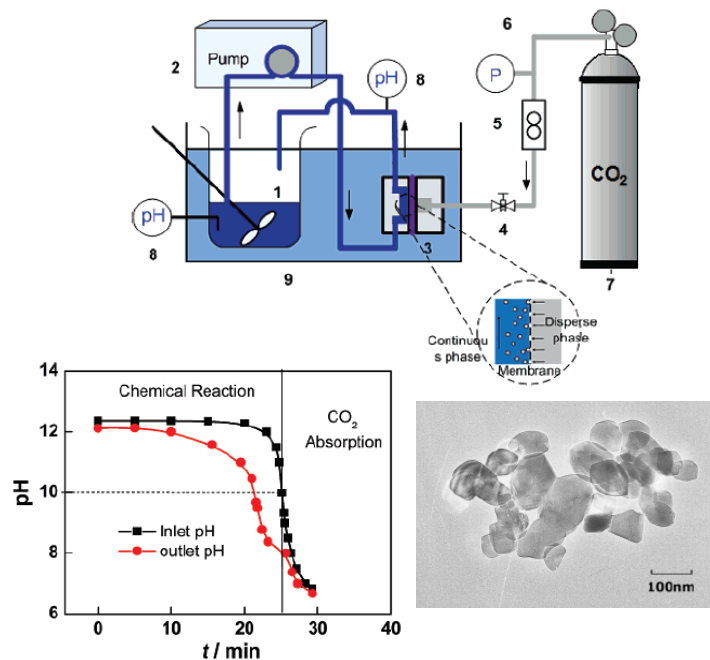


Figure 2.12. CaCO_3 production in micro membrane reactor (a) Schematic of the process 1, continuous phase vessel; 2, measuring pump; 3, membrane dispersion minireactor; 4, valve; 5, flow meter; 6, pressure gauges; 7, source of the mixed gas; 8, pH indicator; 9, temperature control bath. (b) Change of pH values with reaction time at the inlet and the outlet of the reactor. (c) TEM images of CaCO_3 particles prepared by the minireactor⁸⁰.

It could be possible to produce nano CaCO_3 with different morphologies by adjusting the reactor configuration. For example, Jung et al. (2000)¹⁷, could produce CaCO_3 particles with the sizes of less than 1 μm with an oval shape by applying shear in a Couette–Taylor reactor. When shear stress was increased, the morphologies of the calcite particles changed from cube shape into a needle-like shape. Considering various applications in different fields, producing calcite with such morphologies could be important.

In order to produce nano CaCO_3 particle with a narrow size distribution, Chen et al., (2000)³⁹ suggested that the reaction / nucleation section and the crystal growth section should be separated from each other in a crystallization. They indicated that the particle size distribution in a stirring reactor could not be achieved at the desired levels considering the characteristic nucleation time is about less than 1 micro second (μs) in an aqueous phase, and the mixing time of ions in molecular level is about 5-50 milliseconds (ms). In order to separate the nucleation and growth section, they used a High-Gravity reactor as shown in Figure 2.13. The reactor consisted of a fixed bed rotated on its own axis. While the $\text{Ca}(\text{OH})_2$ solution flow through the fixed bed under the influence of high gravity, it was separated into a thin film in the reactor and small droplets. Therefore, the mixing rate could be increased at the gas-liquid interface and the mixing time could be reduced to about 10-100 μs . In this reactor, $\text{Ca}(\text{OH})_2$ solution were recirculated to the mixing tank after a short contact time between $\text{Ca}(\text{OH})_2$ and CO_2 gas by a pump until the crystallization was completed. As can be seen in the figure, nano CaCO_3 particles could be produced with almost a homogeneous size distribution.

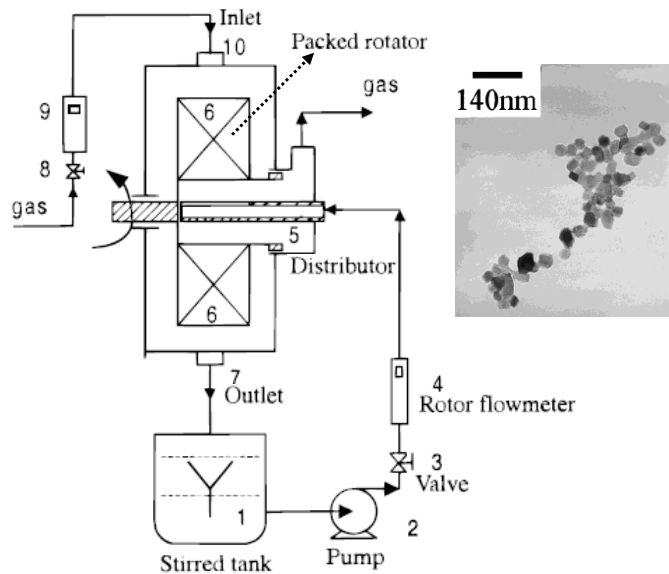


Figure 2.13. CaCO_3 production under the influence of high gravity³⁹. 1, stirred tank; 2, pump; 3, valve; 4, rotor flowmeter; 5, distributor; 6, packed rotator; 7, outlet; 8, valve; 9, rotor flowmeter; 10, inlet

The CaCO_3 crystallization process was modeled by Vucak et al. (2002)⁷⁸, in a solution in the presence of monoethanolamine. The possible changes in the concentrations during the crystallization were shown in Figure 2.14. As shown in the figure, the CaCO_3 nucleation was increased in 30 min. Afterwards, CaCO_3 crystals began to appear in the solution. There was a significant increase in the crystallization rate during the completion of the crystallization. Here, it can be concluded that the particle size and size distribution could be affected especially during the completion stage of the crystallization. In addition, as shown in the figure, the chain-like and aggregated particles were produced. In CaCO_3 crystallization, the changes and the crystal completion step must be carefully investigated, and the necessary improvements need to be made.

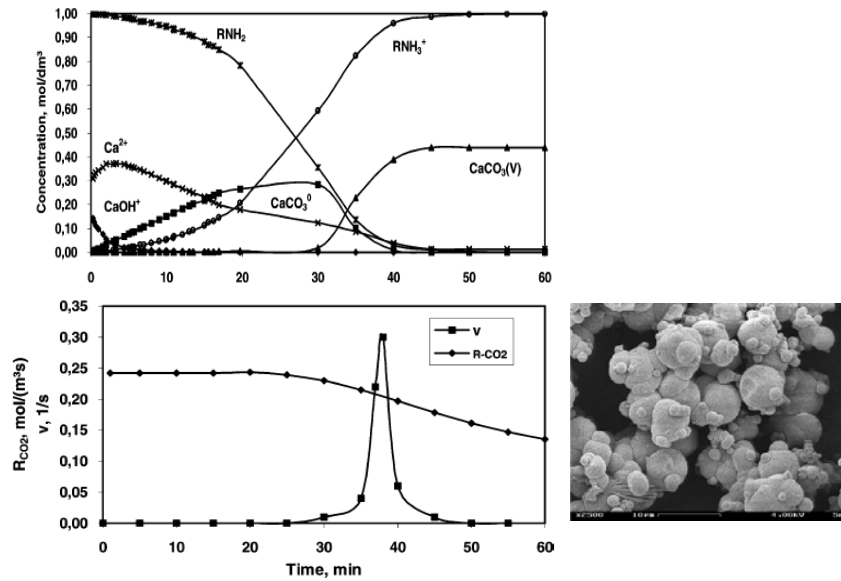


Figure 2.14. Absorption rate of CO₂ and rate of precipitation process⁷⁸

Effect of pH on the CaCO₃ crystallization rate, particle size and size distribution were investigated. Wang et al., (1998)⁷¹ reported that the Ca(OH)₂ dissolution rate decreased at pH between 4 and 7. Because pH value is generally greater than 12 during CaCO₃ crystallization, the Ca(OH)₂ dissolution rate would be much lower at these pH levels. Therefore, the formation rate of Ca⁺⁺ and OH⁻ ions would be low during the initial CaCO₃ crystallization in a Ca(OH)₂ slurry. The neutralization of OH⁻ ions and the production of CO₃⁼ ions were achieved by the dissolution of CO₂. When the CO₃⁼ ions react with Ca⁺⁺ ions, stable CaCO₃ would form. However, the types of ions and the electrical charges on the clusters and on the growing particles could be different at various pH. As shown in Figure 2.15, Fenter et al., (2000)⁷⁰ reported that the surface of CaCO₃ particles would be negatively charged ($\equiv\text{CaCO}_3^-$) at higher pH's (pH>10), and it would be positively charged ($\equiv\text{CO}_3\text{Ca}^+$) at lower pH's (pH<8). At pH's between 8 and 10, the surface would be covered by water molecules and become positively charged ($\equiv\text{CaOH}_2^+$). Because pH decreases suddenly at the completion stage of the crystallization, the changes in the sizes of the CaCO₃ crystals, the changes in the surface charges, and the tendency of aggregation formation must be considered.

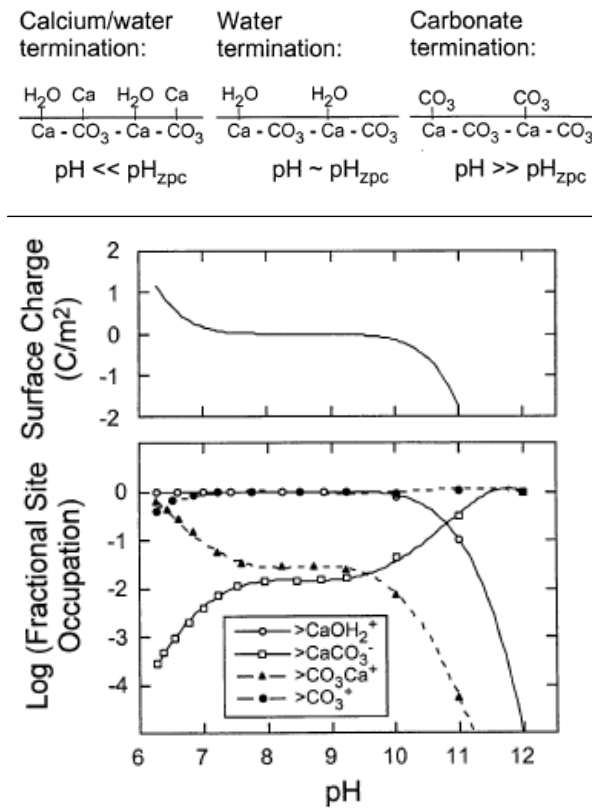


Figure 2.15. The predicted variation of the calcite surface speciation as a function of pH with a schematic summary of the different surface terminations, and the predicted the most abundant surface speciation as a function of pH under conditions of calcite–water equilibrium ($P_{\text{CO}_2} = 5 \cdot 10^{-3.5}$ atm; $T = 25^\circ\text{C}$)⁷⁰.

The CaCO_3 crystal size and size distribution may be controlled by the slow dissolution rate of CO_2 . In literature, the supersaturation level of the solution was considered to be the main parameter in the CaCO_3 crystallization kinetic as indicated in Eq (2.28). Here, the supersaturation is related to the multiplication of the concentrations of the two Ca^{++} and $\text{CO}_3^{=}$ ions, Eq (2.25). However, the effect of different concentrations of these ions on the crystal size and size distribution were not thoroughly investigated, until the attention was given for the first time in 2007. As shown in Figure 2.16, when the ratio of Ca^{++} and $\text{CO}_3^{=}$ concentrations was 1.0 the crystallization rate was maximum, when this ratio was greater or higher than 1.0, the crystallization rate decreased⁸⁷. It can be seen from the figure that, the crystallization rate shows the same trend at different saturation levels. We think that if the $\text{CO}_3^{=}$ ions as a result of CO_2 dissolution were introduced to the solution in a controllable fashion, the CaCO_3 crystal size and size distribution could be controlled.

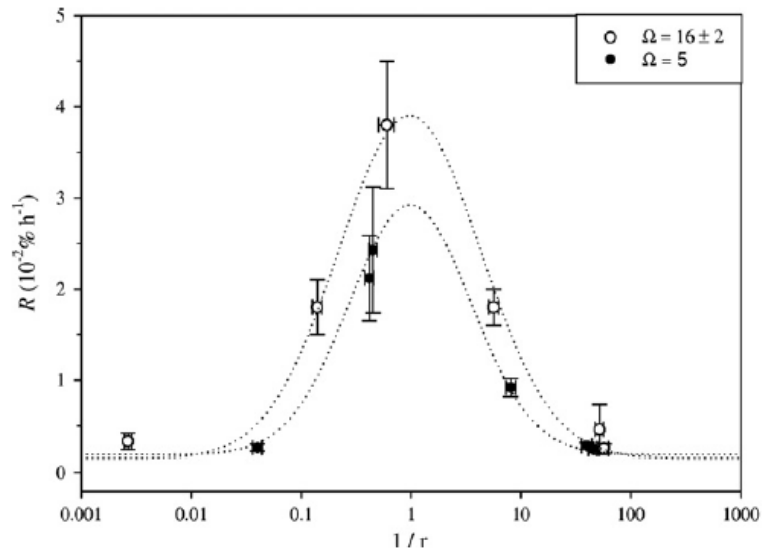


Figure 2.16. Growth rate (R) versus the inverse of the solution $[\text{Ca}^{++}]/[\text{CO}_3^{--}]$ ratio, r , for two different degrees of supersaturation with respect to calcite⁸⁷.

2.7. Factors Affecting CaCO_3 Production

There are many factors affecting the particle size distribution of precipitated CaCO_3 produced by carbonization method. The morphology and polymorph of PCC significantly depend on the local conditions of precipitation. Temperature, supersaturation, pH, CO_2 gas flow rate, CO_2 bubble diameter, stirring rate, molar ratio of reactants, the presence of additives, impurities, the type of polar functional groups contained in the additives, the number of polar functional groups per molecule, hydrophobic and hydrophilic regions, the molecular weight and the concentration of additives were considered to be the most important factors that influence crystallization⁵⁷. Monolayer properties (ionization, epitaxial matching, charge density, and head group orientation) were shown to affect the crystallization in some ways⁸⁸. Identity of a head group could also control the crystal growth. Supersaturation was usually considered to be the main controlling factor¹⁵. According to the general knowledge, low supersaturation, low temperature and weak water hardness is necessary for heterogeneous CaCO_3 precipitation. At high supersaturation, homogeneous nucleation became predominant⁸⁹. However, it is not only important which parameters control the crystallization, but also it is important how these parameters would control it.

Temperature itself was reported to have significant effect on the growth of CaCO_3 . At low temperatures, the calcite form can be possible to obtain, at higher temperatures, aragonite is possible to obtain⁹⁰. The solubility product decreases as temperature increases and it has the lowest for calcite, and the highest for amorphous calcium carbonate (ACC). Temperature should be higher in order to obtain aragonite and vaterite. Vaterite is often reported as the result of the aggregation of smaller nano-sized particles. However, if aragonite was obtained at lower temperatures, it would be due to the supersaturation conditions.

Surface charge neutralization is the major factor that affect the aggregation of the chain-like particles⁴⁰. When two nano particles come into contact, this means that, approximately infinite surface is created per volume. In that case, relatively higher particles occur by surface diffusion, annealing and even nucleation. This is the explanation of the mechanism for the morphology of the chain-like calcite. Electrical surface charge of the particles is reduced by adsorption of the anionic or cationic additives, and this is the reason for the primary aggregation. Nano particles in water create high specific surface area, and most of the additives are consumed to reduce the charges around the particles. However, neutralization of the particles is never being completed because of the lower molecular adsorption; so, aggregates are dispersed by repulsion due to the neutralization, but this phenomena occurs very weakly⁴⁰. If the surface charge of the particles in solution is completely removed, individual particles can be obtained by dispersion.

2.8. Effect of Additives

The morphology of the produced CaCO_3 crystals can be affected and changed by the additives⁹¹⁻⁹³. In order to minimize the particle size, various surfactants and additives have been used as modifiers such as terpineol⁹⁴, Dispex A40 and Dispex A40V⁹⁴, poly acrylic acid^{66,95}, octadecyl dihydrogen phosphate²⁷, EDTA⁹⁴, polyethylene glycol⁹⁶, poly (styrene-alt-maleic acid) (PSMA)⁹⁷, polyvinyl alcohol⁹⁶, zinc chloride, magnesium chloride⁹⁸, cetyltrimethyl ammonium bromide (CTAB)^{97,99} octadecyl dihydrogen phosphate⁹³, polyacrylamide, sodium dodecyl sulfite (SDS)^{89,100}, sodium dodecyl sulfonate (DDS)⁸⁹, sodium dodecyl benzene sulfonate (SDBS), amino acids and some proteins^{13,22,101}, stearic acid³⁴, carboxylic acid⁸⁷, oleic acid¹⁰², ethanol^{92,96,100} and

methanol⁹⁶. However, in the presence of additives, micron sized vaterite and aragonite structures occur in general. On the other hand, additives increase the cost of the product.

Surfactants were reported as dispersing agents to obtain monodisperse CaCO₃ as well as size reductive⁹⁵. Any long-chain surfactant has hydrophilic heads and hydrophobic tails. It has a significant effect on the surface charge of the CaCO₃ particles adsorbing both charged and uncharged surfaces. In order to see the effect of surfactant concentration on the surface charge of the CaCO₃ particles, zeta potential is measured at different pH values^{103,104}. The electrostatic interactions dominate the mechanism for the adsorption of surfactants. Since the growth of CaCO₃ crystals is controlled by surface processes, their growth morphology is quite sensitive to the aggregation state of the surfactants, which is mainly determined by the concentration. The critical micelle concentration values of surfactants are important at that point. At low concentration, surfactant monomers are dispersed in bulk solution. CaCO₃ molecules are much larger than surfactant molecules and, each crystal face can only adsorb surfactant molecules. Therefore, stable calcite crystals are generally formed in the presence of low concentrations of surfactant. When the surfactant concentration increases, aggregates formed providing below critical micelle concentration. If the surfactant concentration continues to increase over the critical micelle concentration, micelles are formed and their surface is covered by the little nuclei although the electrostatic interaction of CaCO₃ and the polar head groups of surfactant. Therefore, narrow size CaCO₃ production is induced⁸⁹.

Organic additives can also inhibit the precipitation reaction. At lower [CO₃⁼/Ca⁺⁺] ratios and lower pH values, natural organics inhibit the calcium carbonate precipitation more effectively. If the solution is undersaturated, adsorption of organics onto a mineral surface develops the dissolution of the mineral, otherwise, precipitation is inhibited. A significant decrease in precipitation rate can be explained by a Langmuir adsorption model.

Additives show a high affinity for Ca(OH)₂. During the dissolution period, ion concentrations of Ca⁺⁺, OH⁻, HCO₃⁻, CO₃⁼, CaOH⁺, CaHCO₃⁺, CaCO₃⁰ increase. When the additives present in solution, the concentration of their anionic or cationic forms also increase. During the consumption of Ca⁺⁺ and CO₃⁼ ions, especially agglomerated calcite occurs. After the complete consumption of the ions, aggregated crystals can be divided into individual crystals⁹⁵. On the other hand, the number of axial -OH⁻ comes from additives is reported to responsible for the degree of vaterite re-stabilization. As

the number of axial -OH^- ratio increases, the degree of vaterite re-stabilization also increases¹⁰⁵. The amphiphilic property of an organic solvent is a critical factor on the crystal forms and morphologies of CaCO_3 particles at high temperature⁹⁹. Additives can reduce or increase the energy barriers for nucleation steps. They reduce the local supersaturation to produce stable calcite¹⁰⁵. The other important effect of the additives on CaCO_3 production is to make nano particles hydrophobic¹⁰⁶.

CHAPTER 3

INTERPARTICLE RELATIONS AND COLLOIDAL STABILITY OF CALCITE –WATER SYSTEM

3.1. Electrostatic Double Layer around Calcite Particles

When $\text{Ca}(\text{OH})_2$ powders are added into the water, a solution or suspension is obtained depending on the concentration. A liquid – solid system is obtained with $\text{Ca}(\text{OH})_2$ powders at the beginning of the carbonization. The produced CaCO_3 in water is also a part of liquid – solid system. Powders have electrostatic charge surfaces in the presence of liquids. The net charge of the particle surface has influences on the ion distribution of surrounding interfacial region. The concentration of opposite charged ions (counter ions) to the particles increases due to the development of a net charge at particle surface. Therefore, the accumulation of charge on the surface of colloidal particles causes the formation of an electrical double layer (EDL) at the solid/liquid interface around each individual particle¹⁰⁷ as shown in Figure 3.1.

The liquid layer surrounding the particle consists of two parts: These are Stern layer (inner region) and diffuse layer (outer region). At Stern layer, ions are strongly bounded. They are less attached at diffuse layer. The ions and particles exist in a stable form in a conceptual boundary within the diffuse layer. A particle moves due to the gravity with ions and the boundary (the surface of hydrodynamic shear or slipping plane in Figure 3.1.). However, any ions beyond the boundary do not move with the particle. A potential exists at this boundary and called as the Zeta potential.

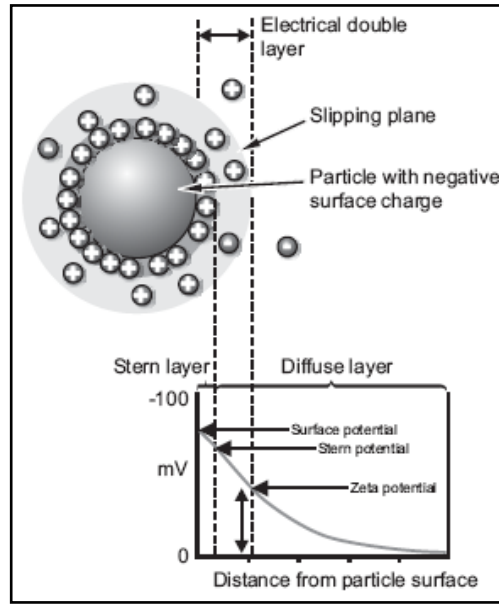


Figure 3.1. Electrokinetic phenomena and electrical double layer (EDL) around a particle¹⁰⁸

Oppositely charged ions in solution are attached at the surface (Helmholtz double layer model). Assuming the ions at solution side of double layer, at low electrolyte concentrations large thickness of solution may occur to accumulate ions in order to balance the surface charge (Gouy-Chapman model). As a result of thermal motion, the electrical charge increases with the distance from the particle surface and decreases with larger distance into the bulk liquid phase. In this theory, potential function is related to the Poisson-Boltzman equation. The potential profile in the diffuse layer is calculated by Eq (3.1 to 3.3) if the solution contains a single and symmetrical electrolyte¹⁰⁹.

$$\psi(x) = \frac{2RT}{zF} \cdot \ln \left[\frac{1 + \gamma \cdot e^{-\kappa x}}{1 - \gamma \cdot e^{-\kappa x}} \right] \quad (3.1)$$

$$\gamma = \frac{\left[e^{\frac{zF\psi_0}{2RT}} - 1 \right]}{\left[e^{\frac{zF\psi_0}{2RT}} + 1 \right]} \quad (3.2)$$

$$\kappa = \sqrt{\frac{2z^2 F^2 C_0}{RT\epsilon\epsilon_0}} \quad (3.3)$$

where, $\psi(x)$ is potential of the particle in solution at a point X (volts), R is gas constant (8.314 J/mol.K), T is temperature in Kelvin, z is valency of electrolyte (1.0 for water), F is Faraday constant (96484.5 C/mol), κ is reciprocal thickness of double layer (m^{-1}), H is the length of distance separating two particles, C_0 concentration of electrolyte (1 mM for water), ϵ is relative permittivity of water (78.5) and ϵ_0 is relative permittivity of vacuum ($8.854 \times 10^{-12} \text{ C}^2/\text{J.m}$).

High ionic strength causes the strong ionic attraction, makes the diffuse layer more compact and also causes the shielding effect. A potential field occurs around the particle and the field affects the interaction of particles. Therefore, stability of colloid is reached. The potential stability of the colloidal system is related to the magnitude of the zeta potential. If all the particles have a large zeta potential (negative or positive) then they will tend to repel each other and there is no tendency to aggregate. However, if the particles have low zeta potential, then there will be no force to prevent the particles coming together and particles will aggregate. Stability of molecular or ionic solutions is also known as a function of difficulty or slowness of the phase transition¹¹⁰. Particles with zeta potentials more positive than +30mV or more negative than -30mV are normally considered stable¹⁰⁹. Zeta potential is also the most effective parameter to calculate interaction energy between particles for the colloidal stability¹⁰⁹. Based on the thermodynamic view, all colloidal dispersions are naturally unstable and they have tendency for coagulation or cohesion by the reduction of the overall free energy of a dispersed system. However, providing a barrier against the association of dispersed phase can result in considerable stability by decrease the rate of association. The main reason for construction of a potential barrier against the coagulation is electrostatic.

When two identical-charged particles approach each other, their EDL's begin to overlap, causing a repulsive force. Due to the free energy change, the repulsive interaction between the EDL of two particles occur. Therefore, energy is needed to overcome this repulsion. When the particles contact each other, the repulsion energy has a maximum value. If the particles are outside the EDL, the energy approaches to zero. The maximum energy is related to the surface potential. The repulsive interaction (V_{el})

decreases exponentially with increase in the distance between the particles and it is calculated by Eq (3.4).

$$V_{el} = \frac{\pi\epsilon\epsilon_0 d_1 d_2}{2(d_1 + d_2)} \left[2\psi_1 \psi_2 \cdot \ln \left[\frac{1 + e^{-\kappa H}}{1 - e^{-\kappa H}} \right] + (\psi_1^2 + \psi_2^2) \ln(1 - e^{-2\kappa H}) \right] \quad (3.4)$$

where ϵ is relative permittivity of water (78.5), ϵ_0 is relative permittivity of vacuum (8.854×10^{-12} C²/J.m), d is diameter of particle, ψ_1 and ψ_2 are surface potentials of particle 1 and 2, κ is reciprocal thickness of double layer (m^{-1}) and, H is length of the distance separating two particles.

The thickness of EDL (κ) depends on the suspension composition, i.e., the activities and valence of ionic species present in the suspension. The bulk solution is commonly of the order of 3 - 4 κ . It also affects the electrostatic repulsive interaction between colloidal particles. Eq (3.4) express the electrostatic pair interaction potential of “thin” double layers (i.e, $\kappa < r_p$), and it is derived from the Debye–Hückel approximation for low surface potentials ($\psi < 25.7$ mV), and for symmetrical ($z^+ = z^-$) electrolytes¹⁰⁷.

The van der Waals forces basically describe the attractive interaction between especially polar molecules having permanent dipole moment. The properties of attractive interaction between large bodies and the related interaction coefficients (Hamaker constant) were developed by Hamaker (1937). The attraction energy is a result of interatomic electrical forces within particles and the Hamaker constant denotes them as a function of particle volume. The magnitude of the van der Waals interaction energy depends on the Hamaker constant of the particles i and j (A_{ij}), the particle size and the separation distance of the particles (H), and it is calculated by Eq (3.5).

$$V_{vdw} = - \frac{A_{ij} \cdot d_1 \cdot d_2}{12 \cdot (d_1 + d_2) H} \quad (3.5)$$

Hamaker constant is different for each separating spaces. Effective Hamaker constant must be derived for particles in different media. If colloidal dispersion consists of two identical particles, such as calcite – calcite in water ($A_{11} = A_{22}$), the effective Hamaker constant is calculated by Eq. (3.6).

$$A_t = A_{131} = \left(\sqrt{A_{11}} - \sqrt{A_{33}} \right)^2 \quad (3.6)$$

where, A_t is effective Hamaker constant of calcite - water colloidal dispersion, A_{11} is Hamaker constant of calcite in water A_{33} is Hamaker constant for water.

DLVO (Derjaguin, Landau, Verwey, and Overbeek) theory provides a strong explanation for the stability of colloidal dispersions¹¹¹. Colloidal interactions formulated on the basis of the DLVO theory are frequently used to investigate the natural phenomena, such as particle aggregation, coagulation, colloid deposition, and define colloidal stability¹¹². The theory is related to the total energy caused by two competitive forces between two particles: attractive forces (the van der Waals), and the repulsive (electrical double layer) forces¹¹³. The total energy is given by Eq (3.7).

$$V_{tot} = V_{el} + V_{vdw} \quad (3.7)$$

DLVO curves are obtained with the plotting of the total energy vs. distance between colloids as shown in Figure 3.2. At each distance, the net energy is obtained by the subtraction of the smaller value from the larger value. If the repulsive section occurs, the point of maximum repulsive energy is energy barrier of colloidal system. The height of the barrier denotes how stable the system is. If the barrier is removed, then the net interaction becomes only attractive, and the particles agglomerate¹⁰⁹.

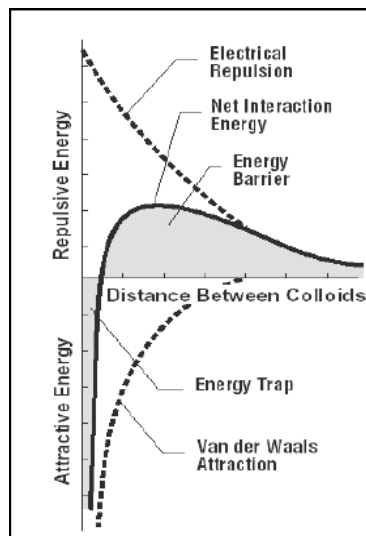


Figure 3.2. DLVO Curve¹⁰⁸

3.2. Settling of Particles

To determine the extent to which a particle or agglomerated solid clumps can be collected by gravitational settling, it is necessary to calculate the forces applied on the material. These forces are the gravitational force (F_g), buoyant force (F_b), and the drag force, (F_d).

The gravitational force F_g , which causes the particles and masses to fall, can be expressed by Eq (3.8).

$$F_g = m_p \cdot g = \rho_p \cdot V_p \cdot g = \rho_p \frac{\pi \cdot d_p^3}{6} \cdot g \quad (3.8)$$

where, F_g is force of gravity ($\text{kg} \cdot \text{m}^{-1} \text{sec}^{-2}$), m_p is mass of the particle (g), g is acceleration of particle due to gravity (9.81 m sec^{-2}), ρ_p is density of the particle (kg m^{-3}), d_p is particle diameter (μm) and V_p is volume of the spherical particle (m^3).

The buoyant force is the upward force that resist to downward force of gravity. The force of buoyancy depends on fluid density, while the gravitational force depends on particle density. Buoyancy occurs due to the fluid displaced by the particle and is given by Eq (3.9).

$$F_b = m_f \cdot g = \rho_f \cdot V_f \cdot g = \rho_f \frac{\pi \cdot d_p^3}{6} \cdot g \quad (3.9)$$

where, F_b is force of buoyancy ($\text{kg} \cdot \text{m}^{-1} \text{sec}^{-2}$), ρ_f is density of the fluid (kg m^{-3}).

When the particle begins to move downward as a result of gravity force, it encounters a resistive force that increases as the downward velocity increases. This force is called the drag force and is given by Eq (3.10).

$$F_d = \frac{A_p \cdot \rho_f \cdot v_p^2 \cdot C_D}{2} = \frac{\pi \cdot d_p^2 \cdot \rho_f \cdot v_p^2 \cdot C_D}{8} \quad (3.10)$$

where, F_d is force of drag ($\text{kg} \cdot \text{m}^{-1} \text{sec}^{-2}$), A_p is the cross-sectional area of the particle, v_p is velocity of the particle (m sec^{-1}), and C_D is dimensionless drag coefficient. The value of C_D is related to the velocity of the particle and the flow pattern of the fluid around

the particle. The other dimensionless number is Reynolds number (Re) and it is the ratio of interfacial effects to the viscous effects acting on the particle [Eq (3.11)].

$$\text{Re} = \frac{d_p \cdot \rho_f \cdot v}{\mu_f} \quad (3.11)$$

where, μ_f is viscosity of the fluid ($\text{kg m}^{-1} \text{sec}^{-1}$).

The net force (F_{net}) on the particle settling in a fluid is a combination of gravity, buoyancy and drag forces. F_{net} is calculated by Eq (3.12-3.13) (Newton's 2nd law).

$$F_{net} = F_g - F_b - F_d \quad (3.12)$$

$$F_{net} = m_p \cdot g - m_f \cdot g - F_d(t) = m_p \cdot a(t) \quad (3.13)$$

Here, a is acceleration of the particle (m s^{-2}) and it is a differential of velocity with respect to time and depends on the drag force as shown in Eq (3.14).

$$a(t) = \frac{dv_p(t)}{dt} = \frac{F_{net}}{m_p} = \left(1 - \frac{\rho_f}{\rho_p}\right) \cdot g - \frac{6 \cdot F_d(t)}{\rho_p \cdot \pi \cdot d_p^3} \quad (3.14)$$

For low values of the particle Reynolds number ($\text{Re} < 0.2$), the flow is considered laminar in Stoke's region. If the Re is between 0.2 and 2000, a laminar – turbulent transition flow regime occurs in intermediate region. For $\text{Re} > 2000$, the flow regime is called as turbulent in Newton region.

Stokes derived the following equation [Eq (3.15)] for creeping flow conditions where inertial effects are negligible¹¹⁴.

$$C_D = \frac{24}{\text{Re}} = \frac{24}{\frac{d_p \cdot \rho_f \cdot v}{\mu_f}} = \frac{24 \cdot \mu_f}{d_p \cdot \rho_f \cdot v} \quad (3.15)$$

Rearranging Equations (3.10), (3.14) and (3.15), Stokes settling velocity is obtained as a function of time, Eq (3.16) to Eq (3.17).

$$\frac{dv_p(t)}{dt} = \left(1 - \frac{\rho_f}{\rho_p}\right) \cdot g - \frac{18 \cdot \pi \cdot \mu_f \cdot d_p \cdot v_p(t)}{\rho_p \cdot \pi \cdot d_p^3} \quad (3.16)$$

$$v_p(t) = \frac{(\rho_p - \rho_f) \cdot d_p^2 \cdot g}{18 \mu_f} \cdot \left[1 - \exp\left(\frac{18 \mu_f}{\rho_p \cdot d_p^2} \cdot t\right) \right] \quad (3.17)$$

For these creeping flow conditions (Stoke's region), terminal settling velocity occurs when the net gravitational force equals to the drag force¹¹⁴ (*i.e.* $F_{net} = 0$). For infinite time (as t goes to ∞), particle reaches a constant speed, and Eq (3.18) is obtained which is called as terminal velocity for Stoke's region.

$$v_p = \frac{(\rho_p - \rho_f) \cdot d_p^2 \cdot g}{18 \mu_f} \quad (3.18)$$

The critical particle size for Stoke's region can be calculated using the range for $Re < 0.2$ as given by Eq (3.19).

$$Re < 0.2 \quad \rightarrow \quad \frac{d_p \cdot \rho_f \cdot v_p}{\mu_f} < 0.2 \quad \rightarrow \quad d_p < \left[\frac{3.06 \mu_f^2}{\rho_f (\rho_p - \rho_f) g} \right]^{1/3} \quad (3.19)$$

When the calcite particles ($\rho_p = 2710 \text{ kg m}^{-3}$) are considered in water, ($\rho_f = 999 \text{ kg m}^{-3}$; $\mu_f = 1.12 \cdot 10^{-3} \text{ kg m}^{-1} \text{ sec}^{-1}$; $g = 9.81 \text{ m sec}^{-1}$), critical particle size for calcite is calculated as $d_p < 61.173 \text{ }\mu\text{m}$. For the size interval of $50 - 250 \text{ nm}$ produced calcite, or agglomerated grains of $500 \text{ nm} - 2 \text{ }\mu\text{m}$ size interval, the settling velocity of calcites in colloidal media (or during the particle size measurement) must only be calculated in Stoke's region by Eq (3.18).

3.3. Coagulation of Particles

Coagulation caused by the inhibition of repulsion forces acting between particles. When there is no energy barrier against coagulation, rapid coagulation occurs¹¹⁵. At short distances, attraction forces inhibit disaggregation, and lead to cohesion. Therefore, a theory of aggregative stability can only be developed after the nature of the aggregation processes, and taken into account the dependence on distance

of the forces acting between colloidal particles. The calculation procedure of coagulation describes the interaction of two particles under the influence of Brownian motion, until they completely stick to each other, reverse disaggregation process and, the differences between the forces of interaction of aggregates with individual particles as compared to the interaction between primary particles¹¹⁰. The coagulation of colloidal particles can be described as two consecutive processes: collision and attachment¹¹⁶.

Particles have constant collisions in an aqueous suspension. For particles smaller than 1 μm , Brownian motion causes collisions. The kinetic energy is proportional to kT (the product of Boltzmann's constant and the absolute temperature), is transferred to suspended particles by water molecules undergoing thermal motion. Eq (3.20) is valid for the number of collisions (N_{ij}) per unit time per unit volume between two types of particles of volume v_i and v_j . n_i and n_j are the number concentrations of particles with volume v_i and v_j . $\beta(v_i, v_j)$ is collision frequency function (depends on particle size, temperature and pressure). It is obtained by solving steady state particle diffusion equation and the result is given by Eq (3.21) (Smoluchowski's Equation).

$$N_{ij} = \beta(v_i, v_j) n_i n_j \quad (3.20)$$

$$\beta(v_i, v_j) = 4\pi(D_i + D_j) \cdot (R_i + R_j) \quad (3.21)$$

where R is the particles' radius and D stands for the diffusion coefficient given by Stoke's Einstein Equation as Eq (3.22).

$$D_i = \frac{kT}{6\pi\mu R_i} \quad (3.22)$$

For monodisperse system, ($v_i = v_j$), the collision frequency function is reduced to Eq (3.23).

$$\beta(v_i = v_j) = \frac{8kT}{3\mu} \quad (3.23)$$

The rate of formation of particles of volume v_k by collisions between particles of volume v_i and v_j is given by $\left[0.5 \cdot \sum_{i+j=k} N_{ij}\right]$. The notation $i + j = k$ indicates that the summation is taken over all collisions for which $v_i + v_j = v_k$. The rate of loss of particles of volume v_k by collisions with all other particles is $\sum_{i=1}^{\infty} [N_{ik}]$. The equation which describes the rate of change in the number density of particles of volume v_k as a result of Brownian motion is given by Eq (3.24-3.25)¹¹⁶.

$$\frac{dn_k}{dt} = \frac{1}{2} \sum_{i+j=k} N_{ij} - \sum_{i=1}^{\infty} N_{ik} \quad (3.24)$$

$$\frac{dn_k}{dt} = \frac{1}{2} \sum_{i+j=k} \beta(v_i, v_j) n_i n_j - n_k \sum_{i=1}^{\infty} \beta(v_i, v_k) n_i \quad (3.25)$$

Substituting Eq (3.20) into Eq (3.25), the rate of change in the number density of particles of volume v_k for an initially monodisperse system is given by Eq (3.26).

$$\frac{dn_k}{dt} = \frac{1}{2} \beta \sum_{i+j=k} (n_i, n_j) - \beta n_k \sum_{i=1}^{\infty} n_i \quad (3.26)$$

If the total number of particles per unit volume of fluid $\left(\sum_{i=1}^{\infty} n_i\right)$ is marked as N_{∞} ;

$$\frac{dN_{\infty}}{dt} = -\frac{1}{2} \beta \cdot N_{\infty}^2 \quad (3.27)$$

Inserting Eq (3.23) into Eq (3.27), change of total particle number can be rewritten by Eq (3.27) and the result is given by Eq (3.28) and Eq (3.29).

$$\frac{dN_{\infty}}{dt} = \frac{-4kT}{3\mu} \cdot N_{\infty}^2 \quad (3.28)$$

$$N_{\infty} = \frac{N_{\infty}(0)}{1 + \left(\frac{4kT}{3\mu}\right) N_{\infty}(0) \cdot t} \quad (3.29)$$

In reality, particles may be under the influence of other forces such as van der Waals forces in addition to the forces caused by Brownian motion. Charged particles approach each other. Force field on colloids affects the rate of particle coagulation. Based on the Fuch's treatment (1935), If $V(r)$ is the interaction energy due to the force between the centers of two particles separated by a distance r , then the coagulation rate (W) is given by Eq (3.30). W denotes the ratio of the diffusion-controlled (rapid) coagulation rate to the actual coagulation rate in the presence of the force field.

$$W = 2R \int_{r=2R}^{\infty} \frac{1}{r^2} \cdot e^{\left(\frac{V(r)}{kT}\right)} dr \quad (3.30)$$

The slow coagulation is calculated by Eq (3.31). $N_{\infty(s)}$ and $N_{\infty(s)}(0)$ are total and initial numbers of the particles for slow coagulation. The ratio of the rapid coagulation rate to the slow coagulation rate may be assumed to be the measure of the stability of a colloidal system.

$$N_{\infty(s)} = \frac{N_{\infty(s)}(0)}{1 + \frac{\left(\frac{4kT}{3\mu}\right) N_{\infty(s)}(0) \cdot t}{W}} \quad (3.31)$$

An aqueous colloidal suspension is thermodynamically unstable. Because, Gibbs free energy of colloids decreases with aggregation into larger clusters. Therefore, the reduction of their surface energy occurs. The term "stability" refers to the durability of dispersed state throughout the suspension. Stability also relates to the rate of change in particle size distribution by coagulation. Therefore, the stability of a colloid can be determined by coagulation kinetics¹¹⁶.

CHAPTER 4

MATERIALS AND METHODS

4.1. Materials

$\text{Ca}(\text{OH})_2$ used in crystallization experiments was purchased from Merck with a purity of 96 %. A 3% of the impurity was CaCO_3 , and 1% was the other impurities. CO_2 gas was purchased from Carbogas, Turkey. CaCO_3 used in control experiments with a purity of 99.99% and other chemicals such as calcium chloride (CaCl_2), sodium carbonate (Na_2CO_3), sodium hydroxide (NaOH) as well as the solvents such as Acetone, Methanol (CH_3OH , 99.5%), Ethanol ($\text{C}_2\text{H}_5\text{OH}$, 99.5%), Toluene (C_7H_8 , 99.9%), Hexane (C_6H_{14} , 95%) and Benzene (C_6H_6 , 99.5%) were all purchased from Merck. The enzyme, Carbonic Anhydrase from bovine erythrocytes (CA), (89% pure in protein as dialyzed and lyophilized powder), was purchased from Sigma. HYPOL2060, for the immobilization of CA within polyurethane (PU) foam, was a kind gift from DOW Chemical, Istanbul.

4.2. CaCO_3 Synthesis by Chemical Method

CaCO_3 was synthesized using CaCl_2 (Merck) and Na_2CO_3 (Merck) solutions as Ca^{2+} and CO_3^{2-} ion sources. Figure 4.1 shows the experimental set up employed in the study, which consists of a 5-neck jacketed reactor attached to pH and conductivity probes, a syringe pump with an injection syringe, and a computer with data logger. A 250 ml of either CaCl_2 or Na_2CO_3 stock solution was stirred in the reactor on a magnetic stir bar at a rate of 600 rpm. A 20 ml of either CaCl_2 or Na_2CO_3 solution was injected at various concentrations and injection rates. The solutions were prepared in deionized water (DI) obtained from Millipore Elix-5/Milli-Q water purification system. The feeding was applied with a syringe pump (Longer pump - LSPO2-1B). The flowrate of the solutions in 20 ml standard syringes (Tyco Healthcare Sterile EO) were constant at either 0.075 or 0.67 ml/min so that different $[\text{Ca}^{++}] / [\text{CO}_3^{--}]$ ratios were

obtained during different time intervals. 0.25 M NaOH solution was prepared and used to adjust pH when the crystallizer contained Na_2CO_3 . The solutions were stirred by a magnetic bar (600 rpm) and temperature was kept constant at 23 °C with a water circulation device (WiseCircu). The pH and conductivity of the solutions were measured by using a pH meter (Thermo Orion 5-star) with a glass probe and conductivity cell, respectively. Both pH and conductivity probes were washed in chromic acid solution and rinsed with DI water after each experiment.

In a separate experiment, powder $\text{Ca}(\text{OH})_2$ of 0.15 g and 0.30 g were dissolved in a 100 ml of ultra pure water in a 2 L glass reactor with a stirring rate of 400 rpm to prepare 20 mM and 40 mM of $\text{Ca}(\text{OH})_2$ solutions, respectively. CO_2 was also dissolved in a 2 L of ultra pure water to prepare a solution with bicarbonate (HCO_3^-) ions at pH 4.0. A 100 ml of this solution was added into the 100 ml of 20 mM or 40 mM of $\text{Ca}(\text{OH})_2$ solutions with a flow rate of 0.1 or 1.0 ml/sec. During the crystallization, the pHs of the solutions were monitored with a glass pH probe.

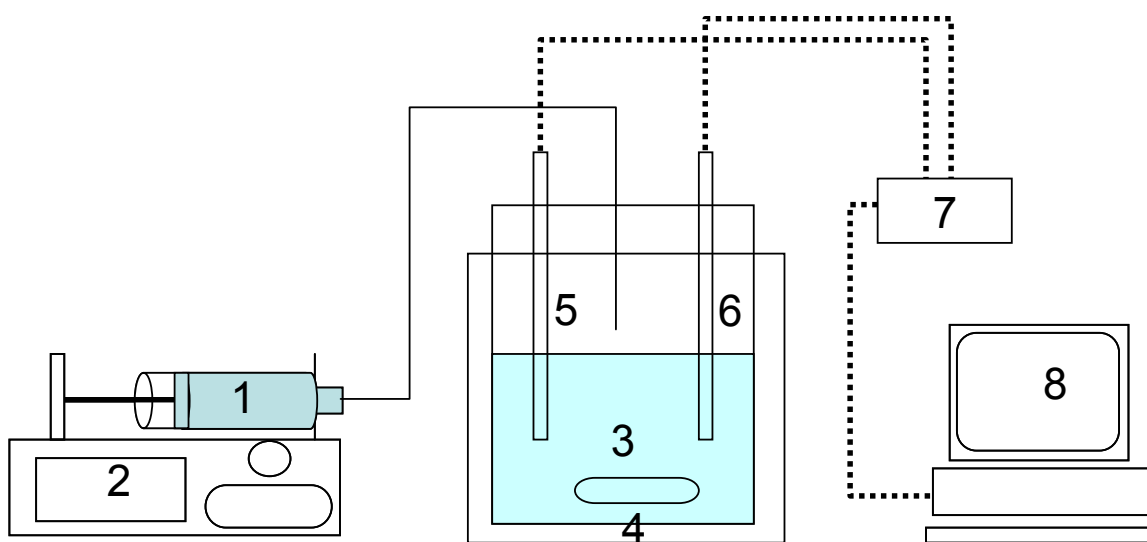


Figure 4.1. Experimental set-up for chemical route (1) 20 ml of CaCl_2 or Na_2CO_3 injection solution (2) syringe pump (3) 250 ml of CaCl_2 or Na_2CO_3 stock solution (4) 5-neck jacketed reactor with magnetic bar (5) pH probe (6) conductivity probe (7) data logger (8) computer

Precipitates were separated from solutions by centrifugation with a Universal 320 – Hettich Zentrifugen at 9000 rpm for 20 min. The particles were washed by Acetone, and then DI water. They were dried at 103 °C in an oven (Nüve FN 500) overnight and prepared for the further analyses.

4.3. Dissolution of Ca(OH)_2

The electrical conductivity values for Ca(OH)_2 and CaCO_3 solutions were measured at their different concentrations. A 0.019 g of Ca(OH)_2 was added into a 250 ml of DI water in a beaker to prepare a 1 mM Ca(OH)_2 solution by stirring on a stir bar at 600 rpm for 5 min. The electrical conductivity was measured for about 1 min. Then, additional amounts of Ca(OH)_2 were added into the solution sequentially and the same procedure was followed to obtain the electrical conductivity values with respect to Ca(OH)_2 concentrations. The electrical conductivity values for CaCO_3 at its various concentrations were also determined by the same procedure.

The dissolution of Ca(OH)_2 in water was studied. A 1, 3, 10, 16, 20 mM of Ca(OH)_2 solutions were prepared in a 5-neck jacketed reactor. The temperature was set to 23 °C during the measurements. Before the experiments, pH and conductivity probes were calibrated. A 14.8 mg of Ca(OH)_2 in powder form was added into a 200 ml of DI water to prepare a 1 mM of Ca(OH)_2 solution. The solution was set on stirring at 600 rpm and both pH and conductivity values were recorded online by the Orion Navigator software program. 2 ml of samples were withdrawn from the solution every 2 min and the particle sizes were measured by Malvern Zeta Sizer - Nano ZS. After the measurements, the samples were returned back to the stirring tank.

The dissolution of Ca(OH)_2 was modeled according to Eqs.(2.1)-(2.3) and Eqs.(2.6)-(2.8). The model equations were solved using the solver in ATHENA computational software program.

4.4. CaCO₃ Synthesis by Carbonization Method

Unless otherwise indicated, the CaCO₃ precipitation experiments were conducted in a 3-neck glass reactor as shown in Figure 4.2. pH and electrical conductivity were measured with a glass pH probe (Orion) and a conductivity cell (Orion), both attached to a Thermo Orion 5 Star pH meter. All data were collected on-line by a 5 Star Navigator software program in a PC.

Different concentrations of Ca(OH)₂ from 0.1 mM to 500 mM were prepared in the 3-neck reactor in a 200 ml ultra pure distilled (DI) water (Millipore Elix-5/Milli-Q water treatment unit). Ca(OH)₂ solutions and/or slurries were stirred at 800 rpm for 5 or 10 min on a magnetic stirrer before the CO₂ injection.

CO₂ gas was filled in a plastic balloon under 50 bar pressure during 10 sec and injected into the solution or slurry in atmospheric pressure using a narrow glass pipe (5 or 10 mm in diameter). The bubbling was prohibited to occur during the CO₂ injection.

Batch experiments were conducted at room temperature at 600 rpm stirring, unless otherwise indicated. Precipitation reactions were ended at about pH ~7. Samples were taken in a 50 ml falcon tube and centrifuged for 10 min at 9000 rpm (Universal 320 – Hettich Zentrifugen). The precipitates were collected and washed by acetone and then DI water. All samples were dried in an oven at 103 °C (Nüve FN 500) overnight before characterization.

Deviations in pH and conductivity were calculated from the two data interval with time.

CaCO₃ was also produced by bubbling of CO₂ through various concentrations of Ca(OH)₂ solutions in a 1 L of glass reactor. A spiral shaped diffuser containing about less than 1 mm of holes in diameter punctuated on a rubber hose of about 1 cm in diameter was placed at the bottom of the reactor. A 500 ml of Ca(OH)₂ solution was prepared in the reactor and stirred at 600 rpm on a stir bar. The reactions were started when CO₂ was injected through the holes of the spiral hose within the solution and exhausted to the open atmosphere. pH and conductivity values were recorded during the experiments. At the end of the experiments, samples were taken for analyses.

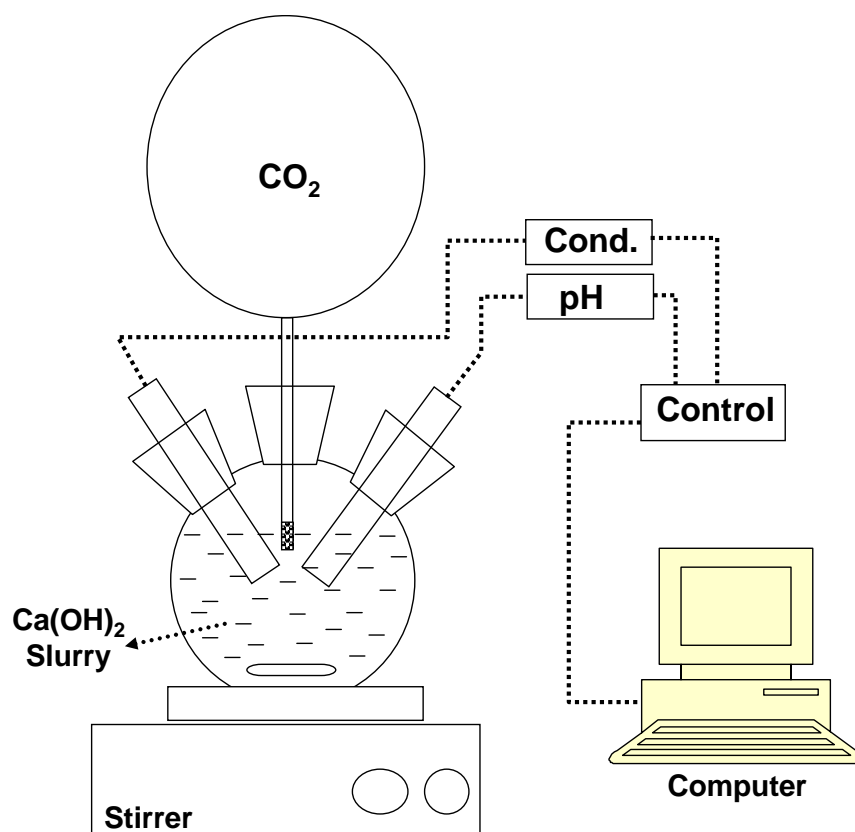


Figure 4.2. Experimental set-up for CaCO_3 carbonization

4.5. Progress in CaCO_3 Formation

Experimental set-up employed to investigate the progress in CaCO_3 formation was shown in Figure 4.3. A volumetric flask was used as the reactor. A 30 mM of Ca(OH)_2 slurry was prepared in the volumetric flask by the addition of 0.55 gr of Ca(OH)_2 in powder form (Merck) and dissolved in a 250 ml of ultra pure DI water (Millipore Elix5/MilliQ) by stirring on a stir bar at 800 rpm for 5 min before the CO_2 injection. The CO_2 gas was filled in a plastic balloon under 50 bar pressure during 10 sec and connected to the top of the 250 ml volumetric flask. The filling conditions of CO_2 gas to the plastic balloon were the same for each run. Before the CO_2 injection, the stirring rate was set to 600 rpm. The reaction was started when CO_2 was released to the top of the solution from the balloon and terminated in about 5 min. Then, the solution was poured into a beaker and pH and conductivity values were measured with a Thermo Orion 5 star pH meter. The volumetric flask was washed in a chromic acid solution and used in the subsequent experiments. Another 30 mM of Ca(OH)_2 slurry was prepared in the volumetric flask and reacted with CO_2 for additional time. Same procedure was

followed. Samples were taken in a 50 ml falcon tube from each experiment for different time intervals and centrifuged for 10 min at 9000 rpm (Universal 320 – Hettich Zentrifugen). The precipitates were collected and washed by acetone, and then, the DI water. All samples were dried in an oven at 103 °C (Nüve FN 500) overnight before characterization.

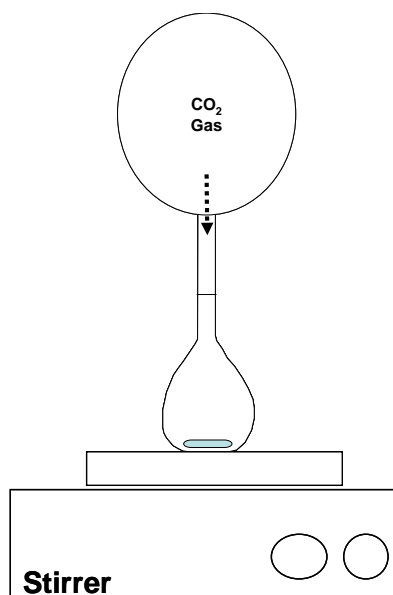


Figure 4.3. Experimental set-up for progress in CaCO₃ formation

The progress in CaCO₃ formation was also studied in the presence of 5 mM and 10 mM of Ca(OH)₂ solutions, which were below the solubility limit. The same procedures used for 30 mM of Ca(OH)₂ were applied for both 5 mM and 10 mM of Ca(OH)₂ solutions. Experiments with one of the two 10 mM of Ca(OH)₂ solutions were conducted under 800 rpm stirring to show the effect of stirring rate.

The effects of mass transfer surface area and shear on the CaCO₃ carbonization were studied in a stirred round bottom flask as shown in Figure 4.4. The levels of the solution were adjusted from 100 ml to 600 ml so that different surface areas were used for different CO₂ transfer rate. Various volumes of the solution were also resulted in different shear rates or power per volume. A 30 mM of Ca(OH)₂ slurry was prepared in the round bottom reactor and used in the CaCO₃ crystallization experiments. The slurries were initially stirred for 5 min before the CO₂ injection. The filling conditions of CO₂ gas to the plastic balloon were the same for each run, it was under 50 bar pressure during 10 seconds. CO₂ gas was fed on the top of the solution during the

experiments. The reactions were run for a fixed time of 20 min at 600 rpm. At the end of the 20 min of the reactions, samples were taken for further analyses.

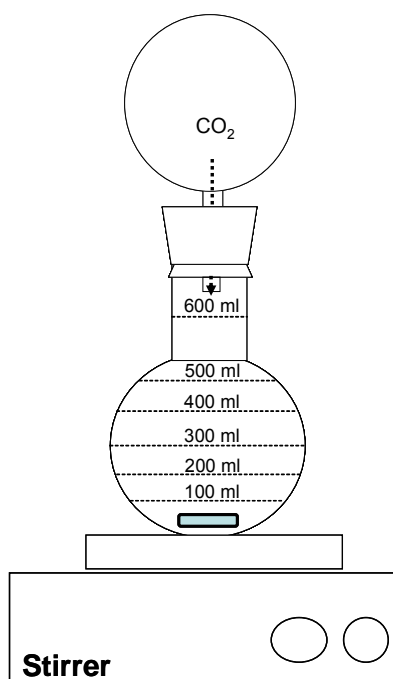


Figure 4.4. Experimental set-up for CaCO₃ carbonization in a round bottom flask reactor

Similar experiments were conducted in a 500 ml volumetric flask reactor as shown in Figure 4.5. Here, a 30 mM of Ca(OH)₂ slurry was used with varied volumes from 100 ml to 520 ml in a batch mode. The reactions were completed in 30 min under 600 rpm stirring. At the end of the 20 min of the reactions, the solutions were poured into a beaker. Here, pH and conductivity values were measured. Also, samples were taken in a 50 ml falcon tube and centrifuged for 10 min at 9000 rpm. The precipitates were collected and washed by acetone and then DI water. All samples were dried in an oven at 103 °C overnight before characterization.

The particle aggregation was modeled with respect to a colloidal stability with MATHCAT software program.

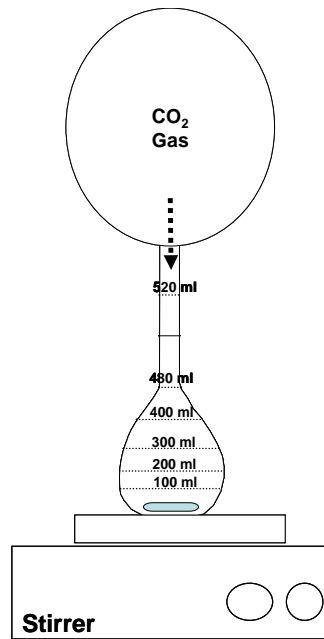


Figure 4.5. Experimental set-up for progress in CaCO_3 formation in a 500 ml volumetric flask reactor.

4.6. Effect of Carbonic Anhydrase on CaCO_3 Crystallization

Calcite crystals were produced in the reactor as shown in Figure 4.2 in the presence of either free form or immobilized form of Carbonic Anhydrase (CA) enzyme. A 12.55 mg of CA enzyme was dissolved in a 6 ml of ultra pure DI water (Millipore Elix-5/Milli-Q) by stirring at 600 rpm on a magnetic stir bar to prepare stock solution of the enzyme. A 20 mM of $\text{Ca}(\text{OH})_2$ solution was also prepared by the addition of about 0.3 gr of powder $\text{Ca}(\text{OH})_2$ (Merck) in 200 ml of DI water and stirred for 5 min before the addition of free CA enzyme. The 250 μl of free CA enzyme from its stock solution (0.09 μM) was added into the $\text{Ca}(\text{OH})_2$ slurry and stirred at 600 rpm for 5 min before the addition of CO_2 . CO_2 gas was filled in a plastic balloon under 50 bar pressure during 10 seconds and added into the solution at atmospheric pressure using a narrow glass pipe (10 mm in diameter) as the mini reactor. pH and conductivity values were recorded by Thermo Orion 5 star pH meter during the crystallization. Up to 2000 μl (0.71 μM) free CA enzyme were used in crystallization experiments. At the end of each experiment, samples were withdrawn in a 50 ml falcon tube and centrifuged for 10 min at 9000 rpm. The precipitates were collected and washed with DI water. All samples were dried in an oven at 103 $^\circ\text{C}$ overnight before characterization.

Carbonic Anhydrase enzyme has been immobilized within polyurethane (PU) foam in our lab and characterized for the enzyme activity^{74,117}. In order to compare the effect of immobilized enzyme on the CaCO₃ crystallization, control experiments were conducted by using bare PU porous foams. PU foam and enzyme immobilization were achieved by mixing equal amounts of water and prepolymer named HYPOL2060. A structure of the PU is given in Figure 4.6.

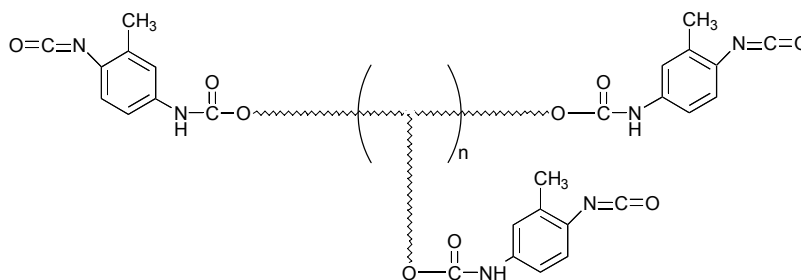


Figure 4.6. Structures of the polyurethane prepolymer⁷⁴.

The immobilization occurs in the prepolymer covalently via isocyanate groups of the PU and amine groups of the enzyme. Immobilization of enzymes in PU foam is illustrated in Figure 4.7. A certain amount of CA enzyme in powder form was dissolved in 3 ml of DI water and poured onto about 3 g of viscous HYPOL2060 prepolymer in a 50 ml falcon tube. The two phase system was mixed vigorously for 30 sec by a drill with a hand-made mixer blade to achieve a homogeneous distribution of the enzyme within the prepolymer. The level of the white polymeric solution was started to increase as a result of a CO₂ release during the polymerization. The level, and thus, the polymerization settled in 2-3 min. Polymerization took place at room temperature. After polymerization, the foam was stored for at least 2 h before use.

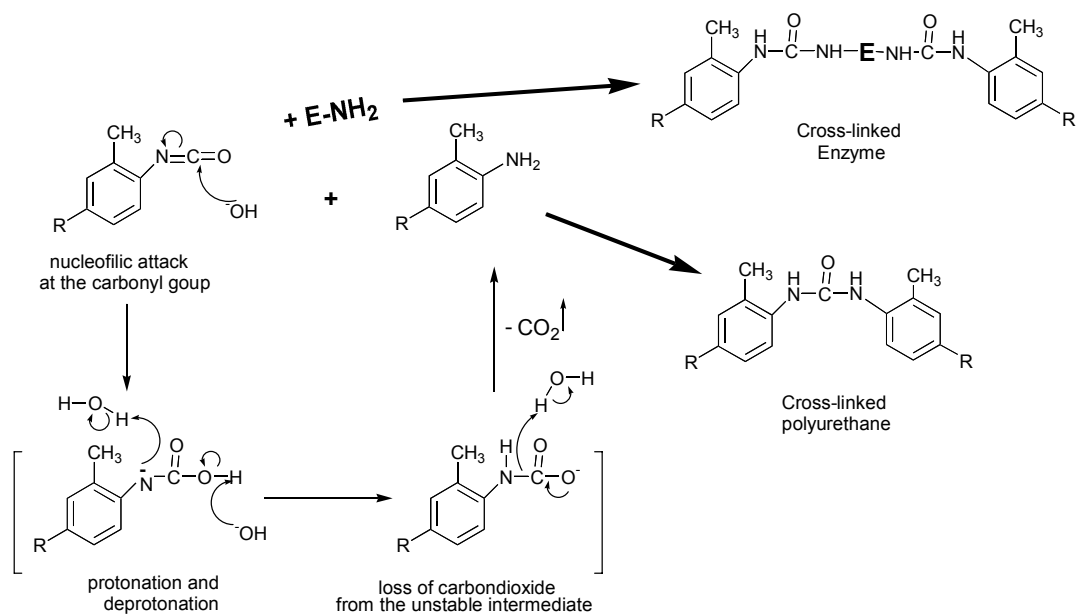


Figure 4.7. Enzyme immobilization by cross-linking within polyurethane foam ⁷⁴.

In order to suspend the foam within the aqueous solution, the foam was cut into very small pieces of about 2 mm by a seizer. The volume of the small pieces was about 10 mm³. A 0.10, 0.25, 0.50, 0.75, 1.00 g of CA immobilized mini foams were mixed with 20 mM of Ca(OH)₂ slurry in a 200 ml of solution stirring at 600 rpm. pH and conductivity values were recorded during the experiments. Samples were taken in a 50 ml falcon tube and centrifuged for 10 min at 9000 rpm (Universal 320 – Hettich Zentrifugen). The precipitates were collected and washed by acetone and then DI water. All samples were dried in an oven at 103 °C (Nüve FN 500) overnight before characterization.

The experiment matrix of the foam and the immobilized CA was given in Table 4.1.

Table 4.1. Matrix of the CaCO₃ production in the presence of polyurethane foam and Carbonic Anhydrase and their sample codes

Foam (g)	BCA (mg)				
	0	1.60	2.40	5.60	10.3
0.10	Excess 1	-	-	-	Excess 3
0.25	S1	S4	S7	S10	S13
0.50	S2	S5	S8	S11	S14
0.75	S3	S6	S9	S12	S15
1.00	Excess 2				Excess 4
mg- BCA/g-HYPOL	0.00	0.55	0.80	1.81	3.45

4.7. Effect of Organic Solvents on CaCO₃ Crystallization

Calcite crystals were produced in a 3-neck glass reactor in the presence of organic additives such as methanol, ethanol, hexane, toluene, and benzene as described in Figure 4.2. The physicochemical properties of additives were given in Table 4.2

Table 4.2. Physicochemical properties of additives

Chemical	Mol. Weight	Density	Solubility*	Dielectric	Mass ⁺	Mass**	Mass ⁺⁺	Mass [†]
Formula	(g/mol)	(g/ml)	μL/200mL	constant	slurry (g)	slurry (g)	%	%
water	18.02	0.998		78.54	159.68	189.62		
methanol	32.04	0.791	Miscible	32.60	31.64	7.91	16.54	4.00
ethanol	46.07	0.789	Miscible	24.60	31.56	7.89	16.50	3.99
hexane	86.18	0.659	42.40	1.89	26.36	6.59	14.17	3.36
toluene	92.14	0.867	115.11	2.38	34.68	8.67	17.84	4.37
benzene	78.11	0.879	408.74	2.28	35.16	8.79	18.05	4.43

*Solubility in water

⁺Mass for solvent/water mixture of 5/100 (v/v) in slurry

**Mass for solvent/water mixture of 20/100 (v/v) in slurry

⁺⁺Mass % for solvent/water mixture of 5/100 (v/v) in slurry

[†]Mass % for solvent/water mixture of 20/100 (v/v) in slurry

The ratios of the mixtures (organic additives / water) were 5 % and 20 % (v/v) for each. Organic additives / water mixtures were stirred at 800 rpm for 5 min and measured their pH and conductivity before the addition of the Ca(OH)₂ powder. A 20 mM and 40 mM slurries of Ca(OH)₂ were prepared by the addition of 0.2964 g and 0.5928 g powders, respectively. Ca(OH)₂ powder was introduced to the organic additive/water mixtures and continued to stir at 800 rpm for 5 more min. CO₂ gas was injected onto the surface of the mixture in atmospheric pressure using a glass pipe (mini

reactor) of 10 mm in diameter. Bubbles were not allowed to form in the 3-neck reactor. pH and conductivity values were recorded by pH meter. Precipitates were collected from the mixture by centrifugation (Universal 320-Hettich Zentrifugen) for 10 min at 9000 rpm, and then washed by deionized water. All samples were dried in an oven at 103 °C overnight.

Variables and their ranges in experiments were listed in Table 4.3 with the sample codes.

Table 4.3. Variables and their ranges in experiments with sample codes.

No	Additive	Ca(OH) ₂ (mM)	Additive % (v / v)	Stirring (rpm)
1		20	5	400
2		20	20	400
3	<i>SET-1</i>	40	5	400
4		40	20	400
5	<i>Methanol</i>	20	5	800
6		20	20	800
7		40	5	800
8		40	20	800
1		20	5	400
2		20	20	400
3	<i>SET-2</i>	40	5	400
4		40	20	400
5	<i>Ethanol</i>	20	5	800
6		20	20	800
7		40	5	800
8		40	20	800
1		20	5	400
2		20	20	400
3	<i>SET-3</i>	40	5	400
4		40	20	400
5	<i>Hexane</i>	20	5	800
6		20	20	800
7		40	5	800
8		40	20	800
1		20	5	400
2		20	20	400
3	<i>SET-4</i>	40	5	400
4		40	20	400
5	<i>Toluene</i>	20	5	800
6		20	20	800
7		40	5	800
8		40	20	800
1		20	5	400
2		20	20	400
3	<i>SET-5</i>	40	5	400
4		40	20	400
5	<i>Benzene</i>	20	5	800
6		20	20	800
7		40	5	800
8		40	20	800

4.8. Sample Characterization

4.8.1. SEM Analyses

The morphologies of the CaCO_3 crystals were analyzed using a scanning electron microscope (SEM) fitted with a field emission source (Philips XL 30 S FEG), operating at an accelerating voltage of 15 kV. The CaCO_3 crystals were mounted on copper sample stubs with conducting carbon tape for SEM viewing.

4.8.2. XRD Analyses

The X-ray powder diffraction (XRD) measurements were carried out using a modified computer-controlled Philips X'Pert Pro X-ray diffractometer. The crystal structure was determined using Cu K α radiation (45kV and 40 mA) equipped with a diffracted-beam monochromator - accelerating detector. The fine powder was packed into a zero background sample holder. The packed powder was introduced to detector as received. The weight of loaded sample was not important and varied. The diffraction pattern was recorded for 2θ from 10° to 80° and a 2θ step scan of 0.033° was used, counting for 10.16 sec at every step. The total scan time for each sample was 3 min. X-ray patterns were also used to determine crystal size from the broadening of the diffraction line at half the line of maximum intensity. References XRD peaks for various forms of CaCO_3 crystals and amorphous CaCO_3 are given in Figure 4.8.

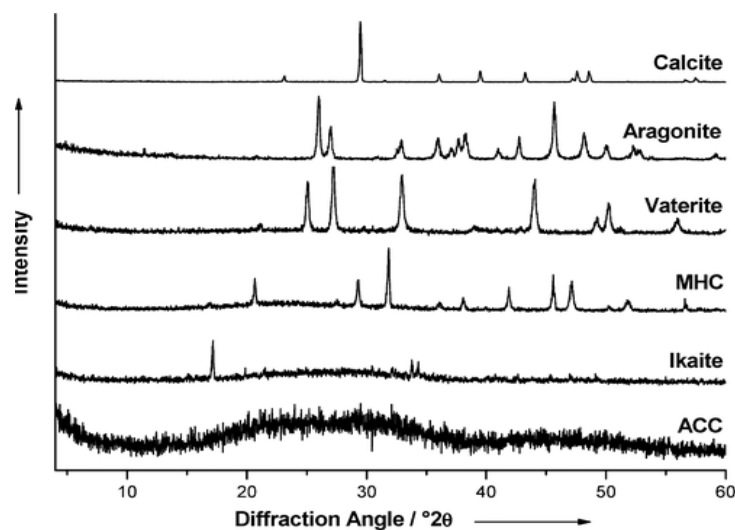


Figure 4.8. XRD patterns of all CaCO_3 phases based on JCPDS. MHC: mono hydrate calcium carbonate; ACC: amorphous calcium carbonate¹¹⁸

4.8.3. FTIR Analyses

An analytical technique, Fourier Transform Infrared Spectroscopy (FTIR) analysis was performed to investigate the structure of the precipitates. FTIR spectra of the precipitates were obtained in KBr using a Shimadzu FTIR-8601 PC spectrometer (Kyoto, Japan with a resolution of 1.5 cm^{-1}). Spectra were traced in the range $4000\text{--}400\text{ cm}^{-1}$, and the band intensities were expressed in absorbance. Calcite is identified by its main absorption bands at $1426, 1092, 876$ and 712 cm^{-1} ¹⁴. References infrared spectra for various forms of CaCO_3 crystals and amorphous CaCO_3 are given in Figure 4.9.

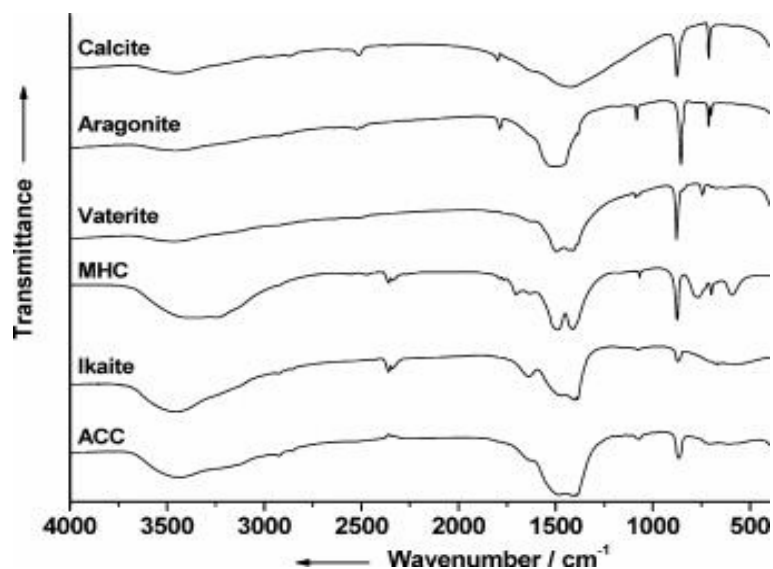


Figure 4.9. Infrared spectra of various CaCO_3 phases¹¹⁸.

4.8.4. Particle Size Distribution Analyses

Dynamic light scattering (DLS) technique was used to obtain particle size distribution of $\text{Ca}(\text{OH})_2$ slurries and selected precipitates (CaCO_3) by Malvern Nano ZS. Samples (1.5 ml) were placed in a disposable cuvet without any dilution and automatic measurement program was chosen. For the dispersion of the particles in water, sonication was applied by a sonicator (Misonix – Ultrasonic Liquid Processors) when it was needed.

4.8.5. Zeta Potential Measurements

Zeta potential of the selected precipitates was determined in the presence of distilled water. 0.1 wt % CaCO₃ suspensions were prepared and electrophoretic mobility's of dispersed particles were measured by a Malvern Instruments Zeta Sizer – Nano ZS with several individual measurements. Geometric mean of at least ten-measurement sequence was calculated and the magnitudes were used for the determination of particle interactions and the colloidal stability of the precipitation system.

CHAPTER 5

RESULTS AND DISCUSSIONS

5.1. CaCO₃ Synthesis by Chemical Method

Recent studies^{87,88} have shown that the CaCO₃ crystallization rate is maximum when [Ca⁺⁺] / [CO₃⁼] ratio is 1.0. The crystallization rate is lower when this ratio is much lower or higher. On the other hand, the novel CaCO₃ crystallization mechanisms indicated that stable clusters will form from Ca⁺⁺ and CO₃⁼ ions before nucleation, whether the solution is undersaturated or supersaturated, and crystal particles will grow from these ions and clusters^{25,28}. Although the general practice is to mix equal concentrations of ions in a solution, we propose that if the [Ca⁺⁺] / [CO₃⁼] ratio of 1 is approached slowly from left or from right starting with very low [Ca⁺⁺] concentrations or very high [CO₃⁼] concentrations, the nano clusters may form and grow to produce stable nano CaCO₃ particles.

Two experiments were conducted such that a 20 ml Na₂CO₃ solution with a concentration of 94 mM was added into a 250 ml of CaCl₂ solution at a concentration of 7.4 mM with two addition rates; one is at 0.67 ml/min and the other is at 0.077 ml/min. pH and conductivity values were recorded during fast and slow additions of Na₂CO₃ into CaCl₂ solution. Figure 5.1 shows the calculated concentrations for [Na₂CO₃] and [CaCl₂] solutions with the calculated [CaCl₂] / [Na₂CO₃] ratios, and the measured pH and conductivity values. As shown in Figure 5.1a, the addition of 20 ml of Na₂CO₃ was completed in 30 min with fast addition. On the other hand, as shown in Figure 5.1c, the Na₂CO₃ addition was completed in 260 min with slow addition. The [CaCl₂] / [Na₂CO₃] ratio was about 30 to 60 initially and decreased almost exponentially to a value of 1.

pH was almost constant initially at 9.64 for the fast addition, on the other hand, pH decreased from 8.77 to 7.70 for slow addition. The conductivity values were almost constant at 1.46 and 1.34 mS/cm for the fast and slow additions, respectively, during this initial step which lasted almost half of the total duration for the addition of 20 ml of solutions. These values are 13 min and 124 min for fast and slow additions. At these times, the [CaCl₂] / [Na₂CO₃] ratios were 2.26 and 2.05 for fast and slow

additions, respectively. For the fast additions, the pH and conductivity increased slightly, for instance, pH from 9.55 to 10.0 and conductivity from 1.46 to 1.50 mS/cm. For slow additions, while pH increased significantly from 7.77 to 10.0, the conductivity slightly increased from 1.34 to 1.37 mS/cm. After these $[\text{CaCl}_2] / [\text{Na}_2\text{CO}_3]$ ratios, while the conductivity values slightly decreased, from 1.50 to 1.40 mS/cm for fast addition and from 1.37 to 1.30 mS/cm for slow addition, the pH values dropped to almost constant values of 9.63 and 9.26 for fast addition and slow addition, respectively. At the late stage of the fast addition, both the conductivity and pH values seemed to decrease considerably to value of 1.38 mS/cm and 8.88, respectively. It seems that clusters were formed up to $[\text{CaCl}_2] / [\text{Na}_2\text{CO}_3]$ ratio of 2.2 and grow with additional ions.

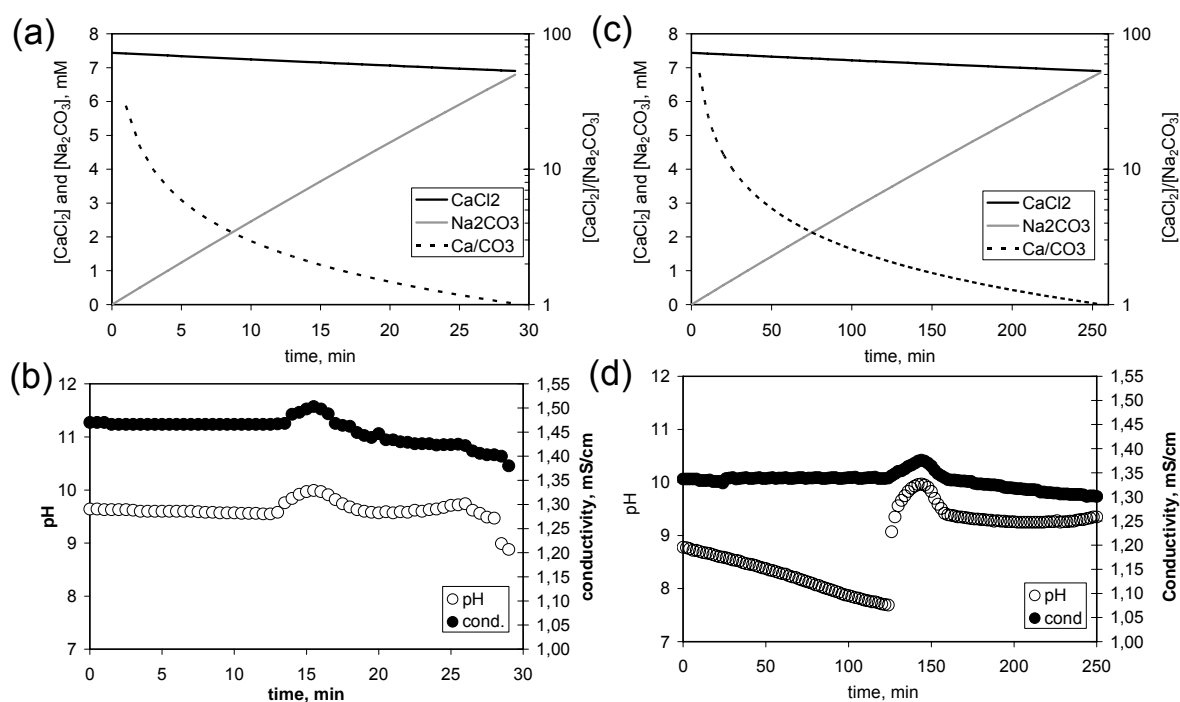


Figure 5.1. (a) Fast addition of Na_2CO_3 (94 mM) into CaCl_2 solution (7.4 mM) (at a rate of 0.67 ml/min) (b) pH and conductivity change during fast addition (c) Slow addition of Na_2CO_3 (94 mM) into CaCl_2 solution (7.4 mM) (at a rate of 0.077 ml/min) (d) pH and conductivity change during slow addition. pH was adjusted to 11.5 by the addition of 5 ml of 250 mM NaOH solution.

Figure 5.2 shows SEM images of the CaCO_3 particles obtained from the fast and slow additions of Na_2CO_3 into 7.4 mM of CaCl_2 solution. As shown in Figure 5.2a, the particles obtained from the fast addition of Na_2CO_3 are generally round shape composed of mostly nano particles. On the other hand, as shown in Figure 5.2b, the particles obtained from the slow addition of Na_2CO_3 are mostly plate-like shape and look like

composed of mostly aggregated nano particles. It can be clearly seen from these images that different addition rates of Na_2CO_3 into 7.4 mM of CaCl_2 solution resulted in forming large particles more than 5 μm in different shapes, which later were converted into, for instance, spherical and plate like vaterite forms^{119,120}.

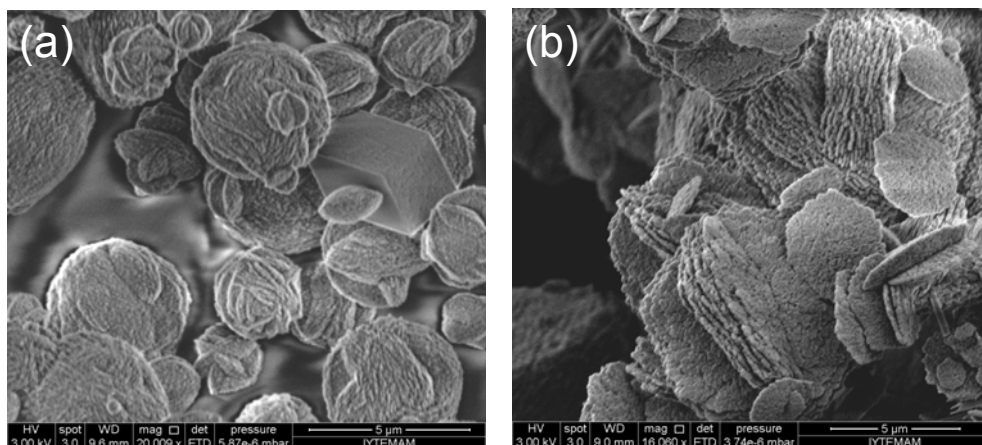


Figure 5.2. SEM images of the precipitates obtained from addition of Na_2CO_3 (94 mM) into CaCl_2 solution (7.4 mM) (a) fast addition at a rate of 0.67 ml/min (b) slow addition at a rate of 0.077 ml/min.

When CaCl_2 was increased and the Na_2CO_3 concentration slightly decreased, more stable cubical calcite crystals of about 6 μm in sizes were obtained. Figure 5.3 shows the decrease in $[\text{CaCl}_2]$ concentration upon the addition of Na_2CO_3 solution as well as the calculated $[\text{CaCl}_2] / [\text{Na}_2\text{CO}_3]$ ratios. As can be seen in the figure, when the $[\text{CaCl}_2] / [\text{Na}_2\text{CO}_3]$ ratio was 3.7, the 20 ml of Na_2CO_3 was fully injected at a fast addition rate of 0.67 ml/min and the reaction was terminated. The pH was 9.35 initially and did not change during the reaction. As shown in Figure 5.4, cubical shaped, almost mono dispersed calcite particles were obtained.

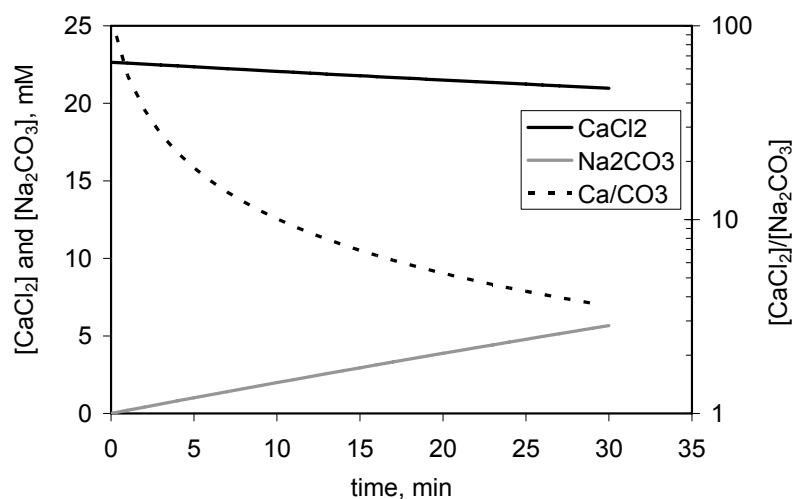


Figure 5.3. Addition of (a) Na₂CO₃ (76 mM) into CaCl₂ solution (23 mM) at a rate of 0.67 ml/min, initial pH 9.35

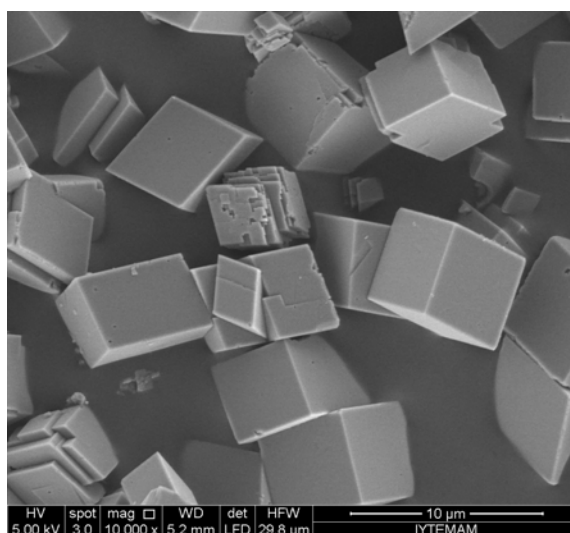


Figure 5.4. SEM image of the precipitates obtained from addition of Na₂CO₃ (76 mM) into CaCl₂ solution (23 mM) at a rate of 0.67 ml/min.

In the follow-up experiments, low (15 mM) and high (760 mM) concentrations of CaCl₂ solutions were injected into Na₂CO₃ solution (75 mM) with a slow addition at a rate of 0.077 ml/min. pH was adjusted to 11.5 by NaOH. Conductivity changes were recorded during the addition of low and high CaCl₂ concentrations. As shown in Figure 5.5, the Na₂CO₃ concentrations slightly decreased by the addition of constant total volume of 20 ml of CaCl₂ solutions, however, the [CaCl₂] / [Na₂CO₃] ratio was nearly zero for the low concentration of CaCl₂ (Figure 5.5a). On the other hand, this ratio increased almost linearly for the addition of high concentration of CaCl₂ (Figure 5.5b).

Figure 5.5c shows the conductivity values for the two solutions. As shown in the figure, the conductivity values were constant during the addition of low and high concentrations of CaCl_2 in the first 115 min. At this point, interestingly, while the conductivity values continuously decreased during the addition of low concentration of CaCl_2 , they increased during the addition of the high concentration solution. It seems that the CaCO_3 clusters were formed in the initial 115 min and then ions were consumed for the low concentration of CaCl_2 addition. For the high concentration, while crystallization consumed some of the Ca^{++} ions, because the concentration was high, the rest of the ions were accumulated in the solution.

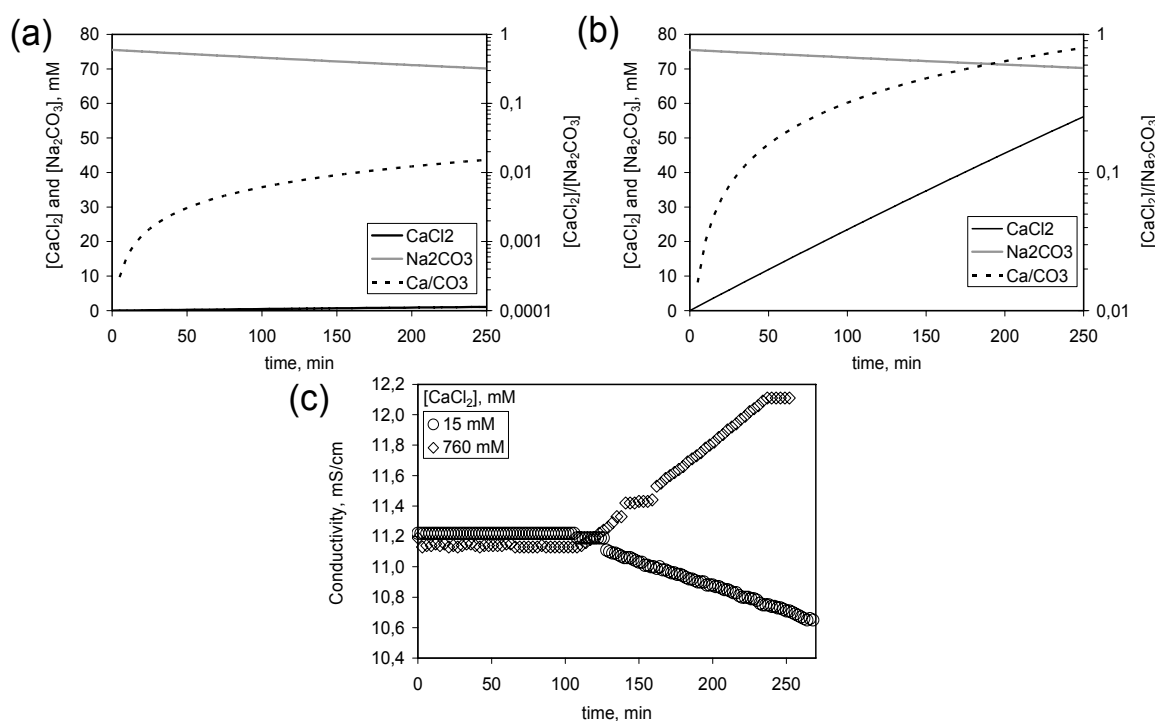


Figure 5.5. Addition of low (15 mM) and high (760 mM) concentrations of CaCl_2 into Na_2CO_3 solution (75 mM) at a rate of 0.077 ml/min (a) low CaCl_2 concentration (b) high CaCl_2 concentration (c) pH and conductivity change during low CaCl_2 concentration (d) pH and conductivity change during high CaCl_2 concentrations.

Figure 5.6 shows the SEM images of the CaCO_3 particles obtained from the addition of low and high concentrations of CaCl_2 solutions into the Na_2CO_3 solution at pH 11.5. As shown in the figure, low concentration of CaCl_2 addition resulted in almost aggregated nano particles, in the vaterite form. The high concentration of CaCl_2 addition resulted in both aggregated nano CaCO_3 particles and cubical calcite crystals of about 8

μm . It seems that, there are some aggregated particles which have not completed their conversion into cubical calcite form.

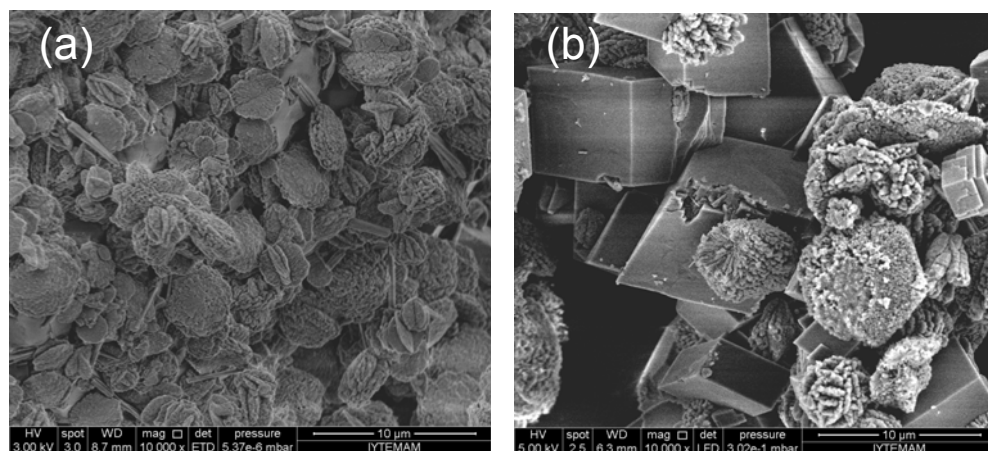


Figure 5.6. SEM images of the precipitates obtained from addition of (a) low (15 mM) and (b) high (760 mM) concentrations of CaCl_2 into Na_2CO_3 solution (75 mM) at a rate of 0.077 ml/min. pH was adjusted to 11.5 by the addition of 5 ml of 250 mM NaOH solution.

The CaCO_3 formation was studied by directly adding the bicarbonate (HCO_3^-) ions into $\text{Ca}(\text{OH})_2$ solution. The pure CO_2 gas was bubbled in a 2 L of DI water and saturated to a concentration of 33 mM which was estimated from its solubility in water¹²¹. A 100 ml of HCO_3^- solution in total was added into a 100 ml of $\text{Ca}(\text{OH})_2$ solutions. The concentrations of $\text{Ca}(\text{OH})_2$ and HCO_3^- ions as well as $[\text{Ca}(\text{OH})_2] / [\text{HCO}_3^-]$ ratios were calculated as shown in Figure 5.7. As shown in Figure 5.7a, during the slow addition of CO_2 saturated solution into 20 mM of $\text{Ca}(\text{OH})_2$ solution, while the concentration of HCO_3^- was increasing, $\text{Ca}(\text{OH})_2$ concentration was decreasing due to dilution by time. The calculated $[\text{Ca}(\text{OH})_2] / [\text{HCO}_3^-]$ ratio was about 1.0 in 10 min and further decreased until the completion of 100 ml of solution added. For the fast addition (1 ml/sec), as shown in Figure 5.7b, the completion of the addition took about 2 min and showed the same trend as the slow addition. On the other hand, as shown in Figure 5.7b, the fast addition of CO_2 saturated solution into 40 mM of $\text{Ca}(\text{OH})_2$ solution took about 2 min but, at the end the $[\text{Ca}(\text{OH})_2] / [\text{HCO}_3^-]$ ratio was higher than 1.0. It can be clearly seen from these figures that the added $[\text{HCO}_3^-]$ ion concentrations were enough to be able to cover the stoichiometric $[\text{Ca}(\text{OH})_2]$ concentrations in the solutions.

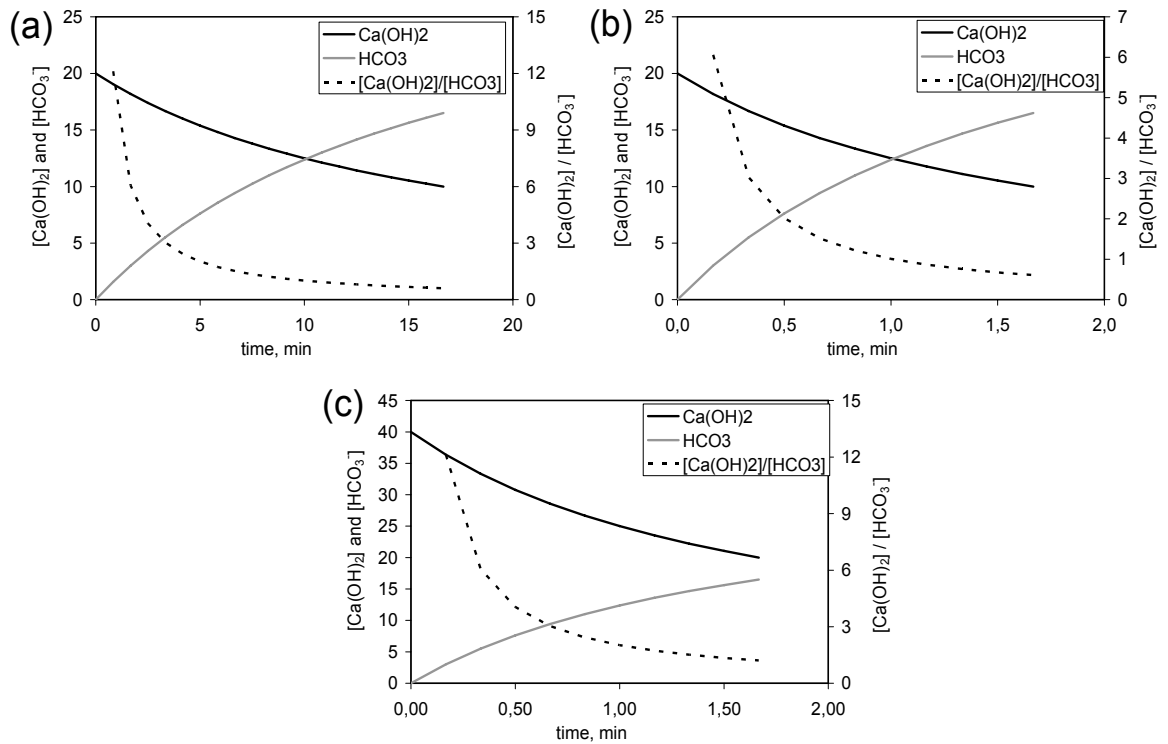


Figure 5.7. Calculated concentrations of Ca(OH)_2 and HCO_3^- and $[\text{Ca(OH)}_2] / [\text{HCO}_3^-]$ ratio. (a) slow addition of $[\text{HCO}_3^-]$ (0.1 mL/sec) into 20 mM of $[\text{Ca(OH)}_2]$ (b) fast addition of $[\text{HCO}_3^-]$ (1.0 mL/sec) into 20 mM of $[\text{Ca(OH)}_2]$ and (c) fast addition of $[\text{HCO}_3^-]$ (1.0 mL/sec) into 40 mM of $[\text{Ca(OH)}_2]$.

pH change during slow and fast addition of CO_2 saturated solution into 20 mM and 40 mM Ca(OH)_2 solutions were shown Figure 5.8. As shown in the figure, the change in pH was slow in 10 min for the slow addition of CO_2 saturated solution in the 20 mM Ca(OH)_2 solution, it was increased when $[\text{HCO}_3^-]$ concentration was equal to $[\text{Ca(OH)}_2]$ concentration. The decreasing pH was considerably steep for fast addition of CO_2 saturated solution into 20 and 40 mM solutions. In any case, pH only decreased from 12.5 to 11.2 indicating that CaCO_3 crystallization took place during the addition.

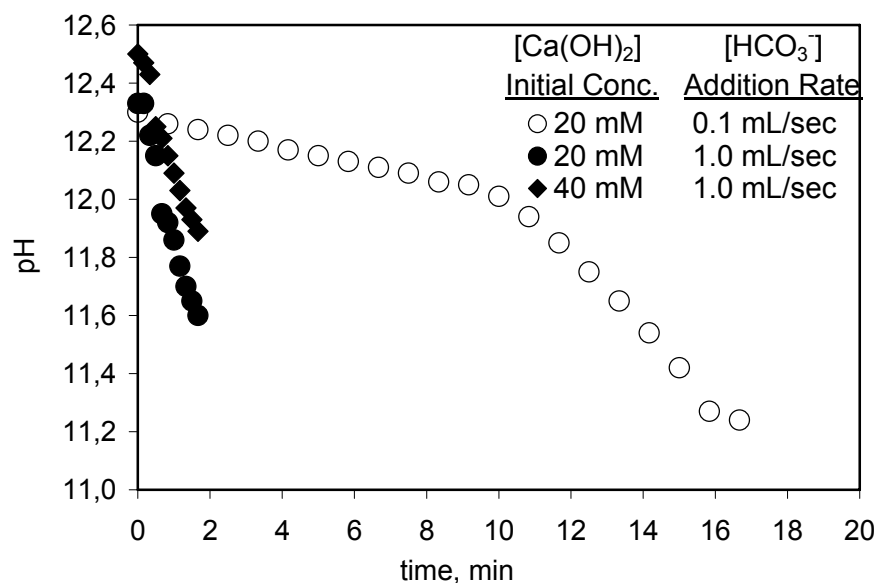


Figure 5.8. pH change during the slow (0.1 mL/sec) and fast (1.0 mL/sec) addition of 100 mL of bicarbonate ions into 100 mL of 20 mM and 40 mM of Ca(OH)₂ solution.

The SEM images of CaCO₃ crystals produced during the slow and fast addition of CO₂ saturated solution into 20 mM and 40 mM of Ca(OH)₂ solutions were shown in Figure 5.9. As shown in Figure 5.9a, the CaCO₃ crystals were formed from aggregated nano particles, which were identified as calcite from the XRD patterns as shown in Figure 5.10. The newborn calcite crystals converted from these aggregated nano particles were also shown. These immature CaCO₃ crystals were seen in their early completion stages as a result of the slow addition of HCO₃⁻ ions into 20 mM of Ca(OH)₂ solution. As shown in Figure 5.9b and Figure 5.9c, fast addition of CO₂ saturated solution into 20 mM and 40 mM of Ca(OH)₂ solutions resulted in chain-like CaCO₃ particles. The chain-like structures were seen to composed of nano size crystals less than 60 nm. All precipitated solids obtained were typical calcite crystals with different orientation and lattice positions as shown in their XRD patterns in Figure 5.10.

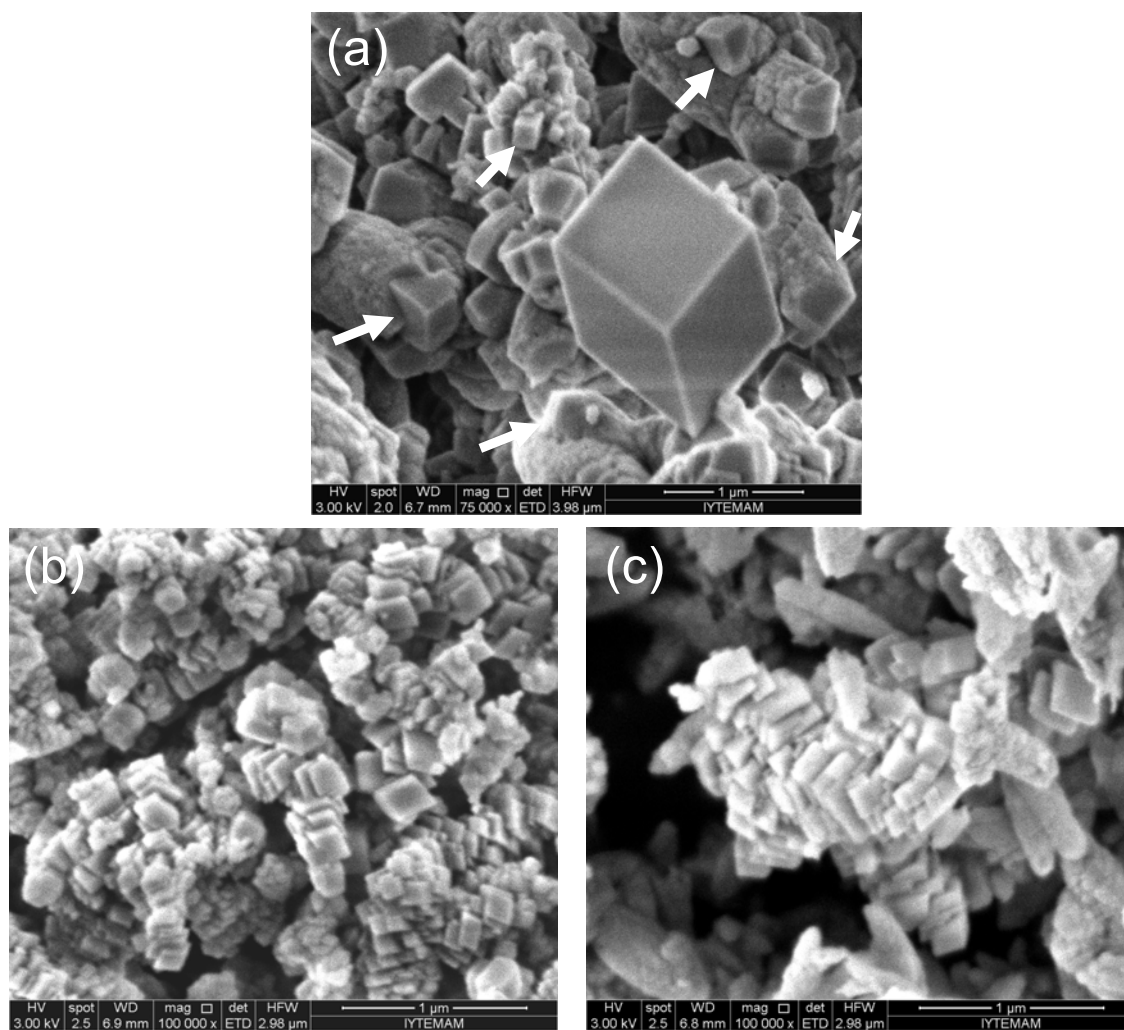


Figure 5.9. SEM images of the precipitates obtained by adding into $\text{Ca}(\text{OH})_2$ solution (a) slow addition of bicarbonate ions at 0.1 ml/sec into 20 mM $\text{Ca}(\text{OH})_2$ solution (b) fast addition at 1.0 ml/sec into 20 mM $\text{Ca}(\text{OH})_2$ solution, and (c) fast addition at 1.0 ml/sec into 40 mM $\text{Ca}(\text{OH})_2$ solution.

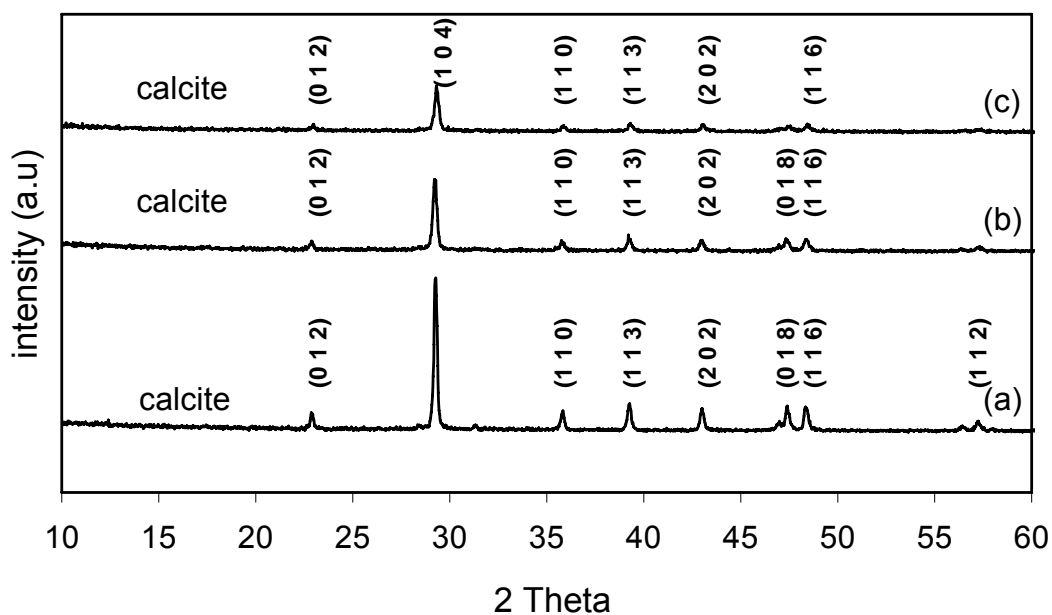


Figure 5.10. XRD patterns of the precipitates for the slow and fast addition of bicarbonate ions into 20 mM and 40 mM Ca(OH)_2 solutions. (a) slow addition of bicarbonate ions at 0.1 ml/sec into 20 mM Ca(OH)_2 solution (b) fast addition at 1.0 ml/sec into 20 mM Ca(OH)_2 solution, and (c) fast addition at 1.0 ml/sec into 40 mM Ca(OH)_2 solution.

5.2. Ca(OH)_2 Dissolution

pH and electrical conductivity values are the two parameters in CaCO_3 crystallization processes. In order to obtain nano size, mono disperse, homogeneous and individual crystals, these parameters should be monitored and controlled during the CaCO_3 crystallization. Conductivity is related to the ionic strength of a solution containing positive and negative ions. Therefore, conversion of CO_2 to CaCO_3 can be monitored by measuring the conductivity.

The conductivity values were measured for various concentrations of Ca(OH)_2 and CaCO_3 (from 0 to 150 mM) in water as shown in Figure 5.11. The conductivity values for Ca(OH)_2 reported by Burns et al. (2005)⁷³, were also included in the figure. The solubility of Ca(OH)_2 has been reported as 0.185 g/100 ml at 25 °C¹²², which is about 25 mM. As shown in the figure, the conductivity values increase linearly with Ca(OH)_2 concentrations up to this solubility limit. After the solubility value, the conductivity does not change for additional Ca(OH)_2 or CaCO_3 concentrations. The ionic conductivities for 0.5 Ca^{++} and OH^- were reported to be $5.95 \times 10^{-3} \text{ m}^2 \text{ S}^{-1} \text{ mol}^{-1}$ and

$1.98 \times 10^{-2} \text{ m}^2 \text{ S}^{-1} \text{ mol}^{-1}$, respectively¹²³. These values give the theoretical electrical conductivity of $5.15 \times 10^{-2} \text{ m}^2 \text{ S}^{-1} \text{ mol}^{-1}$ for $\text{Ca}(\text{OH})_2$ solution. Burns et al. (2005)⁷³, reported that their experimental conductivity values deviated 24% from the theoretical values. The deviation in our experiments were even higher than what Burns et al., (2005) were reported. When a small amount of $\text{Ca}(\text{OH})_2$ was dissolved in water, probably a high portion of $\text{Ca}(\text{OH})_2$ was dissociated into its Ca^{++} and OH^- ions. When subsequent $\text{Ca}(\text{OH})_2$ powders were added into the solution, before equilibrium was reached, probably much of the powder was left undissolved. On the other hand, the conductivity for CaCO_3 is nearly zero indicating that any decrease in conductivity in CaCO_3 crystallization can be related to decreasing $\text{Ca}(\text{OH})_2$ concentration and increasing CaCO_3 formation.

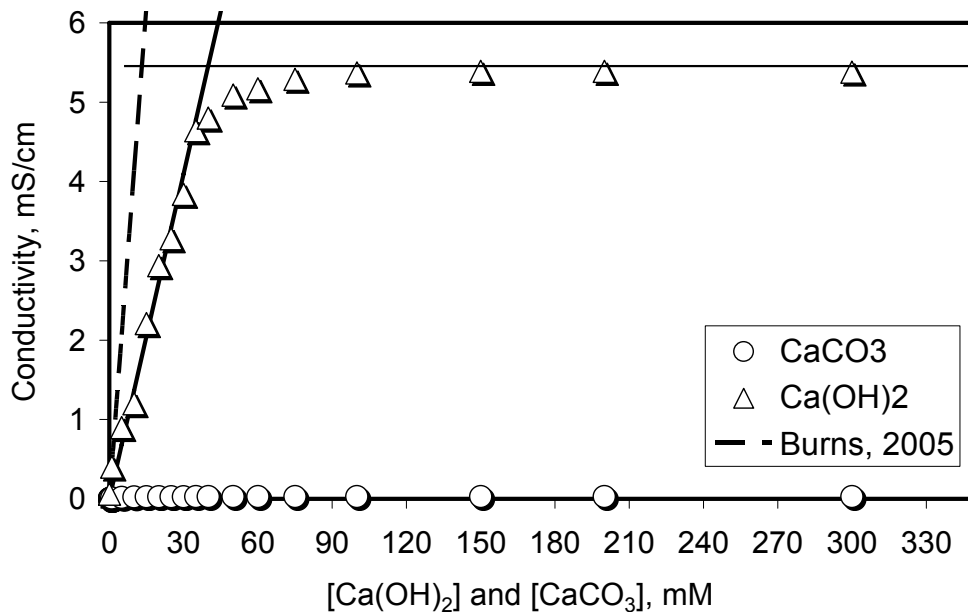


Figure 5.11. Change in conductivity (mS/cm) for the incomplete dissolution of $\text{Ca}(\text{OH})_2$ and CaCO_3 ($T=25^\circ\text{C}$) and comparison with the observation by Burns et al. (2005)⁷³ ($T=18^\circ\text{C}$).

The dissolution of $\text{Ca}(\text{OH})_2$ in water was studied. A 1, 3, 10, 16, 20 mM of $\text{Ca}(\text{OH})_2$ solutions were dissolved in a reactor at 23°C . pH and conductivity values were recorded during the dissolution. Particle sizes were measured every 2 min. As shown in Figure 5.12a and Figure 5.12b, both pH and conductivity values are proportional to the concentration of $\text{Ca}(\text{OH})_2$. Both pH and conductivity values increase slightly indicating that the dissolution of $\text{Ca}(\text{OH})_2$ is a dynamic process. Especially, the

increase in pH and conductivity are very small for low concentrations of $\text{Ca}(\text{OH})_2$ while the change in conductivity values for higher concentrations looks significant.

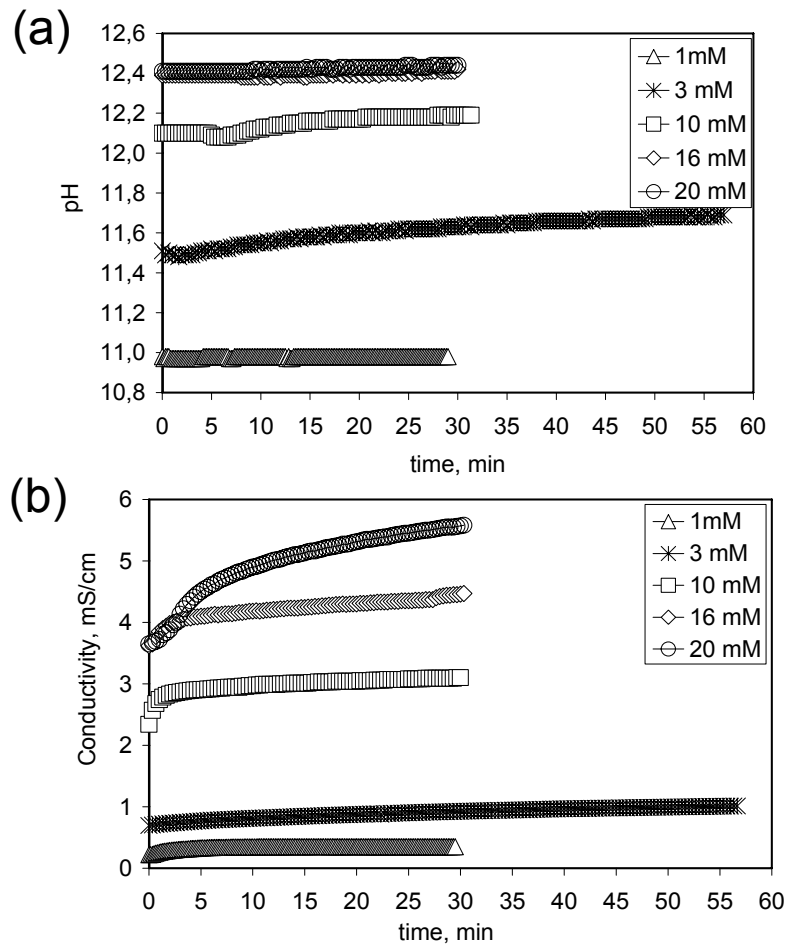


Figure 5.12. Change of pH and conductivity in the presence of various amounts of $\text{Ca}(\text{OH})_2$ ($T = 25^\circ\text{C}$)

The particle size distribution and the average particle size were estimated during the $\text{Ca}(\text{OH})_2$ dissolution. Figure 5.13 shows the particle size distribution taken for 1, 3, 10, 16, 20 mM of $\text{Ca}(\text{OH})_2$ solutions at different time intervals in $\text{Ca}(\text{OH})_2$ dissolution experiments. As shown in the figure, the particle size decreases from 1.0 -1.2 μm to 100-200 nm in 20 min and the distribution of particles narrowed as time were elapsed.

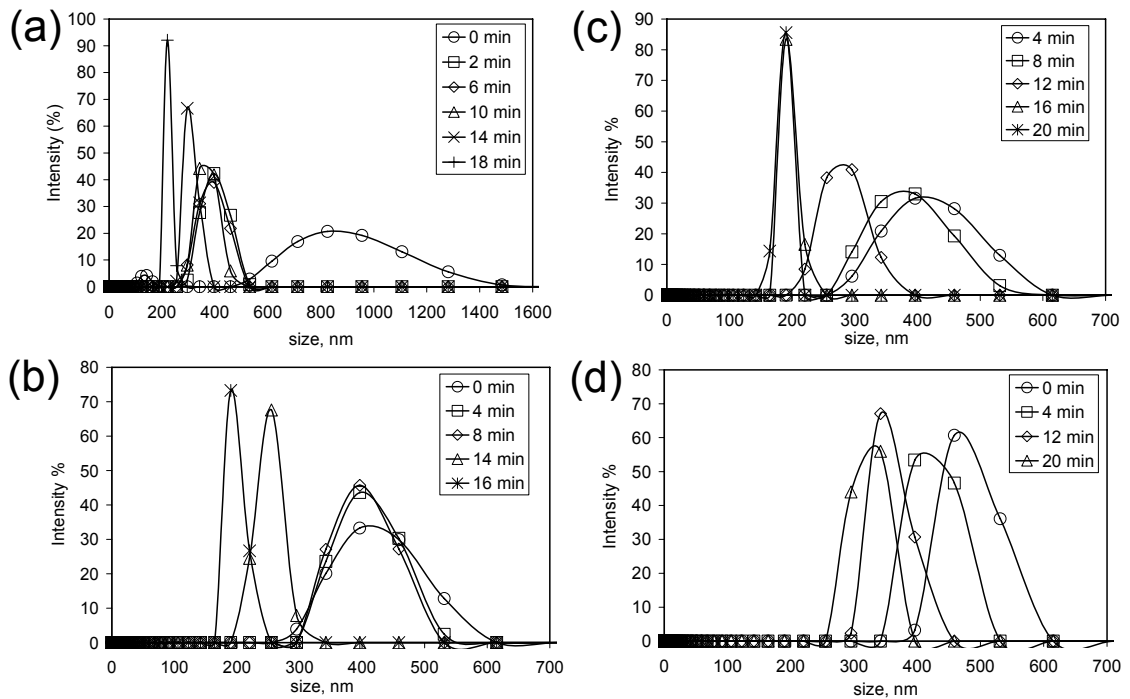


Figure 5.13. Change of size distribution with time during the dissociation of (a) 1 mM, (b) 5 mM, (c) 10 mM, and (d) 20 mM Ca(OH)₂ (T= 25 °C ; stirring rate: 600 rpm)

Figure 5.14 shows the change in mean particle diameter with time for different concentrations of Ca(OH)₂ during their dissolution. While the average particle size for 20 mM of Ca(OH)₂ was measured initially about 750 nm, the average particle size for lower concentrations were measured about 450 nm indicating that much of the particles were undissolved at concentrations higher than the saturation limit. Besides, the particle size was initially about 450 nm and decreased to about 250 nm indicating that there are incomplete dissolution at all concentrations in 20 min. This is important because the undissolved Ca(OH)₂ particles would serve as a template for CaCO₃ crystallization by the carbonization method.

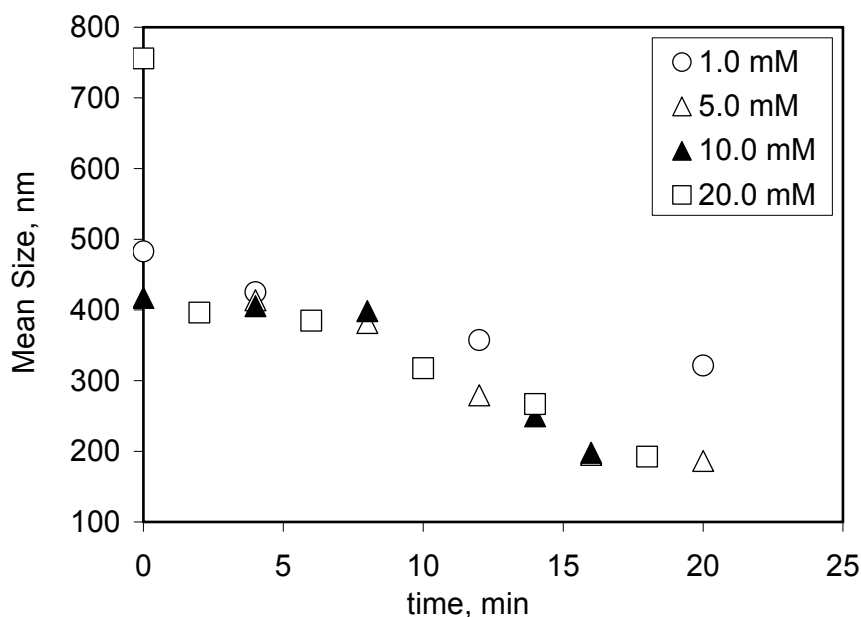


Figure 5.14. Change of mean size diameter for various concentrations of Ca(OH)_2 .

The dissolution of Ca(OH)_2 was modeled with respect to change in concentrations in solution by using Eq (2.2) to Eq (2.8). As shown in Figure 5.15a, the Ca(OH)_2 amount or its concentration decreases by time in solution. When the concentration is below the solubility limit, the concentration seems to decrease to zero. However, as shown in Figure 5.15b, the concentration decreases almost completely in 30 min for low concentrations. This is probably due to the way how the kinetic parameters were estimated and reported in the literature. For instance, the time required for 80% of dissolution was used in kinetic parameter estimation⁷². On the other hand, the decrease in concentrations above the solubility limit seems to reach equilibrium faster while some Ca(OH)_2 was left undissolved in solution. Although 80% of the Ca(OH)_2 dissolves in 10 min, at least 20 min dissolution time is needed for the complete dissolution of Ca(OH)_2 up to 10 mM concentrations. If the concentration of the Ca(OH)_2 is 20 mM, which is almost at its solubility limit, approximately 50% of the Ca(OH)_2 powders (non-solute part) remain in the reactor. In this case, there is a colloidal suspension or a slurry at above the solubility limit.

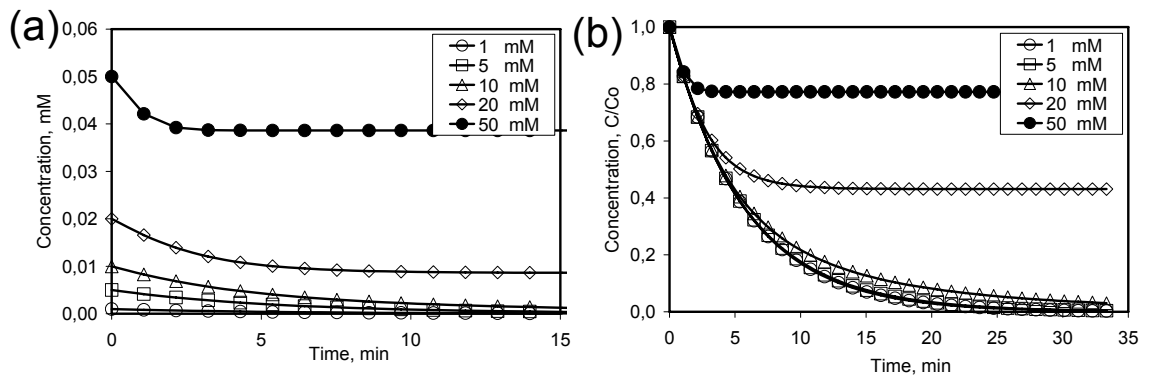


Figure 5.15. Modeling of the dissolution of Ca(OH)_2 for different concentrations

Figure 5.16 shows concentrations of different species in Ca(OH)_2 dissolution. As shown in the figure, Ca(OH)_2 decreases almost exponentially and the Ca^{++} and OH^- concentrations increase. As expected, the OH^- concentration is almost doubles compared to the Ca^{++} concentration. On the other hand, the pH jumps to about 12 and slightly increases as more OH^- ions were produced during the dissolution. The CaOH^+ concentration due to the complexation looks negligible. It seems that the dissolution of Ca(OH)_2 is almost complete in 35 min. Again, this modeling result is highly influenced by the kinetic parameters reported in the literature for the 80% dissolution, which was considered as a complete dissolution.

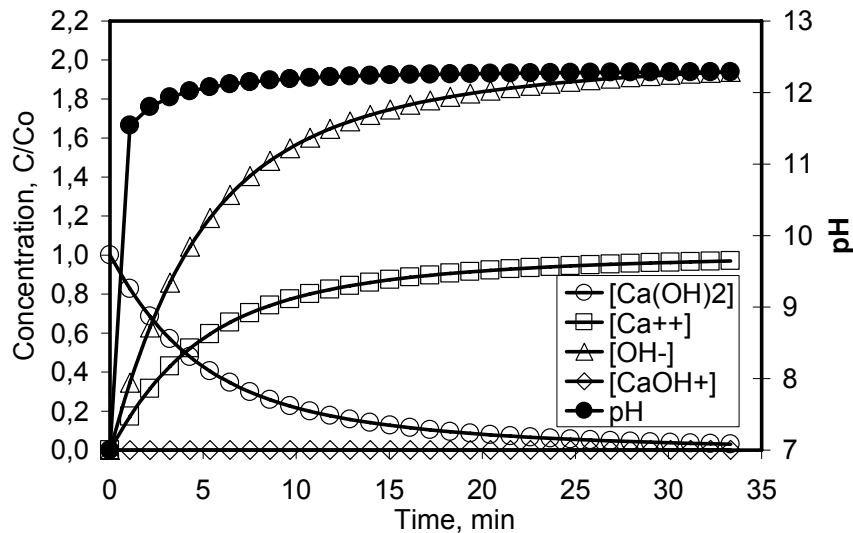


Figure 5.16. Modeling of concentrations of species during the dissolution of Ca(OH)_2 in solution.

5.3. CaCO₃ Synthesis by Carbonization Method

The carbonization method has been used in CaCO₃ synthesis especially in industry. The general procedure in carbonization is to blow the CO₂ through the Ca(OH)₂ solution and convert the Ca(OH)₂ into the CaCO₃. However, the control of crystal size, size distribution, and crystal morphology are highly difficult. Especially, Ca(OH)₂ concentration, CO₂ flow rate, pH, conductivity, temperature, stirring rate, and chemical additives were studied in the literature but nano calcite were rarely produced. Here, we designed a mini reactor within a stirring tank reactor and CO₂ was introduced on the top of the liquid level in the mini reactor. It was aimed that after the clusters, nucleation, and nano CaCO₃ were formed in the mini reactor due to the limited addition of CO₂, the nano crystals were produced in the stabilized form in the stirred tank reactor.

The changes in pH and conductivity during the CaCO₃ synthesis by the carbonization method were shown in Figure 5.17. In the first 10 min as shown in the figure, the conductivity of pure water was about ~ 0 (24 μs/cm) and pH was ~6.5. When Ca(OH)₂ powder was added into the water for a 10 mM of solution, pH and conductivity were suddenly increased to the values of about 12.0 and 3.2 mS/cm, respectively. A slight increase in pH and a continuous increase in conductivity indicate the progress in the Ca(OH)₂ dissolution. When CO₂ was introduced, both pH and conductivity were seen to decrease. A zero conductivity value in about 6 min indicated that all the Ca(OH)₂ would be consumed and the Ca⁺⁺ ions were converted. The increase in the conductivity beyond this value could be related to the increase in charged species due to the CO₂ dissolution as well as Ca⁺⁺ ions as a result of the redissolution of CaCO₃.

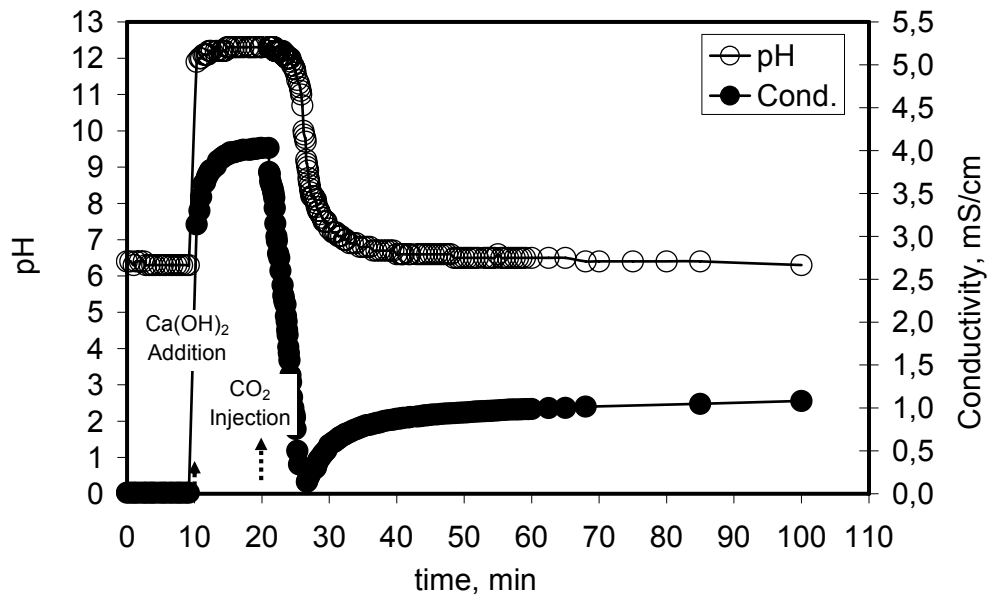


Figure 5.17. Change of conductivity and pH in the presence of 10 mM $\text{Ca}(\text{OH})_2$ (stirring rate : 600 rpm) (diameter of glass tube for CO_2 injection: 5 mm)

Figure 5.18a shows the pH and conductivity values for a 20 mM of $\text{Ca}(\text{OH})_2$ solution. When the CO_2 was introduced, both the pH and conductivity values decreased slightly. Such behavior during the process of the PCC formation in a reactor could be explained as a consequence of nucleation and growth of calcium carbonate precursors. Both the pH and conductivity values were steeply decreased through the completion of the reaction. Since the precursor is extremely unstable, it rapidly dissolves during its transformation into the stable calcite, causing the uncontrolled increase in conductivity.

Figure 5.18b shows the deviation in pH and conductivity, which were calculated by taking the difference between two subsequent values per the time interval. As shown in the figure, the time derivative for conductivity decreases to a minimum at about 35 min and then increases to the positive values. Whenever the derivative for conductivity reaches its minimum value, the pH starts to decrease. The derivative data may be more informative on the control of the carbonization reaction.

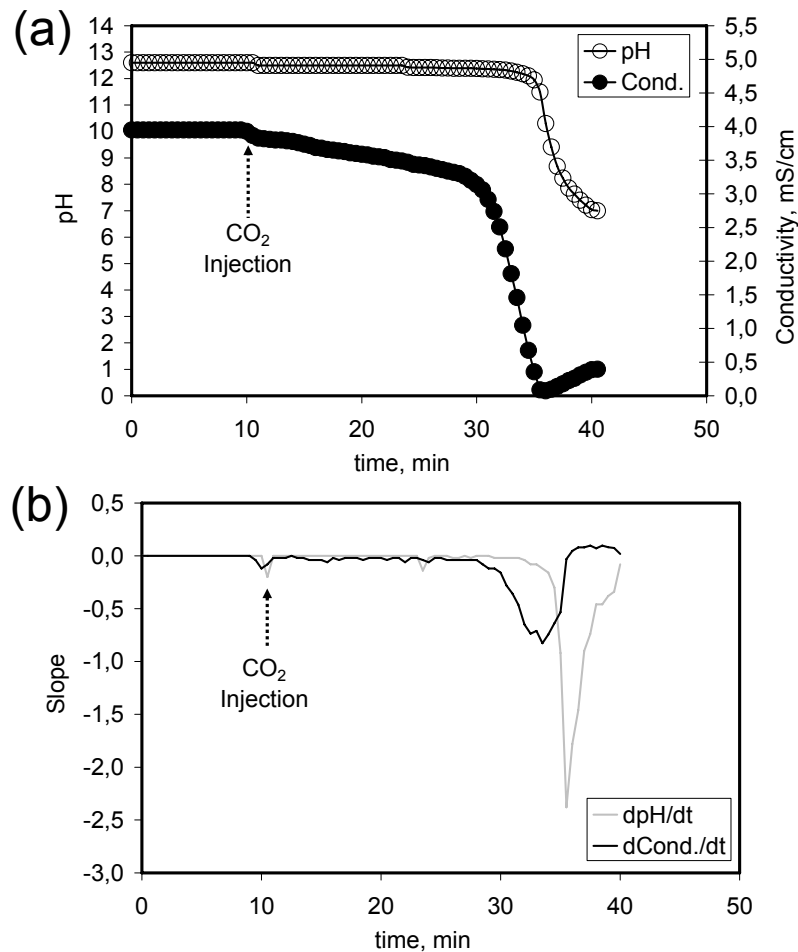


Figure 5.18. Change of (a) pH and conductivity (b) deviation in pH and conductivity in the presence of 20 mM Ca(OH)₂ (stirring rate : 600 rpm) (diameter of glass tube for CO₂ injection: 5 mm)

The solubility of Ca(OH)₂ and the manner of pH-conductivity curves are important for the precipitation of CaCO₃ as explained in section 5.1. Because of this importance, some experiments were expressed in the presence of Ca(OH)₂ below the solubility limit using extreme low amount of powder Ca(OH)₂ (0.1 mM) and above the solubility limit using extreme high amount of powder Ca(OH)₂ (50 mM, 200 mM and 500 mM), where the solubility limit of Ca(OH)₂ is approximately 25 mM at 25 °C. The pH and conductivity curves obtained during the CO₂ injection were shown in Figure 5.19.

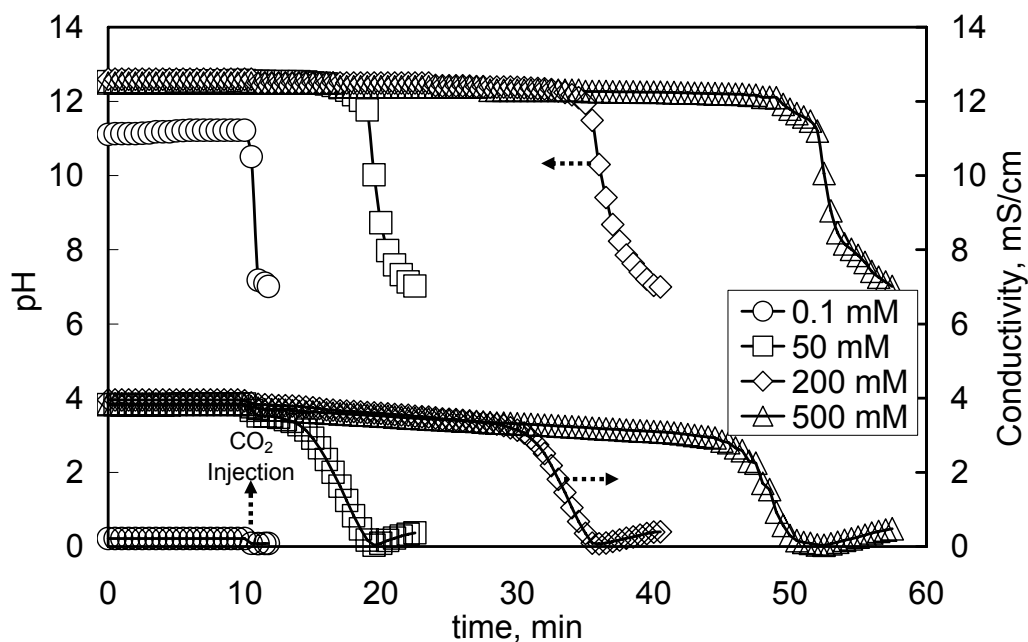


Figure 5.19. Change of pH and conductivity in the presence of extreme amounts of Ca(OH)_2 on the precipitation of CO_2 (stirring rate : 600 rpm; diameter of glass tube for CO_2 injection: 10 mm; $T = 25^\circ\text{C}$)

Figure 5.19 indicates that there is a strong correlation between the amounts of Ca(OH)_2 and precipitation time. Considering the CO_2 injection started at 10 min, a sudden consumption of the ions was observed for extreme low amount of Ca(OH)_2 . For 0.1 mM Ca(OH)_2 , the conductivity of the solution was almost zero because of the absence of enough Ca^{++} and OH^- ions, initially. For 50 mM, 200 mM and 500 mM Ca(OH)_2 , total conductivity was consumed at about 10, 25 and 40 min respectively, with CO_2 injection. Figure 5.20 shows the slopes of the pH and conductivity curves. They can give an opinion about the consumption rates of the total ions or conversion rates. When the Ca(OH)_2 amount increases, the conversion rate decreases. Considering the Ca^{++} and OH^- ion consumption through the formation of CaCO_3 , it is easy to explain the magnitudes of the slopes, such that the retardation in precipitation time may be caused by higher concentrations of ions in solution. The derivatives of these curves may be connected to the precipitation reaction rate. As shown in the Figure 5.20, all derivatives had negative slopes for pH, and some positive values for conductivity after the neutralization was completed the slurry at basic pH. Positive slopes indicate the dissociation of surface species, remaining carbonic acid, and metastable forms of CaCO_3 . When the concentration of Ca(OH)_2 in slurry increases, slope of the derivative curves for both pH and conductivity decreases due to the slow conversion from CO_2 to

CaCO₃. Conductivity change is always faster than the pH change, indicating that faster Ca⁺⁺ ions consumption would take place comparing to consumption of OH⁻ ions in solution.

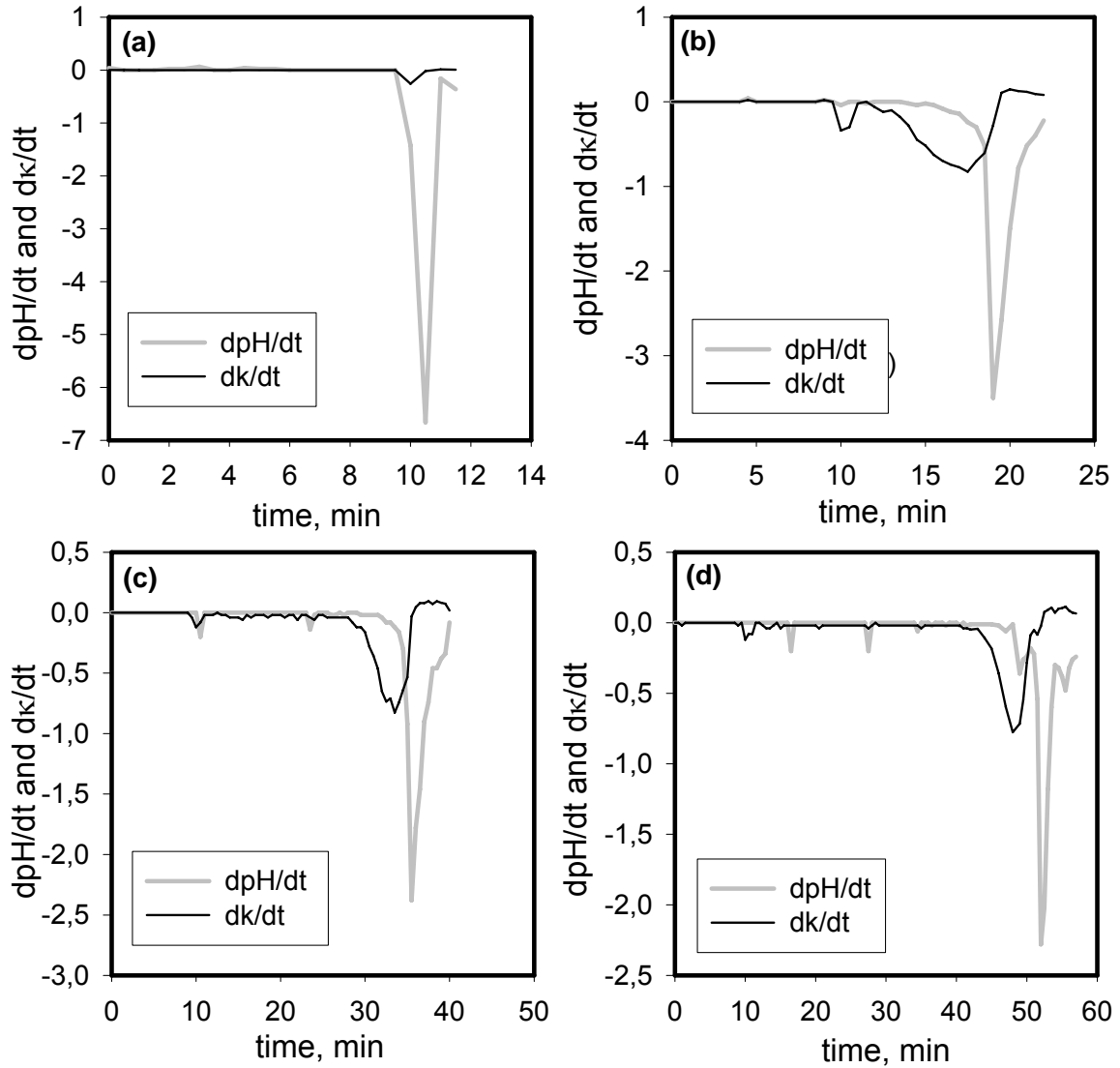


Figure 5.20. Change of pH and conductivity in presence of (a) 0.1 mM, (b) 50 mM (c) 200 mM (d) 500 mM Ca(OH)₂ on the CaCO₃ precipitation (derivative curves).

The SEM images of the precipitates obtained from the experiments in the presence of extremely high amounts of Ca(OH)₂ were shown in Figure 5.21. As shown in the figure, extreme amounts of Ca(OH)₂ solutions produced aggregated crystals in nano size with different shapes.

The pH and conductivity data of the precipitation reactions in the presence of various amounts of Ca(OH)₂ by CO₂ bubbling were obtained under ambient pressure at

room temperature as shown in Figure 5.22. While 10 min was needed for 20 mM $\text{Ca}(\text{OH})_2$ solution by traditional carbonization method, 2.5 min precipitation time was enough to produce calcite by CO_2 bubbling. Precipitation time decreased from 25 – 50 min by limited CO_2 injection to 13-18 min by CO_2 bubbling in the slurry. Because, heterogeneous nucleation can occur during the CaCO_3 production by CO_2 bubbling. The bubble surfaces may reduce activation barrier of the nucleation. They also improve the nucleation rate. When the bubbles dissolved in water, a concentrated ion layer will occur on the surface. This layer behaves like a surfactant layer and, reduces the surface energy¹²⁴. The nanoparticles approach the bubble with the help of surface forces and these forces determine the adsorption process. During the precipitation, particles are under the influences of electrostatic double layer force, the van der Waals force and the hydrophobic force in aqueous solution. Neutral and basic conditions are needed for the precipitation of CaCO_3 , and both CaCO_3 particles and the bubbles are negatively charged at those conditions. Therefore, repulsion between nanoparticle and bubble occurs due to the electrostatic double layer force between similarly charged particles. At the same time, since the very small distance (in nanometers) between nanoparticle and bubble in solution, the van der Waals force between nanoparticle and bubble is also repulsive force. Since the bubbles are hydrophobic, only repulsive forces between hydrophilic CaCO_3 nanoparticles and bubble occur. However, attraction force between CaCO_3 particles causes the aggregation. It is reported 10^9 fold-increases in nucleation rate with the 30% decrease in surface free energy. HCO_3^- ions strongly adsorb on the bubble surface when the CO_2 dissolves. The concentration of HCO_3^- is more significant than that of OH^- at the bubble/solution interface¹²⁴.

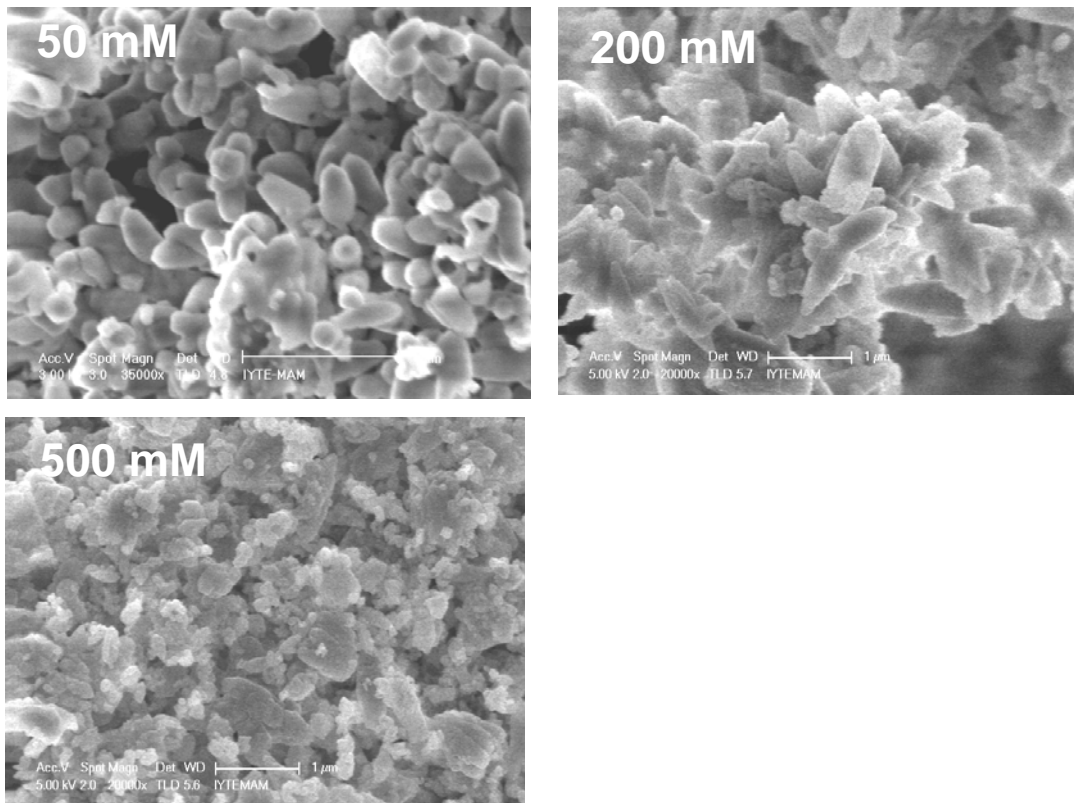


Figure 5.21. Effect of extremely high amounts of $\text{Ca}(\text{OH})_2$ on the shape and the size of the PCC's.

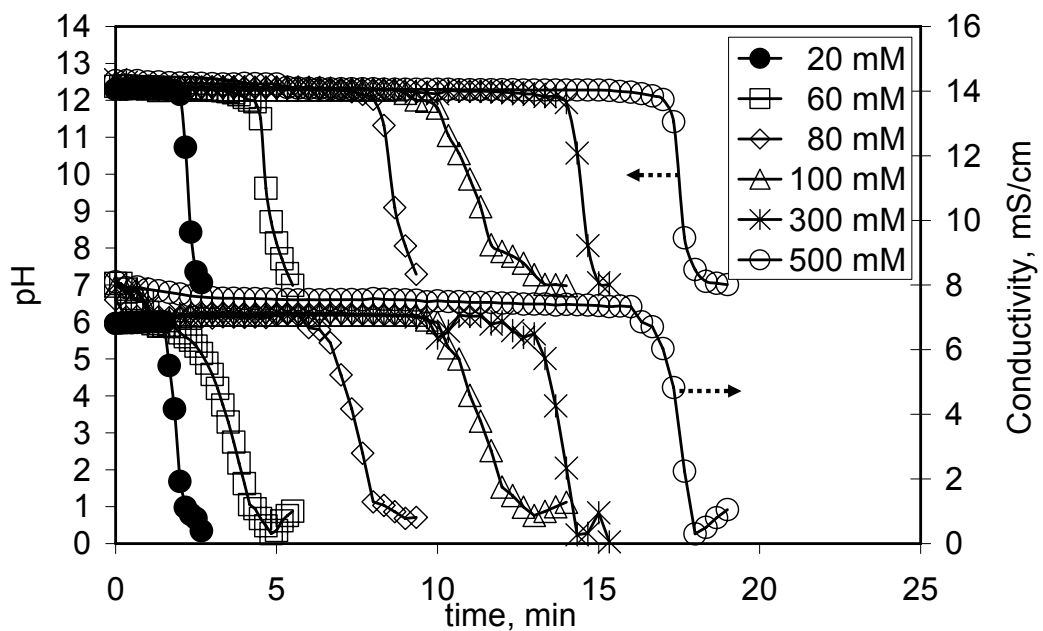


Figure 5.22. Change of pH and conductivity in the presence of various $\text{Ca}(\text{OH})_2$ amounts by CO_2 bubbling.

According to the derivative plots of pH and conductivity with time as shown in Figure 5.23, the consumption behavior of pH and conductivity for 20 to 500 mM of $\text{Ca}(\text{OH})_2$ solutions showed a fast decrease for the CO_2 bubbling.

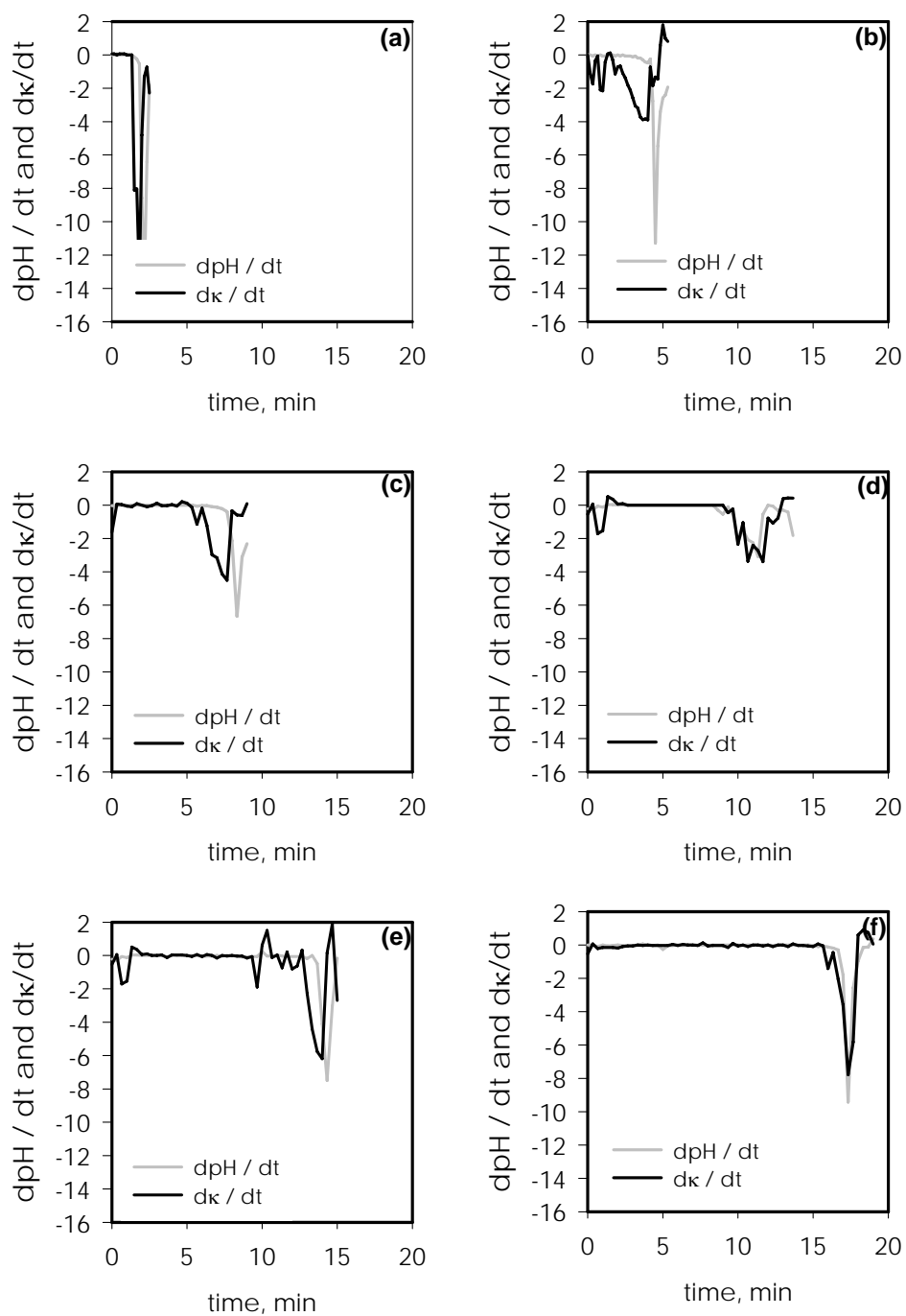


Figure 5.23. Change of derivatives of the pH and conductivity in the presence of (a) 20 ml (b) 60 ml (c) 100 ml (d) 300 ml (e) 500 ml of $\text{Ca}(\text{OH})_2$ by CO_2 bubbling.

SEM images of the precipitates obtained from CO₂ bubbling for various amounts of Ca(OH)₂ were shown in Figure 5.24. The XRD patterns for these crystals were also shown in Figure 5.25. As shown in SEM images, characteristic cubic crystals were obtained with the Ca(OH)₂ amounts which are close to the solubility limit of about 20 mM. 300 mM Ca(OH)₂ allows to produce irregular crystals in submicron size by CO₂ bubbling. The size of cubic crystals in each aggregate was about ~ 200 nm, and no single crystal having its size above 1 μm detected by SEM. The size of the particles in the presence of high amounts of Ca(OH)₂ (300 mM) were relatively larger comparing to the precipitates obtained in the presence of lower Ca(OH)₂ concentrations. The size ranges of the precipitates (grains) were approximated as 150 – 300 nm by SEM images.

All the diffraction peaks are readily indexed to calcite polymorph of CaCO₃ (space group: R3c (167)] with a lattice constant $a = 4.988$ and $c = 17.05 \text{ \AA}$)⁵⁷. According to the Bragg's reflections which are given in Joint Committee on Powder Diffraction Standards (JCPDS) files, Card 5-586, and Card 86-2334, the 2θ value of the characteristic peaks were at about 29° indicating the stable calcite formation. On the other hand, the lattice position (1 0 4) indicate the most of the precipitates are rhombohedral calcites. The other lattice formation of calcite detected by different 2θ position was also obtained as shown in Figure 5.25. The crystals have nearly identical peak positions and narrow peak widths. The strong and sharp peaks indicate that the samples were well crystallized. No obvious characteristic diffraction peaks of any impurities, or vaterite and aragonite formations were detected. Also, the sharp diffractions at the d -spacings, 3.02864, 1.9166 and 1.8796 confirm the presence of stable calcite crystals.

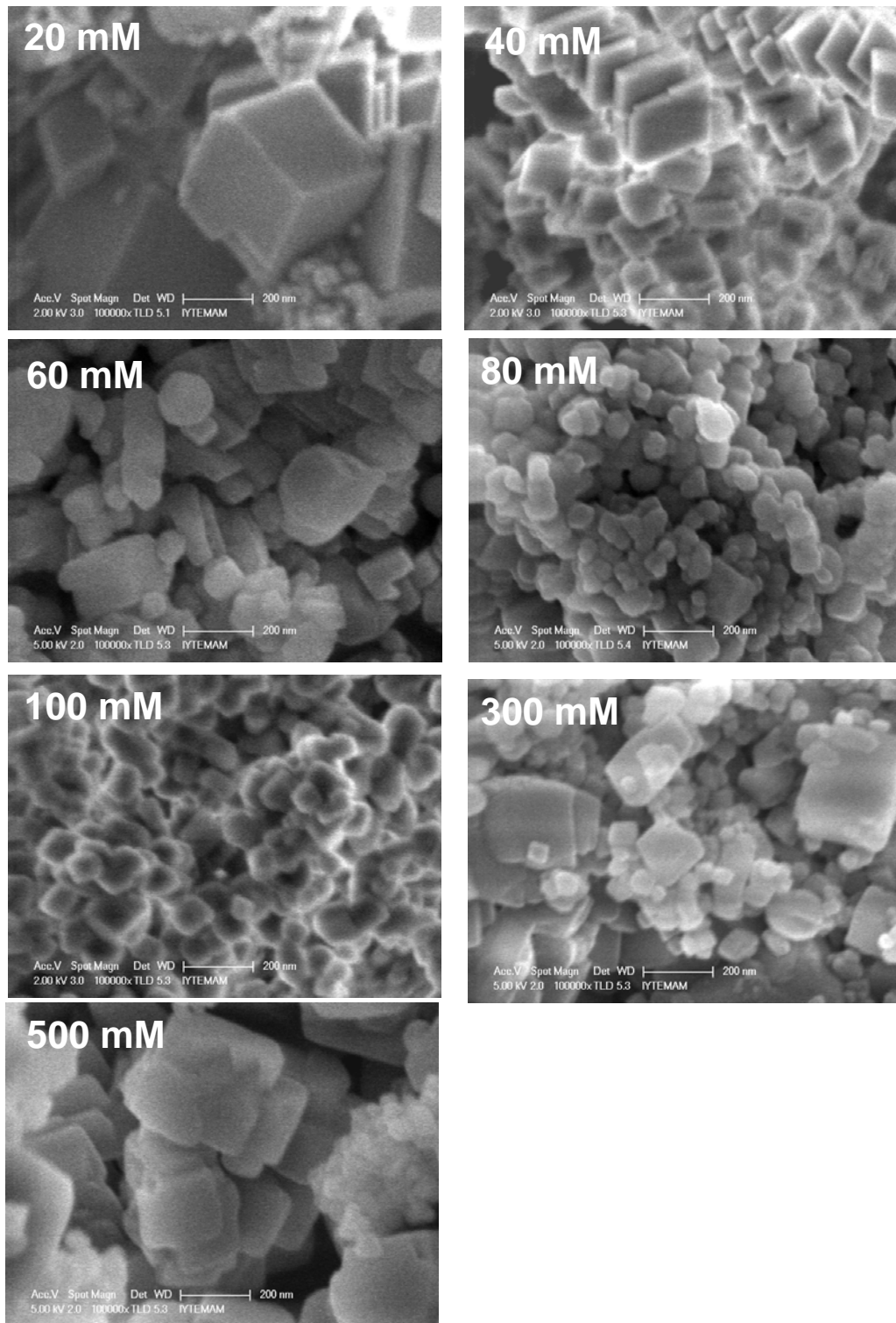


Figure 5.24. SEM images of the precipitate in the presence of various Ca(OH)_2 concentrations by CO_2 bubbling.

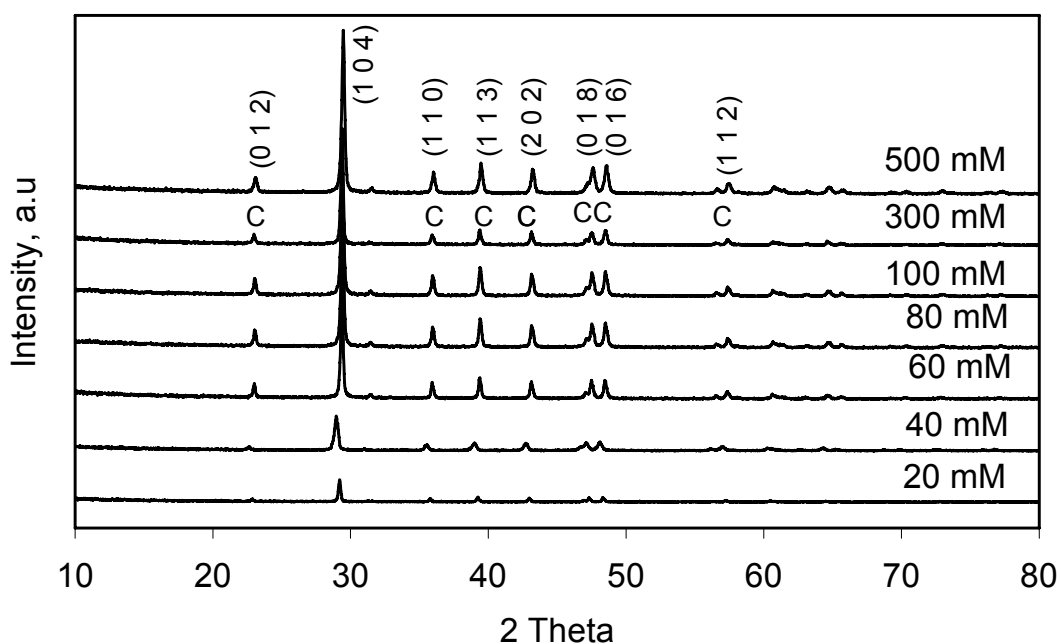


Figure 5.25. XRD patterns of the precipitate in the presence of various $\text{Ca}(\text{OH})_2$ concentrations by CO_2 bubbling (C: calcite).

The crystallite sizes for the PCC's were calculated by Debye Scherrer Equation*, and given in Table 5.1.

Table 5.1. Evaluation of the precipitates obtained by the CO_2 bubbling

Molarity of $\text{Ca}(\text{OH})_2$	t_1^*	t_2^+	Peak** angle (2 θ)	d-spacing	Ref Code ⁺⁺	Crystal Structure	size [†] (nm)
20 mM	2.67	2.67	29.20705	3.05510	05-0586	cubic	46.48
40 mM			28.97763	3.07877	05-0586	cubic	46.54
60 mM	4.83	5.50	29.38875	3.03663	86-2334	cubic +sphere	46.68
80 mM	9.00	9.33	29.41990	3.03348	86-2334	cubic +sphere	40.52
100 mM	14.00	13.00	28.84202	3.09293	86-2334	cubic +sphere	40.82
300 mM	14.33	15.33	29.38102	3.03741	86-2334	cubic +sphere	39.41
500 mM	18.00	19.00	29.48821	3.02661	86-2334	cubic +sphere	33.80

* Elapsed time from CO_2 injection to zero conductivity (minutes)

+ Elapsed time from CO_2 injection to 7.0 pH (minutes)

** Peak parameters detected with 100 % relative intensity

⁺⁺ Bragg's reflections given in Joint Committee on Powder Diffraction Standards (JCPDS) files

[†] Crystallite size calculated by Debye Scherrer Equation representing the minimum dimension (nm)

* Crystal sizes of the precipitates were calculated based on a well-established method widely employed to calculate particle size from X-ray patterns from the broadening of a diffraction line at half the line maximum intensity by employing only ordinary principles of optical diffraction and starting from Bragg's equation: $n\lambda = 2d \sin \theta$. The Debye Scherrer Equation is as follows: $\beta_{hkl} = 0.90 \lambda / L_{hkl} \cos \theta$ where β_{hkl} is the broadening of the diffraction line measured at half the line maximum intensity (forward width half maximum -FWHM), λ is the X-ray wavelength, L_{hkl} is the crystal size, and θ is the diffraction angle. The broadening of a peak is related to the crystal size and to the wavelength λ provided by the equipment used. Usually, the peak is not a line but an interval.

5.4. Progress in CaCO₃ Crystallization

Progress in CaCO₃ crystallization was studied with batch experiments at the same conditions. A 30 mM of Ca(OH)₂ slurry was reacted with CO₂ which contacted the solution on the surface in a volumetric flask. The stirring rate was 600 rpm. The filling conditions of CO₂ gas to the plastic balloon were the same for each run. The reaction was terminated at different time intervals for each individual run, and pH and conductivity values were measured.

The pH and conductivity values measured for each identical run were shown in Figure 5.26. The samples taken from each run for analyses were also shown in the figure. As shown in the figure, up to 10 min of contact time for CO₂, both pH and conductivity values slightly decreased. It seems that either there was a retardation during the CO₂ addition within the solution due to the diffusion limitations, or, CaCO₃ clusters were formed due to the slow addition of CO₂ within the solution. Interestingly, at the end of this initial step, a sudden decrease in conductivity from 6.7 to 2.5 mS/cm was seen while the pH values were constant at 12.5. At the third step of the crystallization, the conductivity values were seen to gradually decrease while the pH values were slightly decreasing from 12.2 to 11.8. At the fourth step, a sudden decrease in pH was seen while the decrease in conductivity was slightly accelerated. This step was the completion step for the crystallization, where the conductivity values were slightly increased and pH values were slightly decreased to its equilibrium value.

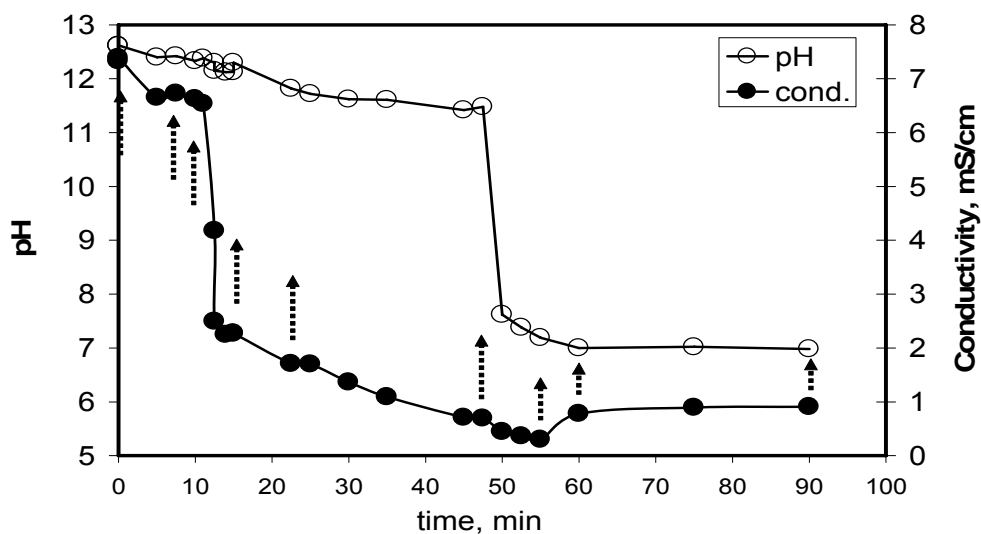


Figure 5.26. pH and conductivity curves of the stepwise carbonization reaction with direct CO₂ injection. (Ca(OH)₂: 30 mM; stirring: 600 rpm; T=25 °C; reactor: 250 ml volumetric flask).

SEM images of the particles produced were shown in Figure 5.27. The FTIR spectra and XRD patterns for these samples were also shown in Figure 5.28. The first image in Figure 5.27 shows the Ca(OH)_2 amorphous particles which were dissolved in solution and samples were withdrawn for analyses. For this first sample before CO_2 , as shown in Figure 5.28, the broadening lines of FTIR spectra in the region of $4000\text{-}3500\text{ cm}^{-1}$ and XRD patterns in 2 Theta position ranges of $10\text{-}20^\circ$ and $30\text{-}35^\circ$ represent the various formations of Ca(OH)_2 such as portlandite and ikaite. In the first reaction period of 10 min, CaCO_3 in the form of calcite and amorphous Ca(OH)_2 structure were observed. The images for particles in the first stage consisted of the mixture of amorphous Ca(OH)_2 and calcite particles which were seen at their early development stages.

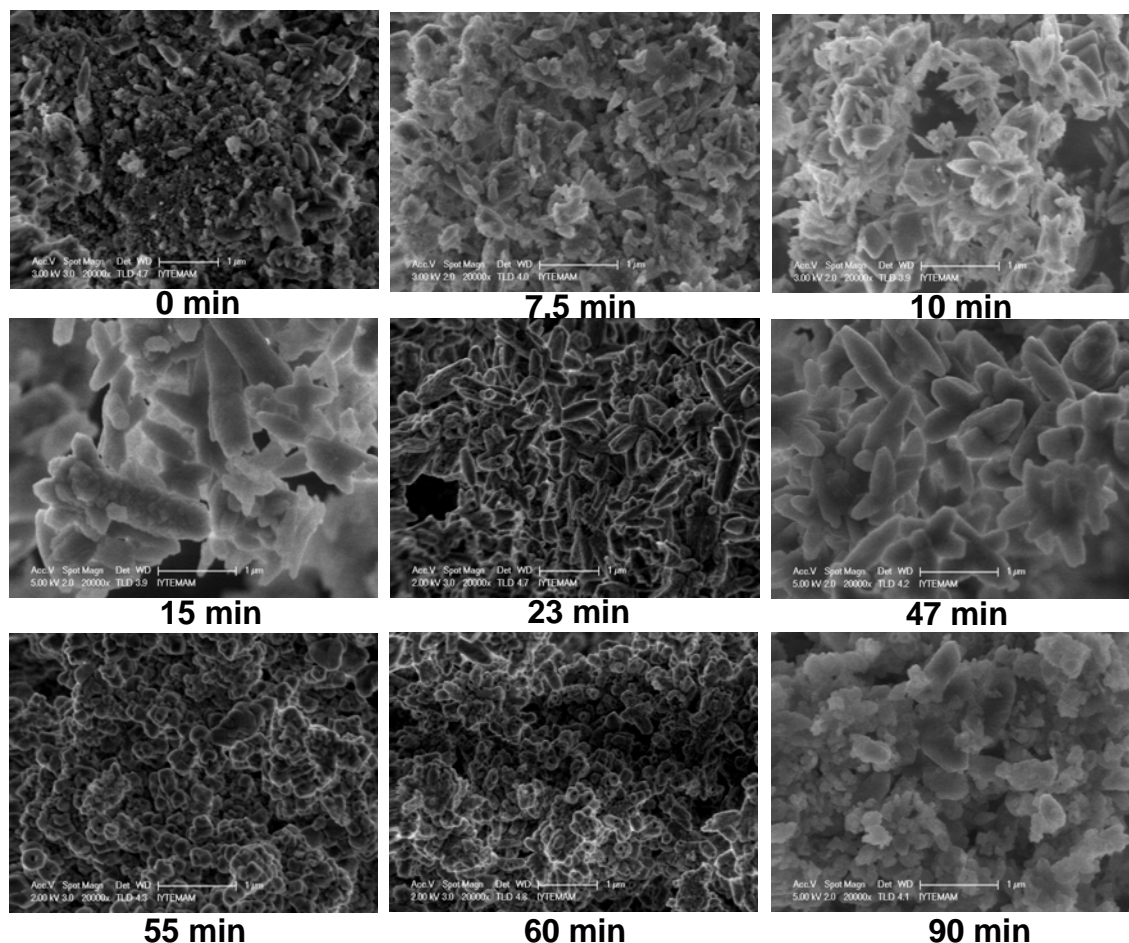


Figure 5.27. SEM images of the precipitates obtained by the stepwise carbonization reaction with direct CO_2 injection. (Ca(OH)_2 : 30 mM; stirring: 600 rpm; $T=25\text{ }^\circ\text{C}$; reactor: 250 ml volumetric flask)

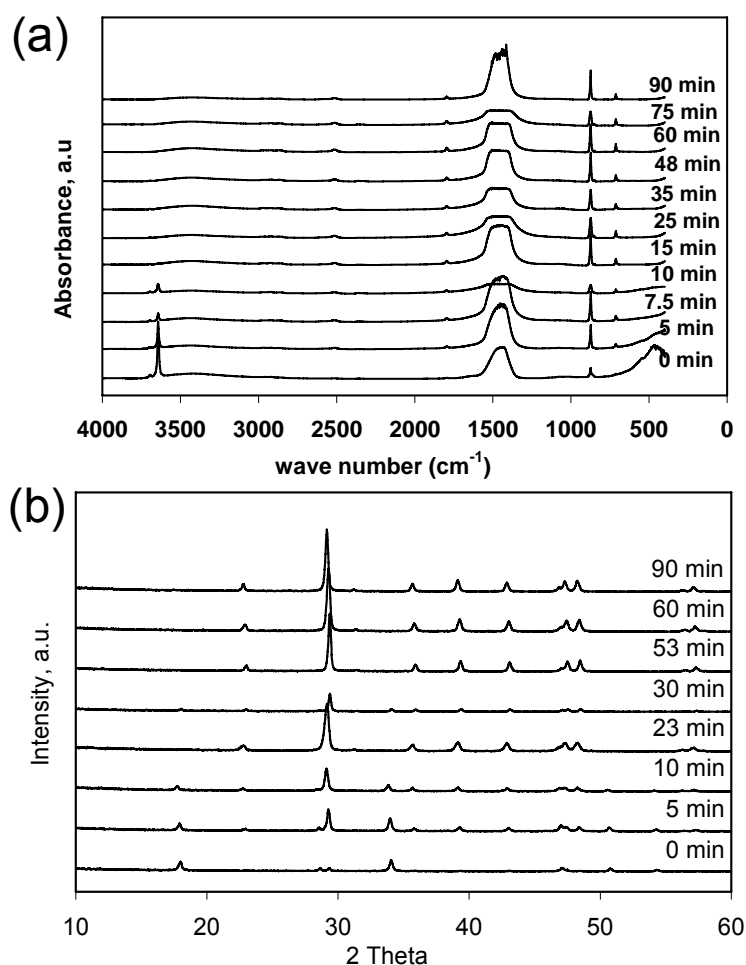


Figure 5.28. (a) FTIR spectra and (b) XRD patterns of the precipitates obtained by the stepwise carbonization reaction with direct CO₂ injection. (Ca(OH)₂: 30 mM; stirring: 600 rpm; T=25 °C; reactor: 250 ml volumetric flask)

The second stage was a sudden decrease due to the consumption of Ca(OH)₂ and formation of CaCO₃ as a result of collapsing the clusters in the solution. In the third stage, there is evidence that the peaks for Ca(OH)₂ in XRD patterns and FTIR spectra were completely removed, only calcite form of the crystals was seen. The structure of particles formed at this stage indicated a rod-like shape, on which submicron particles were found. The rod-like shape particles were formed probably due to shear occurred in the neck of the volumetric flask due to vortex formation as a result of the stirring at the bottom. When these images obtained in the third stage were closely investigated, as evidenced from FTIR spectra and XRD patterns, many nano crystalline particles were seen to grow on a templated surface. It can also be seen that there are nucleation sites on these particles which were seen to grow to different directions.

In the fourth stage, where pH suddenly decreased from 11.6 to about 7.0 and conductivity was at its minimum, aggregated nano calcite particles of about 60 nm were formed. It can be seen from these images (55 and 60 min) that voids on the surface and within these particles were started to form. The voids could form due to the dissolution of small clusters on the particles at low pH. Or, these particles were formed on a templated surface as a result of dissolution-reprecipitation mechanisms. On the other hand, the aggregation of these particles, and grow on the templated surface, could be due to the alternating the surface charges on the particles as a result of formation and dissociation of different species such as $\equiv\text{CaH}^0$, $\equiv\text{CaHCO}_3^0$, $\equiv\text{CaOH}^+$, $\equiv\text{CaCO}_3^-$, $\equiv\text{Ca}^+$, $\equiv\text{CaCO}_3^0$.

For the late stage of this step (90 min), the calcite particles were seen as their surfaces were deformed as a result of the dissolution at low pH. Although both FTIR spectra and XRD patterns showed a calcite form, these particles were different than their usual cubical rhombohedral structure.

In order to investigate the progress in particle formation at concentrations lower than the solubility limit, similar experiments were conducted for 5 and 10 mM of $\text{Ca}(\text{OH})_2$ solutions. Each run was conducted at different time intervals and obtained a reproducible consistent pH – conductivity data. As shown in Figure 5.29, when CO_2 was introduced on the top of the liquid in the neck of the volumetric flask filled with 5 mM of $\text{Ca}(\text{OH})_2$ solution, while the pH decreased slightly, conductivity decreased steeply from 2.2 to 1.3 mS/cm. This is called the first step in crystallization. For the second step, both the pH and conductivity values did not change. For the third step, both the pH and conductivity values were decreased to their minimum values. The samples taken from the runs were also shown by arrows at different time intervals in the figure.

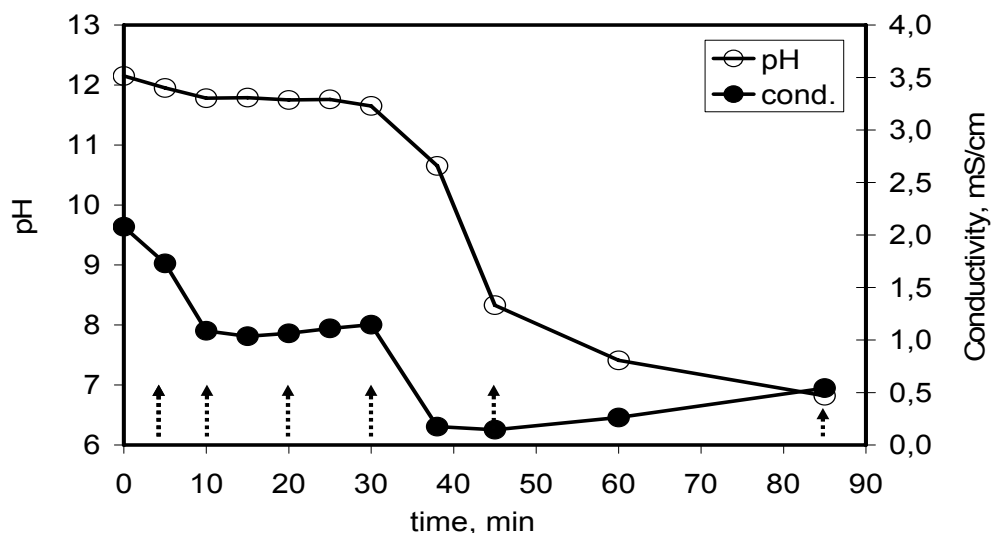


Figure 5.29. pH and conductivity curves of the stepwise carbonization reaction with direct CO₂ injection. (Ca(OH)₂ : 5 mM; stirring: 600 rpm; T=25 °C; reactor: 250 ml volumetric flask)

Figure 5.30 shows the SEM images of the crystals obtained for the carbonization of 5 mM of Ca(OH)₂ solution. As shown in the figure, in the first step, both aggregated nano particles and chain-like crystals were obtained. In the second step, mostly round and cubical shape submicron particles of up to 500 nm in size were obtained. In the third stage where pH dropped to about 7.0, the broken-up of particles were seen.

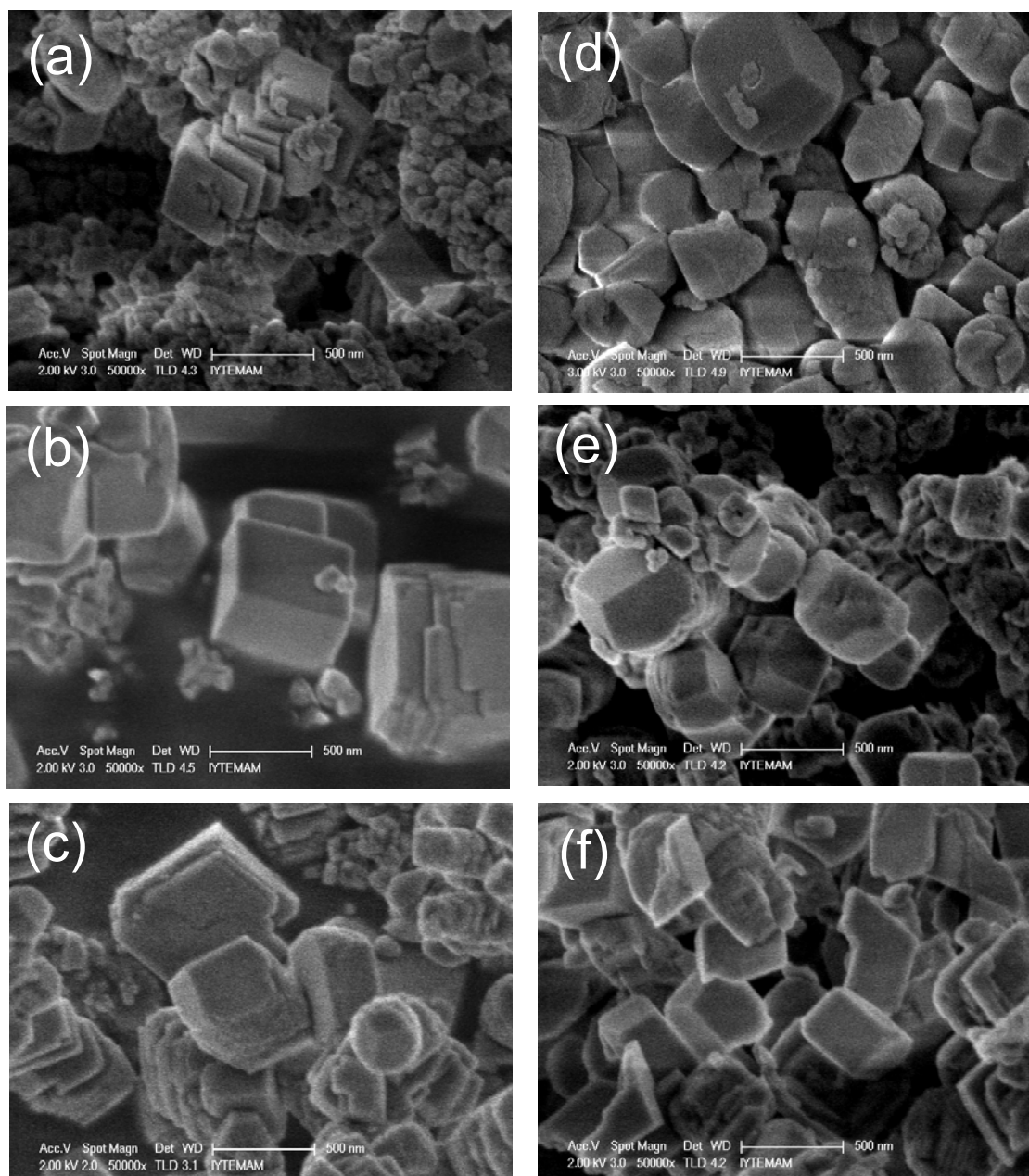


Figure 5.30. SEM images of the precipitates obtained by the stepwise carbonization reaction with direct CO₂ injection. (Ca(OH)₂: 5 mM; stirring: 600 rpm; T=25 °C; reactor: 250 ml vol flask) (a) 5 min (b)10 min (c) 20 min (d) 30 min (e) 45 min (f) 85 min precipitation time.

For 10 mM of Ca(OH)₂ solutions, the same procedure was applied at two stirring rates of 600 rpm and 800 rpm. As shown in Figure 5.31, although the concentration of 10 mM was the same for each stirring rates, because different amounts of Ca(OH)₂ were dissolved for the two cases. While the pH values were the same initially, the initial conductivity values were different. As can be seen in the figure, the precipitation time decreased approximately 4-fold when the stirring rate was increased from 600 rpm to 800 rpm.

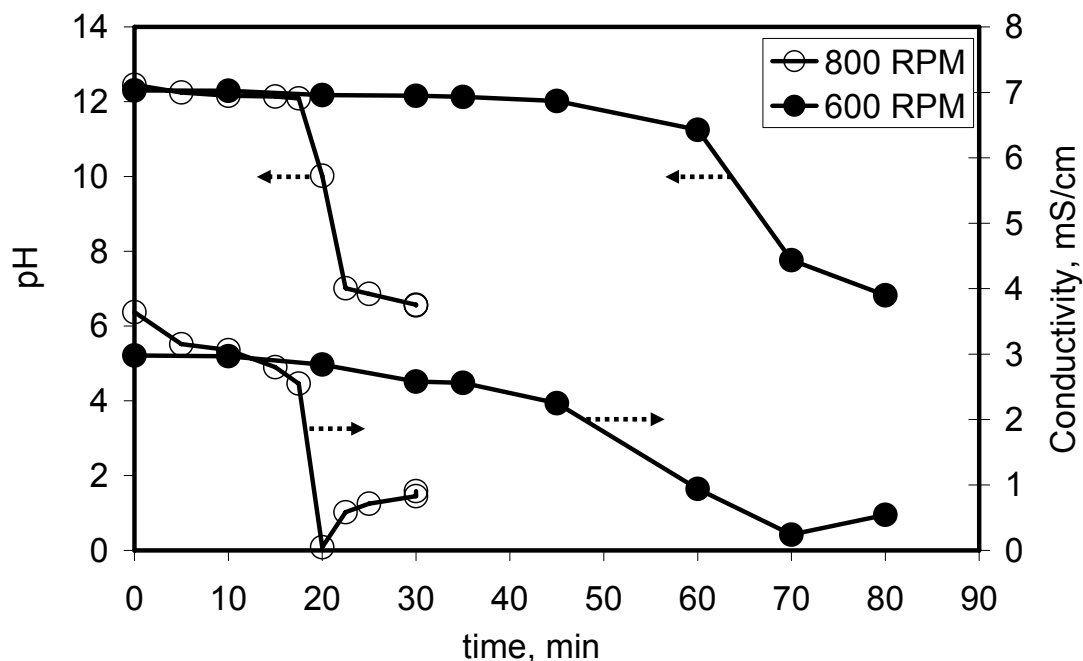


Figure 5.31. Change of pH and conductivity of the slurry with time, showing effect of stirring rate under shear (Ca(OH)_2 : 10 mM; $T=25$ °C; reactor: 250 ml volumetric flask).

The SEM images taken from each runs at different time intervals were shown in Figure 5.32 for 600 rpm and in Figure 5.33 for 800 rpm. For 600 rpm stirring, as shown in Figure 5.32, nano particles were aggregated on the surface of undissolved Ca(OH)_2 particles as soon as the CO_2 was initially introduced to the solution. In the first step, when pH and conductivity slightly decreased at about 12 and 2.6 mS/cm, almost cubical shaped calcite crystals were obtained. The later stages, when pH and conductivity values decreased to their minimum, the particles were seen to be deformed and broken-up at low pH. When the last sample was stirred overnight at pH 7.0, under CO_2 atmosphere, round calcite particles were produced in submicron size.

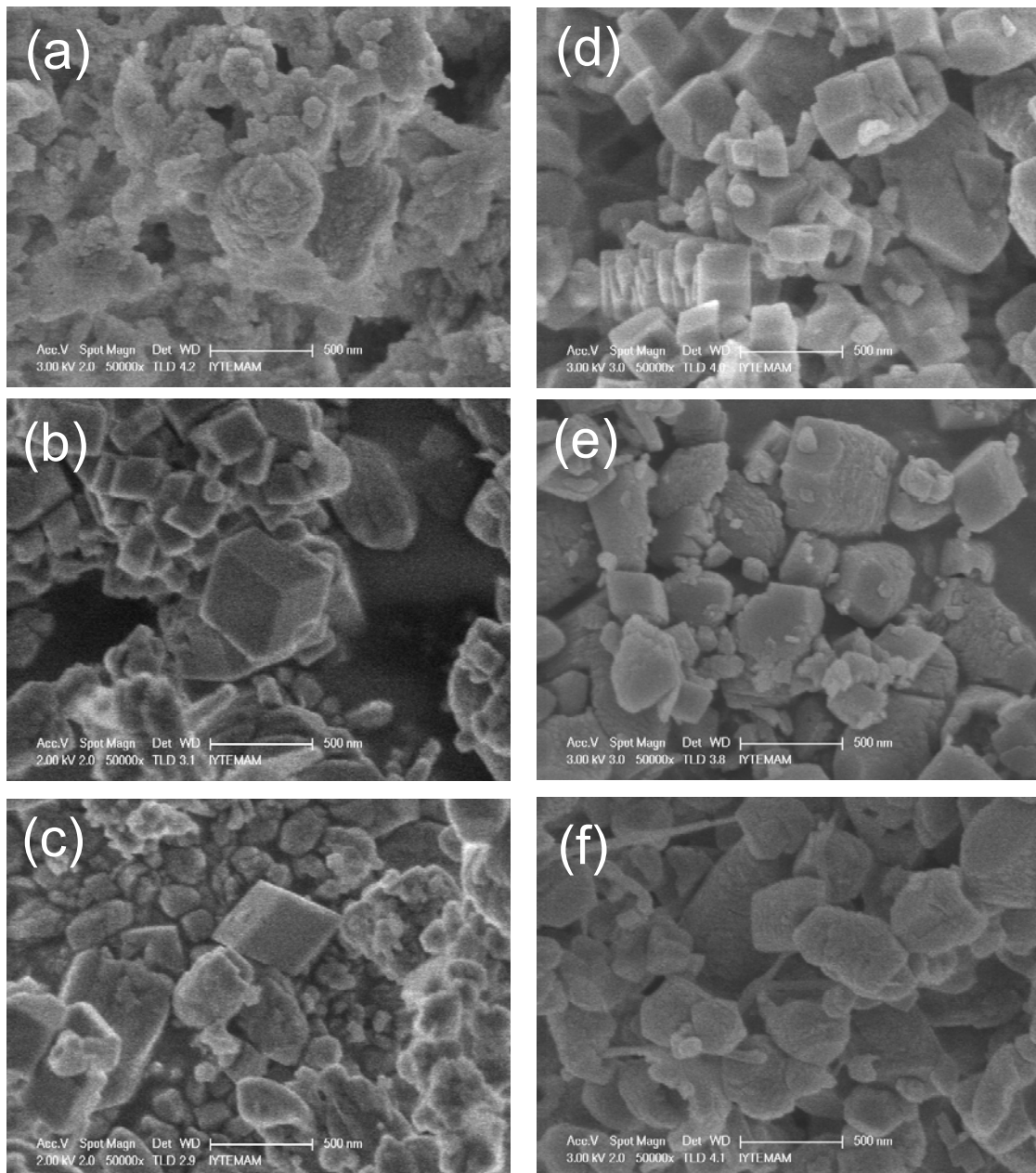


Figure 5.32. SEM images of the precipitates obtained from the stepwise carbonization at 600 rpm (a) 0 min (b) 10 min (c) 15 min (d) 45 min (e) 80 min (f) 24 h showing effect of stirring rate under shear (Ca(OH)_2 : 10 mM; $T=25^\circ\text{C}$; reactor: 250 ml volumetric flask).

For 800 rpm stirring, as shown in Figure 5.33, the conductivity decreased while the pH was constant indicating that a fast transformation of Ca(OH)_2 into CaCO_3 occurred due to high stirring rate. Because the stirring rate was higher, the shear rate was considerably higher forming vortex at the neck of the volumetric flask. As a result, rod-like shape of particles was formed in the first 5 min from nano sized particles nucleated on their surfaces. After much of the ions were consumed, round shape

particles were formed in the late stages of the conversion when both pH and conductivity decreased to their minimum. The particles were seen to break-up at high stirring rate. It is obvious that inside of some particles were empty. It can be inferred from these broken particles that (i) the particles can be broken at higher stirring rates, and (ii) smaller particles could be produced at higher stirring rates.

Comparing the final products with respect to the source of Ca^{++} ions, saturated concentrations (slurry) would be advantageous for the production of finer size calcite crystals. It was understood that, amorphous $\text{Ca}(\text{OH})_2$ was used as template in nucleation period. In other words, when the crystallization occurs in supersaturation conditions with respect to Ca^{++} ions, production of monodisperse and nano size calcite could be possible.

According to the novel crystallization theory, when the saturation ratio increases, the critical nucleus size and the work done during the reaction decrease, the activation energy barrier is reduced, and enhancement of nucleation occurs at finer sizes as shown in Figure 5.30. Nucleation is heterogeneous when the nuclei were developed on a support ¹²⁵ such as amorphous CaCO_3 or undissolved $\text{Ca}(\text{OH})_2$. The energy required for heterogeneous nucleation is less than the energy needed for homogeneous nucleation. As a result of lower energy barrier, heterogeneous nucleation and/or crystal growth rates would be higher than the growth rates of homogeneous nucleation¹²⁶.

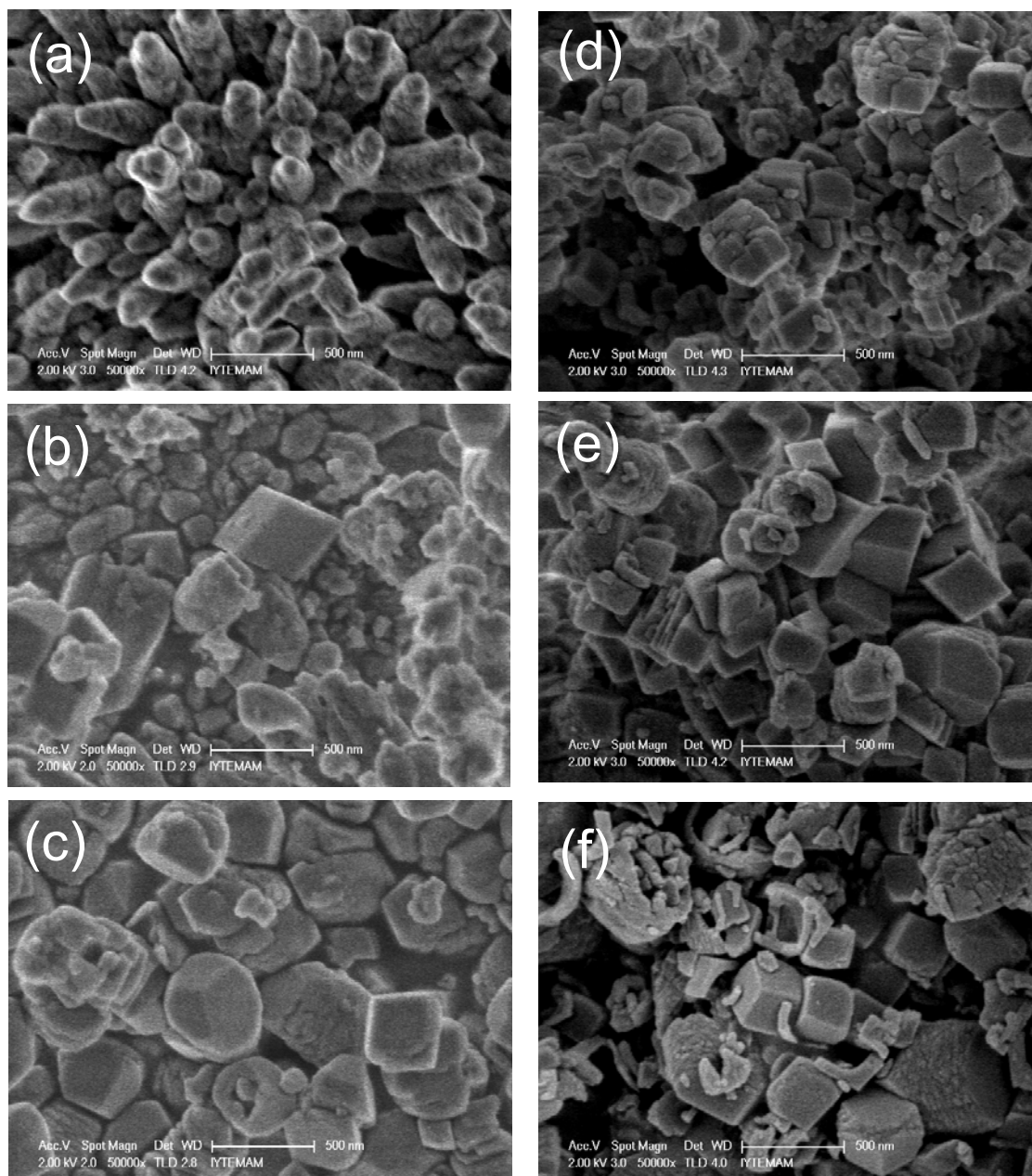


Figure 5.33. SEM images of the precipitates obtained from the stepwise carbonization at 800 rpm (a) 5 min (b) 15 min (c) 20 min (d) 23 min (e) 25 min (f) 30 min showing effect of stirring rate under shear (Ca(OH)_2 : 10 mM; $T=25^\circ\text{C}$; reactor: 250 ml volumetric flask)

We have shown that the particles can be broken and smaller particles could be obtained at high stirring rates. We have also shown that the particle morphology could be changed at higher shear rates. Here, we show that the particle size and morphology could be modified by shear rate and mechanical stirring. For this purpose, a stirred round bottom flask was filled with a 30 mM of Ca(OH)_2 slurry to the levels from 100 ml to 600 ml. In this case, different shear rates and power per volumes were obtained.

CO₂ gas was fed on the top of the solution during the experiments. Therefore, different surface areas were also considered for various CO₂ transfer rates. For a 20 min of reactions, samples were analyzed. Figure 5.34 shows the SEM images of the particles, and Figure 5.35 shows the FTIR spectra and XRD patterns of the samples.

When the tank was full, a shear was created due to the vortex as a result of stirring by a stir bar at the bottom. Because transfer area at the neck was smaller, CO₂ dissolution rate per volume was lower. As shown in Figure 5.34a, needle-like particles were obtained when the solution filled completely the neck of the flask. For 600 ml of solution, the FTIR band at 3642 cm⁻¹ represents the portlandite form of Ca(OH)₂ and 2θ positions of XRD patterns for Ca(OH)₂ indicates the presence of Ca(OH)₂ in precipitates (JCPDS files 87-0674; 44-1481; 78-0315). Therefore, there was an incomplete conversion for Ca(OH)₂.

When the half of the tank was full, agglomerated crystals changed from needle-like to rhombohedral structure (Figure 5.34b) and their size started to decrease. Based on the XRD and FTIR analyses, rhombohedral crystals were calcite.

When the volume of the Ca(OH)₂ slurry was 100 ml, the shear in the slurry was maximum due to the effect of magnetic stirring mediated vortices. As shown in Figure 5.34c, a 100 nm of nano size, spheroidal, almost mono disperse calcite crystals were obtained.

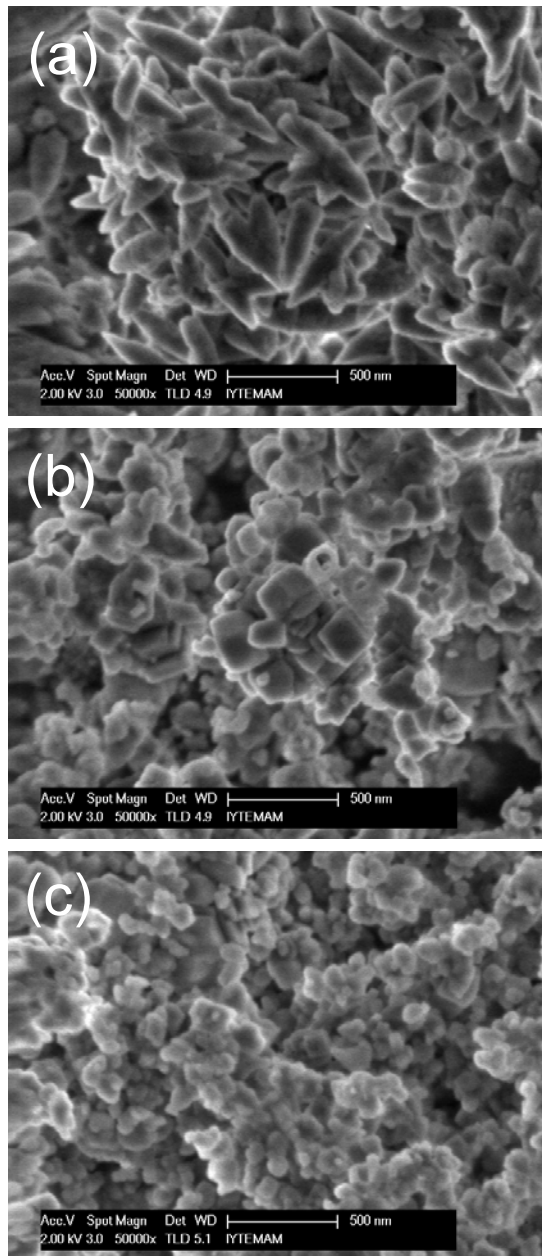


Figure 5.34. SEM images of the precipitates produced at various volumes (a) 600 ml (b) 300 ml (c) 100 ml of the slurry and fixed reaction time. ($\text{Ca}(\text{OH})_2$:30 mM; $T=25^\circ\text{C}$; reaction time: 20 min)

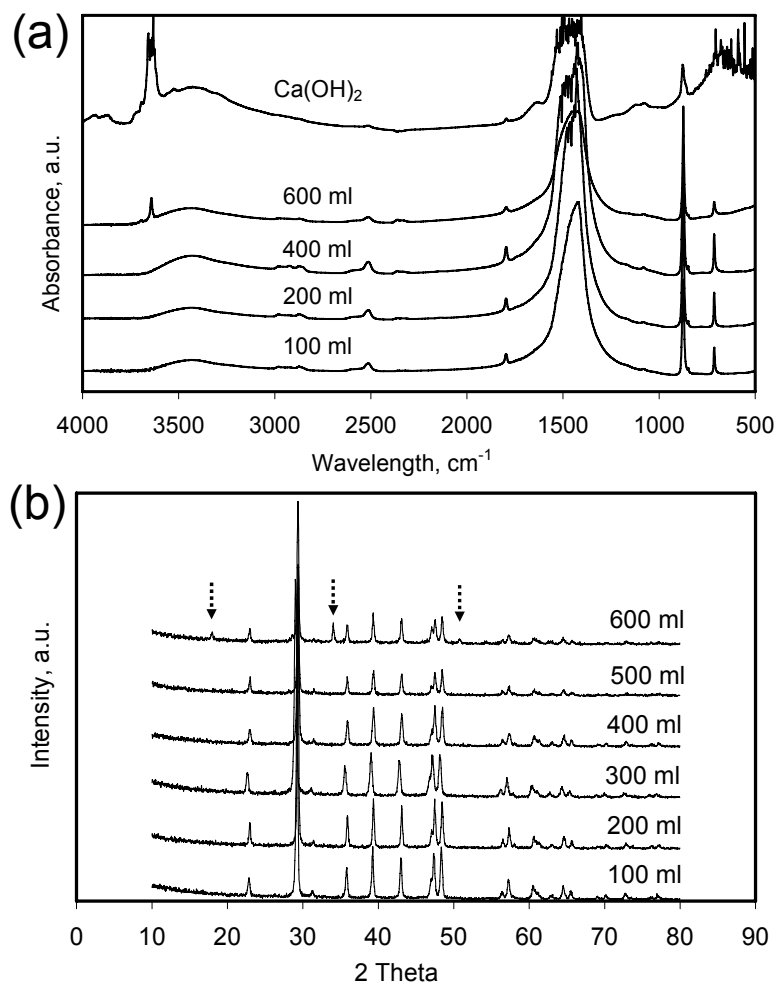


Figure 5.35. Conversion of the precipitates produced at various volumes of slurry and fixed reaction time. (a) FTIR spectra, (b) XRD patterns (Ca(OH)_2 :30 mM; $T= 25\text{ }^\circ\text{C}$; reaction time: 20 min)

A 500 ml of volumetric flask was also used to test the shear effect on the particle morphology. The level of the 30 mM of Ca(OH)_2 slurry was varied from 100 ml to 520 ml. The final pH and conductivity at the end of 30 min were obtained for the reactions for 6 different levels as shown in Figure 5.36. pH and conductivity values were higher when the flask reactor was full of Ca(OH)_2 solution. However, when the level is below the neck the pH and conductivity values were at their minimum. An incomplete conversion were seen when the pH and conductivity were high at 400 ml, 500 ml, and 520 ml of Ca(OH)_2 solutions.

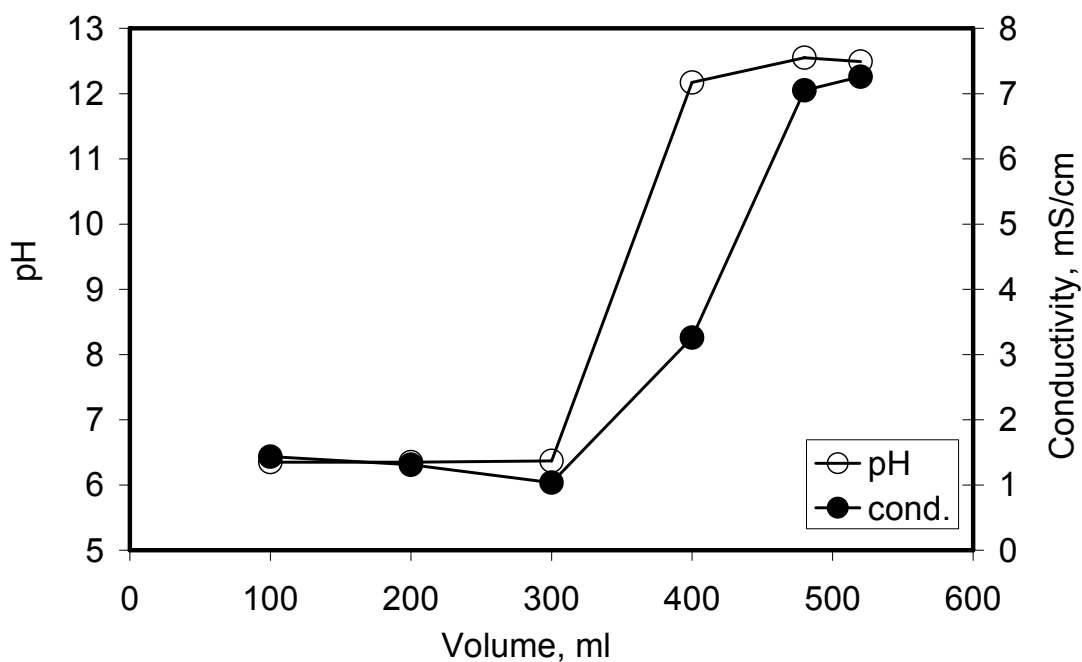


Figure 5.36. Final pH and conductivity values of the slurry under shear at various volume, fixed reaction time. (Ca(OH)_2 : 30 mM; stirring: 600 rpm; $T=25^\circ\text{C}$; reactor: 500 ml volumetric flask, time: 30 min).

Figure 5.37 shows the SEM images of the particles obtained for different shear rates and completion level of the reactions. As shown in the figure, when the level in the flask reactor is high, nano particles on the templated surface of either Ca(OH)_2 particles or on the already grown calcite particles were formed. When the level was low and shear stress was high due to the stirring, the nano sized aggregated calcite particles were produced.

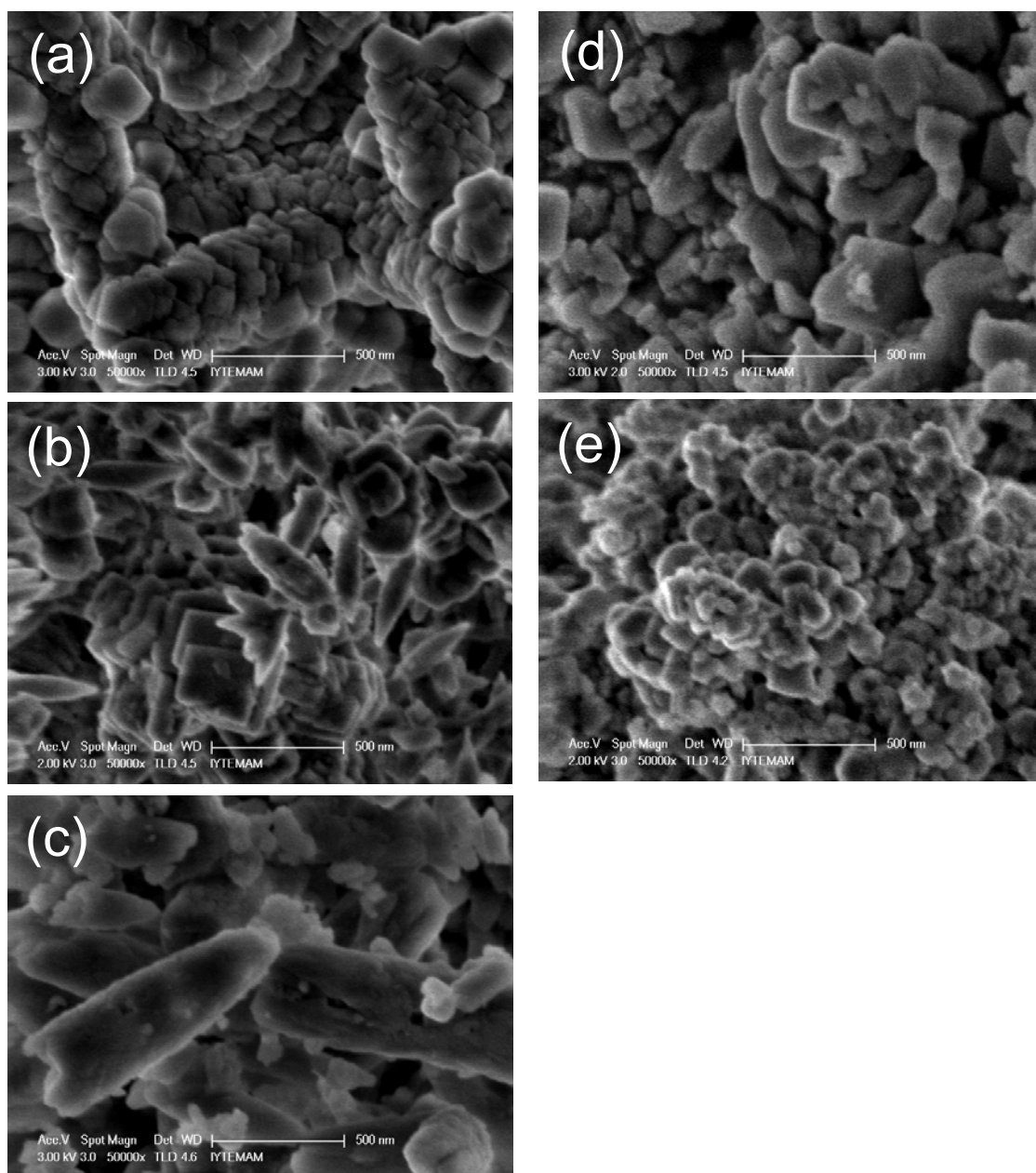


Figure 5.37. SEM images of the precipitates obtained from stepwise carbonization at various volume (a) 520 ml (b) 500 ml (c) 400 ml (d) 300 ml (e) 100 ml, at fixed reaction time. (Ca(OH)_2 : 30 mM; stirring: 600 rpm; $T=25^\circ\text{C}$; reactor: 500 ml volumetric flask, time: 30 min)

5.5. Colloidal Stability of Calcite –Water System

Figure 5.38 shows the zeta potential of the nano calcite particles obtained from stepwise carbonization reaction at different pH values. As shown in the figure, calcite particles have the point of zero charge at about $\text{pH} \sim 7 - 7.5$. The calcite particles were negatively charged during the carbonization reactions which were ended at about pH 7. Figure 5.39 shows the total interaction potential energy curves as a function of the distance of closest approach for precipitated calcium carbonate (PCC) suspensions which were obtained at different pH values. The particle diameter for all calculations was assumed as 100 nm and particles were assumed to be spherical in shape. The thickness of EDL (κ) was calculated as 4.793 nm corresponding the ratio of (d/κ) about 10. This is in the range of the applicability of Hogg et al. relations of closest approach. The potential profile exhibited a primary minimum at short interparticle distances; however, a positive energy barrier was not obtained at short interparticle distances. As shown in the figure, the total interaction is attractive at all distances of separation between two nano calcite particles. This was caused by the low surface charges of precipitated calcites obtained at different pH's. The model was also applied for an imaginary calcite particle having the zeta potential of -30 mV to show the difference in energy barrier. As Campos et al. (2009)¹²⁷, pointed out; when the height of energy barrier is about 0 kT, nano particles tend to coagulate, and when it is in the range of 0 to 15 kT, particles tend to flocculate. The precipitated calcite suspensions were not stable at measured pH's and zeta potential values ($\text{pH}=12$; $\psi_0=-14.92$ mV), ($\text{pH}=7.5$; $\psi_0=-6.49$ mV) and ($\text{pH}=6.5$; $\psi_0=+11.42$ mV). It is difficult to determine the size of the individual precipitates by dynamic light scattering (DLS) technique, because, they cannot be stabilized without dispersant addition at any solution pH. On the other hand, if the precipitates had the magnitude of 30 mV or greater surface charge, a significant energy barrier would have occurred as shown in Figure 5.39 to prevent aggregation.

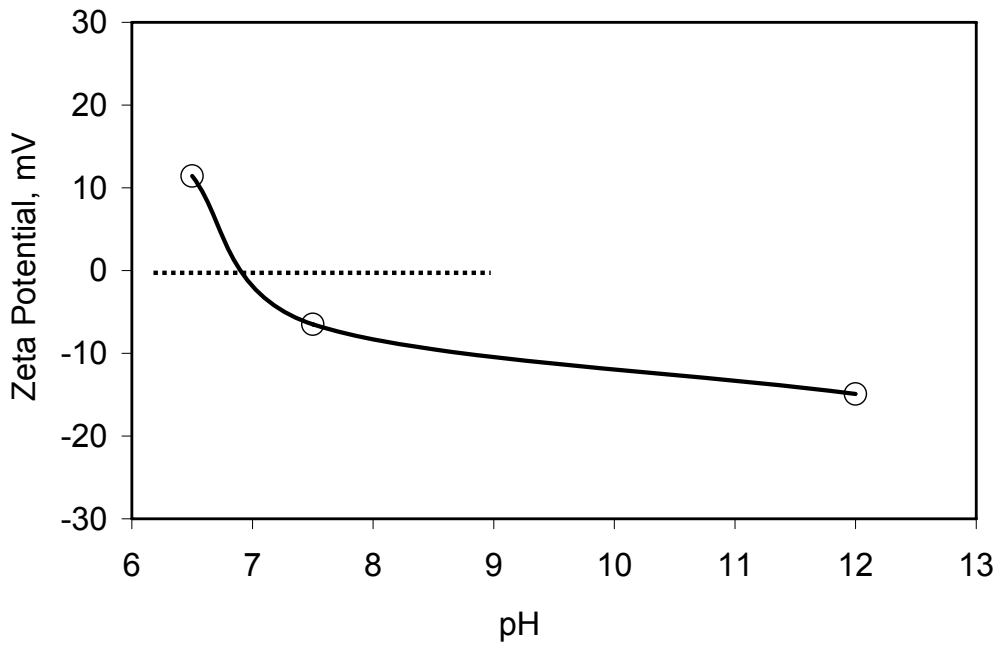


Figure 5.38. Change of zeta potential distribution during stepwise carbonization reaction with direct CO₂ injection (Ca(OH)₂ : 30 mM; stirring: 600 rpm; T=25 °C; reactor: 250 ml volumetric flask)

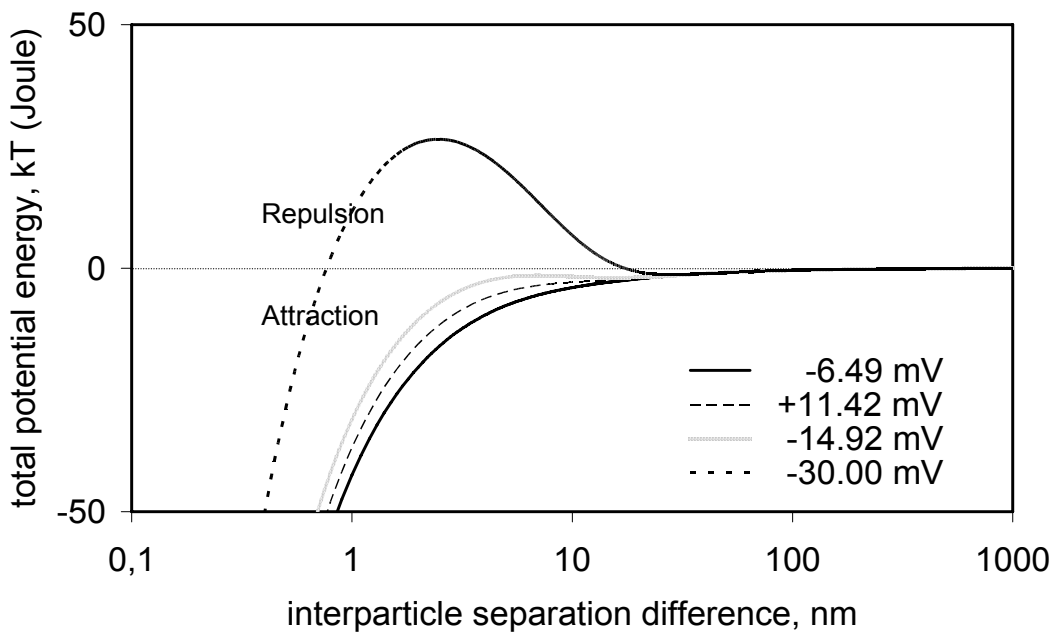


Figure 5.39. Total interaction energy curve (DLVO) for calcite particles in water in terms of kT (Joule) ($d=100$ nm, $A_{CWC}=2.23 \times 10^{-20}$ J, $\psi_0=-14.92$ mV at pH=12 ; $\psi_0=-6.49$ mV at pH=7.5 ; $\psi_0=+11.42$ mV at pH=6.5)

Figure 5.40 shows the change of surface potential of calcite particles in water. When the surface is charged, κ would be very small. In other words, the double layer would be very thin because of the high ionic strength of solution. Conversely, when the

solution was dilute enough for EDL to extend some distance away from the surface, the surface charge would be very low. 30 nm away from EDL, the surface charge was zero.

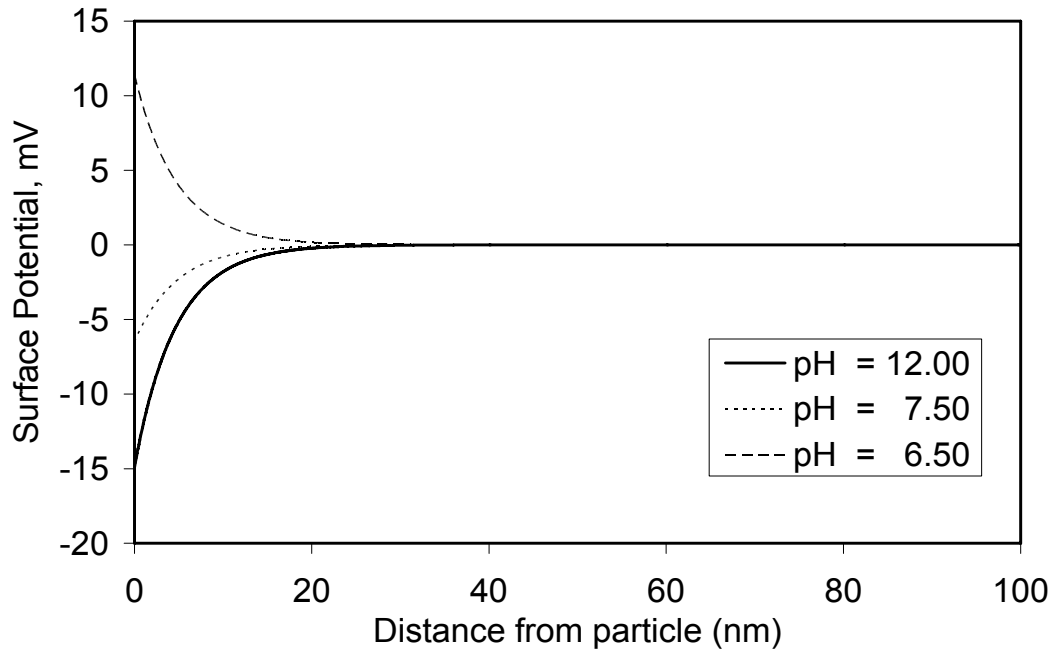


Figure 5.40. Potential profile for calcite powder in pure water ($\psi_0 = -14.92$ mV at pH=12 ; $\psi_0 = -6.49$ mV at pH=7.5 ; $\psi_0 = +11.42$ mV at pH=6.5 $A_{cwc} = 2.23 \times 10^{-20}$)

Based on the literature¹²⁷, when the energy barrier was lower than 5 kT as obtained in Figure 5.39, the thermal fluctuations induce rapid coagulation with a sharp macroscopic fluid-solid phase separation. This phase transition is irreversible due to the strong van der Waals forces which maintain the particles held together and do not break apart without strong external forces. Figure 5.41 shows the change of total number concentration of nano calcite particles with time during the rapid coagulation. When the repulsion barrier does not exist, spontaneous coagulation occurs and more than 99 % of the total particles coagulate in less than 1 sec. Other parts of the particles (less than 1 %), continue to coagulate during 2.7 h under slow coagulation conditions as shown in Figure 5.42. The ratio of rapid coagulation to actual coagulation gives the stability ratio (W). The ratio is close to zero (0.033) indicating the unstable colloidal system. If a 25 kT energy barrier were existed, the ratio would jump to $2.4 \cdot 10^{10}$, and the system would have become stable. Due to the domination of attraction potential, particles tend to adhere each other and aggregate under given conditions.

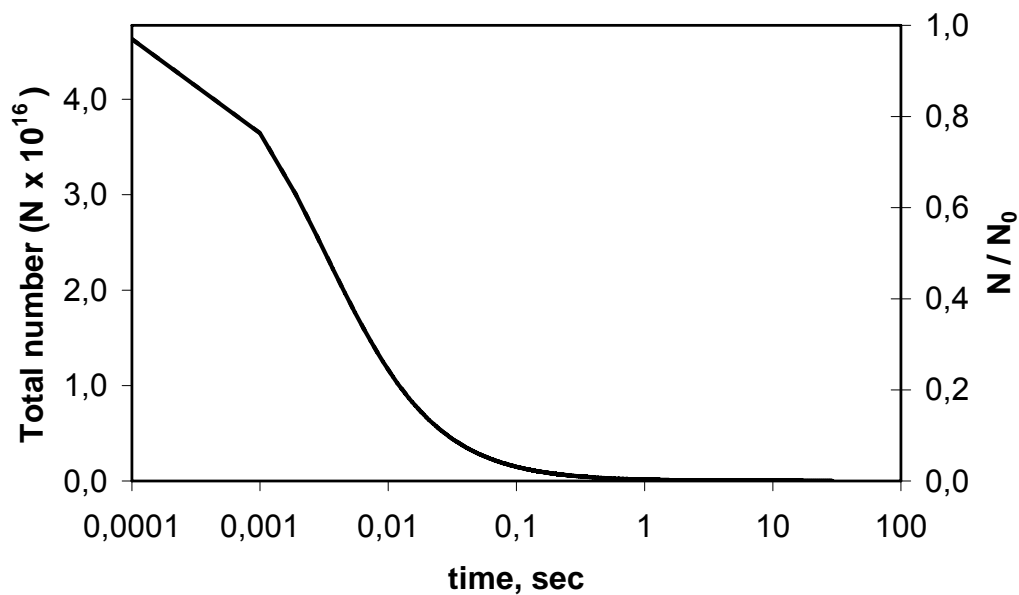


Figure 5.41. Change in particle number concentration of nano calcite particles for rapid coagulation ($V_t=0$ kT; $C_{CaCO_3} = 30$ Mm; $N_0 = 4.773 \cdot 10^{16}$)

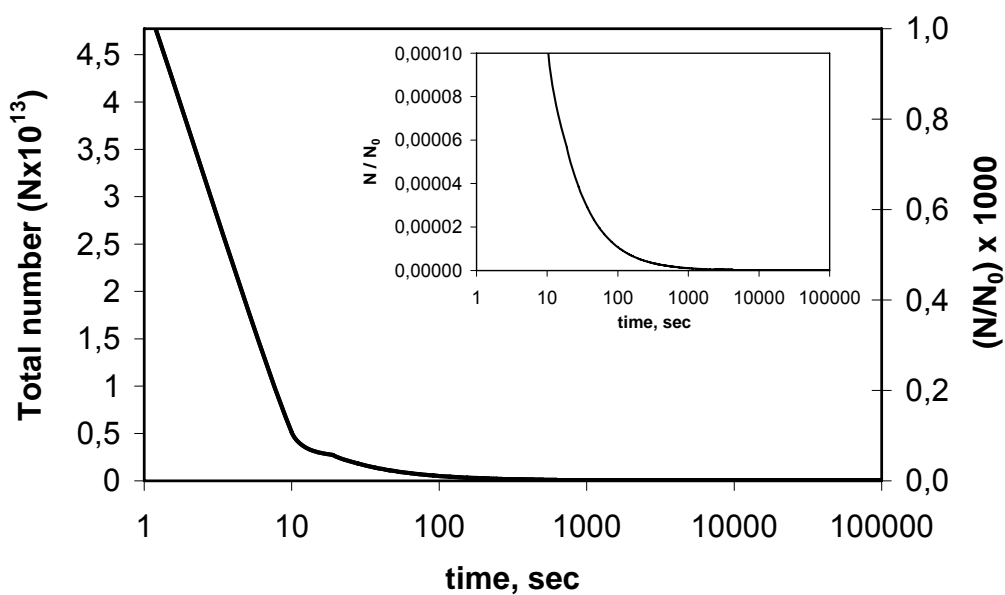


Figure 5.42. Change in particle number concentration of nano calcite particles for slow coagulation ($V_t=0$ kT; $C_{CaCO_3} = 30$ Mm; $N_0 = 4.773 \cdot 10^{16}$)

The size distribution of the precipitated calcite particles was obtained by DLS technique. The number intensity was shown in Figure 5.43 and cumulative number distribution was shown in Figure 5.44. As shown in Figure 5.43, the size interval narrowed with respect to the carbonization time. At initial stage of the carbonization, the pH was about 12 and the surface of the nano calcite particles was negatively charged. The size distribution of the particles obtained at 1 min carbonization time

indicates a strength aggregation between amorphous $\text{Ca}(\text{OH})_2$ and new borne calcites. As shown in Figure 5.44, almost 99% of the particles were under the size of 3 micron. Figure 5.44 also indicates that 50 % of the particles were under the size of 300 – 400 nm within 10 min carbonization reaction up to the 50 min carbonization. The pH of the calcite particles obtained at 50 min by carbonization was about 7.5 having the zeta potential value of -6.49 mV. Aggregated particles occurred with the negative potential energy in that case. pH of the calcite particles obtained from 60 min carbonization period was about 7. A nano size distribution was obtained for that case. However, the size distribution is bimodal having a curve also in submicron size region indicating the aggregation. As a result, because of the attraction energy, particles were not stable, they were coagulated rapidly and it was difficult to determine exact size distributions by DLS technique, although a sonication process was applied.

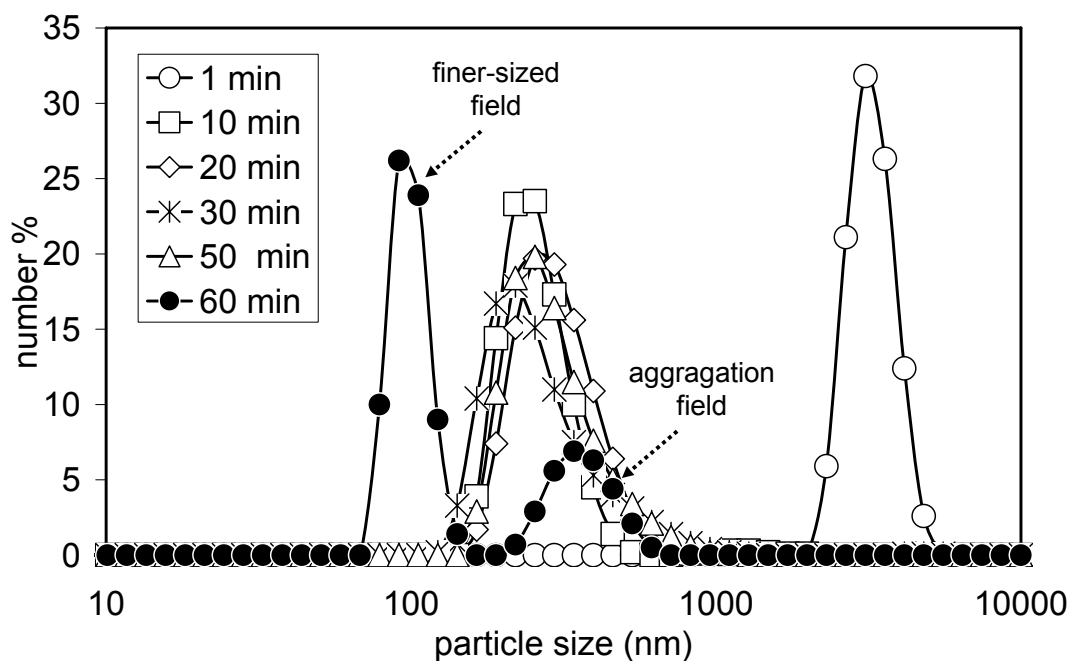


Figure 5.43. Change of particle size distribution (number intensity) during stepwise carbonization reaction with direct CO_2 injection ($\text{Ca}(\text{OH})_2$: 30 mM; stirring: 600 rpm; $T=25^\circ\text{C}$; reactor: 250 ml volumetric flask)

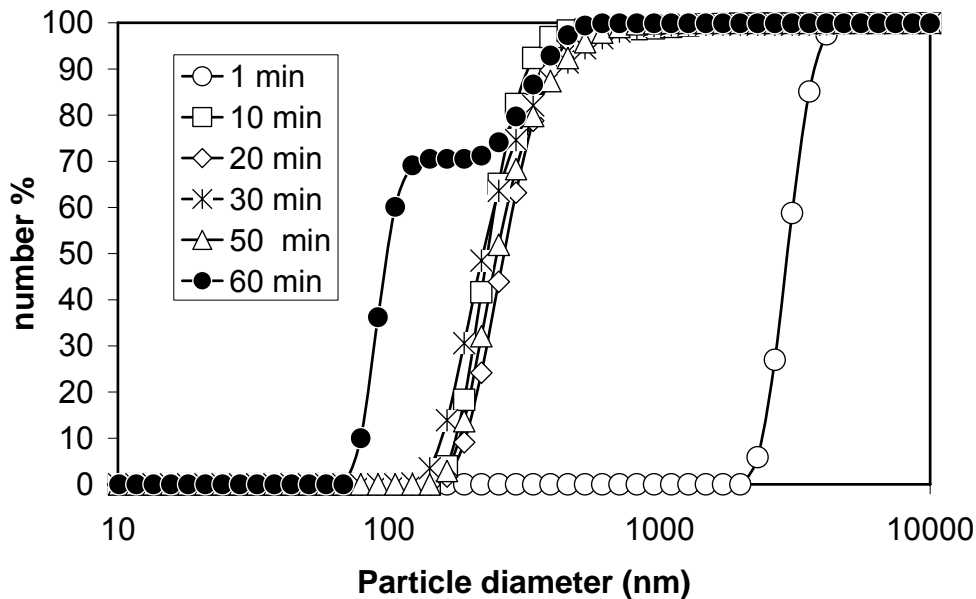


Figure 5.44. Change of particle size distribution (cumulative number) during stepwise carbonization reaction with direct CO₂ injection (Ca(OH)₂ : 30 mM; stirring: 600 rpm; T=25 °C; reactor: 250 ml volumetric flask)

Figure 5.45 shows the calculated settling of nano calcite particles in water. The terminal settling velocity for a 50 nm spherical calcite particle in water was estimated to be 2.081 nm/sec and 8.326 nm/sec for 100 nm particle. When the particle sizes were close to 1 μm in diameter, the velocity would reach approximately 1 μm/s. Considering the nano calcite particles were under the influence of attraction forces, and they would coagulate in water to form aggregates, the settling velocity of aggregated particles in micron sizes would also be necessary to take into account. Figure 5.45 also shows the terminal settling velocity for micron sized calcite aggregates in water. The settling velocity of 1-2 μm sized aggregates was about 0.1 mm/min. During particle size analysis by DLS technique, coagulated unstable calcite particles cannot be settled completely with such slow velocity, however, coagulation would affect the size measurement adversely.

All calculations for colloidal stability, potential profiles, coagulation kinetics and settling of the particles were given in Appendix A.

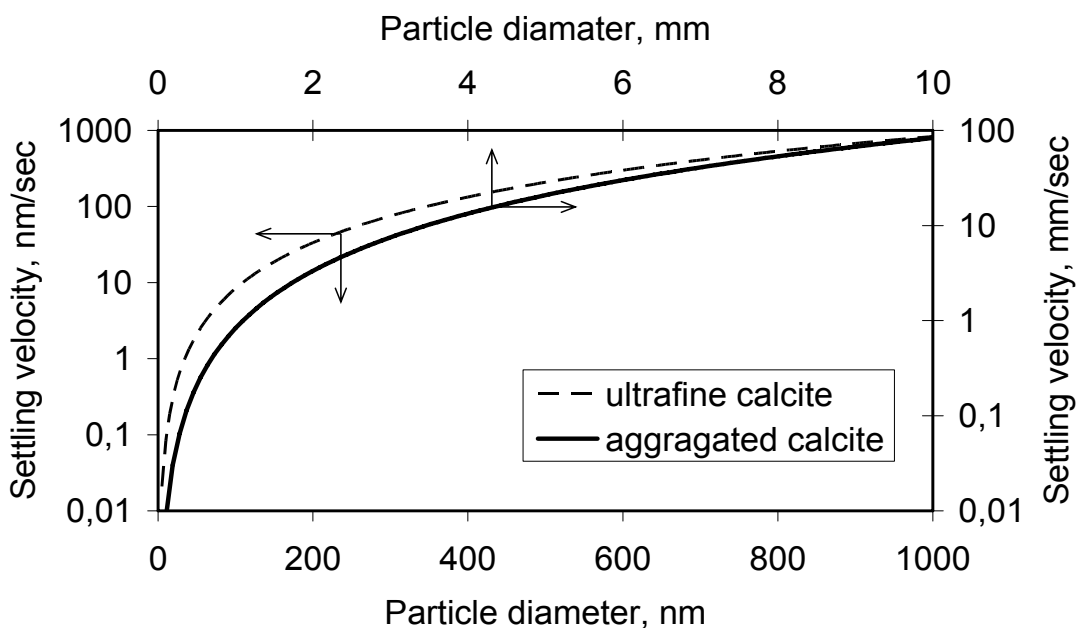


Figure 5.45. Terminal settling velocity of nano Calcite particles in water.

5.6. Effect of Free Carbonic Anhydrase on CaCO_3 Crystallization

The effect of free Carbonic Anhydrase (CA) enzyme on CaCO_3 crystallization was investigated by the carbonization method. A 20 mM of $\text{Ca}(\text{OH})_2$ solution was prepared in a 3-neck glass reactor stirred on a magnetic stir bar. A mini reactor was created in the solution by inserting a glass pipe with a 5 mm of diameter. CO_2 was introduced through this glass pipe on the top of the aqueous phase within the mini reactor. Before the CA was added into the solution from its stock solution, $\text{Ca}(\text{OH})_2$ slurry was stirred 5 min for dissolution. Stirring of the solution continued for another 5 min after the CA enzyme was added. The reactions started when CO_2 was introduced at 10th min.

Figure 5.46 shows the change in pH and conductivity values during the carbonization reaction in the presence of various concentrations of CA enzyme. As shown in the figure, after a short initial period of about 2-3 min after CO_2 injection, the conductivity started to decrease, while pH was about constant. When the conductivity dropped to its minimum, pH started to decrease. The elapsed time, t_1 , defined as the time from CO_2 injection to zero conductivity, and the elapsed time, t_2 , defined as the time from CO_2 injection to pH 7, were given in Table 5.2. Comparing these curves in Figure 5.46 and elapsed times in Table 5.2, it can be seen that the time required for

crystallization decreases when free CA concentration increases. The slight increase of the conductivity after its minimum value depends on the nucleation and growth of unstable CaCO_3 precursor phase (amorphous CaCO_3) on the surfaces of suspended Ca(OH)_2 particles. Unstable precursor rapidly dissolves during the stable calcite nucleation, and the conductivity increases slightly⁴⁰. The rate of the consumptions of pH and conductivity were increased with the addition of free enzyme. Reactions were faster for higher free CA concentration in the reactor.

Although the time for crystallization at different CA concentrations looks insignificant, considering the reproducibility in the experimental set-up, this trend is somewhat valid. The small difference could be due to the enzyme inactivation at high pH and stirring conditions. Or, the increase in crystallization at high concentration of free CA could be due to the templating effect of the enzyme in the solution²⁵.

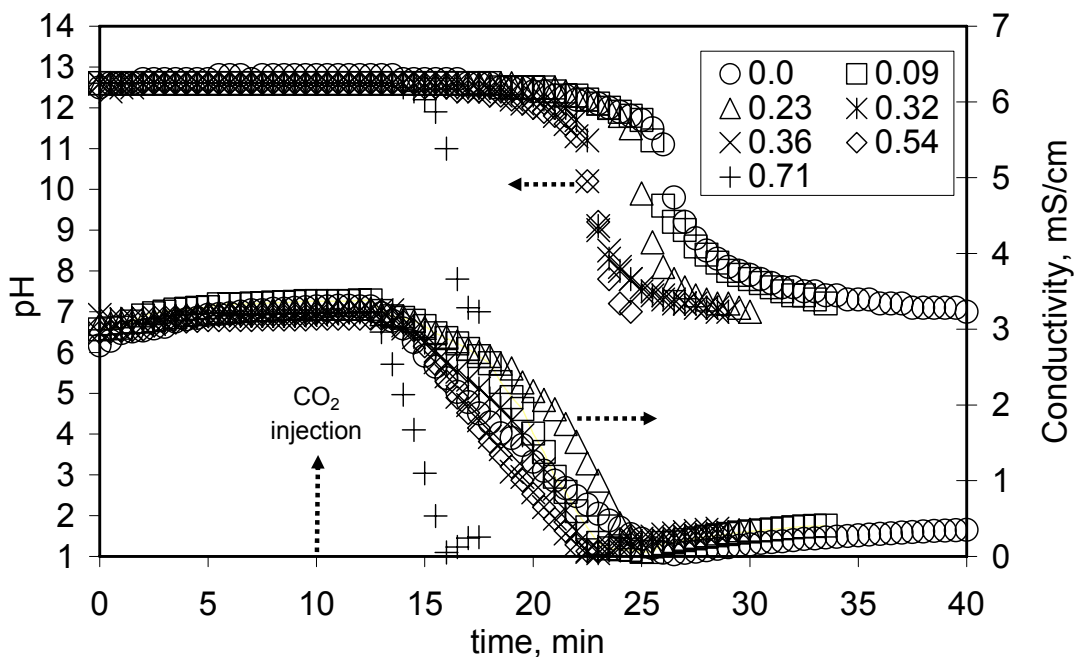


Figure 5.46. pH and conductivity curves for the precipitation of CO_2 in the presence various amounts of free carbonic anhydrase and 20 mM Ca(OH)_2 (diameter of glass pipe : 5 mm)

Table 5.2. Evaluation of the PCC's obtained by free Carbonic Anhydrase

CA Conc. (μM)	t_1^*	t_2^+	peak angle**	d-spacing	Ref Code ⁺⁺	Relative score [‡]	size [†]
0.00	16	30	29.28783	3.04686	81-2027	0.80	34.9
0.09	15	26	29.25182	3.05053	81-2027	0.56	46.3
0.18	15	20	29.36172	3.03936	83-1762	0.83	44.2
0.36	10	17	29.28910	3.04673	81-2027	0.87	38.0
0.54	10	14	29.38559	3.03695	83-1762	0.79	41.6
0.71	4	7	29.27047	3.04863	81-2027	0.81	35.2

* Elapsed time from CO₂ injection to zero conductivity (minutes)

+ Elapsed time from CO₂ injection to 7.0 pH (minutes)

** Peak parameters detected with 100 % relative intensity

⁺⁺ Bragg's reflections given in Joint Committee on Powder Diffraction Standards (JCPDS) files

[‡] Maximum score as percent which was calcite detection for relative intensity

[†] Crystallite size which represents the minimum dimension (nm)

Figure 5.47 shows the SEM images of the produced crystals in the presence of free CA. As shown in the figure, the particles produced in the control experiment composed of mostly cubical chain-like large particles, and aggregated small crystals. On the other hand, all the particles produced in the presence of free CA enzyme were round shape, aggregated, and nano sized. Figure 5.48 shows the XRD patterns of the crystals obtained in the presence of free CA. All the diffraction peaks detected by XRD refers to index of calcite polymorph of CaCO₃ (space group: R3c (167)]⁵⁷ with the Bragg's reflections which were given in JCPDS files, Card 5–586, the 2 θ value at 29.468°. The sharp diffractions at the d-spacings, 3.02864, 1.91257 and 1.87567 confirm the presence of rhombohedral calcite structure in (1 0 4) lattice position for control (blank) experiment. 2 θ values at about 29.4° and d-spacings at about 3.03 indicate the presence of calcite crystals for each CA containing samples. The crystals have nearly identical peak positions and narrow peak widths as calcite. The strong and sharp peaks indicate the well crystallization of the samples. No obvious characteristic diffraction peaks of any impurities were detected. The crystal sizes were calculated by Debye Scherrer Equation. As shown in Table 5.2, the average crystal size was found as approximately 40 nm with the standard deviation of 4.73 nm (11.83 %).

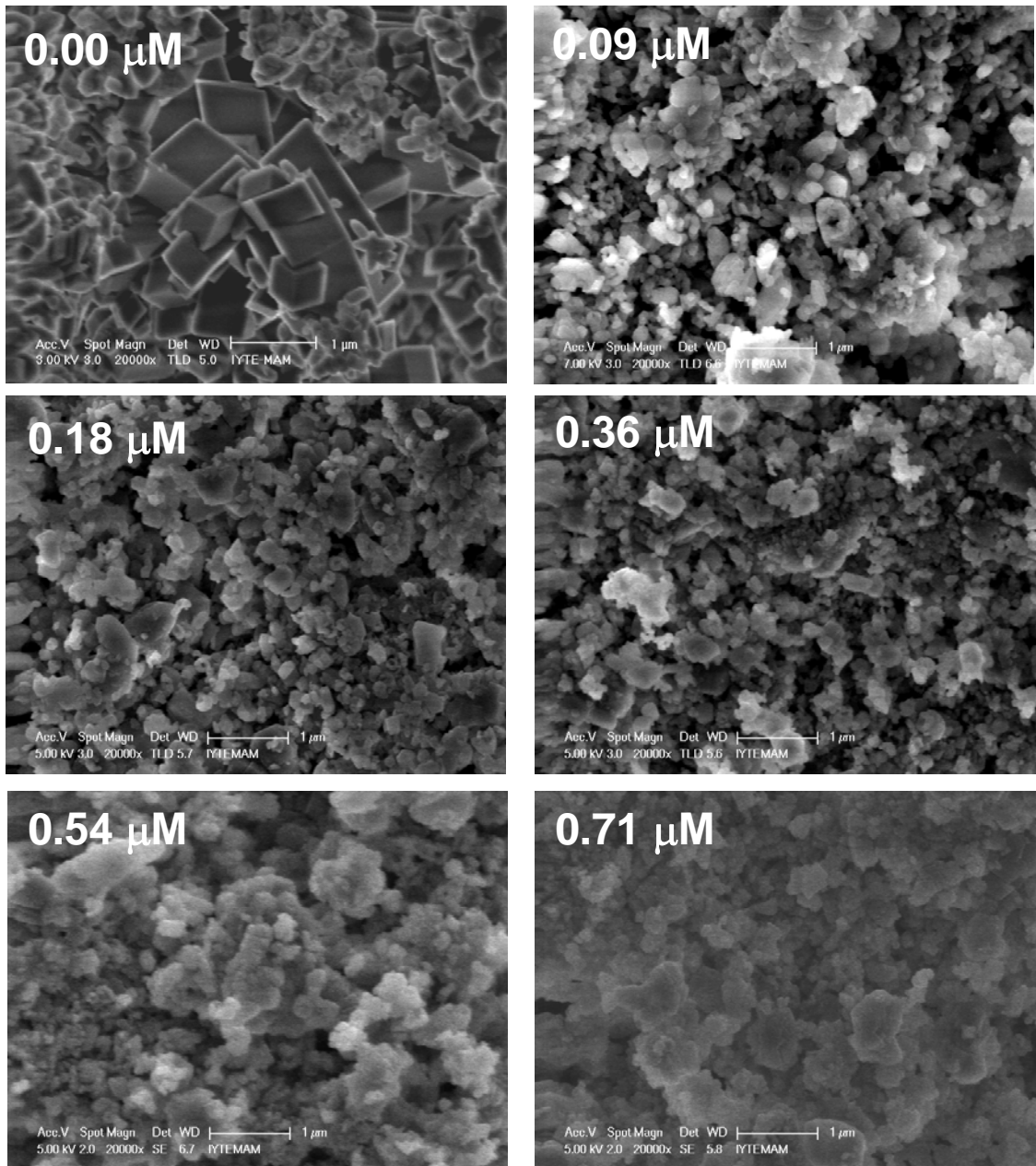


Figure 5.47. SEM images of the precipitated solids in the presence of various concentrations of free CA enzyme.

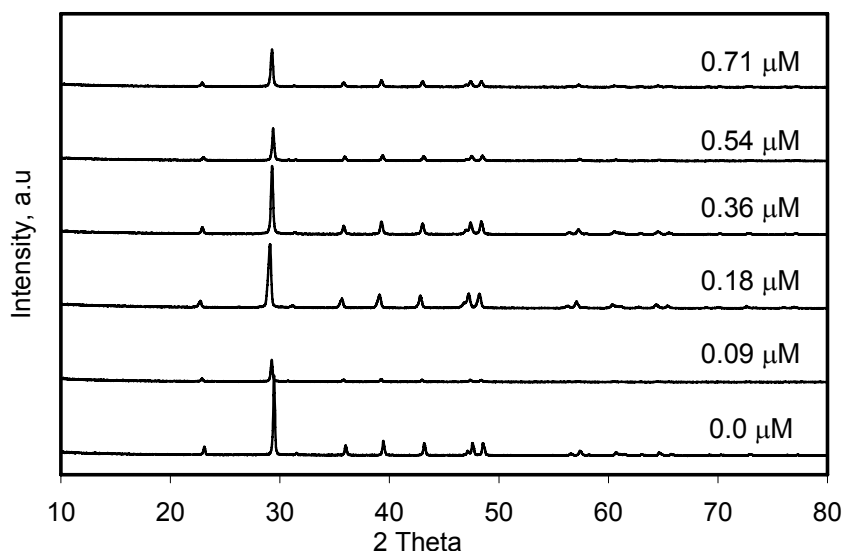


Figure 5.48. XRD patterns of the crystals in the presence of various concentrations of free CA

5.7. Effect of Polyurethane Foam on CaCO₃ Production

Carbonic Anhydrase enzyme has been immobilized within polyurethane (PU) foam in our lab and characterized for the enzyme activity^{74,117}. In order to compare the effect of immobilized CA on the CaCO₃ crystallization, control experiments were conducted by using bare PU porous foams. PU foam and enzyme immobilization were achieved by mixing equal amounts of water with prepolymer, HYPOL2060. Figure 5.49 shows the SEM images of the porous PU foam and its surface. The changes in pH and conductivity during CaCO₃ carbonization in the presence of different amounts of PU foam were not significant as shown in Figure 5.50. This also indicates the reproducibility of the experiments in the mini reactor.

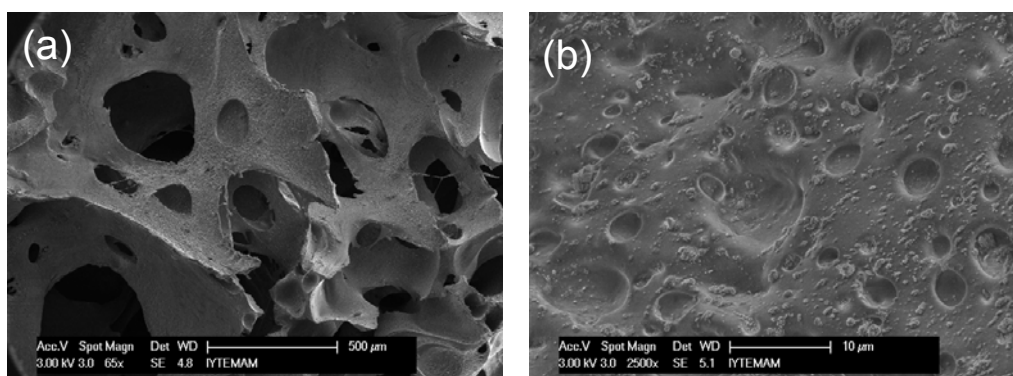


Figure 5.49. SEM images of PU foam showing its porous structure PU foam and its hydrophilic surface

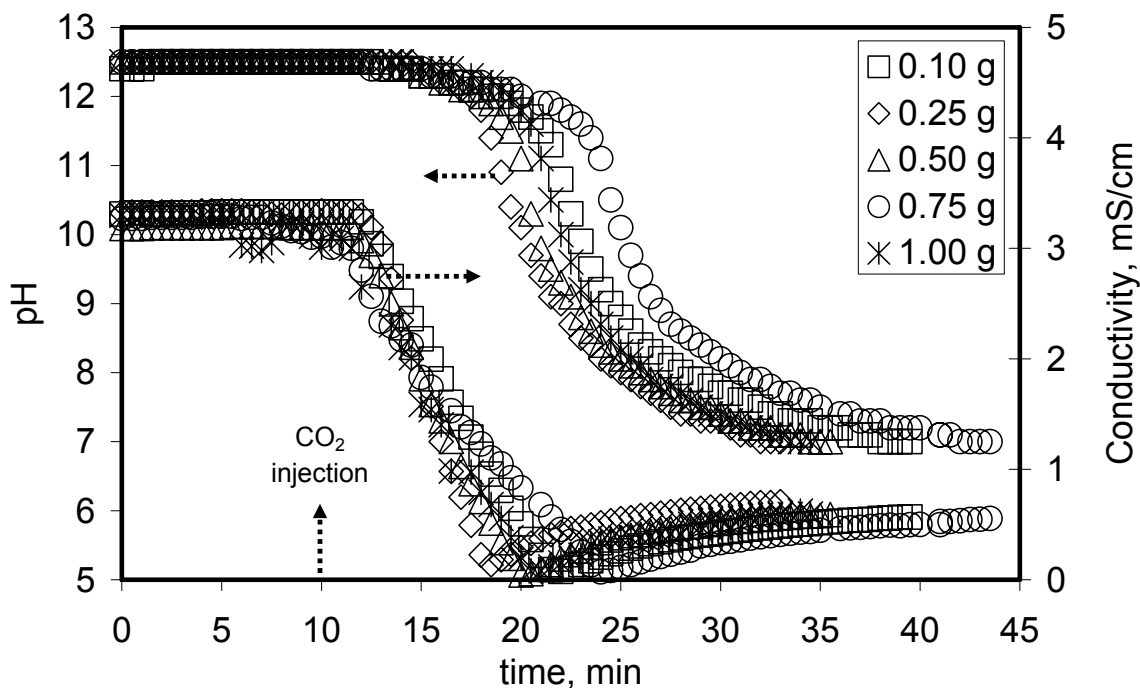


Figure 5.50. Change of pH and conductivity in the presence of various foam amounts (only foam, no CA)

Figure 5.51 shows the CaCO_3 particles formed on the surface (Figure 5.51a) and within the pores (Figure 5.51b) of the PU foam. The nature of the polymeric additives such as PU foam composed of polar groups that may influence the CaCO_3 crystallization by adsorbing and the growing nuclei on the available polar groups⁶. As shown in the figure, CaCO_3 particles were clearly precipitated on the hydrophilic surface of the foam and these particles are rounded and cubic chain-like and aggregated nano calcite as understood from the XRD patterns.

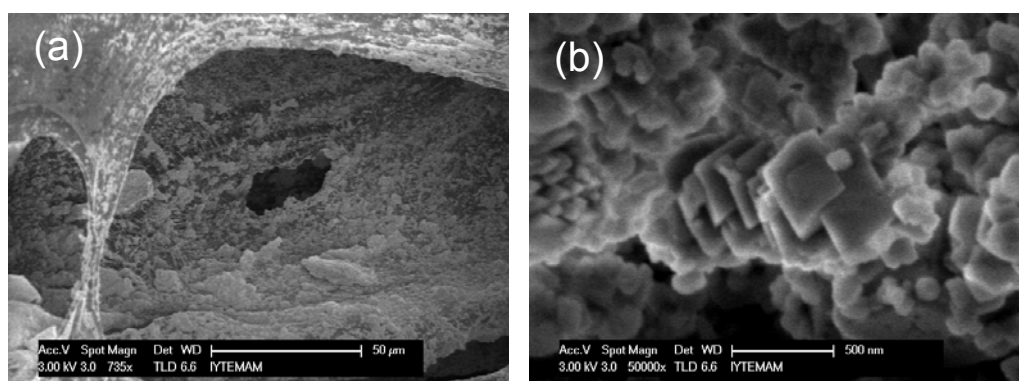


Figure 5.51. SEM images of precipitated CaCO_3 crystals on the surface and (b) within the pore of the PU foam

The SEM images of CaCO_3 particles obtained in the presence of PU foams (Figure 5.52) shows that these particles are nano, aggregated, chain like calcite crystals as indicated from XRD patterns of the precipitates, as shown in Figure 5.53. The characteristic calcite peaks obtained at 2 Theta of about $\sim 29.3^\circ$. The crystal thicknesses were calculated as 40-50 nm based on the XRD patterns. Although the intensities of the calcites appeared to be decreasing with amounts of PU foam, it is only related to the amount of sample used in XRD analyses so that, the intensities are evaluated arbitrarily.

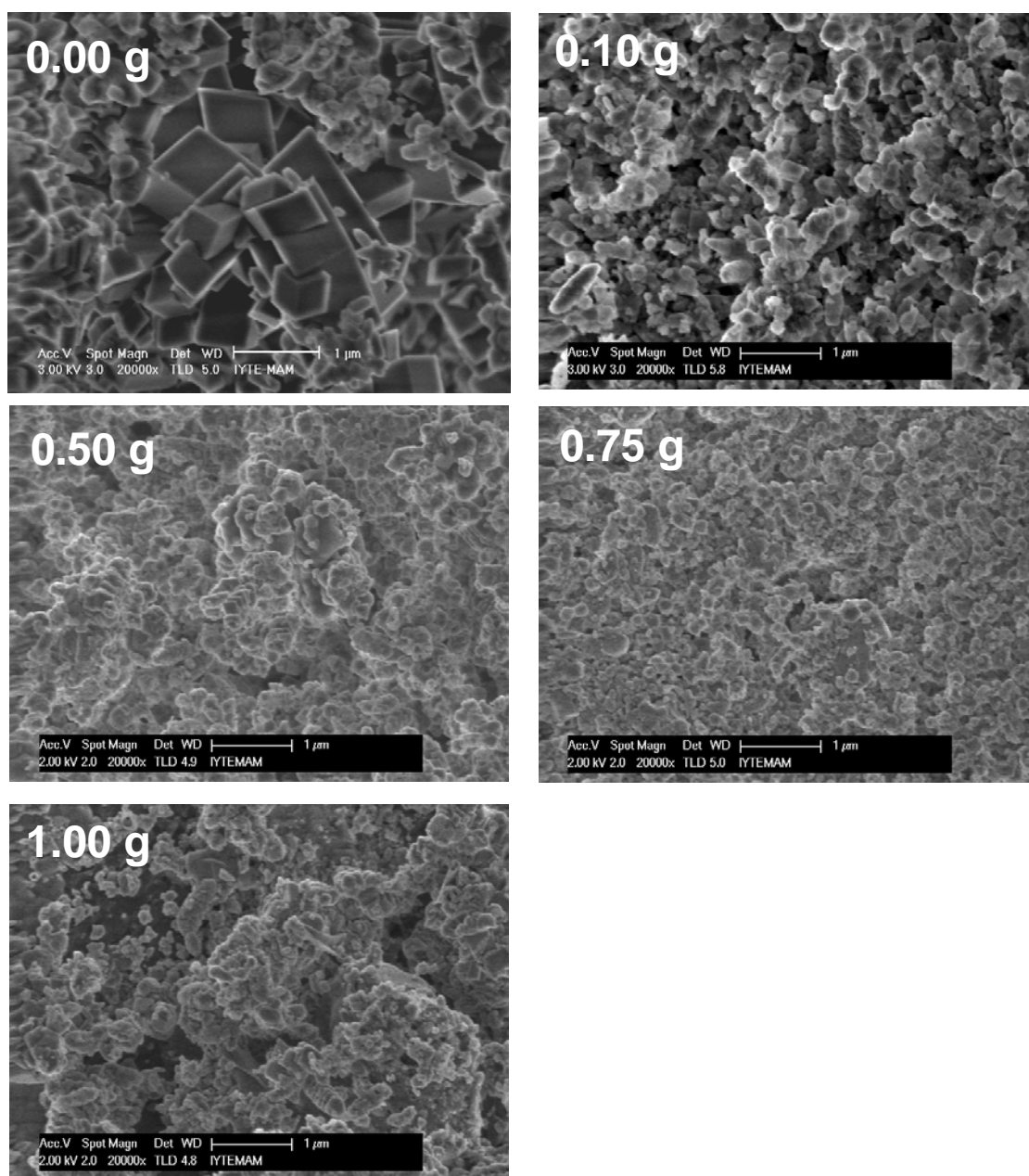


Figure 5.52. SEM images of the precipitates obtained from the carbonization experiments in the presence of various amount of PU foam (CA: 0.00 μM; $\text{Ca}(\text{OH})_2$:20 mM).

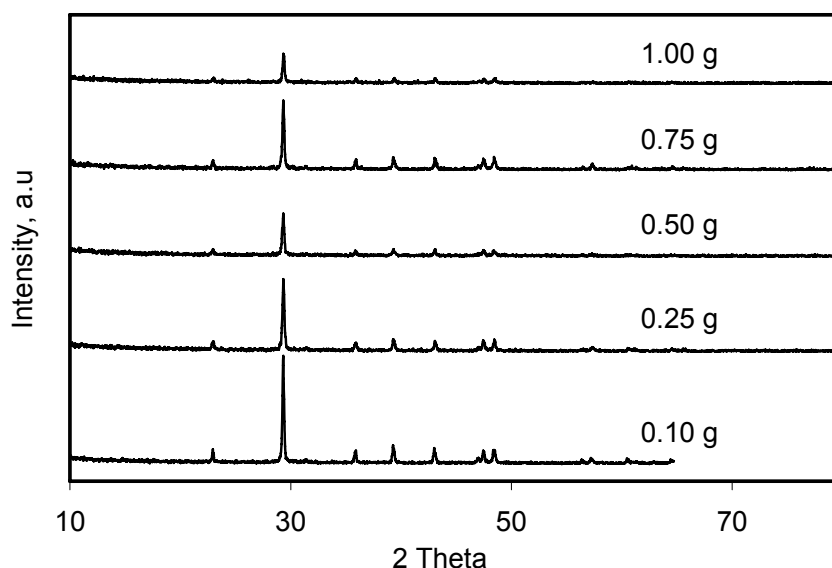


Figure 5.53. XRD patterns of the precipitates obtained from the carbonization experiments in the presence of various amount of PU foam. (CA: 0.00 μ M; Ca(OH)₂: 20 mM)

5.8. Effect of Immobilized Carbonic Anhydrase on CaCO₃ Production

The CaCO₃ crystallization was studied in the mini reactor in the presence of immobilized CA enzyme. The CA enzyme was immobilized within the PU foam at concentrations ranging from 0.55 mg CA / g-Hypol to 3.45 mg CA / g-Hypol. The foam was cut into very small pieces of about 2 mm having their volumes of about 10 mm³ in order to suspend the CA immobilized foam within the aqueous solution and added into the Ca(OH)₂ solution. In order to investigate the effect of immobilized enzyme on the CaCO₃ crystallization, an experiment matrix was formed as shown in Table 4.1.

Figure 5.54 shows the changes in pH and conductivity values during the precipitation experiments using foams at the highest CA concentration available (3.45 mg CA / g-Hypol) with an amount of 0.10, 0.25, 0.50, 0.75, 1.00 g of CA immobilized foams, respectively, in 20 mM of Ca(OH)₂ slurry stirring at 600 rpm. As can be seen in the figure, the crystallization time relatively decreased as the amounts of CA immobilized foam was increased. For the 0.75 g of foam used, the induction time for clustering and nucleation took longer, but crystallization was completed relatively similar to the others. From the conductivity data, it seems that when low amount of CA immobilized foam was used, two step crystallization occurred. Because the PU foam

did not affect the crystallization time significantly, the decreasing crystallization time with the enzyme concentration is consistent with those for free enzyme.

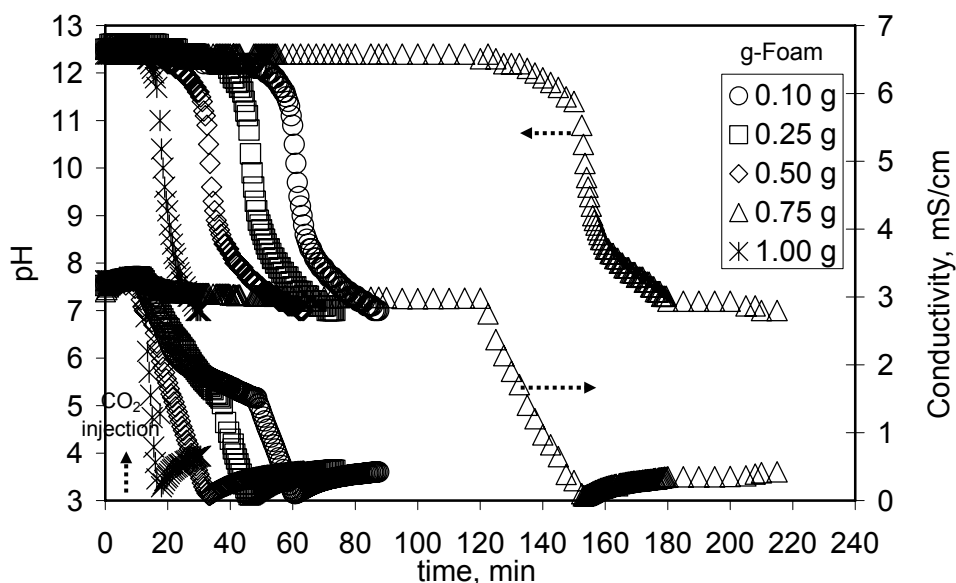


Figure 5.54. Change of pH and conductivity in the presence of im-BCA (3.45 mg BCA / g HYPOL) with various amounts of PU foam ($\text{Ca}(\text{OH})_2$: 20 mM)

The SEM images of the CaCO_3 particles obtained in the presence of different amount of foam immobilized with the highest amount of CA enzyme were shown in Figure 5.55. As shown in the figure, generally round shape aggregated and nano sized calcite particles were produced as evidence from the XRD patterns as shown in Figure 5.56. The particles obtained for the 0.75 g of CA immobilized PU foam showed a different morphology, being cubical calcite crystals of the sizes of about 200 - 300 nm. These particles look separated from each other indicating that they have a neutralized surface in stable form. The particles obtained for 1 g of foam gave a much lower particle size but aggregated.

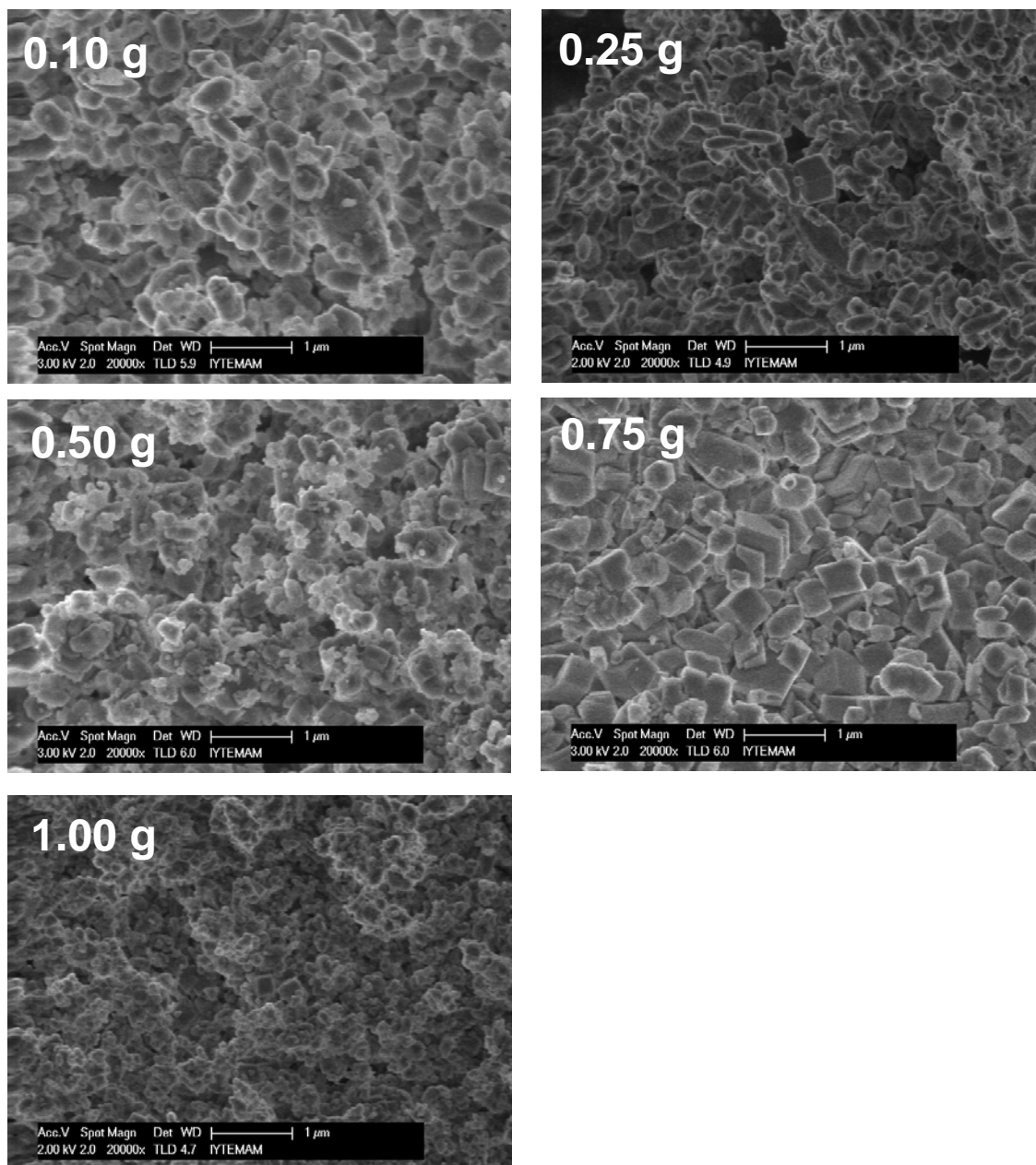


Figure 5.55. SEM images of CaCO₃ particles obtained in the presence of immobilized CA (3.45 mg BCA / g HYPOL) with various amounts of PU foam (Ca(OH)₂ : 20 mM)

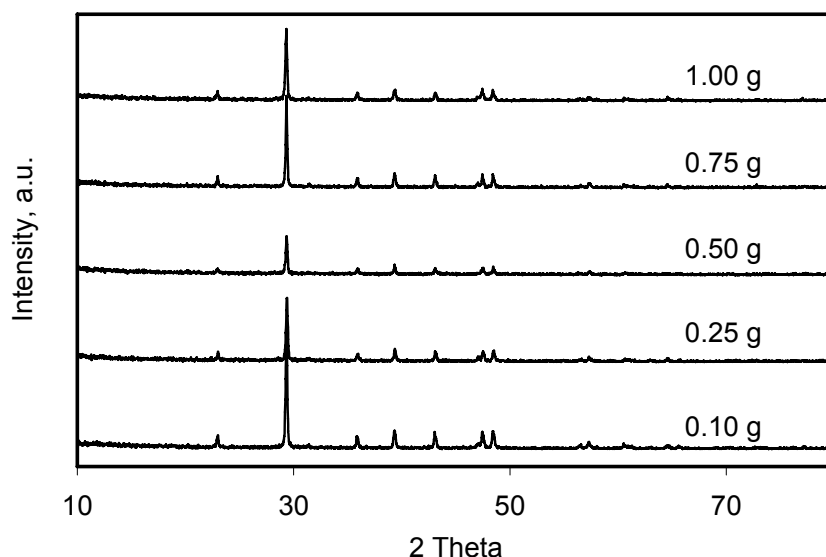


Figure 5.56. XRD patterns of CaCO_3 particles obtained in the presence of immobilized CA (3.45 mg BCA / g HYPOL) with various amounts of PU foam (Ca(OH)_2 : 20 mM)

On the other hand, the pH and conductivity curves gave different results for fixed amount of foam used for different immobilized CA concentrations. As shown in Figure 5.57, a 0.25 g of foam immobilized with different amount of CA enzyme was used in the crystallization experiments. The crystallization time decreased compared to the foam without immobilized enzyme. It can be seen from the conductivity data that, the crystallization rates were different for different cases. For all the cases, as shown in Figure 5.58, round shape, almost mono dispersed calcite crystals were produced as understood from XRD patterns as shown in Figure 5.59.

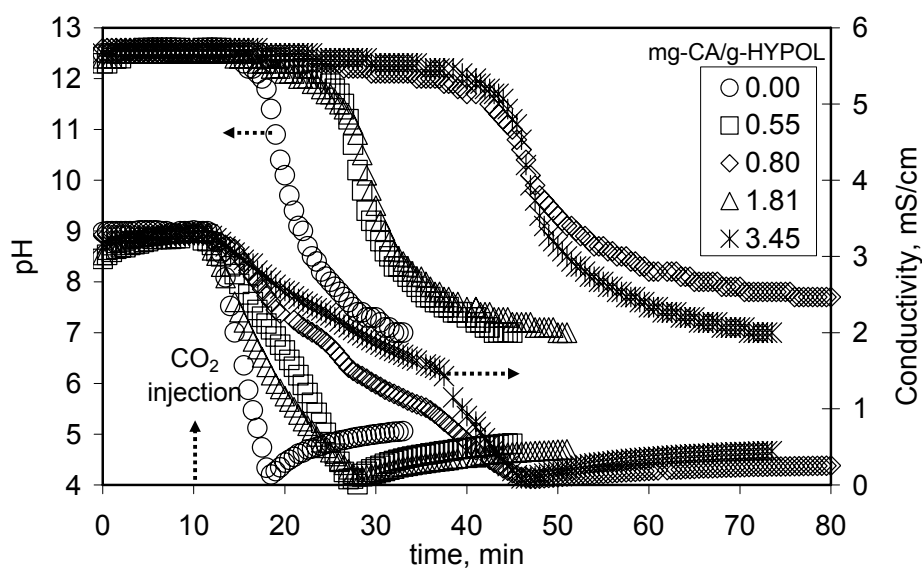


Figure 5.57. Change of pH and conductivity with increasing BCA amount on PU foam (PU foam : 0.25 g)

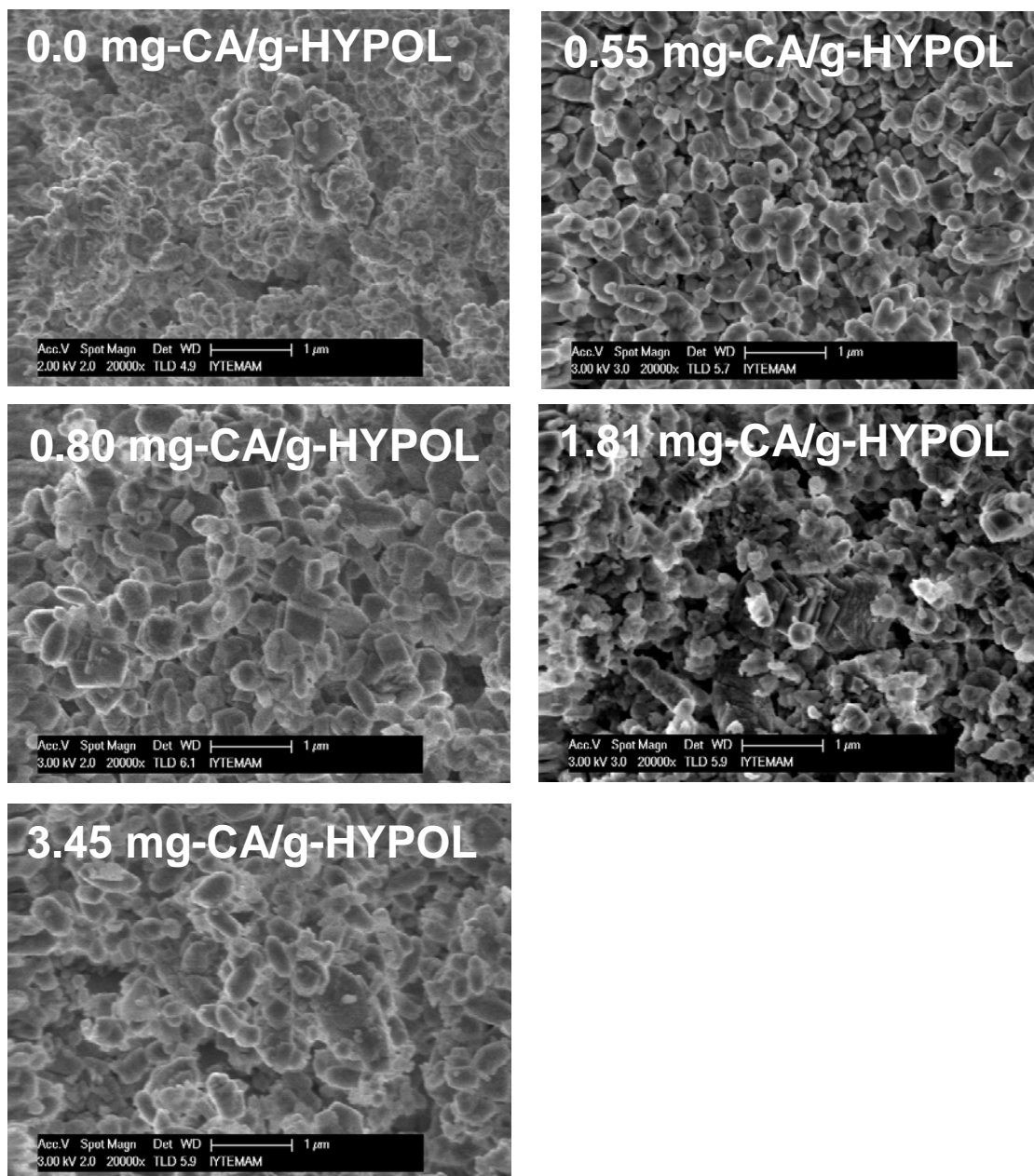


Figure 5.58. SEM images of the precipitates obtained by various BCA amounts immobilized on PU foam (PU foam: 0.25 g)

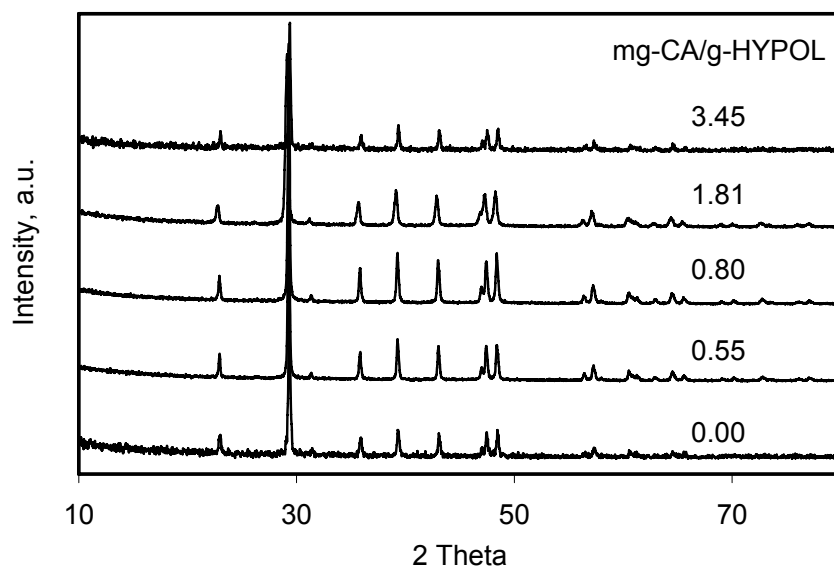


Figure 5.59. XRD patterns of the precipitates obtained by various BCA amounts immobilized on PU foam (PU foam : 0.25 g)

Similar conclusions can be made for the 0.50 g and 0.75 g of foam used in the precipitation experiments using different amounts of immobilized CA. For 0.50 g of CA immobilized foam, as shown in Figure 5.60, the crystallization time increased with the amount of enzyme was increased. For 0.50 g of CA immobilized foam, as shown in Figure 5.60, the crystallization time increased with the amount of enzyme was increased. For 1.81 mg CA /g-hypol, although crystallization was in progress, the pH was still high throughout the crystallization indicating that very slow equilibrium reactions would take place during crystallization as evidenced from the SEM images of the particles as shown in Figure 5.61. Here, generally mono dispersed cubical calcite particles were obtained. The other particles are all round shape aggregated nano calcites as evidence from XRD patterns as shown in Figure 5.62.

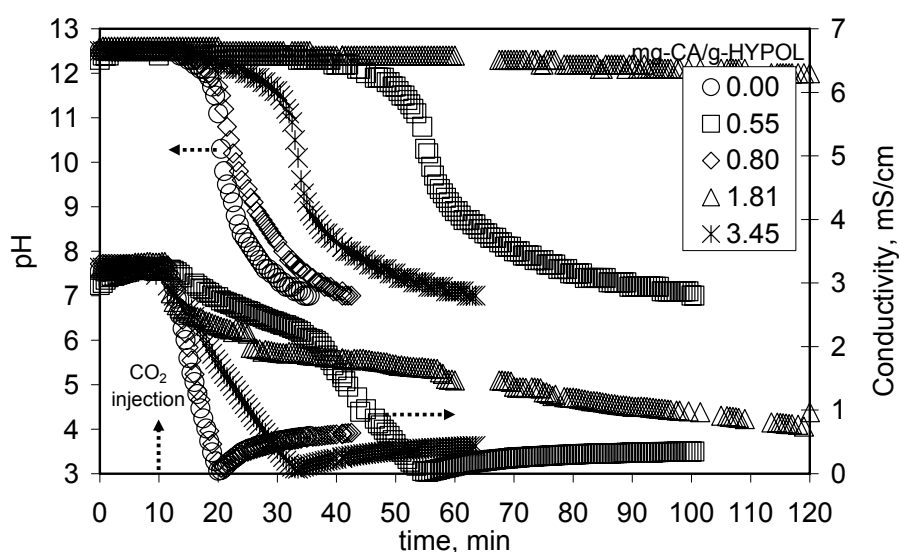


Figure 5.60. Change of pH and conductivity with increasing BCA amount on PU foam (PU foam : 0.50 g)

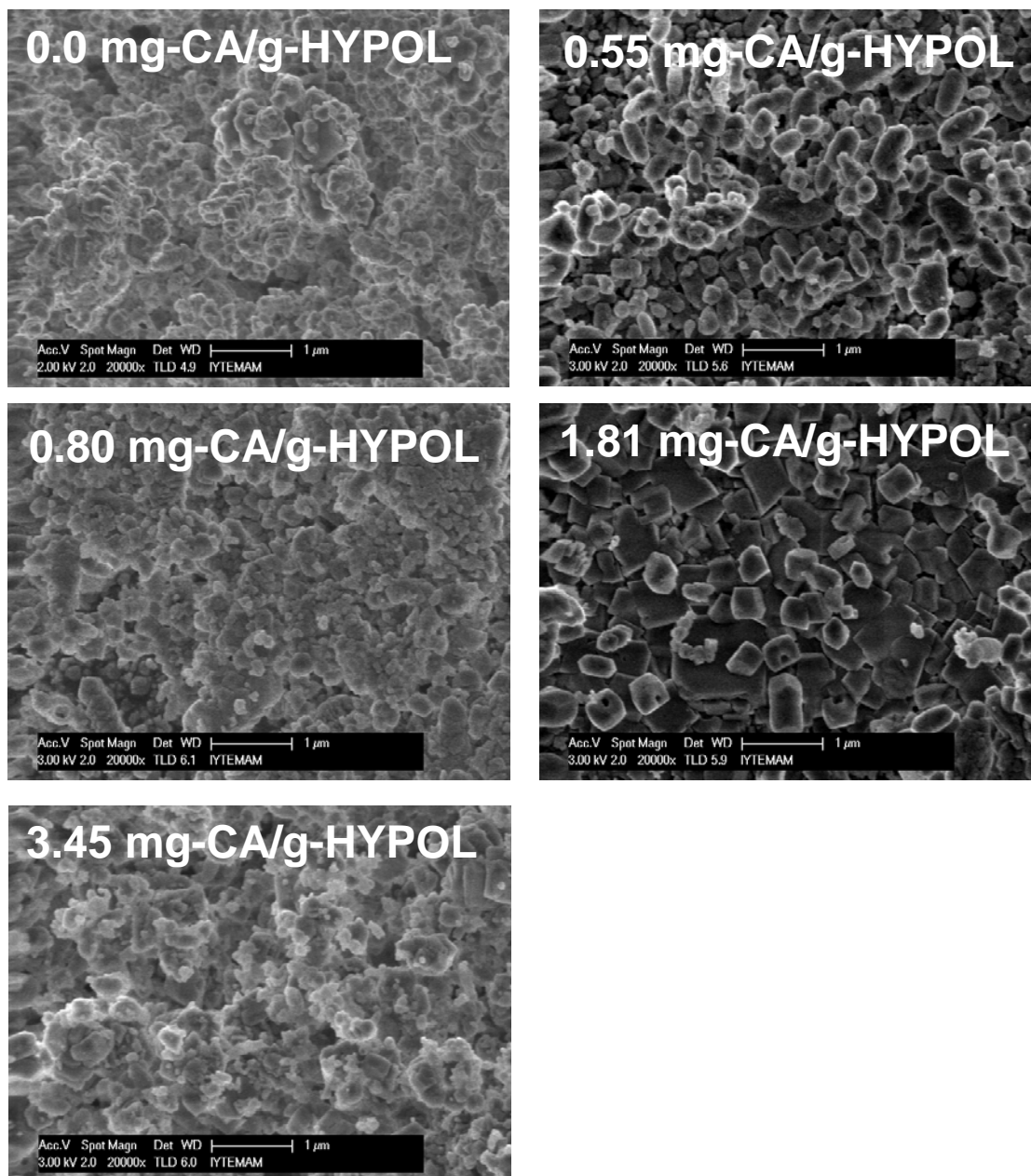


Figure 5.61. SEM images of the precipitates obtained by various BCA amounts immobilized on PU foam (PU foam : 0.50 g)

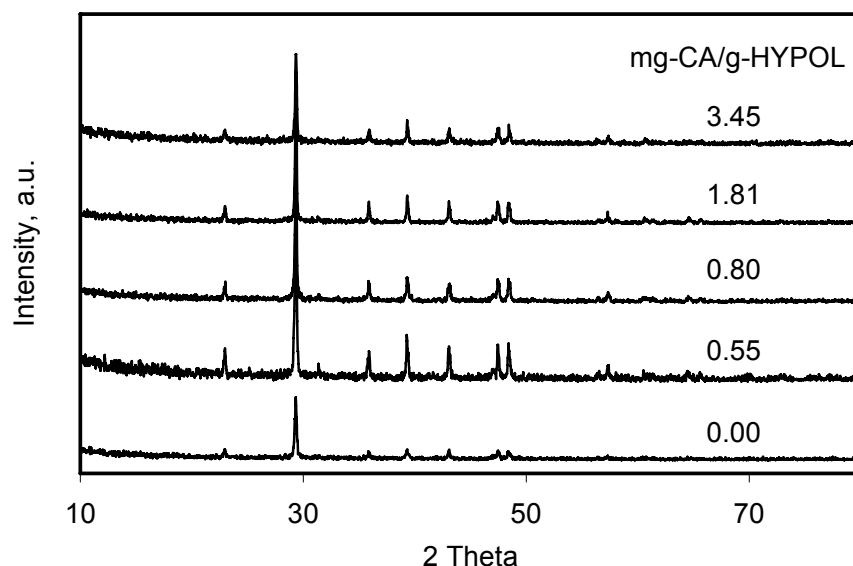


Figure 5.62. XRD patterns of the precipitates obtained by various BCA amounts immobilized on PU foam (PU foam : 0.50 g)

For the 0.75 g of CA immobilized foam, as shown in Figure 5.63, the crystallization time varied with the amount of enzyme. For 1.81 mg CA /g-hypol, a sudden drop in conductivity was seen and stayed constant up to 180 min indicating that there are still Ca^{++} ions or charged particles, may be in the form of charged clusters, would be available in the solution. However, as shown in Figure 5.64, the SEM images of all these particles are round shape aggregated and chain-like nano crystals as calcite as evidenced from their XRD patterns as shown in Figure 5.65. Here, also 50 nm of grape-like aggregated nano calcite particles were obtained.

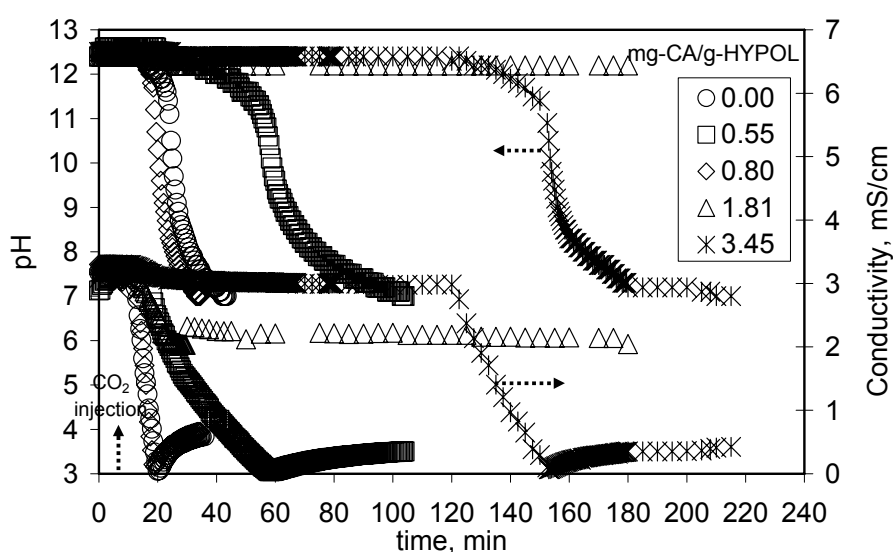


Figure 5.63. Change of pH and conductivity with increasing BCA amount on PU foam (PU foam : 0.75 g)

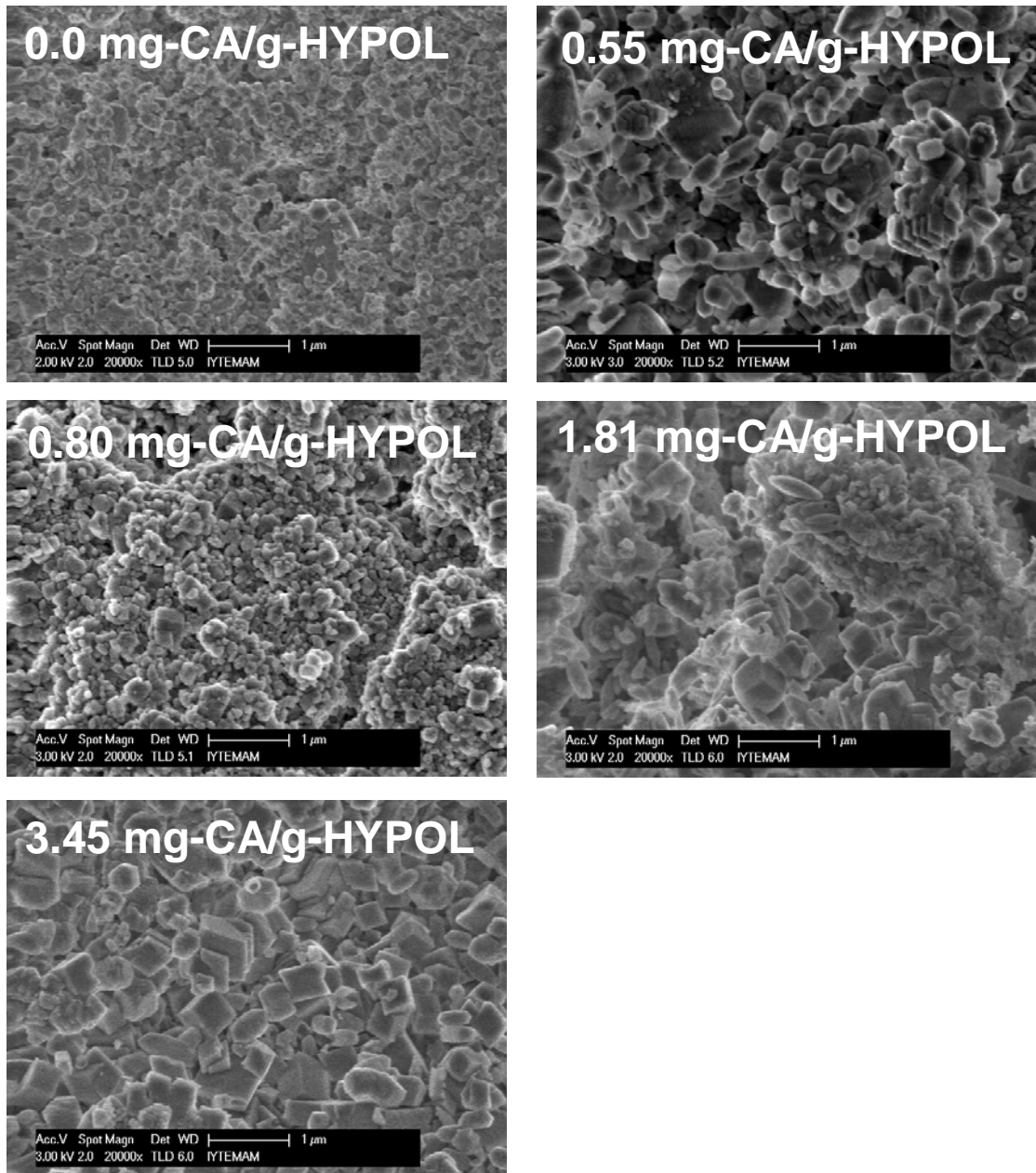


Figure 5.64. SEM images of the precipitates obtained by various BCA amounts immobilized on PU foam (PU foam : 0.75 g)

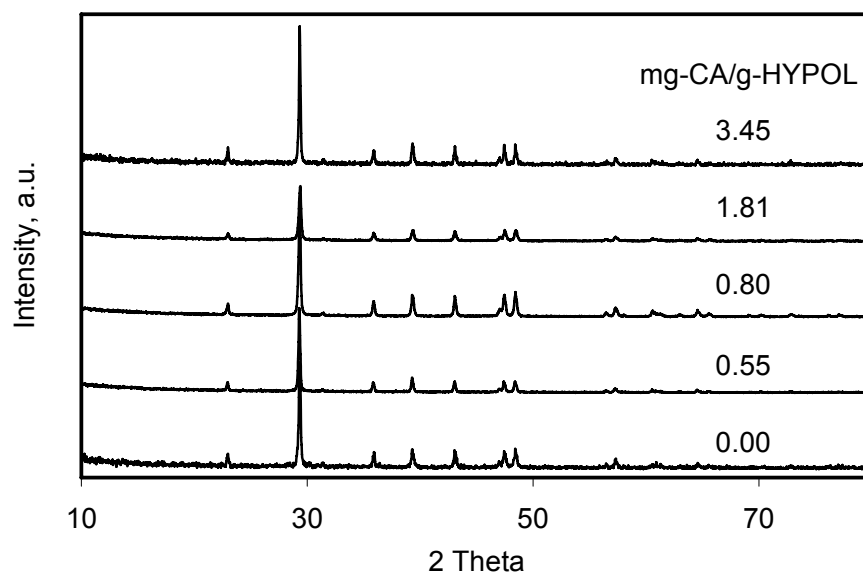


Figure 5.65. XRD patterns of the precipitates obtained by various BCA amounts immobilized on PU foam (PU foam : 0.75 g)

In order to have detail knowledge on the mechanism of the calcium carbonate production, the final view of the foam and porous structures were investigated by SEM (Figure 5.66). Pores of the foams were full of the CaCO_3 crystals in different sizes. For instance, thousands of the crystals were detected in a $2\ \mu\text{m}$ pore. It is important to note that, $2\ \mu\text{m}$ - pore was in a $20\ \mu\text{m}$ pore, and $20\ \mu\text{m}$ - pore was in a $100\ \mu\text{m}$ pore, and all pores were full of CaCO_3 crystals in calcite form. This is an indication of possible adsorption mechanism of crystals into the foam. Crystals might have also been occurred in a porous structure of PU foam.

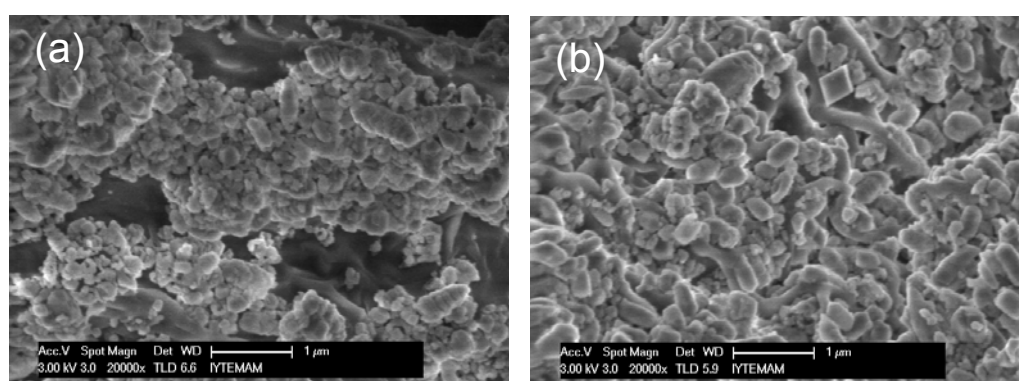


Figure 5.66. SEM images of CaCO_3 crystals (a) inside and (b) on the surface of a PU pore immobilized with CA.

According to the results of mineralogical analyses of the final products given in related XRD plots, calcite was the major CaCO_3 polymorph obtained at the end of each experiment in the presence of immobilized CA. Based on the analysis of d-spacing in

XRD, some aragonite and vaterite polymorphs were also detected. Low concentration of CA and increase in amount of PU foam caused the change of crystal morphology from cubic shape to spheroid (spherical). Calcite appeared in the form of nanosized, predominantly both rhombohedral and spheroidal morphology as shown in the SEM images. Although the CA concentrations were low; it is possible to obtain nanosize calcites as precipitates. Amount of foam has little effect on the crystallite size with the low concentrations of CA and their effects were more significant when the PU foam was used as carrier for CA. Therefore, CA could have a positive effect on small crystal size formation. The immobilized CA might have been also a template for nano CaCO₃ crystallization.

Average crystal size for the precipitated calcium carbonates was calculated by the Debye Scherrer Equation and found approximately 45 nm with a standard deviation of 5.88 nm (13 %) as tabulated in Table 5.3. No exact relationships were found between CA immobilized foam and crystal sizes. However, for all conditions, fine crystals were obtained.

Table 5.3. Size of the crystals obtained by biomimetic reactions by immobilized CA

<i>mg-BCA/ g-HYPOL</i>	<i>Sample Code</i>	<i>Foam amount (g)</i>	β <i>(FWHM)</i>	2 θ	cos(θ)	<i>Size*</i> (nm)
0.00	Excess 1	0.10	0.1636	29.32736	0.967428416	50.2
0.00	S1	0.25	0.1962	29.34266	0.967394609	41.9
0.00	S2	0.50	0.2001	29.33242	0.967417237	41.0
0.00	S3	0.75	0.1941	29.33371	0.967414387	42.3
0.00	Excess 2	1.00	0.1822	29.36131	0.967353375	45.1
0.55	S4	0.25	0.1830	29.28628	0.967519104	44.9
0.55	S5	0.50	0.1658	29.33130	0.967419712	49.5
0.55	S6	0.75	0.1663	29.30530	0.967477131	49.4
0.80	S7	0.25	0.1876	29.28739	0.967516656	43.8
0.80	S8	0.50	0.1802	29.33648	0.967408266	45.6
0.80	S9	0.75	0.1901	29.33294	0.967416089	43.2
0.18	S10	0.25	0.3069	29.13435	0.967853423	26.7
0.18	S11	0.50	0.1633	29.33350	0.967414851	50.3
0.18	S12	0.75	0.2159	29.37445	0.967324308	38.0
0.35	Excess 3	0.10	0.1850	29.33895	0.967402808	44.4
0.35	S13	0.25	0.1776	29.37933	0.967313510	46.2
0.35	S14	0.50	0.1715	29.35519	0.967366909	47.9
0.35	S15	0.75	0.1496	29.33596	0.967409415	54.9
0.35	Excess 4	1.00	0.1896	29.31625	0.967452955	43.3
Average						44.7

* Calculated by Debye Scherrer Equation

5.9. Effect of Organic Solvents on CaCO₃ Crystallization

Crystallization of calcite was performed in the presence of varying complexity of organic molecules. This section reports the effects of Ca(OH)₂ amount in slurry, additives (methanol, ethanol, hexane, toluene, benzene), and stirring rate on the precipitation time and the morphology of the precipitates.

The organics were added into the water above their solubilities and formed mixtures (not solutions) in order to obtain attraction with the Ca(OH)₂ powders. Ca(OH)₂ in mixtures was both around the solubility limit (20 mM) and above the solubility limit (40 mM). The main purpose of the usage of those additives was to modify the precipitate morphologies and create a database for the precipitation time.

If CaCO₃ crystals are produced in the presence of an organic additive, the addition of organic matters are either reducing the barrier to calcite nucleation or increasing the barrier to vaterite nucleation. These mean that, organic additives reduce the local supersaturation to produce stable calcite¹⁰⁵. Additionally, organic matters cause some decrease in crystallization energy and improves the crystallization³⁴. Studies on the interaction of macromolecules with calcite suggest that these molecules can bind specifically to certain crystal planes during crystal growth, thereby modifying the final morphology attained¹²⁸. The interaction between organic molecules and the calcite surface (endothermic chemisorption) is caused by the entropy change. The physical and chemical properties of organics affect the inhibition degree. These properties are hydrophobicity, functionality, and molecular size. The inhibition degree of the precipitation increases with the molecular weight and aromatic content of the organics¹²⁹ (i.e. toluene and benzene). Dissolution of CO₂ and mass transfer between CO₂ and Ca(OH)₂ are the key parameters in CaCO₃ crystallization. The solubility of CO₂ in a nonpolar organic solvent (i.e. hexane, toluene, benzene) is always lower than its solubility in water at constant temperature and pressure¹³⁰. On the other hand, solubility of CO₂ increases in the presence of polar organic solvents such as methanol and ethanol¹³¹.

The solubility of CO₂ in the presence of some organic additives may affect the precipitation time. It was reported that, comparing in pure water, there was only 1 μS/cm rise in electrical conductivity and higher, unstable pH in pure ethanol. These indicate that the CO₂ gas in water make more than 100 times the HCO₃⁻ and CO₃⁼ than those in ethanol. The formation of HCO₃⁻ and CO₃⁼ in ethanol is so unstable that this

reaction would be more reversible. The similar behaviors are also valid for methanol. The previous work also reported the solubility of CO_2 gas at 20°C as 0.9 ml/ml for pure water and 2.8 ml/ml for ethanol. Therefore, CO_2 gas dissolved favorably in the existence of an aqueous form of CO_2 rather than the state of HCO_3^- and $\text{CO}_3^{=}$ because of lower conductivity, higher and unstable pH in pure ethanol and/or methanol. On the other hand, solubility of $\text{Ca}(\text{OH})_2$ in pure ethanol and methanol increases by introducing CO_2 in water accelerating the crystallization of CaCO_3 ¹³².

Figure 5.67 represents the change of pH and conductivity during precipitation in the presence of additives (5 % v/v) in 20 mM of $\text{Ca}(\text{OH})_2$ solution under 800 rpm stirring. In this case, the precipitation time for toluene and hexane was significantly higher than that for methanol, ethanol and benzene. These solvents at these conditions resulted in elliptical shape of particles as shown in Figure 5.68. The precipitates obtained by the modification of these two solvents were almost monodispersed and individual particles.

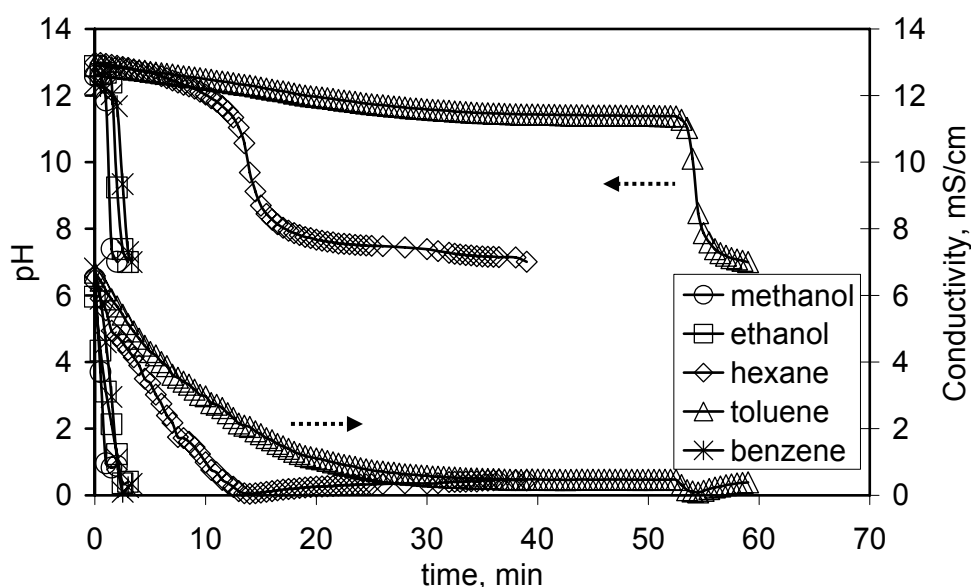


Figure 5.67. Change of pH and conductivity during precipitation in the presence of additives. Amount of $\text{Ca}(\text{OH})_2$:20 mM stirring: 800 rpm additives : 5 % (v/v).

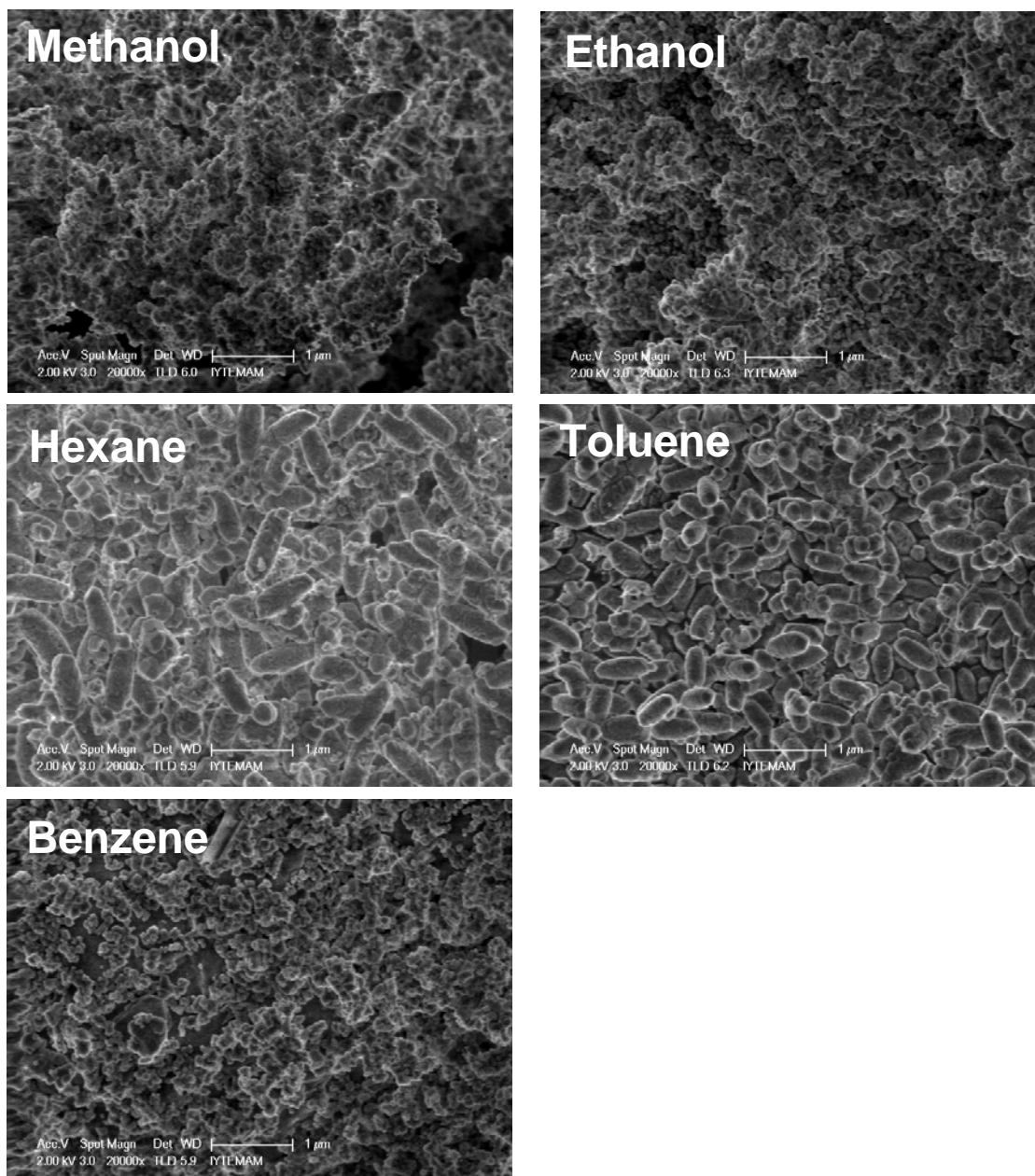


Figure 5.68. SEM images of the precipitates obtained by the modification of the additives. Amount of $\text{Ca}(\text{OH})_2$:20 mM stirring: 800 rpm additives : 5 % (v/v)

Methanol as a polar solvent with a dielectric constant of 32.60 has a strong interaction with inorganic surfaces, and has the potential to control the nucleation and growth of crystals¹³³. Similarly, ethanol is also a polar compound with a dielectric constant of 24.60 and it affects the nucleation and crystal growth, modifies the inorganic CaCO_3 surfaces. Because of the methanol and ethanol have hydrophilic tails and they are miscible in water, their interaction with both Ca^{++} ions and CaCO_3 particles will be more significant than hydrophobic, nonpolar solvents such as hexane, toluene and benzene. These interactions during the precipitation would affect the nucleation and

growth of CaCO_3 particles to form smaller sized particles in different morphologies. Here, the sizes of the precipitates which were obtained in the presence of methanol and ethanol were finer, however, they were strongly aggregated due to the lower potential energy.

As shown in Figure 5.69, the XRD patterns of the precipitates indicated the existence of the stable crystals with the characteristic peak of calcite at 2θ of about 29° . There were not metastable or non stable forms of CaCO_3 crystals after the modifications under given conditions.

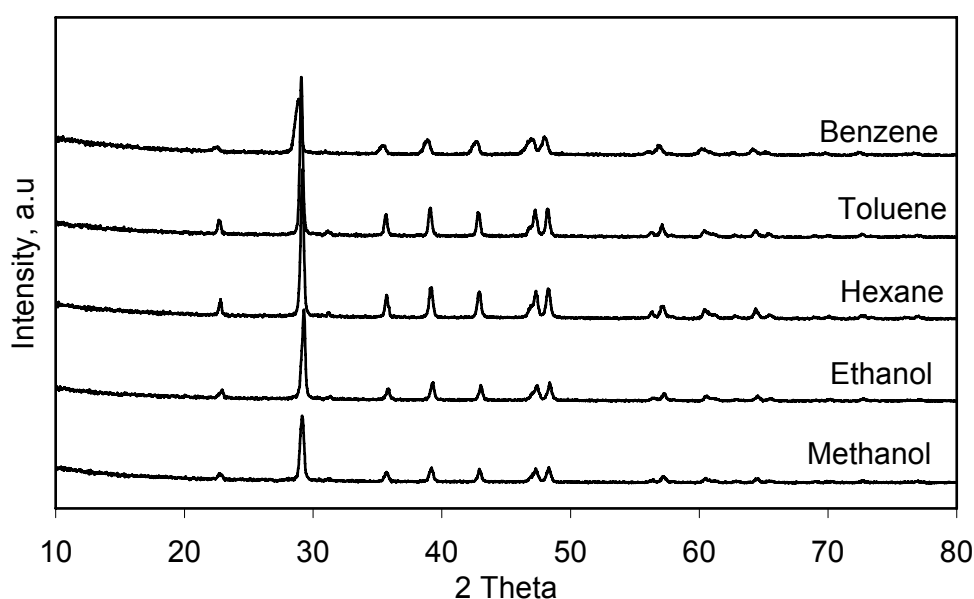


Figure 5.69. XRD patterns of the precipitates obtained by the modification of the additives. Amount of $\text{Ca}(\text{OH})_2$:20 mM stirring: 800 rpm additives : 5 % (v/v)

Figure 5.70 shows pH and conductivity curves during precipitation in the presence of these additives (20 % v/v) in a 20 mM $\text{Ca}(\text{OH})_2$ solution under 800 rpm stirring. Similar to its 5 % addition into the 20 mM $\text{Ca}(\text{OH})_2$, the precipitation time for hexane was significantly higher than other additives, but toluene accelerated the precipitation time at this case. Because the film layer would have been formed within water containing a 20 % of such additives, the transfer of CO_2 to the solid-liquid suspension would be inhibited.

Methanol prevents the formation of solid hydrates¹³⁴. One of the adverse effects for the excess amount of methanol in water would be the reduction in the solubility of the ionic solids, particularly solids with divalent charges. Therefore, methanol was also shown to retard the precipitation when its concentration increased by 4-fold. On the

other hand, conductivity for the ethanol mixture was always measured lower than those for other solvents, which may have caused the precipitation faster comparatively.

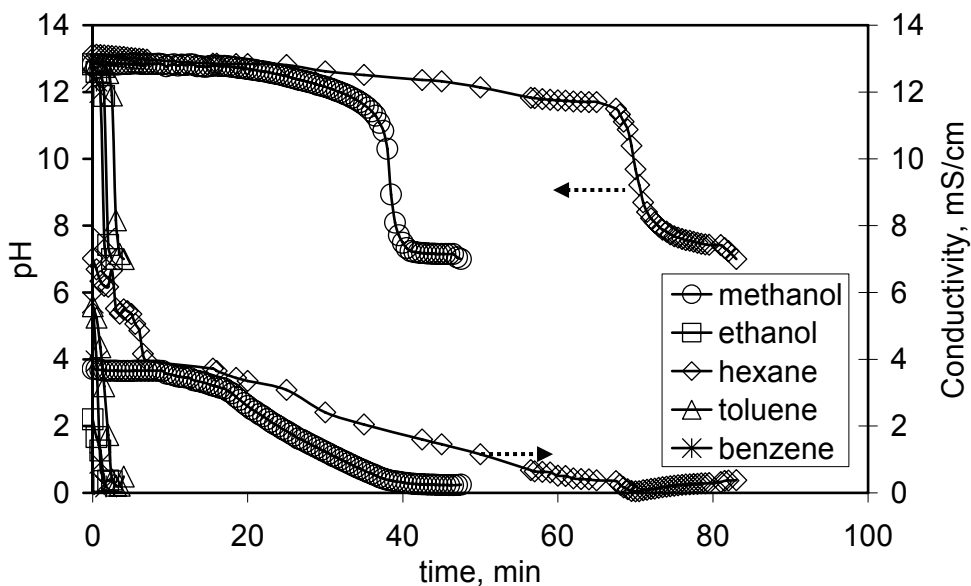


Figure 5.70. Change of pH and conductivity during precipitation in the presence of additives. Amount of $\text{Ca}(\text{OH})_2$:20 mM stirring: 800 rpm additives : 20 % (v/v)

When toluene was added in excess amounts, the morphology of the precipitates was significantly changed to spheroidal chains. Nano CaCO_3 crystals were obtained as shown in Figure 5.71, and these crystals were calcite evidenced by XRD patterns as given in Figure 5.72. The presence of ethanol in the spontaneous precipitation process caused the formation of stable nano calcite crystals in a regular chain-like cubic morphology. The precipitated calcite crystals were highly aggregated because of the presence of the additive in the solute which would probably influence the surface charge of the calcite crystals.

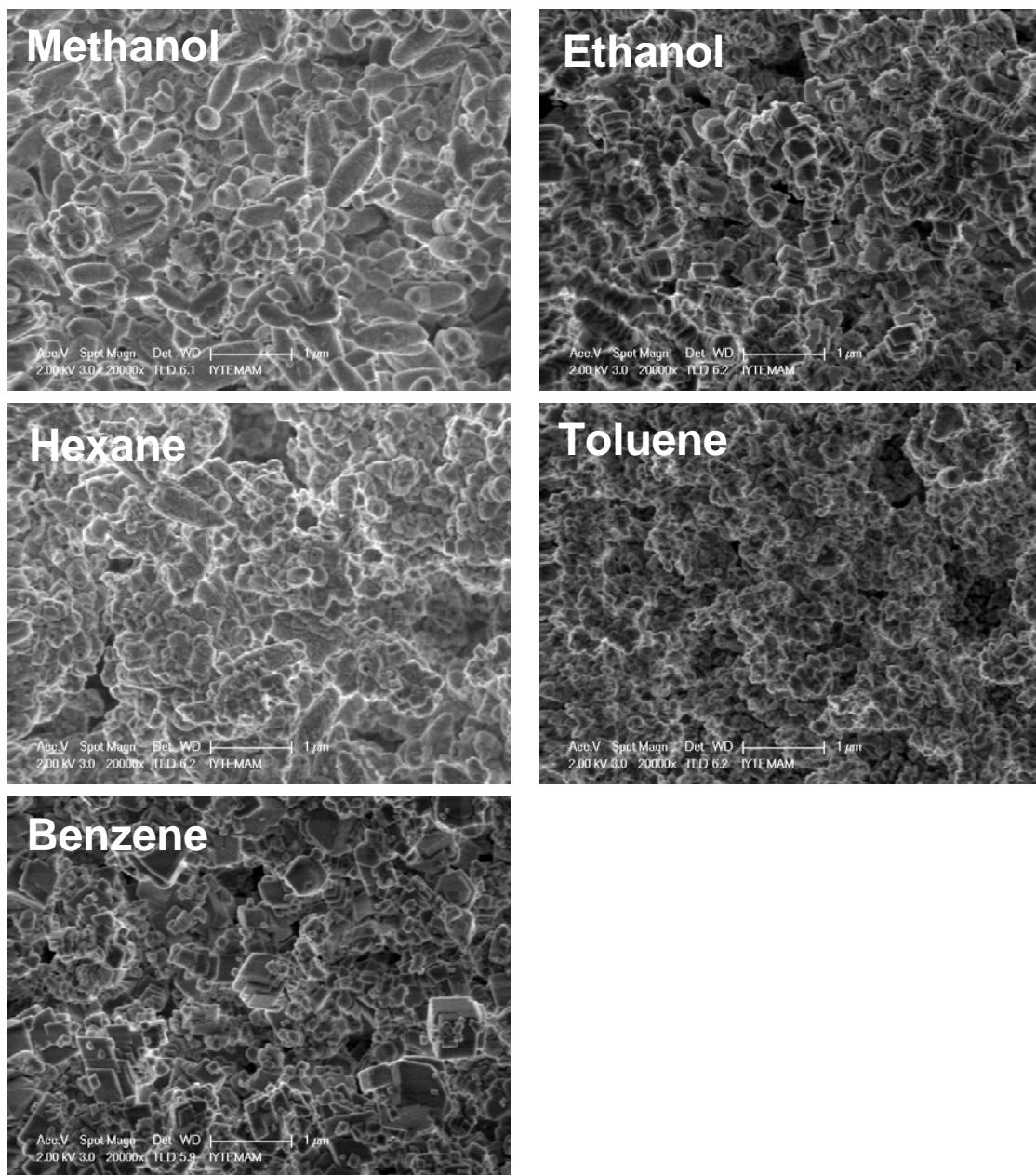


Figure 5.71. SEM images of the precipitates obtained by the modification of the additives. Amount of $\text{Ca}(\text{OH})_2$:20 mM stirring: 800 rpm additives : 20 % (v/v)

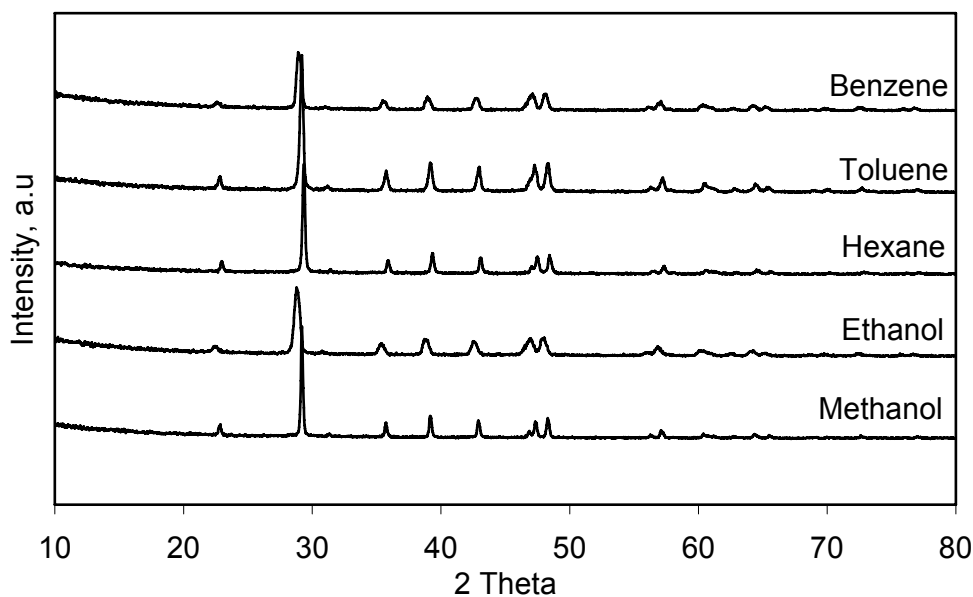


Figure 5.72. XRD patterns of the precipitates obtained by the modification of the additives. Amount of $\text{Ca}(\text{OH})_2$:20 mM stirring: 800 rpm additives : 20 % (v/v).

Figure 5.73 shows the FTIR spectra which were obtained for the precipitates synthesized in 20 mM of $\text{Ca}(\text{OH})_2$ solution in the presence of 20 % of organic additives such as methanol, ethanol, hexane, toluene, benzene under 800 rpm stirring. The nonpolar and hydrophobic additives of hexane, toluene and benzene showed a similar behavior under the FTIR spectroscopy. In the FTIR spectra, all the calcium carbonate samples were found to be in the symmetric stretching (ν_1), out-of-plane bending (ν_2), the asymmetric stretching (ν_3), and the in-plane-bending (ν_4) modes, of the carbonate group of ions. In addition to the first order internal modes, the ($\nu_1 + \nu_3$) and ($\nu_1 + \nu_4$) combination modes[♦] were also observed¹³⁵.

♦ As with any oscillatory system, vibrations are possible not just for these three modes, but also for higher harmonics - that is, overtones - and for combinations of different modes of oscillation. Indeed, bumps in the absorption curve can be identified with a combination of all three modes ($\nu_1 + \nu_2 + \nu_3$), with a combination of the first overtone of mode 1 and mode 3 ($\nu_1 + \nu_3$), and with a combination of the second overtone of mode 1 and mode 3 ($\nu_1 + \nu_3$). For the higher harmonics, the frequency of oscillation is higher, and hence, absorption occurs at shorter wavelengths.

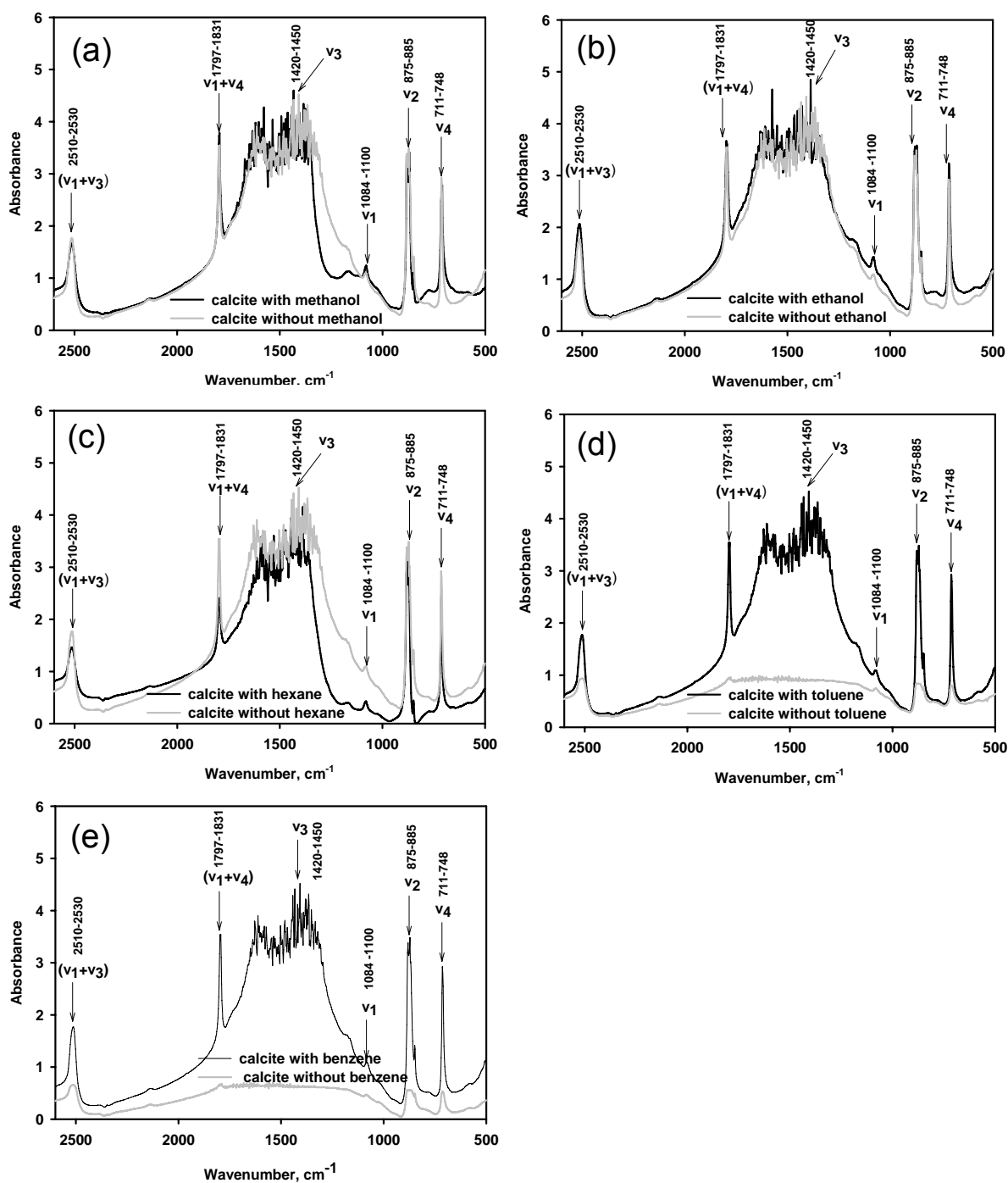


Figure 5.73. FTIR Spectra's of calcites which obtained in the presence of (a) methanol (b) ethanol (c) hexane (d) toluene (e) benzene: Amount of $\text{Ca}(\text{OH})_2$:20 mM stirring: 800 rpm additives : 20 % (v/v)

In a symmetric stretching mode, atoms are vibrating along the bonds, and stretching them. The molecule retains its tetrahedral symmetry throughout, and there is no induced dipole. More than one atom in the same bond are vibrating, and it is an in-phase vibration. In asymmetric stretching mode, there are two atoms stretching along the bond direction, and they are an out of phase to each other. Asymmetric stretch

modes are generally of a higher frequency than symmetric stretch modes in FTIR spectrometry. Combination modes depends on the potential in which the atoms sit, there can be many atoms vibrating in several different directions. In plane bending mode, the atoms take place in a direction perpendicular to the bond direction^{*}. In order to have knowledge of the molecular geometries determined by infrared spectra, illustration of vibrational modes of molecules and their oscillation directions were given in Figure 5.74.

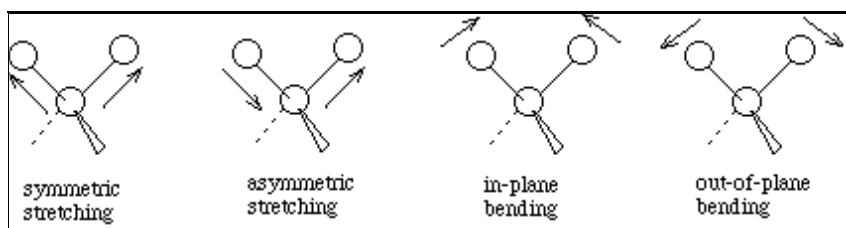


Figure 5.74. Vibrational modes of the molecules and their oscillation directions

Significant bands of methanol ($3750 - 3550 \text{ cm}^{-1}$), ethanol ($1150 - 950 \text{ cm}^{-1}$), hexane ($3013 - 2808 \text{ cm}^{-1}$), toluene ($3150 - 2825 \text{ cm}^{-1}$) and benzene ($1000 - 500 \text{ cm}^{-1}$) were not observed in the investigated wavelength region ($4000 - 0 \text{ cm}^{-1}$) indicating the absence of these compounds in the structure of produced calcite crystals. Also, the bands for CO_2 ($2081 - 2074 \text{ cm}^{-1}$) and H_2O ($1969 - 1964 \text{ cm}^{-1}$)^{136,137} were not detected.

Produced calcite in the presence of methanol, ethanol, and hexane could be considered to have similar chemical structure and there was not significant difference between their bond formations before and after the solvent modifications.

FTIR spectra of CaCO_3 crystals obtained from toluene and benzene mixtures look different such that calcite bands at symmetric stretching mode (ν_1), out-of-plane bending (ν_2), the asymmetric stretching (ν_3), and the in-plane-bending (ν_4) modes of the carbonate ion group were detected. Besides the first order internal modes, the ($\nu_1 + \nu_3$) and ($\nu_1 + \nu_4$) combination modes but their absorption bands were very weak. Chemical structure of the precipitates showed some differences after the addition of toluene and benzene. Crystals occurred on different chemical structures.

Modification of the calcite crystals with the organic additives was re-tested in the presence of 40 mM of saturated $\text{Ca}(\text{OH})_2$ slurry. Precipitation of CaCO_3 was accelerated in the presence of undissolved $\text{Ca}(\text{OH})_2$ particles, as shown in Figure 5.75.

^{*} <http://newton.ex.ac.uk/research/qsystems/jones/projects/oxygen/lvms.html>

The presence of lower amount of organic additives (5 % v/v) under high stirring of 800 rpm would be another reason for the rapid precipitation.

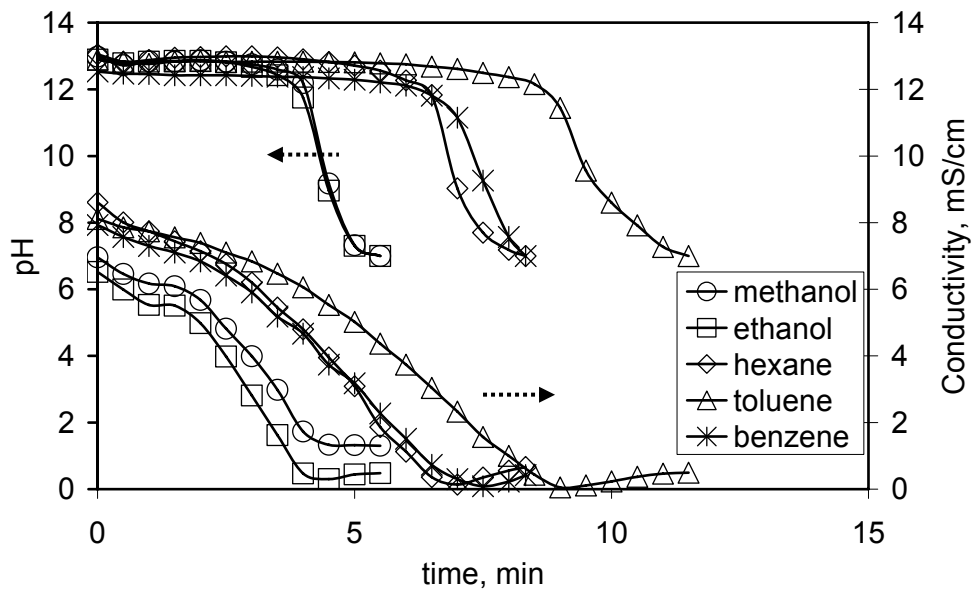


Figure 5.75. Change of pH and conductivity during precipitation in the presence of additives. Amount of $\text{Ca}(\text{OH})_2$:40 mM stirring: 800 rpm additives : 5 % (v/v)

All crystal formation turned into rhombohedral chain-like calcite crystals in aggregated form under supersaturation conditions as shown in Figure 5.76 and Figure 5.77. There are strong interactions between the functional groups of additives and the Ca^{++} ions. These interactions during the precipitation affect the nucleation and growth of CaCO_3 particles to form smaller sized particles in different morphologies⁹⁴. There is a strong affinity of the polar or nonpolar organics for CaCO_3 particles than for free Ca^{++} ions in the solution¹³⁸. The functional groups attract Ca^{++} ions and then cause the local concentration of Ca^{++} increased. This would be responsible for reducing the activation energy of nucleation. Therefore, the number of crystals increases accelerating the reaction¹³⁹, however, they were coagulated due to the reduced activation energy.

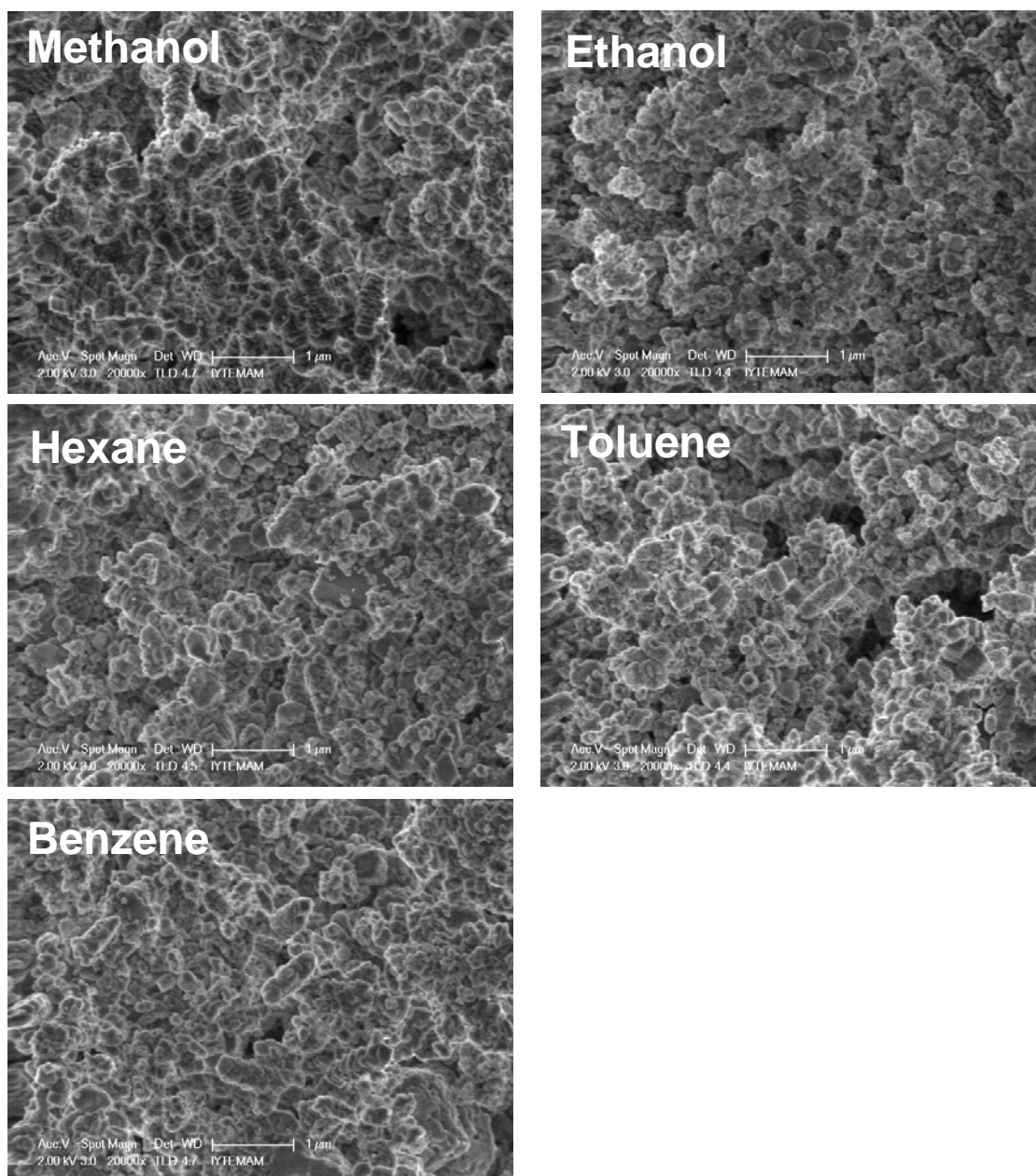


Figure 5.76. SEM images of the precipitates obtained by the modification of the additives. Amount of $\text{Ca}(\text{OH})_2$:40 mM stirring: 800 rpm additives : 5 % (v/v)

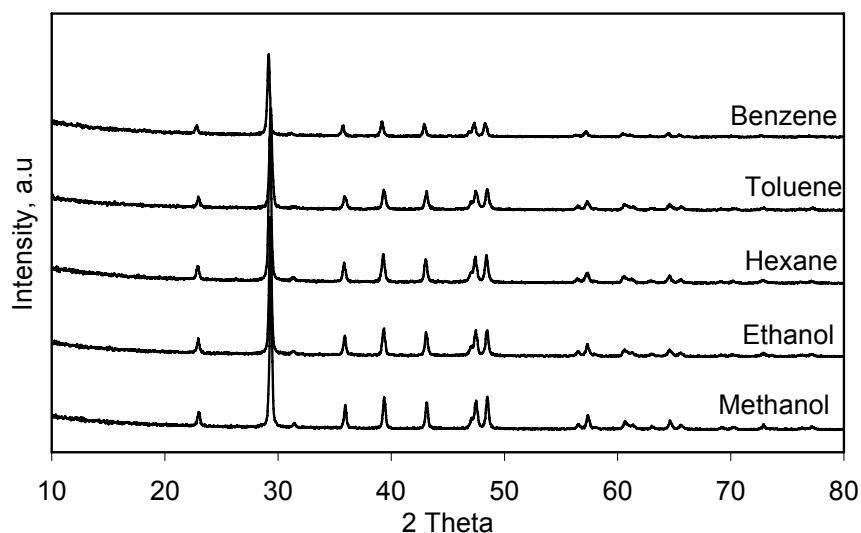


Figure 5.77. XRD patterns of the precipitates obtained by the modification of the additives. Amount of $\text{Ca}(\text{OH})_2$:40 mM stirring: 800 rpm additives : 5 % (v/v)

Change of pH and conductivity, SEM images of the precipitates, and their XRD patterns showing similar results as previous findings as shown in Figure 5.78 to Figure 5.80. The increase in organic / inorganic ratio may reduce the barrier to calcite nucleation or increase the barrier to vaterite nucleation. This means that these additives may reduce the local supersaturation to produce stable calcite¹⁰⁵

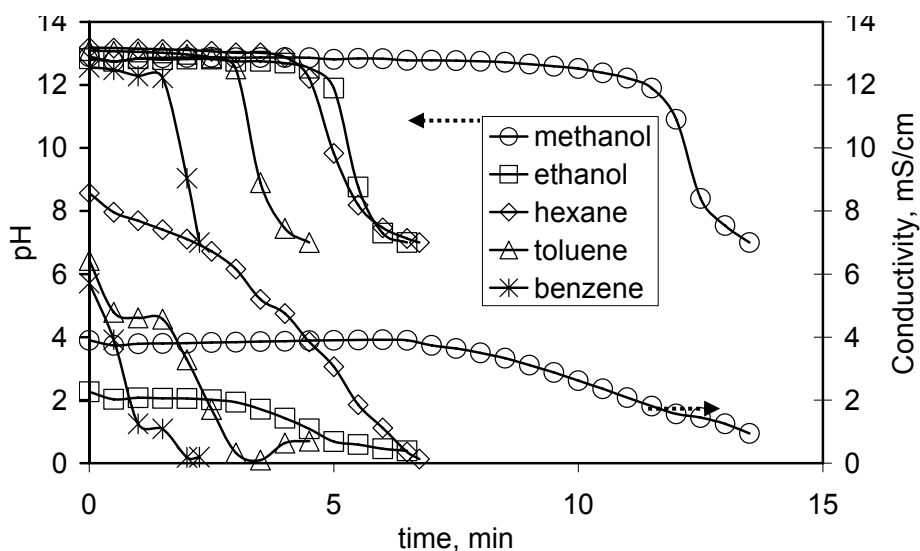


Figure 5.78. Change of pH and conductivity during precipitation in the presence of additives. Amount of $\text{Ca}(\text{OH})_2$:40 mM stirring: 800 rpm additives : 20 % (v/v).

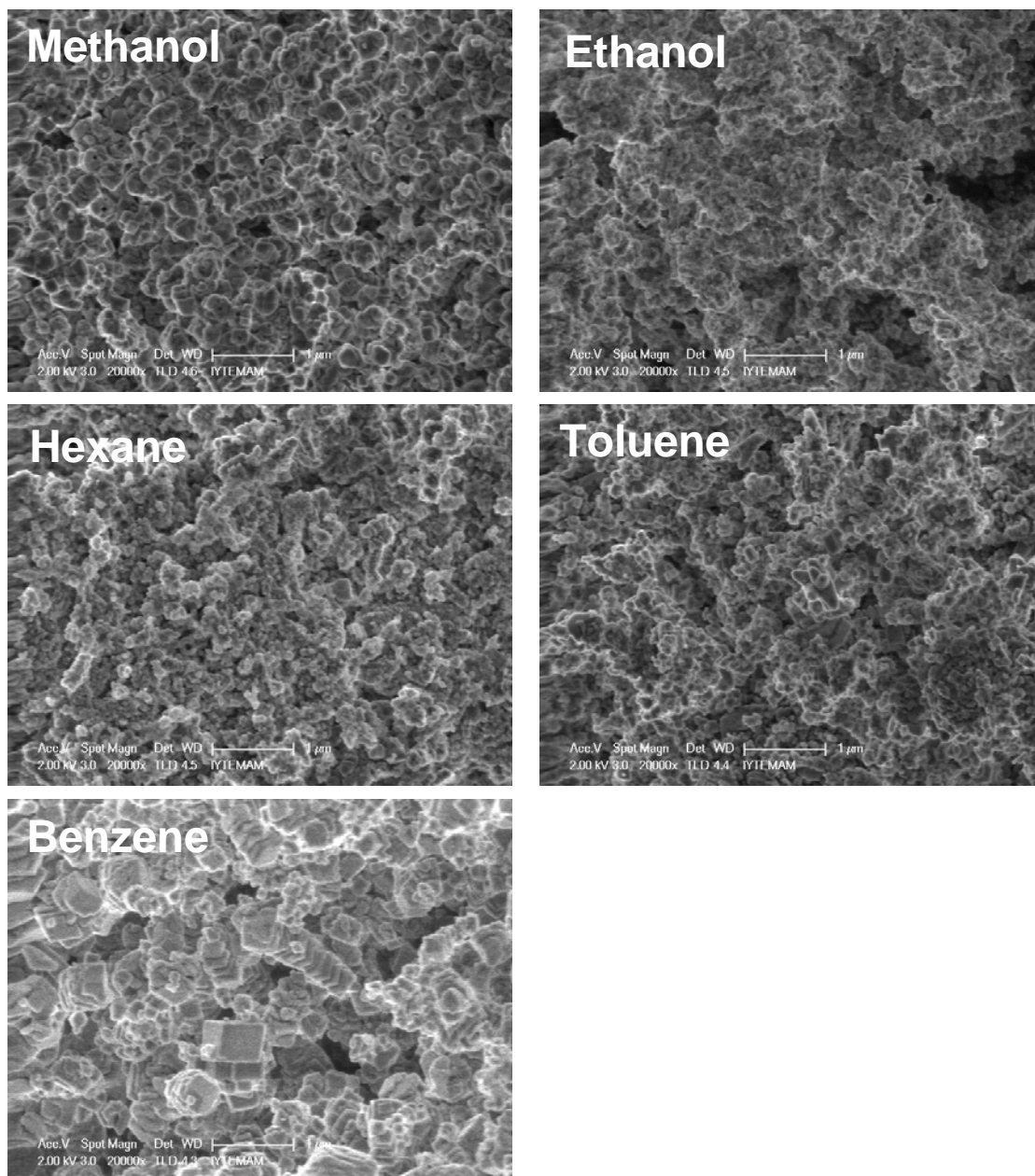


Figure 5.79. SEM images of the precipitates obtained by the modification of the additives. Amount of $\text{Ca}(\text{OH})_2$:40 mM stirring: 800 rpm additives : 20 % (v/v).

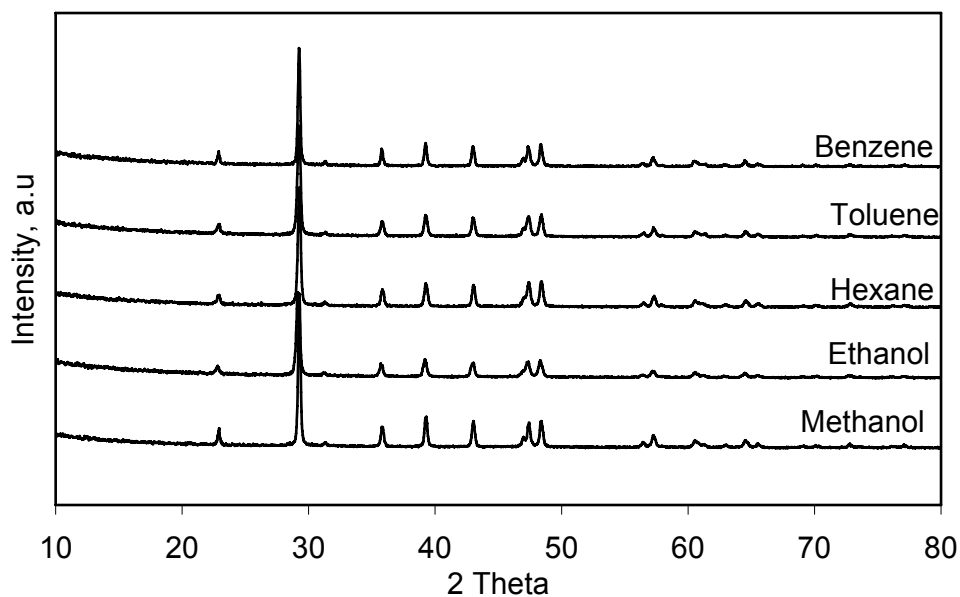


Figure 5.80. XRD patterns of the precipitates obtained by the modification of the additives. Amount of Ca(OH)₂ :40 mM stirring: 800 rpm additives : 20 % (v/v)

As can be seen, those organic molecules certainly influence the morphology of the CaCO₃ crystals during the precipitation. Both the organic solvents and water have co-effect on the polymorphism and morphology of CaCO₃ particles at room temperature.

Amphiphilic property of the organics such as methanol and ethanol have a great influence on the structural framework, and the solvating degree, the dielectric constant of the system, the polarity, the interaction among the ions (such as Ca⁺⁺) in the solution. Generally, molecular structural framework and solvating degree of the additives may affect the initial formation of crystallization by blocking of the growth sites. They can also limit the reaction in the solutions and can lead to high localized accumulations of the ionic charges. Therefore, the amphiphilic properties of the organic solvents may play an important role to determine the size, the shape, and the organization of the crystal forms^{99,105}. Some organic solvents, such as hexane, toluene and benzene can not exhibit amphiphilic property since they are not miscible in water at room temperature. However, vigorous stirring can redound to increase solubility of these organic solvents⁷⁶.

Various unusual crystal morphologies, such as elliptical, spheroidal, rod-like, flowerlike, cubical, spherical etc. were obtained in the presence of organic additives depending on the experimental conditions. Surface modifications of calcite crystals

were achieved by the hydrophobic solvents such as hexane, toluene, and benzene. Effects of toluene and hexane on the morphology of the crystals were more significant than that of benzene. Especially, monodisperse pure nano calcites were obtained in 20 mM of Ca(OH)_2 in the presence of 5 % (v/v) toluene. When toluene amount was increased, the morphology changed to the flower-like aggregates. Experiments with these nonpolar organic additives demonstrated the retardation of the time for crystal growth. They were modified the surfaces by making complexation with the cations (Ca^{++}) in solution, changing the activity of the ions and the supersaturation, or binding to growth sites on the nuclei.

In general, reactions between Ca(OH)_2 and CO_2 were faster in the presence of methanol and ethanol than those for toluene, hexane and benzene. Precipitates belong to methanol mixtures were chain-like or flower-like calcite aggregates. When methanol was used in supersaturated Ca(OH)_2 slurry, aggregates were chain-like and closer to monodisperse form.

All the precipitates were calcite crystals with given reference codes (JCPDS Card No) in Table 4.6. They have at least one nano-scale dimension (up to 40 nm), and the crystallite thicknesses were calculated between ~25 and 45 nm by Debye Scherrer equation. The diffraction peaks of the precipitates which have the relative scores of less than 0.50 may contain amorphous-crystal mixture or composites. However, they were not the characteristic peaks of aragonite (JCPDS Card No. 41-1475) and vaterite (JCPDS Card No. 33-0268). For example, if a precipitate contains 0.88 relative score of calcite in any pattern, this means that, the pattern detect 0.12 impurities in mass. FTIR analyses of the selected precipitates gave idea about the composition and chemical structure of the last products. Accordingly, there were no organic bonds with produced calcites. In other words, all the organic additives only modified the physical and surface morphologies without changing the chemical structure. Ionic strength of the mixtures, polarities of the additives, dielectric constants, dissolution of the precipitates in additives would be the parameters affecting the crystal formation and could be investigated in detail as a future study. A summary of the results obtained from the experiments with organic additives were listed in Table 5.4. Here, the precipitation time was obtained from pH – conductivity curves, relative scores was obtained from XRD patterns, and the crystal structure and crystal thickness were calculated by Debye Sherer equation.

Table 5.4. Evaluation of the PCC's obtained by organic solvent sets

PCC code*	t ₁ [†]	t ₂ [‡]	peak angle (2θ)	d-spacing [§]	Ref Code	Relative score**	Crystal Structure	size ^{††} (nm)
SET1-1	6.5	5.0						
SET1-2	9.5	9.5	29.25865	3.04991	86-2334	0.78	chain-like calcites	36.8
SET1-3	10.5	7.5						
SET1-4	83.5	83.5	29.32004	3.04366	86-2334	0.78		42.5
SET1-5	2.0	1.5	29.14796	3.06124	72-1937	0.61		24.2
SET1-6	47.5	47.5	29.19340	3.05658	86-2341	0.28	chain-like cubic crystals	45.7
SET1-7	5.5	5.5	29.36394	3.03921	72-1214	0.87		
SET1-8	13.5	13.5	29.26145	3.04962	86-2334	0.81		39.4
SET2-1	7.0	5.0						
SET2-2	6.0	6.0	29.28399	3.04733	86-2334	0.80		35.5
SET2-3	9.5	7.5						
SET2-4	16.0	16.0	29.20086	3.05581	86-2340	0.52	chain-like calcites	31.9
SET2-5	3.0	2.5	28.27299	3.04845	86-2334	0.70		
SET2-6	2.5	2.5	28.81392	3.09596	--	--		17.4
SET2-7	5.5	5.5	29.31949	3.04372	86-2334	0.77		33.2
SET2-8	6.5	5.0	29.16336	3.05966	86-2340	0.52		28.4
SET3-1	224.0	208.0					rhombohedral calcite crystals as aggregates	
SET3-2	27.5	19.0						
SET3-3	139.0	125.5						
SET3-4	161.5	155.5						
SET3-5	39.0	14.0	29.15773	3.06023	86-2334	0.39		30.2
SET3-6	83.0	70.0	29.34505	3.04113	86-2334	0.77		38.9
SET3-7	8.33	7.0	29.27364	3.04838	86-2334	0.76		30.8
SET3-8	6.75	6.75	29.26576	3.04918	86-2334	0.86		34.0
SET4-1	16.0	12.5					monodisperse nano calcite crystals	
SET4-2	20.5	18.0						
SET4-3	69.0	63.0						
SET4-4	65.0	59.5						
SET4-5	59.0	54.5	29.08403	3.06782	86-2341	0.37		
SET4-6	4.0	3.5	29.17881	3.05807	86-2340	0.41		
SET4-7	11.5	9.0	29.35640	3.03998	86-2334	0.82		
SET4-8	4.5	3.5	29.24343	3.05137	83-1762	0.83		
SET5-1	11.5	9.0					chain-like cubic calcites	
SET5-2	62.0	55.0						
SET5-3	42.5	36.5						
SET5-4	--	--						
SET5-5	3.33	2.5	28.86883	3.09020	86-2343	0.21		
SET5-6	1.75	1.75	28.96354	3.08031	03-0569	0.50		
SET5-7	8.33	7.5	29.16188	3.05981	86-2341	0.48		
SET5-8	2.25	2.0	29.36394	3.05117	72.1937	0.79		

* The conditions given in Table 3.4

† Elapsed time from CO₂ injection to zero conductivity (minutes)

‡ Elapsed time from CO₂ injection to 7.0 pH (minutes)

§ Peak parameters detected with 100 % relative intensity

** Maximum score as percent which was calcite detection for relative intensity

†† Crystallite size which represents the minimum dimension (nm)

Because toluene and hexane helped to obtain monodisperse, regular, and elliptical shaped nano calcite crystals, the experiments were repeated in the presence of these additives as toluene and hexane solutions (not mixture in this case). The maximum concentration of toluene or hexane was two fold of their solubility in water. As an impressive comparison to previous experimental set, where these solvents was approximately 4000 and 1500 -fold- of their solubility limits for hexane and toluene, respectively. Therefore, these experiments were planned in the presence of these solvents in the aqueous solution of $\text{Ca}(\text{OH})_2$ at their below solubility limit, at the solubility limit, and above the solubility limit. As shown in Figure 5.81, Figure 5.83, and Figure 5.85, the precipitation reactions were significantly faster for both 20 mM and 40 mM of $\text{Ca}(\text{OH})_2$ solutions. Also, both toluene and hexane had impressive effects on precipitation time.

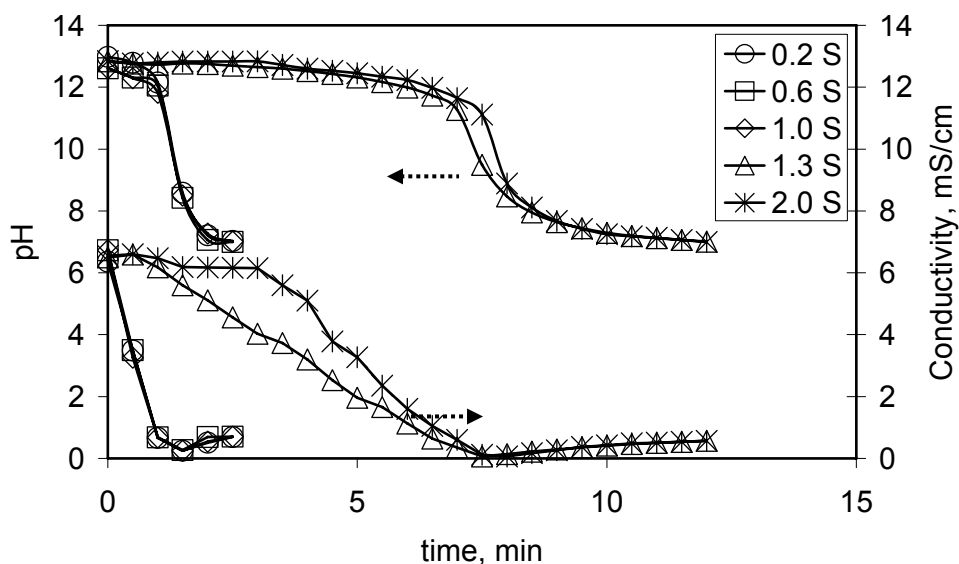


Figure 5.81. Change of pH and conductivity during precipitation in the presence of toluene. Amount of $\text{Ca}(\text{OH})_2$: 20 mM stirring: 800 rpm (from 0.2 S to 2.0 S in legend indicates from 0.2-fold to 2-fold of toluene solubility in water).

Nano CaCO_3 particles were produced in the presence of soluble organic additive, hexane and toluene, by carbonization method at room temperature. Similar morphologies were obtained as shown in the SEM images in Figure 5.82, Figure 5.84, and Figure 5.86. When the hexane or toluene concentration was below their solubility limit in water, the precipitates were chain-like cubic aggregates in nano size. When their solubility limit exceeded, irregular shapes were obtained in addition to the cubic ones.

At the first stage of the nucleation process, both toluene and hexane preferences to the slurry, $\text{Ca}(\text{OH})_2$ - CaCO_3 - CO_2 interface. There are electrostatic potential

interactions between hexane (or toluene) and Ca^{++} , and the organic additive is adsorbed on CaCO_3 . Soluble additive can be formed as micelles and free molecules at the interface of the slurry. The micelle increases the solubility of hexane (or toluene) and free molecule behaves as template in the crystallization process. Ca^{2+} adsorbed by the organic molecule and interacts with the functional group and oxygen atoms by covalent bond and hydrogen bonds, respectively. Adsorption of organic matters causes some decrease in crystallization energy and improves the crystallization. Hydrogen bonds between oxygen atoms (come from hexane or toluene) and surface hydroxyl groups (come from produced CaCO_3) cause the aggregation. The crystal growth continues until organic chains collide with each other³⁴.

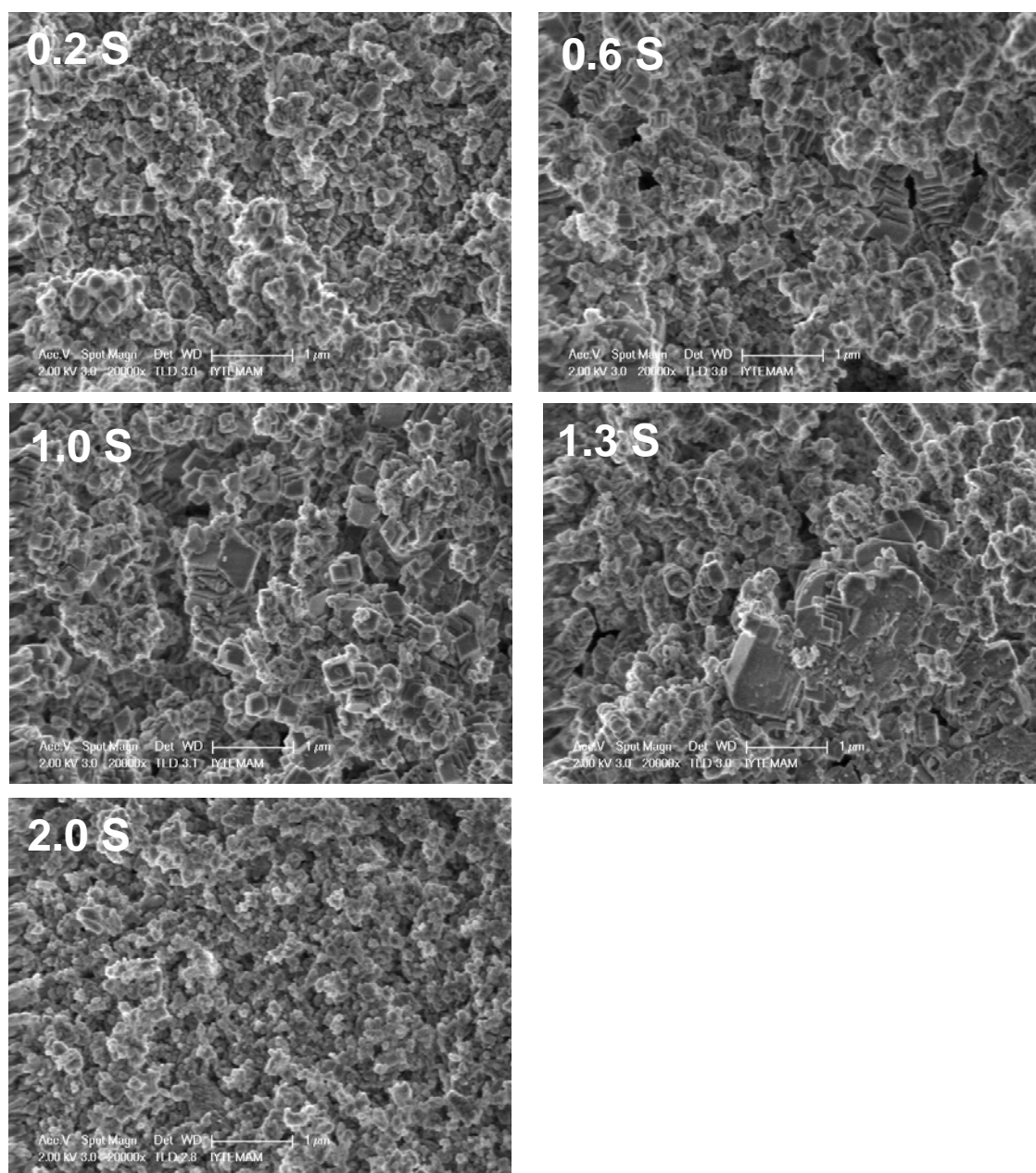


Figure 5.82. SEM images of the precipitates obtained from toluene solution. Amount of $\text{Ca}(\text{OH})_2$:20 mM stirring: 800 rpm (from 0.2 S to 2.0 S in legend indicates from 0.2-fold to 2-fold of toluene solubility in water).

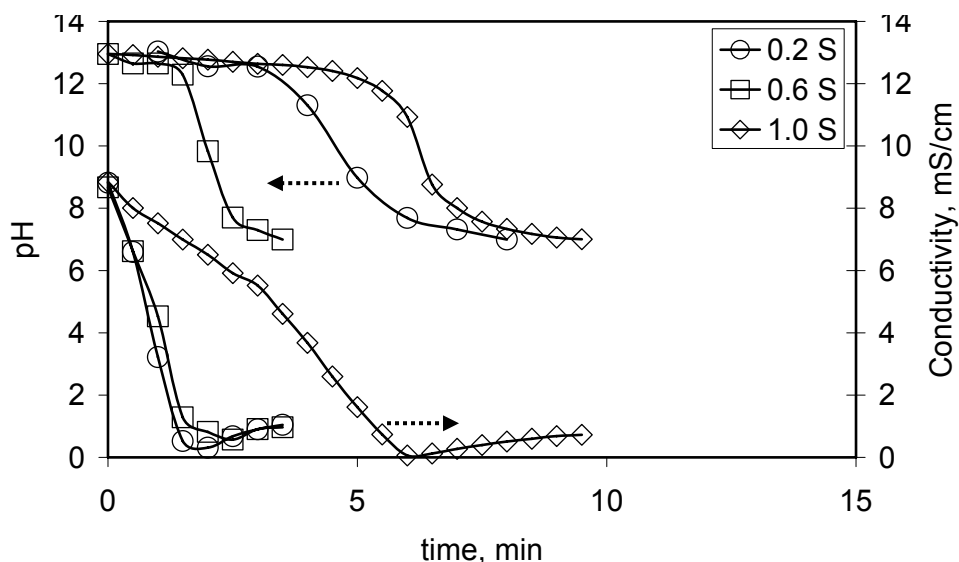


Figure 5.83. Change of pH and conductivity during precipitation in the presence of toluene. Amount of $\text{Ca}(\text{OH})_2$:40 mM stirring: 800 rpm (from 0.2 S to 1.0 S in legend indicates from 0.2-fold to 1-fold of toluene solubility in water).

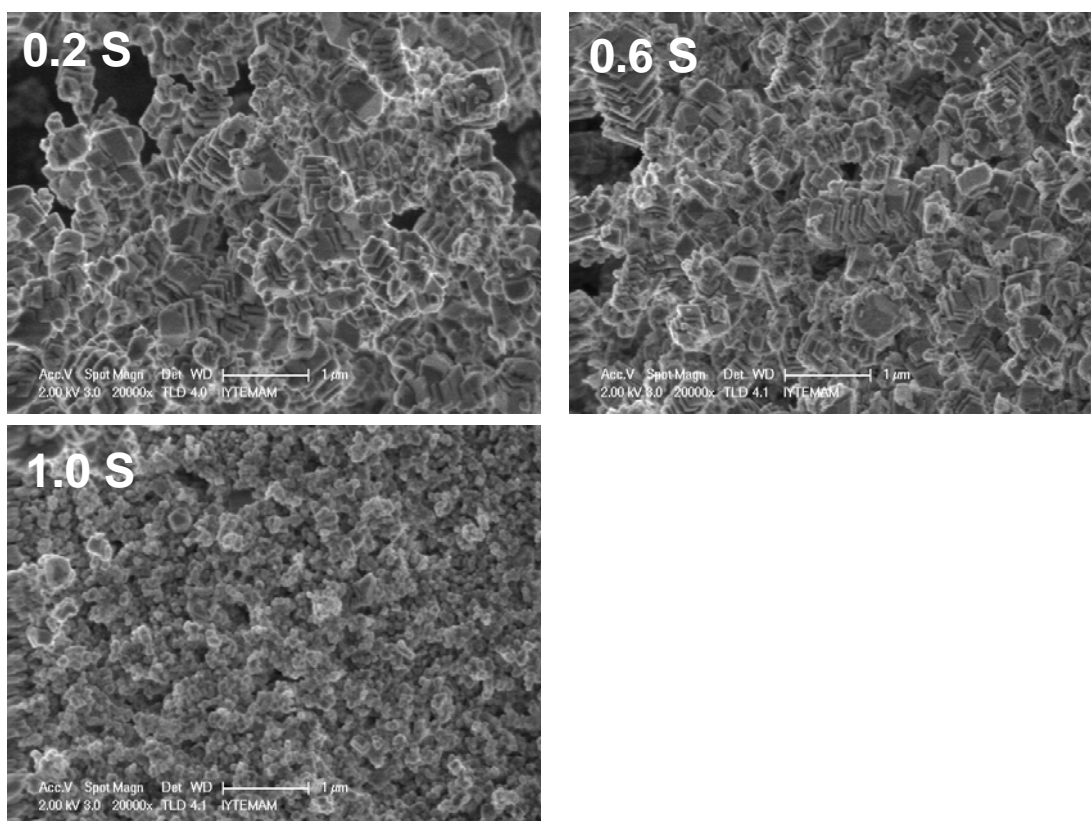


Figure 5.84. SEM images of the precipitates obtained from toluene solution. Amount of $\text{Ca}(\text{OH})_2$:40 mM stirring: 800 rpm (from 0.2 S to 1.0 S in legend indicates from 0.2 – fold to 1-fold of toluene solubility in water).

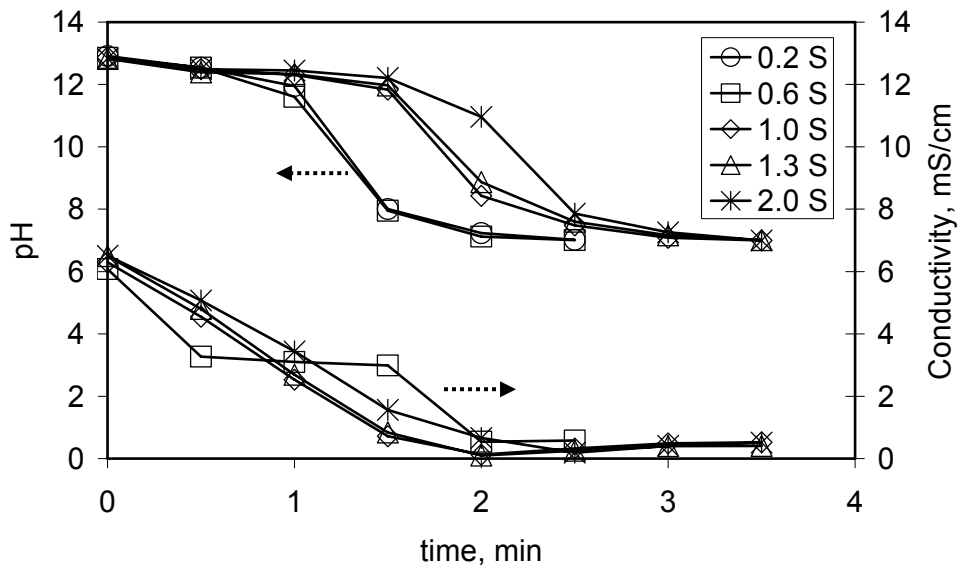


Figure 5.85. Change of pH and conductivity during precipitation in the presence of hexane. Amount of $\text{Ca}(\text{OH})_2$:20 mM stirring: 800 rpm (from 0.2 S to 2.0 S in legend indicates from 0.2 – fold to 2-fold of hexane solubility in water).

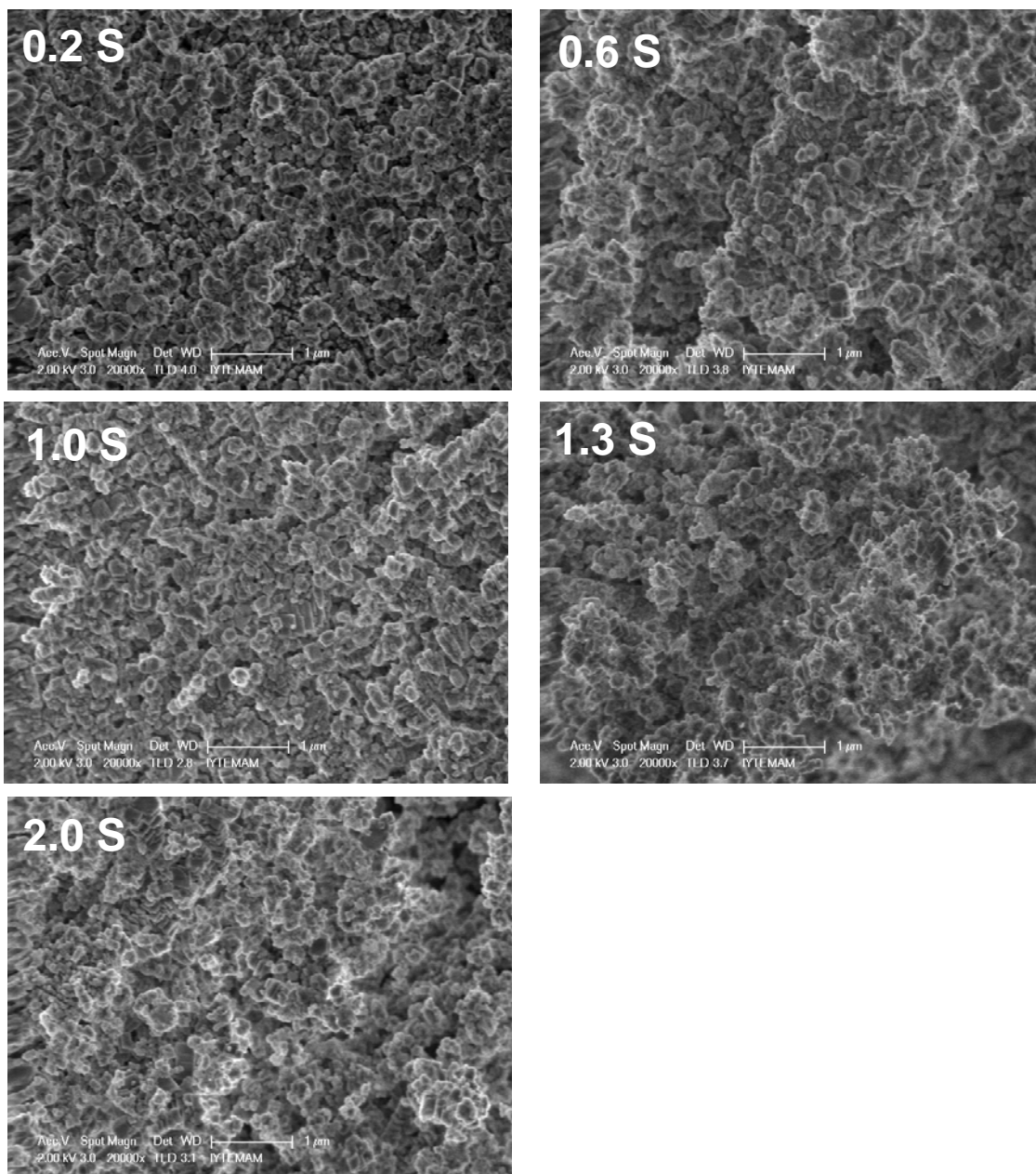


Figure 5.86. SEM images of the precipitates obtained from hexane solution. Amount of $\text{Ca}(\text{OH})_2$:20 mM stirring: 800 rpm (from 0.2 S to 2.0 S in legend indicates from 0.2 – fold to 2-fold of hexane solubility in water).

CHAPTER 6

CONCLUSIONS

Calcite has been used extensively in polymeric composites. Recent studies have reported that the $[Ca^{++}] / [CO_3^{--}]$ ratio is one of the most important parameters that affect the $CaCO_3$ crystallization rate. It was also reported that stable clusters will form from Ca^{++} and CO_3^{--} ions before nucleation, the chemical method was studied for different $[Ca^{++}] / [CO_3^{--}]$ ratios and it combined with the carbonization method using CO_2 saturated solution. We proposed that if the $[Ca^{++}] / [CO_3^{--}]$ ratio of 1 is approached slowly from left or from right starting with very low $[Ca^{++}]$ concentrations or very high $[CO_3^{--}]$ concentrations, the nano clusters may form and grow to form stable nano $CaCO_3$ particles. The $CaCO_3$ crystals were obtained in their early completion stages as a result of the slow addition of CO_2 saturated solutions into $Ca(OH)_2$. Fast addition of CO_2 saturated solution resulted in chain-like $CaCO_3$ particles. The chain-like structures were seen to compose of nano size crystals less than 60 nm.

When calcite was used in nano size, some of the physical and mechanical properties of the polymeric composites were enhanced. Therefore, production of calcite in nano sizes is highly important. Because the crystallization is an ionic reaction, the crystal growth rate can not be easily controlled, and thus, it is difficult to obtain particles in nano sizes, homogeneous size distribution, and different morphologies. Here, a mini reactor was created in a $Ca(OH)_2$ solution and the CO_2 was introduced on the surface of this mini reactor so that the reactions such as nucleation and crystal growth can be controlled. We achieved reproducible results producing calcite particles of about 60 nm. These particles in some cases aggregated to larger particles. Different morphologies such as cubic, round, chain-like shapes of particles were obtained.

We were expecting that the $Ca(OH)_2$ was fully dissolved at concentrations even lower than its solubility limit. However, it was shown that there were still $Ca(OH)_2$ particles in the solution in 20 min $Ca(OH)_2$ dissolution. It was found that nano sized calcite crystals were nucleated and grown on these $Ca(OH)_2$ particles during crystallization. Nano $CaCO_3$ particles were also found to be nucleated and grown on the

surfaces of the already grown CaCO_3 particles. It was also seen that these nano sized calcite particles can be broken into small stable particles by shear.

The effects of free Carbonic Anhydrase (CA), Polyurethane foam (PU), and immobilized CA were also investigated. Nano sized particles were produced. The time required for the completion in the crystallization reaction relatively reduced by the free CA concentrations. However, the time for crystallization was delayed in the presence of immobilized CA.

The effects of organic solvents such as methanol, ethanol, hexane, toluene and benzene on the size and morphology of calcite were investigated. These organic additives caused a co-effect on the polymorphism and morphology of CaCO_3 particles and influenced the morphology of the CaCO_3 crystals during the precipitation. The morphology of the precipitates was significantly changed to spheroidal chains and elliptic and almost mono disperse particles were synthesized in the presence of hydrophobic solvents including toluene, benzene and hexane. Stable nano calcite crystals in a regular chain-like cubic morphology were obtained in the presence of hydrophilic solvents such as methanol and ethanol.

The zeta potential values for calcite were measured as -14.92 mV at pH=12 ; - 6.49 mV at pH=7.5 ; +11.42 mV at pH=6.5. The colloidal stability tests showed that the nano sized calcite particles produced in our system are vulnerable to coagulate in water due to their surface charges, which is less than ± 30 mV.

REFERENCES

- 1 Sorrentino, L., Berardini, F., Capozzoli, M. R., Amitrano, S. & Iannace, S. Nano/micro Ternary Composites Based on PP, Nanoclay, and CaCO₃. *J Appl Polym Sci* 113, 3360-3367, doi:Doi 10.1002/App.30241 (2009).
- 2 Campos, J. S. D., Ribeiro, A. A. & Cardoso, C. X. Preparation and characterization of PVDF/CaCO₃ composites. *Mat Sci Eng B-Solid* 136, 123-128, doi:DOI 10.1016/j.mseb.2006.09.017 (2007).
- 3 Lam, T. D., Hoang, T. V., Quang, D. T. & Kim, J. S. Effect of nanosized and surface-modified precipitated calcium carbonate on properties of CaCO₃/polypropylene nanocomposites. *Mat Sci Eng a-Struct* 501, 87-93, doi:DOI 10.1016/j.msea.2008.09.060 (2009).
- 4 Sheng, Y. *et al.* In situ preparation of hydrophobic CaCO₃ in the presence of sodium oleate. *Appl Surf Sci* 253, 1983-1987, doi:DOI: 10.1016/j.apsusc.2006.03.071 (2006).
- 5 Beskova, B., Starkova, M., Sarka, E., Gojny, J. & Bubnik, Z. Application of carbonatation lime as a filler for adhesives. *Zuckerindustrie* 134, 486-490 (2009).
- 6 Matahwa, H., Ramiah, V. & Sanderson, R. D. Calcium carbonate crystallization in the presence of modified polysaccharides and linear polymeric additives. *J Cryst Growth* 310, 4561-4569, doi:DOI 10.1016/j.jcrysgro.2008.07.089 (2008).
- 7 Sondi, I., Skapin, S. D. & Salopek-Sondi, B. Biomimetic precipitation of nanostructured colloidal calcite particles by enzyme-catalyzed reaction in the presence of magnesium ions. *Cryst Growth Des* 8, 435-441, doi:Doi 10.1021/Cg070195n (2008).
- 8 Sahebian, S., Zebarjad, S. M., Khaki, J. V. & Sajjadi, S. A. The effect of nano-sized calcium carbonate on thermodynamic parameters of HDPE. *J Mater Process Tech* 209, 1310-1317, doi:DOI 10.1016/j.jmatprotec.2008.03.066 (2009).
- 9 Global Information, I. The Economics of Ground Calcium Carbonate, 3rd edition. (Roskill Information Services, Ltd. , 2008).
- 10 Global Industry Analysts, I. Calcium Carbonate - Global Strategic Business Report. (2011).
- 11 Uyanık, T. Mining Industry in Turkey. (Export Promotion Center of Turkey, 2010).
- 12 Stepkowska, E. T., Perez-Rodriguez, J. L., Sayagues, M. J. & Martinez-Blanes, J. M. Calcite, vaterite and aragonite forming on cement hydration from liquid and gaseous phase. *J Therm Anal Calorim* 73, 247-269 (2003).

- 13 Xu, A. W., Ma, Y. R. & Colfen, H. Biomimetic mineralization. *J Mater Chem* 17, 415-449, doi:Doi 10.1039/B611918m (2007).
- 14 Gunasekaran, S. & Anbalagan, G. Spectroscopic study of phase transitions in natural calcite mineral. *Spectrochim Acta A* 69, 1246-1251, doi:DOI 10.1016/j.saa.2007.06.036 (2008).
- 15 Montes-Hernandez, G., Fernández-Martínez, A., Charlet, L., Tisserand, D. & Renard, F. Textural properties of synthetic nano-calcite produced by hydrothermal carbonation of calcium hydroxide. *J Cryst Growth* 310, 2946-2953, doi:DOI: 10.1016/j.jcrysgro.2008.02.012 (2008).
- 16 Carmona, J. G., Morales, J. G. & Clemente, R. R. Rhombohedral-scalenohedral calcite transition produced by adjusting the solution electrical conductivity in the system Ca(OH)(2)-CO₂-H₂O. *J Colloid Interf Sci* 261, 434-440, doi:Doi 10.1016/S0021-9797(03)00149-8 (2003).
- 17 Jung, W. M., Kang, S. H., Kim, W.-S. & Choi, C. K. Particle morphology of calcium carbonate precipitated by gas-liquid reaction in a Couette-Taylor reactor. *Chem Eng Sci* 55, 733-747, doi:Doi: 10.1016/s0009-2509(99)00395-4 (2000).
- 18 Fu, S. Y., Feng, X. Q., Lauke, B. & Mai, Y. W. Effects of particle size, particle/matrix interface adhesion and particle loading on mechanical properties of particulate-polymer composites. *Compos Part B-Eng* 39, 933-961, doi:DOI 10.1016/j.compositesb.2008.01.002 (2008).
- 19 Sant'Anna, S. S. e., Souza, D. A. d., Araujo, D. M. d., Carvalho, C. d. F. & Yoshida, M. I. Physico-chemical analysis of flexible polyurethane foams containing commercial calcium carbonate. *Materials Research* 11, 433-438 (2008).
- 20 Ukrainczyk, M., Kontrec, J., Babic-Ivancic, V., Brecevic, L. & Kralj, D. Experimental design approach to calcium carbonate precipitation in a semicontinuous process. *Powder Technol* 171, 192-199, doi:DOI 10.1016/j.powtec.2006.10.046 (2007).
- 21 Sant'Anna, S. S. E., de Souza, D. A., de Araujo, D. M., Carvalho, C. D. & Yoshida, M. I. Physico-chemical Analysis of Flexible Polyurethane Foams Containing Commercial Calcium Carbonate. *Mater Res-Ibero-Am J* 11, 433-438 (2008).
- 22 Briones, M. J. I., Lopez, E., Mendez, J., Rodriguez, J. B. & Gago-Duport, L. Biological control over the formation and storage of amorphous calcium carbonate by earthworms. *Mineral Mag* 72, 227-231, doi:DOI 10.1180/minmag.2008.072.1.227 (2008).
- 23 Han, Y. S., Hadiko, G., Fuji, M. & Takahashi, M. Influence of initial CaCl₂ concentration on the phase and morphology of CaCO₃ prepared by carbonation. *J Mater Sci* 41, 4663-4667, doi:DOI 10.1007/s10853-006-0037-4 (2006).
- 24 Hari, B. *et al.* Multigram scale synthesis and characterization of monodispersed cubic calcium carbonate nanoparticles. *Mater Lett* 60, 1515-1518, doi:DOI: 10.1016/j.matlet.2005.11.062 (2006).

- 25 Pouget, E. M. *et al.* The Initial Stages of Template-Controlled CaCO₃ Formation Revealed by Cryo-TEM. *Science* 323, 1455-1458, doi:DOI 10.1126/science.1169434 (2009).
- 26 Spanos, N. & Koutsoukos, P. G. Kinetics of precipitation of calcium carbonate in alkaline pH at constant supersaturation. Spontaneous and seeded growth. *J Phys Chem B* 102, 6679-6684 (1998).
- 27 Wang, C. Y. *et al.* Biomimetic synthesis of hydrophobic calcium carbonate nanoparticles via a carbonation route. *Powder Technol* 170, 31-35, doi:DOI 10.1016/j.powtec.2006.08.016 (2006).
- 28 Gebauer, D., Volkel, A. & Colfen, H. Stable Prenucleation Calcium Carbonate Clusters. *Science* 322, 1819-1822, doi:DOI 10.1126/science.1164271 (2008).
- 29 Rieger, J., Thieme, J. & Schmidt, C. Study of precipitation reactions by X-ray microscopy: CaCO₃ precipitation and the effect of polycarboxylates. *Langmuir* 16, 8300-8305 (2000).
- 30 Dreybrodt, W., Eisenlohr, L., Madry, B. & Ringer, S. Precipitation kinetics of calcite in the system CaCO₃-H₂O-CO₂: The conversion to CO₂ by the slow process H⁺+HCO₃⁻-->CO₂+H₂O as a rate limiting step. *Geochim Cosmochim Acta* 61, 3897-3904 (1997).
- 31 Liu, Z. H. & Dreybrodt, W. Dissolution kinetics of calcium carbonate minerals in H₂O-CO₂ solutions in turbulent flow: The role of the diffusion boundary layer and the slow reaction H₂O+CO₂ reversible arrow H⁺+HCO₃⁻. *Geochim Cosmochim Acta* 61, 2879-2889 (1997).
- 32 Zhang, Y. & Grattoni, C. Comment on "precipitation kinetics of calcite in the system CaCO₃ - H₂O - CO₂: the conversion to CO₂ by the slow process H⁺ + HCO₃⁻ --> CO₂ + H₂O as a rate limiting step" by W. Dreybrodt, L. Eisenlohr, B. Madry, and S. Ringer. *Geochim Cosmochim Acta* 62, 3789-3790 (1998).
- 33 Dreybrodt, W. Reply to the Comment by Y.Zhang and C.A.Grattoni on: "precipitation kinetics of calcite in the system CaCO₃ - H₂O - CO₂: the conversion to CO₂ by the slow process H⁺ + HCO₃⁻ --> CO₂ + H₂O as a rate limiting step" by W. Dreybrodt, L. Eisenlohr, B. Madry, and S. Ringer. *Geochim Cosmochim Acta* 62, 3791-3792 (1998).
- 34 Wang, C. *et al.* Synthesis of hydrophobic CaCO₃ nanoparticles. *Mater Lett* 60, 854-857, doi:DOI: 10.1016/j.matlet.2005.10.035 (2006).
- 35 Wang, C. Y., Zhao, J. Z., Zhao, X., Bala, H. & Wang, Z. C. Synthesis of nanosized calcium carbonate (aragonite) via a polyacrylamide inducing process. *Powder Technol* 163, 134-138, doi:DOI 10.1016/j.powtec.2005.12.019 (2006).
- 36 Hernandez-Hernandez, A. *et al.* Influence of eggshell matrix proteins on the precipitation of calcium carbonate (CaCO₃). *J Cryst Growth* 310, 1754-1759, doi:DOI 10.1016/j.jcrysgro.2007.11.170 (2008).

- 37 Osman, M. A., Atallah, A. & Suter, U. W. Influence of excessive filler coating on the tensile properties of LDPE-calcium carbonate composites. *Polymer* 45, 1177-1183, doi:DOI 10.1016/j.polymer.2003.12.020 (2004).
- 38 Lin, Y., Chen, H. B., Chan, C. M. & Wu, J. S. High Impact Toughness Polypropylene/CaCO₃ Nanocomposites and the Toughening Mechanism. *Macromolecules* 41, 9204-9213, doi:Doi 10.1021/Ma801095d (2008).
- 39 Chen, J. F., Wang, Y. H., Guo, F., Wang, X. M. & Zheng, C. Synthesis of nanoparticles with novel technology: High-gravity reactive precipitation. *Ind Eng Chem Res* 39, 948-954 (2000).
- 40 García-Carmona, J., Gómez-Morales, J., Fraile-Sainz, J. & Rodríguez-Clemente, R. Morphological characteristics and aggregation of calcite crystals obtained by bubbling CO₂ through a Ca(OH)₂ suspension in the presence of additives. *Powder Technol* 130, 307-315, doi:Doi: 10.1016/s0032-5910(02)00209-7 (2003).
- 41 Domingo, C., Loste, E., Gomez-Morales, J., Garcia-Carmona, J. & Fraile, J. Calcite precipitation by a high-pressure CO₂ carbonation route. *J Supercrit Fluid* 36, 202-215, doi:DOI 10.1016/j.supflu.2005.06.006 (2006).
- 42 Hu, L. N., Dong, P. F. & Zhen, G. W. Preparation of active CaCO₃ nanoparticles and mechanical properties of the composite materials. *Mater Lett* 63, 373-375, doi:DOI 10.1016/j.matlet.2008.10.055 (2009).
- 43 Lin, R. Y., Zhang, J. Y. & Bai, Y. Q. Mass transfer of reactive crystallization in synthesizing calcite nanocrystal. *Chem Eng Sci* 61, 7019-7028, doi:DOI 10.1016/j.ces.2006.04.035 (2006).
- 44 Matsushita, I., Hamada, Y., Moriga, T., Ashida, T. & Nakabayashi, I. Synthesis of vaterite by carbonation process in aqueous system. *J Ceram Soc Jpn* 104, 1081-1084 (1996).
- 45 Sheng, Y. *et al.* In situ preparation of CaCO₃/polystyrene composite nanoparticles. *Mater Lett* 60, 3248-3250, doi:DOI 10.1016/j.matlet.2006.02.090 (2006).
- 46 Wang, M., Zou, H. K., Shao, L. & Chen, J. F. Controlling factors and mechanism of preparing needlelike CaCO₃ under high-gravity environment. *Powder Technol* 142, 166-174, doi:DOI 10.1016/j.powtec.2004.05.003 (2004).
- 47 Yang, J. H. & Shih, S. M. Preparation of high surface area CaCO₃ by reacting CO₂ with aqueous suspensions of Ca(OH)₂: Effect of the addition of sodium polyacrylate. *Powder Technol* 193, 170-175, doi:DOI 10.1016/j.powtec.2009.03.030 (2009).
- 48 Zhang, F. F. *et al.* Substrate-controlled crystallization of calcite and aragonite. *Geochim Cosmochim Acta* 72, A1081-A1081 (2008).

- 49 Fu, S. Y. & Lauke, B. Fracture resistance of unfilled and calcite-particle-filled ABS composites reinforced by short glass fibers (SGF) under impact load. *Compos Part a-Appl S* 29, 631-641 (1998).
- 50 Tang, C. Y. & Liang, J. Z. A study of the melt flow behaviour of ABS/CaCO₃ composites. *J Mater Process Tech* 138, 408-410, doi:Doi 10.1016/S0924-0136(03)00108-0 (2003).
- 51 Bartczak, Z., Argon, A. S., Cohen, R. E. & Kowalewski, T. The morphology and orientation of polyethylene in films of sub-micron thickness crystallized in contact with calcite and rubber substrates. *Polymer* 40, 2367-2380 (1999).
- 52 Kwon, S. *et al.* Tensile property and interfacial dewetting in the calcite filled HDPE, LDPE, and LLDPE composites. *Polymer* 43, 6901-6909, doi:Pii S0032-3861(02)00399-3 (2002).
- 53 Zebarjad, S. M. & Sajjadi, S. A. On the strain rate sensitivity of HDPE/CaCO₃ nanocomposites. *Mat Sci Eng a-Struct* 475, 365-367, doi:DOI 10.1016/j.msea.2007.05.008 (2008).
- 54 Silva, R., Pereira, G. M., Muniz, E. C. & Rubira, A. F. Calcium Carbonate Crystallization on a Polyethylene Surface Containing Ultrathin Layers of Hydrophilic Polymers. *Cryst Growth Des* 9, 3307-3312, doi:Doi 10.1021/Cg900106s (2009).
- 55 Ajikumar, P. K., Low, B. J. M. & Valiyaveetil, S. Role of soluble polymers on the preparation of functional thin films of calcium carbonate. *Surf Coat Tech* 198, 227-230, doi:DOI 10.1016/j.surfcoat.2004.10.028 (2005).
- 56 Liu, X. B., Zou, Y. B., Cao, G. P. & Luo, D. W. The preparation and properties of biodegradable polyesteramide composites reinforced with nano-CaCO₃ and nano-SiO₂. *Mater Lett* 61, 4216-4221, doi:DOI 10.1016/j.matlet.2007.01.065 (2007).
- 57 Guo, H., Yu, J. G. & Cheng, B. Preparation and formation mechanism of wood-block-like calcite particles. *J Solid State Chem* 179, 2547-2553, doi:DOI 10.1016/j.jssc.2006.05.005 (2006).
- 58 Guvendiren, M., Heiney, P. A. & Yang, S. Precipitated Calcium Carbonate Hybrid Hydrogels: Structural and Mechanical Properties. *Macromolecules* 42, 6606-6613, doi:Doi 10.1021/Ma9012576 (2009).
- 59 Kovacevic, V., Lucic, S. & Cerovecki, Z. Influence of filler surface pre-treatment on the mechanical properties of composites. *Int J Adhes Adhes* 17, 239-245 (1997).
- 60 Larena, A. & Villar, M. A. Optical properties of CaCO₃-filled poly(ethylene-co-vinyl acetate) films. *Opt Mater* 17, 437-442 (2001).
- 61 Kiss, A., Fekete, E. & Pukanszky, B. Aggregation of CaCO₃ particles in PP composites: Effect of surface coating. *Compos Sci Technol* 67, 1574-1583, doi:DOI 10.1016/j.compscitech.2006.07.010 (2007).

- 62 Liang, J. Z. Evaluation of dispersion of nano-CaCO₃ particles in polypropylene matrix based on fractal method. *Compos Part a-Appl S* 38, 1502-1506, doi:DOI 10.1016/j.compositesa.2007.01.011 (2007).
- 63 Carmona, J. G., Morales, J. G., Sainz, J. F., Loste, E. & Clemente, R. R. The mechanism of precipitation of chain-like calcite. *J Cryst Growth* 262, 479-489, doi:DOI 10.1016/j.jcrysgro.2003.10.003 (2004).
- 64 Faatz, M., Grohn, F. & Wegner, G. Mineralization of calcium carbonate by controlled release of carbonate in aqueous solution. *Mat Sci Eng C-Bio S* 25, 153-159, doi:DOI 10.1016/j.msec.2005.01.005 (2005).
- 65 Konno, H., Nanri, Y. & Kitamura, M. Effect of NaOH on aragonite precipitation in batch and continuous crystallization in causticizing reaction. *Powder Technol* 129, 15-21, doi:Pii S0032-5910(02)00275-9 (2003).
- 66 Pan, Y. *et al.* Biomimetic synthesis of dendrite-shaped aragonite particles with single-crystal feature by polyacrylic acid. *Colloid Surface A* 297, 198-202, doi:DOI 10.1016/j.colsurfa.2006.10.047 (2007).
- 67 Sommerdijk, N. A. J. M. & de With, G. Biomimetic CaCO₃ Mineralization using Designer Molecules and Interfaces. *Chem Rev* 108, 4499-4550, doi:Doi 10.1021/Cr078259o (2008).
- 68 Garcia-Carmona, J., Morales, J. G. & Clemente, R. R. Morphological control of precipitated calcite obtained by adjusting the electrical conductivity in the Ca(OH)₂-H₂O-CO₂ system. *J Cryst Growth* 249, 561-571, doi:Doi: 10.1016/s0022-0248(02)02173-5 (2003).
- 69 Montes-Hernandez, G., Renard, F., Geoffroy, N., Charlet, L. & Pironon, J. Calcite precipitation from CO₂-H₂O-Ca(OH)₂ slurry under high pressure of CO₂. *J Cryst Growth* 308, 228-236, doi:DOI 10.1016/j.jcrysgro.2007.08.005 (2007).
- 70 Fenter, P. *et al.* Surface speciation of calcite observed in situ by high-resolution X-ray reflectivity. *Geochim Cosmochim Acta* 64, 1221-1228 (2000).
- 71 Wang, J., Keener, T. C., Li, G. & Khang, S. J. The dissolution rate of Ca(OH)₂ in aqueous solutions. *Chem Eng Commun* 169, 167-184 (1998).
- 72 Johannsen, K. & Rademacher, S. Modelling the Kinetics of Calcium Hydroxide Dissolution in Water. *Acta Hydroch Hydrob* 27, 72-78, doi:10.1002/(sici)1521-401x(199902)27:2<72::aid-aheh72>3.0.co;2-h (1999).
- 73 Burns, J. R. & Jachuck, J. J. Monitoring of CaCO₃ production on a spinning disc reactor using conductivity measurements. *Aiche J* 51, 1497-1507 (2005).
- 74 Ozdemir, E. Biomimetic CO₂ Sequestration: 1. Immobilization of Carbonic Anhydrase within Polyurethane Foam. *Energ Fuel* 23, 5725-5730, doi:Doi 10.1021/Ef9005725 (2009).

- 75 Juvekar, V. A. & Sharma, M. M. Absorption of CO_2 in a Suspension of Lime. *Chem Eng Sci* 28, 825-837 (1973).
- 76 Sada, E., Kumazawa, H. & Butt, M. A. Single gas absorption with reaction in a slurry containing fine particles. *Chem Eng Sci* 32, 1165-1170, doi:Doi: 10.1016/0009-2509(77)80048-1 (1977).
- 77 Sada, E., Kumazawa, H. & Lee, C. H. Chemical absorption into concentrated slurry: Absorptions of carbon dioxide and sulfur dioxide into aqueous concentrated slurries of calcium hydroxide. *Chem Eng Sci* 39, 117-120, doi:Doi: 10.1016/0009-2509(84)80136-0 (1984).
- 78 Vucak, M., Peric, J., Zmikić, A. & Pons, M. N. A study of carbon dioxide absorption into aqueous monoethanolamine solution containing calcium nitrate in the gas-liquid reactive precipitation of calcium carbonate. *Chem Eng J* 87, 171-179, doi:Pii S1385-8947(01)00239-X (2002).
- 79 Gómez-Díaz, D., Navaza, J. M. & Sanjurjo, B. Analysis of mass transfer in the precipitation process of calcium carbonate using a gas/liquid reaction. *Chem Eng J* 116, 203-209, doi:10.1016/j.cej.2005.12.004 (2006).
- 80 Wang, K., Wang, Y. J., Chen, G. G., Luo, G. S. & Wang, J. D. Enhancement of mixing and mass transfer performance with a microstructure minireactor for controllable preparation of CaCO_3 nanoparticles. *Ind Eng Chem Res* 46, 6092-6098, doi:Doi 10.1021/ie061502+ (2007).
- 81 McCann, N. *et al.* Kinetics and Mechanism of Carbamate Formation from $\text{CO}_2(\text{aq})$, Carbonate Species, and Monoethanolamine in Aqueous Solution. *J Phys Chem A* 113, 5022-5029, doi:Doi 10.1021/Jp810564z (2009).
- 82 Kedra-Królik, K. & Gierycz, P. Simulation of nucleation and growing of CaCO_3 nanoparticles obtained in the rotating disk reactor. *J Cryst Growth* 312, 1945-1951, doi:10.1016/j.jcrysgro.2010.02.036 (2010).
- 83 Mitchell, M. J., Jensen, O. E., Cliffe, K. A. & Maroto-Valer, M. M. A model of carbon dioxide dissolution and mineral carbonation kinetics. *P Roy Soc a-Math Phy* 466, 1265-1290, doi:DOI 10.1098/rspa.2009.0349 (2010).
- 84 Nilsson, Ö. & Sternbeck, J. A mechanistic model for calcite crystal growth using surface speciation. *Geochim Cosmochim Acta* 63, 217-225, doi:Doi: 10.1016/s0016-7037(99)00026-5 (1999).
- 85 Xu, A.-W., Ma, Y. & Colfen, H. Biomimetic mineralization. *Journal of Materials Chemistry* 17, 415-449 (2007).
- 86 Wu, G. H., Wang, Y. J., Zhu, S. L. & Wang, J. D. Preparation of ultrafine calcium carbonate particles with micropore dispersion method. *Powder Technol* 172, 82-88, doi:DOI 10.1016/j.powtec.2006.10.031 (2007).

- 87 Nehrke, G., Reichart, G. J., Van Cappellen, P., Meile, C. & Bijma, J. Dependence of calcite growth rate and Sr partitioning on solution stoichiometry: Non-Kossel crystal growth. *Geochim Cosmochim Acta* 71, 2240-2249, doi:DOI 10.1016/j.gca.2007.02.002 (2007).
- 88 Freeman, C. L., Harding, J. H. & Duffy, D. M. Simulations of calcite crystallization on self-assembled monolayers. *Langmuir* 24, 9607-9615, doi:DOI 10.1021/La800389g (2008).
- 89 Wei, H. *et al.* On the crystallization of calcium carbonate modulated by anionic surfactants. *J Cryst Growth* 279, 439-446, doi:DOI 10.1016/j.jcrysgro.2005.02.064 (2005).
- 90 Beck, R. & Andreassen, J. P. The onset of spherulitic growth in crystallization of calcium carbonate. *J Cryst Growth* 312, 2226-2238, doi:DOI 10.1016/j.jcrysgro.2010.04.037 (2010).
- 91 Liu, Q., Wang, Q. & Xiang, L. Influence of poly acrylic acid on the dispersion of calcite nano-particles. *Appl Surf Sci* 254, 7104-7108, doi:DOI 10.1016/j.apsusc.2008.05.232 (2008).
- 92 Seo, K. S., Han, C., Wee, J. H., Park, J. K. & Ahn, J. W. Synthesis of calcium carbonate in a pure ethanol and aqueous ethanol solution as the solvent. *J Cryst Growth* 276, 680-687, doi:DOI 10.1016/j.jcrysgro.2004.11.416 (2005).
- 93 Sheng, Y. *et al.* Influence of octadecyl dihydrogen phosphate on the formation of active super-fine calcium carbonate. *J Colloid Interf Sci* 272, 326-329, doi:DOI 10.1016/j.jcis.2003.11.062 (2004).
- 94 Feng, B., Yong, A. K. & An, H. Effect of various factors on the particle size of calcium carbonate formed in a precipitation process. *Mat Sci Eng a-Struct* 445, 170-179, doi:DOI 10.1016/j.msea.2006.09.010 (2007).
- 95 Cho, K., Chang, H., Kil, D. S., Kim, B. G. & Jang, H. D. Synthesis of dispersed CaCO₃ nanoparticles by the ultrafine grinding. *J Ind Eng Chem* 15, 243-246, doi:DOI 10.1016/j.jiec.2008.10.005 (2009).
- 96 Kim, I. W., Robertson, R. E. & Zand, R. Effects of some nonionic polymeric additives on the crystallization of calcium carbonate. *Cryst Growth Des* 5, 513-522, doi:10.1021/cg049721q (2005).
- 97 Yu, J. G., Zhao, X. F., Cheng, B. & Zhang, Q. J. Controlled synthesis of calcium carbonate in a mixed aqueous solution of PSMA and CTAB. *J Solid State Chem* 178, 861-867, doi:DOI 10.1016/j.jssc.2005.01.002 (2005).
- 98 Kitamura, M. & Yasui, A. Crystallization behavior of calcium carbonate polymorphs and the effect of magnesium ion. *8th World Salt Symposium, Vols 1 and 2*, 1191-1192 (2000).

- 99 Lei, M., Li, P. G., Sun, Z. B. & Tang, W. H. Effects of organic additives on the morphology of calcium carbonate particles in the presence of CTAB. *Mater Lett* 60, 1261-1264, doi:DOI 10.1016/j.matlet.2005.11.023 (2006).
- 100 Yan, G., Wang, L. & Huang, J. The crystallization behavior of calcium carbonate in ethanol/water solution containing mixed nonionic/anionic surfactants. *Powder Technol* 192, 58-64, doi:DOI: 10.1016/j.powtec.2008.11.013 (2009).
- 101 Butler, M. F., Frith, W. J., Rawlins, C., Weaver, A. C. & Heppenstall-Butler, M. Hollow Calcium Carbonate Microsphere Formation in the Presence of Biopolymers and Additives. *Cryst Growth Des* 9, 534-545, doi:Doi 10.1021/Cg8008333 (2009).
- 102 Wang, C. *et al.* A novel aqueous-phase route to synthesize hydrophobic CaCO₃ particles in situ. *Materials Science and Engineering: C* 27, 42-45, doi:10.1016/j.msec.2006.01.003 (2007).
- 103 Sayan, P. Effect of sodium oleate on the agglomeration of calcium carbonate. *Cryst Res Technol* 40, 226-232, doi:DOI 10.1002/crat.200410330 (2005).
- 104 Szczes, A. Influence of the surfactant nature on the calcium carbonate synthesis in water-in-oil emulsion. *J Cryst Growth* 311, 1129-1135, doi:DOI 10.1016/j.jcrysgro.2008.12.044 (2009).
- 105 Dickinson, S. R. & McGrath, K. M. Aqueous precipitation of calcium carbonate modified by hydroxyl-containing compounds. *Cryst Growth Des* 4, 1411-1418, doi:Doi 10.1021/Cg049843i (2004).
- 106 Chen, X. *et al.* Carbonization synthesis of hydrophobic CaCO₃ at room temperature. *Colloid Surface A* 353, 97-103, doi:DOI 10.1016/j.colsurfa.2009.10.029 (2010).
- 107 Knez, S., Klinar, D. & Golob, J. Stabilization of PCC dispersions prepared directly in the mother-liquid after synthesis through the carbonation of (hydrated) lime. *Chem Eng Sci* 61, 5867-5880, doi:DOI 10.1016/j.ces.2006.05.016 (2006).
- 108 *Zetasizer nano series user manual*. (Malvern Instruments Ltd., 2009).
- 109 Kes, M. *Determination of the particle interactions - rheology- surface roughness relationship for dental ceramics* Master of Science thesis, İzmir Institute of Technology, (2007).
- 110 Derjaguin, B. V. Main Factors Affecting Stability of Colloids. *Pure Appl Chem* 48, 387-392 (1976).
- 111 Hoek, E. M. V. & Agarwal, G. K. Extended DLVO interactions between spherical particles and rough surfaces. *J Colloid Interf Sci* 298, 50-58, doi:DOI 10.1016/j.jcis.2005.12.031 (2006).

- 112 Bhattacharjee, S., Elimelech, M. & Borkovec, M. DLVO interaction between colloidal particles: Beyond Derjaguin's approximation. *Croat Chem Acta* 71, 883-903 (1998).
- 113 Liu, B. T. & Hsu, J. P. Stability of Soft Colloidal Particles in a Salt-Free Medium. *Langmuir* 25, 9045-9050, doi:Doi 10.1021/La900810g (2009).
- 114 Brown, P. P. & Lawler, D. F. Sphere drag and settling velocity revisited. *J Environ Eng-Asce* 129, 222-231, doi:Doi 10.1061/(Asce)0733-9372(2003)129:3(222) (2003).
- 115 Polat, M. *Particle Interactions & Kinetics of Coagulation*, (2009).
- 116 Liang, L. *Effects of Surface Chemistry on kinetics of coagulation of submicron iron oxide particles in water* PhD thesis, California Institute of Technology, (1988).
- 117 Kanbar, B. & Ozdemir, E. Thermal Stability of Carbonic Anhydrase Immobilized Within Polyurethane Foam. *Biotechnol Progr* 26, 1474-1480, doi:Doi 10.1002/Btbr.452 (2010).
- 118 Nebel, H., Neumann, M., Mayer, C. & Epple, M. On the structure of amorphous calcium carbonate - A detailed study by solid-state NMR spectroscopy. *Inorg Chem* 47, 7874-7879, doi:Doi 10.1021/Ic8007409 (2008).
- 119 Tai, C. Y. & Chen, F. B. Polymorphism of CaCO₃ precipitated in a constant-composition environment. *Aiche J* 44, 1790-1798 (1998).
- 120 Privman, V., Goia, D. V., Park, J. & Matijevic, E. Mechanism of formation of monodispersed colloids by aggregation of nanosize precursors. *J Colloid Interf Sci* 213, 36-45 (1999).
- 121 Duan, Z. H. & Sun, R. An improved model calculating CO₂ solubility in pure water and aqueous NaCl solutions from 273 to 533 K and from 0 to 2000 bar. *Chem Geol* 193, 257-271, doi:Pii S0009-2541(02)00263-2 (2003).
- 122 Windholz, M., Budavari, S., Stroumstos, L. Y. & Fretig, M. N. The Merck Index, 9th Edition. 212 (1976).
- 123 Lide, D. *CRC Handbook of Chemistry and Physics. 75th ed.*, (CRC Press, 1995).
- 124 Han, Y. S., Fujii, M., Shehukin, D., Mohwald, H. & Takahashi, M. A New Model for the Synthesis of Hollow Particles via the Bubble Templating Method. *Cryst Growth Des* 9, 3771-3775, doi:Doi 10.1021/Cg900456t (2009).
- 125 Amor, M. B., Zgolli, D., Tlili, M. M. & Manzola, A. S. Influence of water hardness, substrate nature and temperature on heterogeneous calcium carbonate nucleation. *Desalination* 166, 79-84, doi:DOI: 10.1016/j.desal.2004.06.061 (2004).

- 126 Nason, J. A. & Lawler, D. F. Particle size distribution dynamics during precipitative softening: Constant solution composition. *Water Res* 42, 3667-3676, doi:DOI 10.1016/j.watres.2008.05.016 (2008).
- 127 Campos, A. F. C. *et al.* X-DLVO Interactions between Nanocolloidal Magnetic Particles: The Quantitative Interpretation of the pH-Dependent Phase Diagram of EDL-MF. *Braz J Phys* 39, 230-235 (2009).
- 128 Meldrum, F. C. & Hyde, S. T. Morphological influence of magnesium and organic additives on the precipitation of calcite. *J Cryst Growth* 231, 544-558 (2001).
- 129 Lin, Y. P., Singer, P. C. & Aiken, G. R. Inhibition of calcite precipitation by natural organic material: Kinetics, mechanism, and thermodynamics. *Environ Sci Technol* 39, 6420-6428, doi:Doi 10.1021/Es050470z (2005).
- 130 Leites, I. L. Thermodynamics of CO₂ solubility in mixtures monoethanolamine with organic solvents and water and commercial experience of energy saving gas purification technology. *Energ Convers Manage* 39, 1665-1674 (1998).
- 131 Brooks, B. W. & Shilimkan, R. V. Manufacture of Calcium-Carbonate Dispersions in Lubricating Oil. *Colloid Polym Sci* 257, 981-983 (1979).
- 132 Seo, K.-S., Han, C., Wee, J.-H., Park, J.-K. & Ahn, J.-W. Synthesis of calcium carbonate in a pure ethanol and aqueous ethanol solution as the solvent. *J Cryst Growth* 276, 680-687, doi:10.1016/j.jcrysgro.2004.11.416 (2005).
- 133 Keum, D. K., Naka, K. & Chujo, Y. Unique crystal morphology of hydrophobic CaCO₃ composite by sodium trisilanolate in a mixture of a water-miscible organic solvent and water. *J Cryst Growth* 259, 411-418, doi:DOI 10.1016/j.jcrysgro.2003.07.030 (2003).
- 134 Kim, D. M. & Cho, J. A comparative study of carbon dioxide capture capabilities between methanol solvent and aqueous monoethanol amine solution. *Korean J Chem Eng* 28, 22-26, doi:DOI 10.1007/s11814-010-0419-9 (2011).
- 135 Bottcher, M. E., Gehlken, P. L. & Steele, D. F. Characterization of inorganic and biogenic magnesian calcites by Fourier Transform infrared spectroscopy. *Solid State Ionics* 101, 1379-1385 (1997).
- 136 Kalisz, S., Svoboda, K., Robak, Z., Baxter, D. & Andersen, L. K. Application of FTIR absorption spectroscopy to characterize waste and biofuels for pyrolysis and gasification. *Archives of Waste Management and Environmental Protection* 8, 51-62 (2008).
- 137 Yost, M. G., Rose, M. A. & Morgan, M. S. An evaluation of Fourier transform infrared (FTIR) spectroscopy for detecting organic solvents in expired breath. *Appl Occup Environ Hyg* 18, 160-169, doi:FMGFC85XHP554D95 [pii] (2003).
- 138 Wada, N., Kanamura, K. & Umegaki, T. Effects of carboxylic acids on the crystallization of calcium carbonate. *J Colloid Interf Sci* 233, 65-72 (2001).

139 Wan, P. *et al.* A novel approach to study the dynamic process of calcium carbonate crystal growth by microcalorimetric method. *Mat Sci Eng a-Struct* 458, 244-248, doi:DOI 10.1016/j.msea.2006.12.100 (2007).

140 Studio, A. V. *Modeling, Optimization and Nonlinear Parameter Estimation for Scientists and Engineers*, <http://www.athenavisual.com/>, June, 2011).

APPENDIX A

MATHCAD PROGRAM CODE FOR THE CALCULATION OF COLLOIDAL STABILITY OF CALCITE-WATER SYTEM

A.1. Interaction Energy between Nano Calcite Particles in Water (pH=12.0)

$$\begin{aligned}
 F &:= 96484.56 \cdot \frac{\text{coul}}{\text{mole}} & R &:= 8.3144 \cdot \frac{\text{joule}}{\text{mole} \cdot \text{K}} & k &:= 1.380658 \cdot 10^{-23} \cdot \frac{\text{joule}}{\text{K}} & T &:= 298.15 \cdot \text{K} \\
 \epsilon_0 &:= 8.85 \cdot 10^{-12} \cdot \frac{\text{coul}^2}{\text{joule} \cdot \text{m}} & \epsilon_r &:= 78.5 & H &:= 1 \cdot A, 2 \cdot A .. 10000A & z &:= 2 & A &:= 10^{-10} \text{ m} \\
 \psi_{OC} &:= -0.01492 \cdot \text{volt} & R_C &:= 0.1 \cdot \mu\text{m} & C_0 &:= 1 \frac{\text{mole}}{\text{m}^3} & \mu\text{m} &:= 10^{-6} \cdot \text{m} \\
 A_{CWC} &:= 2.23 \cdot 10^{-20} \cdot \text{J} & \kappa_C &:= \sqrt{\frac{2 \cdot z^2 \cdot F^2 \cdot C_0}{\epsilon_0 \cdot \epsilon_r \cdot R \cdot T}} & \kappa_C &= 2.08 \times 10^8 \frac{1}{\text{m}}
 \end{aligned}$$

Total interaction energy between calcite particles:

$$V_t(H) := \frac{\pi \cdot \epsilon \cdot \epsilon_0 \cdot R_C^2}{2k \cdot T R_C} \cdot \left(2 \cdot \psi_{OC}^2 \cdot \ln \left(\frac{1 + e^{-\kappa_C \cdot H}}{1 - e^{-\kappa_C \cdot H}} \right) + 2 \psi_{OC}^2 \cdot \ln \left(1 - e^{-2 \cdot \kappa_C \cdot H} \right) \right) - \frac{A_{CWC} \cdot R_C^2}{12 \cdot k \cdot T \cdot H \cdot R_C}$$

A.2. Interaction Energy between Nano Calcite Particles in Water (pH=7.5)

$$\begin{aligned}
 F_{\text{m}} &:= 96484.56 \cdot \frac{\text{coul}}{\text{mole}} & R_{\text{w}} &:= 8.3144 \cdot \frac{\text{joule}}{\text{mole} \cdot \text{K}} & k &:= 1.380658 \cdot 10^{-23} \cdot \frac{\text{joule}}{\text{K}} & T_{\text{w}} &:= 298.15 \cdot \text{K} \\
 \epsilon_0 &:= 8.85 \cdot 10^{-12} \cdot \frac{\text{coul}^2}{\text{joule} \cdot \text{m}} & \epsilon_{\text{m}} &:= 78.5 & H_{\text{w}} &:= 1 \cdot \text{A}, 2 \cdot \text{A}.. 10000 \text{A} & z &:= 2 & A_{\text{w}} &:= 10^{-10} \text{m} \\
 \psi_{\text{OC}} &:= -0.00649 \cdot \text{volt} & R_{\text{C}} &:= 0.1 \cdot \mu\text{m} & C_0 &:= 1 \frac{\text{mole}}{\text{m}^3} & \mu\text{m} &:= 10^{-6} \cdot \text{m} \\
 A_{\text{CWC}} &:= 2.23 \cdot 10^{-20} \cdot \text{J} & \kappa_{\text{C}} &:= \sqrt{\frac{2 \cdot z^2 \cdot F^2 \cdot C_0}{\epsilon_0 \cdot \epsilon \cdot R \cdot T}} & \kappa_{\text{C}} &= 2.08 \times 10^8 \frac{1}{\text{m}}
 \end{aligned}$$

Total interaction energy between calcite particles:

$$V_{\text{t}}(H) := \frac{\pi \cdot \epsilon \cdot \epsilon_0 \cdot R_{\text{C}}^2}{2k \cdot T \cdot R_{\text{C}}} \cdot \left(2 \cdot \psi_{\text{OC}}^2 \cdot \ln \left(\frac{1 + e^{-\kappa_{\text{C}} \cdot H}}{1 - e^{-\kappa_{\text{C}} \cdot H}} \right) + 2 \psi_{\text{OC}}^2 \cdot \ln \left(1 - e^{-2 \cdot \kappa_{\text{C}} \cdot H} \right) \right) - \frac{A_{\text{CWC}} \cdot R_{\text{C}}^2}{12 \cdot k \cdot T \cdot H \cdot R_{\text{C}}}$$

A.3. Interaction Energy between Nano Calcite Particles in Water (pH=6.50)

$$\begin{aligned}
 F_{\text{m}} &:= 96484.56 \cdot \frac{\text{coul}}{\text{mole}} & R_{\text{w}} &:= 8.3144 \cdot \frac{\text{joule}}{\text{mole} \cdot \text{K}} & k &:= 1.380658 \cdot 10^{-23} \cdot \frac{\text{joule}}{\text{K}} & T_{\text{w}} &:= 298.15 \cdot \text{K} \\
 \epsilon_0 &:= 8.85 \cdot 10^{-12} \cdot \frac{\text{coul}^2}{\text{joule} \cdot \text{m}} & \epsilon_{\text{m}} &:= 78.5 & H_{\text{w}} &:= 1 \cdot \text{A}, 2 \cdot \text{A} \dots 10000 \text{A} & z &:= 2 & A_{\text{w}} &:= 10^{-10} \text{m} \\
 \psi_{\text{OC}} &:= 0.01142 \cdot \text{volt} & R_{\text{C}} &:= 0.1 \cdot \mu\text{m} & C_0 &:= 1 \frac{\text{mole}}{\text{m}^3} & \mu\text{m} &:= 10^{-6} \cdot \text{m} \\
 A_{\text{CWC}} &:= 2.23 \cdot 10^{-20} \cdot \text{J} & \kappa_{\text{C}} &:= \sqrt{\frac{2 \cdot z^2 \cdot F^2 \cdot C_0}{\epsilon_0 \cdot \epsilon \cdot R \cdot T}} & \kappa_{\text{C}} &= 2.08 \times 10^8 \frac{1}{\text{m}}
 \end{aligned}$$

Total interaction energy between calcite particles:

$$V_{\text{t}}(H) := \frac{\pi \cdot \epsilon \cdot \epsilon_0 \cdot R_{\text{C}}^2}{2k \cdot T \cdot R_{\text{C}}} \cdot \left(2 \cdot \psi_{\text{OC}}^2 \cdot \ln \left(\frac{1 + e^{-\kappa_{\text{C}} \cdot H}}{1 - e^{-\kappa_{\text{C}} \cdot H}} \right) + 2 \psi_{\text{OC}}^2 \cdot \ln \left(1 - e^{-2 \cdot \kappa_{\text{C}} \cdot H} \right) \right) - \frac{A_{\text{CWC}} \cdot R_{\text{C}}^2}{12 \cdot k \cdot T \cdot H \cdot R_{\text{C}}}$$

A.4. Potential Profile for Calcite in Water at pH value of 12.0

$$\begin{aligned} \text{pH} &:= 12 & \psi_{\text{ww}} &:= -14.92 \cdot \text{mV} & h &:= .1 \cdot \text{nm}, .2 \cdot \text{nm} .. 100 \cdot \text{nm} \\ R_{\text{ww}} &:= 8.314 \left(\frac{\text{J}}{\text{mol} \cdot \text{K}} \right) & k_{\text{ww}} &:= 1.380658 \cdot 10^{-23} \frac{\text{J}}{\text{K}} & F_{\text{ww}} &:= 96484.5 \cdot \frac{\text{C}}{\text{mol}} \\ A_{\text{C}} &:= 2.23 \cdot 10^{-20} \cdot \text{J} & A_{\text{W}} &:= 5.47 \cdot 10^{-20} \cdot \text{J} \end{aligned}$$

$$A_{\text{t}} := \left(\sqrt{A_{\text{C}}} - \sqrt{A_{\text{W}}} \right)^2 \quad x := 0 \cdot \text{nm}, .1 \cdot \text{nm} .. 100 \cdot \text{nm}$$

$$\psi_{01} := -0.01492 \cdot \text{volt} \quad \psi_{02} := -0.01492 \cdot \text{volt} \quad \epsilon_{\text{ww}} := 8.85 \cdot 10^{-12} \frac{\text{C}^2}{\text{J} \cdot \text{m}} \quad \epsilon := 78$$

$$C_0 := 0.001 \cdot \frac{\text{mol}}{\text{L}} \quad R_{\text{p1}} := 0.1 \mu\text{m} \quad T_{\text{ww}} := 298 \cdot \text{K} \quad z := 2$$

$$R_{\text{p2}} := 0.1 \mu\text{m}$$

$$\kappa := \sqrt{\frac{2 \cdot z^2 \cdot F^2 \cdot C_0}{\epsilon \cdot \epsilon_0 \cdot R \cdot T}} \quad \frac{1}{\kappa} = 4.793 \cdot \text{nm}$$

Calculation of Potential at a point in solution

$$\gamma := \frac{\exp\left(\frac{z \cdot F \cdot \psi_{01}}{2 \cdot R \cdot T}\right) - 1}{\exp\left(\frac{z \cdot F \cdot \psi_{01}}{2 \cdot R \cdot T}\right) + 1}$$

$$\kappa_{\text{ww}} := \sqrt{\frac{2 \cdot z^2 \cdot F^2 \cdot C_0}{\epsilon \cdot \epsilon_0 \cdot R \cdot T}}$$

$$\psi_{\text{ww}}(x) := \frac{2 \cdot R \cdot T}{z \cdot F} \cdot \ln \left(\frac{1 + \gamma \cdot e^{-\kappa \cdot x}}{1 - \gamma \cdot e^{-\kappa \cdot x}} \right)$$

A.5. Potential Profile for Calcite in Water at pH value of 7.50

$$\begin{aligned}
 \text{pH} &:= 7.5 & \psi_{\text{ww}} &:= -6.49 \cdot \text{mV} & h &:= .1 \cdot \text{nm}, .2 \cdot \text{nm} \dots 100 \cdot \text{nm} \\
 R_{\text{ww}} &:= 8.314 \left(\frac{\text{J}}{\text{mol} \cdot \text{K}} \right) & k_{\text{ww}} &:= 1.380658 \cdot 10^{-23} \frac{\text{J}}{\text{K}} & F_{\text{ww}} &:= 96484.5 \cdot \frac{\text{C}}{\text{mol}} \\
 A_{\text{c}} &:= 2.23 \cdot 10^{-20} \cdot \text{J} & A_{\text{w}} &:= 5.47 \cdot 10^{-20} \cdot \text{J}
 \end{aligned}$$

$$A_{\text{t}} := \left(\sqrt{A_{\text{c}}} - \sqrt{A_{\text{w}}} \right)^2 \quad x := 0 \cdot \text{nm}, .1 \cdot \text{nm} \dots 100 \cdot \text{nm}$$

$$\psi_{01} := -0.00649 \cdot \text{volt} \quad \psi_{02} := -0.0649 \cdot \text{volt} \quad \epsilon_{00} := 8.85 \cdot 10^{-12} \frac{\text{C}^2}{\text{J} \cdot \text{m}} \quad \epsilon := 78$$

$$\begin{aligned}
 C_0 &:= 0.001 \cdot \frac{\text{mol}}{\text{L}} & R_{\text{p1}} &:= 0.1 \mu\text{m} & T_{\text{ww}} &:= 298 \cdot \text{K} & z &:= 2 \\
 & & R_{\text{p2}} &:= 0.1 \mu\text{m}
 \end{aligned}$$

$$\kappa := \sqrt{\frac{2 \cdot z^2 \cdot F^2 \cdot C_0}{\epsilon \cdot \epsilon_0 \cdot R \cdot T}} \quad \frac{1}{\kappa} = 4.793 \cdot \text{nm}$$

Calculation of Potential at a point in solution

$$\gamma := \frac{\exp\left(\frac{z \cdot F \cdot \psi_{01}}{2 \cdot R \cdot T}\right) - 1}{\exp\left(\frac{z \cdot F \cdot \psi_{01}}{2 \cdot R \cdot T}\right) + 1} \quad \kappa_{\text{ww}} := \sqrt{\frac{2 \cdot z^2 \cdot F^2 \cdot C_0}{\epsilon \cdot \epsilon_0 \cdot R \cdot T}} \quad \psi_{\text{ww}}(x) := \frac{2 \cdot R \cdot T}{z \cdot F} \cdot \ln\left(\frac{1 + \gamma \cdot e^{-\kappa \cdot x}}{1 - \gamma \cdot e^{-\kappa \cdot x}}\right)$$

A.6. Potential Profile for Calcite in Water at pH value of 6.50

$$\begin{aligned} \text{pH} &:= 6.5 & \psi_w &:= 11.42 \text{ mV} & h &:= .1 \text{ nm}, .2 \text{ nm} \dots 100 \text{ nm} \\ R_w &:= 8.314 \left(\frac{\text{J}}{\text{mol} \cdot \text{K}} \right) & k_w &:= 1.380658 \cdot 10^{-23} \frac{\text{J}}{\text{K}} & F_w &:= 96484.5 \frac{\text{C}}{\text{mol}} \\ A_C &:= 2.23 \cdot 10^{-20} \cdot \text{J} & A_W &:= 5.47 \cdot 10^{-20} \cdot \text{J} \end{aligned}$$

$$A_t := \left(\sqrt{A_C} - \sqrt{A_W} \right)^2 \quad x := 0 \text{ nm}, .1 \text{ nm} \dots 100 \text{ nm}$$

$$\psi_{01} := 0.01142 \text{ volt} \quad \psi_{02} := 0.01142 \text{ volt} \quad \epsilon_0 := 8.85 \cdot 10^{-12} \frac{\text{C}^2}{\text{J} \cdot \text{m}} \quad \epsilon := 78$$

$$\begin{aligned} C_0 &:= 0.001 \cdot \frac{\text{mol}}{\text{L}} & R_{p1} &:= 0.1 \mu\text{m} & T_w &:= 298 \text{ K} & z &:= 2 \\ & & R_{p2} &:= 0.1 \mu\text{m} & & & & \\ \kappa &:= \sqrt{\frac{2 \cdot z^2 \cdot F^2 \cdot C_0}{\epsilon \cdot \epsilon_0 \cdot R \cdot T}} & \frac{1}{\kappa} &= 4.793 \text{ nm} \end{aligned}$$

Calculation of Potential at a point in solution

$$\gamma := \frac{\exp\left(\frac{z \cdot F \cdot \psi_{01}}{2 \cdot R \cdot T}\right) - 1}{\exp\left(\frac{z \cdot F \cdot \psi_{01}}{2 \cdot R \cdot T}\right) + 1} \quad \kappa_w := \sqrt{\frac{2 \cdot z^2 \cdot F^2 \cdot C_0}{\epsilon \cdot \epsilon_0 \cdot R \cdot T}} \quad \psi_w(x) := \frac{2 \cdot R \cdot T}{z \cdot F} \cdot \ln\left(\frac{1 + \gamma \cdot e^{-\kappa \cdot x}}{1 - \gamma \cdot e^{-\kappa \cdot x}}\right)$$

A.7. Calculation of Rapid Coagulation Kinetics

$$\mu := 0.8466 \cdot 10^{-3} \frac{\text{kg}}{\text{m} \cdot \text{s}}$$

$$k := 1.380658 \cdot 10^{-23} \frac{\text{joule}}{\text{K}}$$

$$R_c := 0.1 \cdot \mu\text{m} \quad T := 298.15 \cdot \text{K}$$

Diffusion Coefficient:

$$D := \frac{k \cdot T}{6\pi \cdot \mu \cdot R_c}$$

$$D = 2.58 \times 10^{-12} \frac{\text{m}^2}{\text{s}}$$

for calcite dispersion of 30 mM by volume in 200 mL water:

Volume of a calcite particle:

$$V_c := \frac{4}{3} \cdot \left(\frac{22}{7}\right) (100)^3$$

$$V_c = 4.19 \times 10^6$$

N_0 : total number of calcite particles per unit volume

$$N_0 := \frac{1}{5 \cdot V_c \cdot \text{nm}^3}$$

$$N_0 = 4.773 \times 10^{16} \frac{1}{\text{L}}$$

when there is no repulsive energy barrier: $V_{t1}(H) := 0 \cdot k \cdot T$

Stability Ratio:
$$W_1(H) := \frac{R_c \cdot e^{\frac{V_{t1}(H)}{k \cdot T}}}{(H + 2 \cdot R_c)^2}$$

$$W_1 := \int_0^{R_c} 2 \cdot W_1(H) \, dH \quad W_1 = 0.333$$

$$N_{r1}(t_{r1}) := \frac{N_0}{1 + 8 \cdot \pi \cdot D \cdot R_c \cdot N_0 \cdot t_{r1}}$$

$$t_{r1} := 0.0001\text{sec}, 0.001\text{sec} \dots 30\text{sec}$$

A.8. Calculation of Slow Coagulation Kinetics

$$N_{s1}(t_{s1}) := \frac{N_0}{1 + \frac{8 \cdot \pi \cdot D \cdot R_C \cdot N_0 \cdot t_{s1}}{W_1}} \quad t_{s1} := 1\text{sec}, 10\text{sec} \dots 1000000\text{sec}$$

there is no energy barrier:

$$V_{t2}(H) := 0 \cdot k \cdot T$$

Stability Ratio:

$$W_2(H) := \frac{R_C \cdot e^{\frac{V_{t2}(H)}{k \cdot T}}}{(H + 2 \cdot R_C)^2}$$

$$W_2 := \int_0^{R_C} 2 \cdot W_2(H) \, dH \quad W_2 = 0.333$$

$$N_{r2}(t_{r2}) := \frac{N_0}{1 + 8 \cdot \pi \cdot D \cdot R_C \cdot N_0 \cdot t_{r2}} \quad t_{r2} := 1\text{sec}, 5\text{sec} \dots 10^6 \text{sec}$$

A.9. Calculation of Terminal Settling Velocity (Stoke's Region)

$$\rho_w := 999 \cdot \frac{\text{kg}}{\text{m}^3}$$

$$\mu_w := 1.12 \cdot 10^{-3} \cdot \frac{\text{kg}}{\text{m} \cdot \text{sec}}$$

$$\rho_s := 2710 \cdot \frac{\text{kg}}{\text{m}^3}$$

$$g := 9.81 \cdot \frac{\text{m}}{\text{sec}^2}$$

$$P := \left[\frac{3 \cdot \mu_w^2}{4 \cdot (\rho_s - \rho_w) \cdot \rho_w \cdot g} \right]^{\frac{1}{3}}$$

$$Q := \left[\frac{4 \cdot (\rho_s - \rho_w) \cdot \mu_w \cdot g}{3 \cdot \rho_w^2} \right]^{\frac{1}{3}}$$

$$d := 0.01 \cdot \mu\text{m}, 0.1 \cdot \mu\text{m}.. 10 \cdot \mu\text{m} \quad D(d) := \frac{d}{P}$$

$$U_{st_w}(d) := \frac{(\rho_s - \rho_w) \cdot d^2 \cdot g}{18 \cdot \mu_w}$$

$$U_{n_w}(d) := 0$$

$$U_{c_w}(d) := 0$$

APPENDIX B

ATHENA PROGRAM CODE FOR CA(OH)₂ DISSOLUTION

Solver in Athena Visual Workpage software¹⁴⁰ is needed.

```
Program MAIN
Implicit Real*8(A-H,O-Z)
Integer MEQ
Parameter (MEQ=6)
Parameter (NCMAX=10,Zero=0.0D0,One=1.0D0,Pi=3.141592653589793D0)
Parameter (LEQ=MEQ,LRW=5000000,LIW=5000)
Parameter (LPAR=0,LPTS=30)
Parameter (LMOD=0,KMOD=0)
Parameter (MPTS=LPTS+2)
!
!:Variable Declarations Section
!
Dimension U(LEQ),UPRIME(LEQ)
Dimension RWORK(LRW),IWORK(LIW),RPAR(0:LPAR),IPAR(0:LPAR)
Dimension Info(50),Tout(LPTS+2)
Dimension TSTOP(0:LMOD),USTOP(0:KMOD)
Dimension Uini(LEQ),Fini(LEQ),UFeed(LEQ)
Real*8 D1,D2,D3,D4,D5,D6,D7,D8,D9,D10,D11,D12,D13,D14,KKF1,KKB1,KKF2,KKB2,KKF
*
3,KKB3,KKF4,KKB4,KKF5,KKB5,KKF6,KKB6,KKF7,KKB7,KKF8,KKB8,KKF9,KKB9,KKF
* 10,KKB10,KKF11,KKB11,KKF12,KKB12,KKF13,KKB13,KKF14,KKB14,RR1,RR2,RR3,R
* R4,RR5,RR6,RR7,RR8,RR9,RR10,RR11,RR12,RR13,RR14,R1,R2,R3,R4,R5,R6,R7,R
* 8,R9,R10,R11,R12,R13,R14,LRR1,LRR2,LRR3,LRR4,LRR5,LRR6,LRR7,LRR8,LRR9,
* LRR10,LRR11,LRR12,LRR13,LRR14,LR1,LR2,LR3,LR4,LR5,LR6,LR7,LR8,LR9,LR10
* ,LR11,LR12,LR13,LR14,ERR1,ERR2,ERR3,ERR4,ERR5,ERR6,ERR7,ERR8,ERR9,ERR1
* 0,ERR11,ERR12,ERR13,ERR14,ER1,ER2,ER3,ER4,ER5,ER6,ER7,ER8,ER9,ER10,ER1
* 1,ER12,ER13,ER14 ION, GAMA1, GAMA2,C1EQ,C2EQ,C3EQ,C4EQ,C5EQ,C6EQ,C7EQ,
* C8EQ,C9EQ,C10EQ,C11EQ,C12EQ,C13EQ,C14EQ,H,PCO2,C1,C2,C3,C4,C5,DTANK,AT
*
ANK,VTANK,RIN,XR1,DPIPE,VREAKTOR,NCACO3,SP1,SP2,ROP1,ROP2,CTCA,W,K1,K2
* ,KW,K4,K5,K6,K7,K8,K9,K10,K11,K12,CC4,CC5,CC7,CC10,ECC4,ECC5,ECC7,ECC1
* 0
!
!:External Declarations, Common Blocks and Data Statements
!
External FDSUB,EDSUB,JDSUB,BDSUB
Common/USRR00D/ Fini,Uini,UFeed
Common/USRI00D/ IOFSET
Common/WEIGHTS/
PROOT(NCMAX),WQ(NCMAX),AX(NCMAX,NCMAX),BXX(NCMAX,NCMAX)
Common/USRR01D/
D1,D2,D3,D4,D5,D6,D7,D8,D9,D10,D11,D12,D13,D14,KKF1,KKB1,KKF2,KKB2,KKF
*
3,KKB3,KKF4,KKB4,KKF5,KKB5,KKF6,KKB6,KKF7,KKB7,KKF8,KKB8,KKF9,KKB9,KKF
*
10,KKB10,KKF11,KKB11,KKF12,KKB12,KKF13,KKB13,KKF14,KKB14,RR1,RR2,RR3,R
* R4,RR5,RR6,RR7,RR8,RR9,RR10,RR11,RR12,RR13,RR14,R1,R2,R3,R4,R5,R6,R7,R
```



```

*      8,R9,R10,R11,R12,R13,R14,LRR1,LRR2,LRR3,LRR4,LRR5,LRR6,LRR7,LRR8,LRR9,
*      LRR10,LRR11,LRR12,LRR13,LRR14,LR1,LR2,LR3,LR4,LR5,LR6,LR7,LR8,LR9,LR10
*
,LR11,LR12,LR13,LR14,ERR1,ERR2,ERR3,ERR4,ERR5,ERR6,ERR7,ERR8,ERR9,ERR1
*      0,ERR11,ERR12,ERR13,ERR14,ER1,ER2,ER3,ER4,ER5,ER6,ER7,ER8,ER9,ER10,ER1
*      1,ER12,ER13,ER14 ION, GAMA1,
GAMA2,C1EQ,C2EQ,C3EQ,C4EQ,C5EQ,C6EQ,C7EQ,
*
C8EQ,C9EQ,C10EQ,C11EQ,C12EQ,C13EQ,C14EQ,H,PCO2,C1,C2,C3,C4,C5,DTANK,AT
*
ANK,VTANK,RIN,XR1,DPIPE,VREAKTOR,NCACO3,SP1,SP2,ROP1,ROP2,CTCA,W,K1,K2
*      ,KW,K4,K5,K6,K7,K8,K9,K10,K11,K12,CC4,CC5,CC7,CC10,ECC4,ECC5,ECC7,ECC1
*      0
!
!:Perfrom Dimensional Initialization
!
  Neq = LEQ
  Npar = LPAR
  NMOD = LMOD
  UMOD = KMOD
  NPTS = LPTS+2
  If(NPTS.LE.1)NPTS=2
  NPTCON = 0
!
!:Prepare Error Messages File
!
  LUN = 6
  LUNERR = 60
  Open(UNIT=LUN,FILE='BATCHCAOH2MODEL.RES',STATUS='UNKNOWN')
  Rewind(UNIT=LUN)
  Open(UNIT=LUNERR,FILE='BATCHCAOH2MODEL.DBG',STATUS='UNKNOWN')
  Rewind(UNIT=LUNERR)
!
!:User Defined Problem Parameters
!
  H=10**-1.5
  PCO2=1.0
  DPIPE=1.0
  VREAKTOR=250.0/1000.0
  SP1=2.7
  SP2=2.7
  ROP1=2.71
  ROP2=2.71
  KKF1=1.6E-4
  KKB1=55.0
  KKF2=3.78E-3
  KKB2=0.06
  KKF3=1.3E11
  KKB3=2.5E-5
  KKF4=6.5E-3*1E-3*Pi/4*DPIPE**2/VREAKTOR
  KKB4=1E10
  KKF5=6.0E-2
  KKB5=20.0
  KKF6=1.0E7
  KKB6=5.0E10
  KKF7=1.24E4
  KKB7=3.86E-4
  KKF8=3.0
  KKB8=5.0E10
  KKF9=13.6

```

```

KKB9=1.0
KKF10=2.0
KKB10=1.0E-3
KKF11=3.28E-7
NCACO3=2
KKB11=1.0
KKF12=0.51
KKB12=1.0
KKF13=3.46E-4
KKB13=1.0
KKF14=1.17E-6
KKB14=1.0
K1=2.91E-6
K2=19.3
KW=6.9E-13
K5=3.0E-3
K6=2.0E-4
K7=3.21E7
K8=6.0E-11
K9=12.9
K10=2.0E3
K11=3.47E-9
CTCA=10.0E-3

```

```

!
!:Calling Arguments for DDAPLUS. Systems of Differential and Algebraic Equations
!

```

```

IOFSET = 0
Tini = 0
TEND = 300
dT = (TEND - Tini)/Float(NPTS-1)
Do J=1,NPTS
  Tout(J)=Tini+dT*Float(J-1)
End Do
Ieform = 0
RTOL = 1.0E-14
ATOL = 1.0E-14

```

```

!
!:Info(1..18) Array
!

```

```

Info(01) = 0
Info(02) = 0
Info(03) = 0
Info(04) = 0
Info(05) = 0
Info(06) = 0
Info(07) = 0
Info(08) = 0
RWORK(3) = 0
Info(09) = 1
IWORK(3) = 5
Info(10) = 0
Info(11) = 1
RWORK(44) = 0
Info(12) = Npar
Info(13) = 0
Info(14) = 1
Info(15) = 0
Info(16) = 0
Info(17) = 0
Info(18) = 0

```

```

Info(26) = 0
Info(28) = 0
Info(29) = 0
Info(30) = 2
Info(31) = 0
IWORK(17) = 30
IWORK(18) = 5
IWORK(21) = 1000
!
!:Initial values for the State variables
!
U(01)=CTCA
U(02)=0.0
U(03)=1.0E-7
U(04)=0.0
U(05)=1.0E-7
U(06)=0.0
!
!:Print Some Input Information
!
Write(LUN,'(A35,I5)')' Number of State Equations.....',Neq
Write(LUN,'(A35,I5)')' Number of Sensitivity Parameters..',Npar
Write(LUN,'(A35,I5)')' Number of Continuation Points.....',NPTCON
Write(LUN,'(A1)')' '
!
!:Call DDAPLUS Integrator and Print the Results
!
100 Continue
Do I=1,NPTS
Iloop = I
ION=0.5*(U(2)*2**2+U(3)*1**2+U(4)*1**2+U(5)*1**2)
GAMA1=10**(-0.509*(1.0**2)*((ION)**0.5/(1.0+(ION)**0.5)-0.3*ION))
GAMA2=10**(-0.509*(2.0**2)*((ION)**0.5/(1.0+(ION)**0.5)-0.3*ION))
Call DDAPLUS(Tini,Tout(I),Neq,U,UPRIME,RTOL,ATOL,Info,RWORK,
* LRW,IWORK,LIW,RPAR,IPAR,Idid,LUNERR,Iform,
* FDSUB,EDSUB,JDSUB,BDSUB)
!
!:Print Modeling results
!
If(I.EQ.1.AND.Iform.EQ.0)Then
Write(LUN,'(A26)') Time U(1:NEQ)==>'
EndIf
Write(LUN,'(1X,10000(1PE12.5,1X))')Tini,(U(J),J=1,Neq)
If(Idid.LT.0)GoTo 60
If(Info(17).GT.0 .AND. Idid.EQ.4)GoTo 80
If(Info(04).GT.0 .AND. Idid.EQ.5)GoTo 90
End Do
GoTo 60
80 Continue
90 Continue
60 Continue
!
!:Exit Code and Integration Run Time Statistics
!
Write(LUN,'(A1)')' '
If(Idid.GE.0)Write(LUN,'(A49,I5)') EXIT DDAPLUS: SOLUTION SUCCESSFUL with
IDID.....',Idid
If(Idid.LT.0)Write(LUN,'(A49,I5)') EXIT DDAPLUS: SOLUTION HAS FAILED with
IDID.....',Idid
Write(LUN,'(A49,I5)')' Number of Steps Taken Thus Far.....',IWORK(11)

```

```

Write(LUN,'(A49,I5)') Number of Function Evaluations.....',IWORK(12)
Write(LUN,'(A49,I5)') Number of Jacobian Evaluations.....',IWORK(13)
Write(LUN,'(A49,I5)') Number of Jacobian Factorizations.....',IWORK(23)
!
!:User Customized Output
!
  Write(6,*), RR1
!
!:End of MAIN Program
!
  End

Subroutine FDSUB(T, Neq, U, F, RPAR, IPAR, Ieform, Ires)
Implicit Real*8(A-H,O-Z)
Integer MEQ
Parameter (MEQ=6)
Parameter (NCMAX=10,Zero=0.0D0,One=1.0D0,Pi=3.141592653589793D0)
Parameter (LEQ=MEQ)
!
!:Variable Declaration Statements section
!
  Dimension F(Neq),U(Neq),RPAR(0:*),IPAR(0:*)
  Dimension Uini(LEQ),Fini(LEQ),UFeed(LEQ)
  Real*8 D1,D2,D3,D4,D5,D6,D7,D8,D9,D10,D11,D12,D13,D14,KKF1,KKB1,KKF2,KKB2,KKF
  *
3,KKB3,KKF4,KKB4,KKF5,KKB5,KKF6,KKB6,KKF7,KKB7,KKF8,KKB8,KKF9,KKB9,KKF
  *   10,KKB10,KKF11,KKB11,KKF12,KKB12,KKF13,KKB13,KKF14,KKB14,RR1,RR2,RR3,R
  *   R4,RR5,RR6,RR7,RR8,RR9,RR10,RR11,RR12,RR13,RR14,R1,R2,R3,R4,R5,R6,R7,R
  *   8,R9,R10,R11,R12,R13,R14,LRR1,LRR2,LRR3,LRR4,LRR5,LRR6,LRR7,LRR8,LRR9,
  *   LRR10,LRR11,LRR12,LRR13,LRR14,LR1,LR2,LR3,LR4,LR5,LR6,LR7,LR8,LR9,LR10
  *   ,LR11,LR12,LR13,LR14,ERR1,ERR2,ERR3,ERR4,ERR5,ERR6,ERR7,ERR8,ERR9,ERR1
  *   0,ERR11,ERR12,ERR13,ERR14,ER1,ER2,ER3,ER4,ER5,ER6,ER7,ER8,ER9,ER10,ER1
  *   1,ER12,ER13,ER14 ION, GAMA1, GAMA2,C1EQ,C2EQ,C3EQ,C4EQ,C5EQ,C6EQ,C7EQ,
  *   C8EQ,C9EQ,C10EQ,C11EQ,C12EQ,C13EQ,C14EQ,H,PCO2,C1,C2,C3,C4,C5,DTANK,AT
  *
ANK,VTANK,RIN,XR1,DPIPE,VREAKTOR,NCACO3,SP1,SP2,ROP1,ROP2,CTCA,W,K1,K2
  *   ,KW,K4,K5,K6,K7,K8,K9,K10,K11,K12,CC4,CC5,CC7,CC10,ECC4,ECC5,ECC7,ECC1
  *   0
!
!:Executable Code and Common Blocks Section
!
  Common/USRR00D/ Fini,Uini,UFeed
  Common/USRI00D/ IOFSET
  Common/WEIGHTS/
PROOT(NCMAX),WQ(NCMAX),AX(NCMAX,NCMAX),BXX(NCMAX,NCMAX)
  Common/USRR01D/
D1,D2,D3,D4,D5,D6,D7,D8,D9,D10,D11,D12,D13,D14,KKF1,KKB1,KKF2,KKB2,KKF
  *
3,KKB3,KKF4,KKB4,KKF5,KKB5,KKF6,KKB6,KKF7,KKB7,KKF8,KKB8,KKF9,KKB9,KKF
  *
10,KKB10,KKF11,KKB11,KKF12,KKB12,KKF13,KKB13,KKF14,KKB14,RR1,RR2,RR3,R
  *   R4,RR5,RR6,RR7,RR8,RR9,RR10,RR11,RR12,RR13,RR14,R1,R2,R3,R4,R5,R6,R7,R
  *   8,R9,R10,R11,R12,R13,R14,LRR1,LRR2,LRR3,LRR4,LRR5,LRR6,LRR7,LRR8,LRR9,
  *   LRR10,LRR11,LRR12,LRR13,LRR14,LR1,LR2,LR3,LR4,LR5,LR6,LR7,LR8,LR9,LR10
  *
,LR11,LR12,LR13,LR14,ERR1,ERR2,ERR3,ERR4,ERR5,ERR6,ERR7,ERR8,ERR9,ERR1
  *   0,ERR11,ERR12,ERR13,ERR14,ER1,ER2,ER3,ER4,ER5,ER6,ER7,ER8,ER9,ER10,ER1
  *   1,ER12,ER13,ER14 ION, GAMA1,
GAMA2,C1EQ,C2EQ,C3EQ,C4EQ,C5EQ,C6EQ,C7EQ,

```

```

*
C8EQ,C9EQ,C10EQ,C11EQ,C12EQ,C13EQ,C14EQ,H,PCO2,C1,C2,C3,C4,C5,DTANK,AT
*
ANK,VTANK,RIN,XR1,DPIPE,VREAKTOR,NCACO3,SP1,SP2,ROP1,ROP2,CTCA,W,K1,K2
*      ,KW,K4,K5,K6,K7,K8,K9,K10,K11,K12,CC4,CC5,CC7,CC10,ECC4,ECC5,ECC7,ECC1
*      0
!
!:Enter the Model Equations Section
!:Retrieve the Sensitivity Parameters
!
RR1=KKF1*SP1*U(1)*1.0*74.0*(1.0-(GAMA2*U(2)*GAMA1*U(3)**2)/K1)
F(1)=-RR1
F(2)=RR1
F(3)=2.0*RR1
F(4)=K2*U(2)*U(3)-U(4)
F(5)=KW/U(3)-U(5)
F(6)=U(3)+U(1)-U(2)-U(5)-CTCA
!
!:End of Subroutine FDSUB
!
Return
End

Subroutine EDSUB(T, Neq, U, E, RPAR, IPAR, Ieform, Ires)
Implicit Real*8(A-H,O-Z)
Integer MEQ
Parameter (MEQ=6)
Parameter (NCMAX=10,Zero=0.0D0,One=1.0D0,Pi=3.141592653589793D0)
Parameter (LEQ=MEQ)
!
!:Variable Declaration Statements section
!
Dimension U(*),E(*),RPAR(0:*),IPAR(0:*)
Dimension Uini(LEQ),Fini(LEQ),UFeed(LEQ)
Real*8 D1,D2,D3,D4,D5,D6,D7,D8,D9,D10,D11,D12,D13,D14,KKF1,KKB1,KKF2,KKB2,KKF
*
3,KKB3,KKF4,KKB4,KKF5,KKB5,KKF6,KKB6,KKF7,KKB7,KKF8,KKB8,KKF9,KKB9,KKF
* 10,KKB10,KKF11,KKB11,KKF12,KKB12,KKF13,KKB13,KKF14,KKB14,RR1,RR2,RR3,R
* R4,RR5,RR6,RR7,RR8,RR9,RR10,RR11,RR12,RR13,RR14,R1,R2,R3,R4,R5,R6,R7,R
* 8,R9,R10,R11,R12,R13,R14,LRR1,LRR2,LRR3,LRR4,LRR5,LRR6,LRR7,LRR8,LRR9,
* LRR10,LRR11,LRR12,LRR13,LRR14,LR1,LR2,LR3,LR4,LR5,LR6,LR7,LR8,LR9,LR10
* ,LR11,LR12,LR13,LR14,ERR1,ERR2,ERR3,ERR4,ERR5,ERR6,ERR7,ERR8,ERR9,ERR1
* 0,ERR11,ERR12,ERR13,ERR14,ER1,ER2,ER3,ER4,ER5,ER6,ER7,ER8,ER9,ER10,ER1
* 1,ER12,ER13,ER14 ION, GAMA1, GAMA2,C1EQ,C2EQ,C3EQ,C4EQ,C5EQ,C6EQ,C7EQ,
* C8EQ,C9EQ,C10EQ,C11EQ,C12EQ,C13EQ,C14EQ,H,PCO2,C1,C2,C3,C4,C5,DTANK,AT
*
ANK,VTANK,RIN,XR1,DPIPE,VREAKTOR,NCACO3,SP1,SP2,ROP1,ROP2,CTCA,W,K1,K2
*      ,KW,K4,K5,K6,K7,K8,K9,K10,K11,K12,CC4,CC5,CC7,CC10,ECC4,ECC5,ECC7,ECC1
*      0
!
!:Executable Code and Common Blocks Section
!
Common/USRR00D/ Fini,Uini,UFeed
Common/USRI00D/ IOFSET
Common/WEIGHTS/
PROOT(NCMAX),WQ(NCMAX),AX(NCMAX,NCMAX),BXX(NCMAX,NCMAX)
Common/USRR01D/
D1,D2,D3,D4,D5,D6,D7,D8,D9,D10,D11,D12,D13,D14,KKF1,KKB1,KKF2,KKB2,KKF
*
3,KKB3,KKF4,KKB4,KKF5,KKB5,KKF6,KKB6,KKF7,KKB7,KKF8,KKB8,KKF9,KKB9,KKF

```

```

*
10,KKB10,KKF11,KKB11,KKF12,KKB12,KKF13,KKB13,KKF14,KKB14,RR1,RR2,RR3,R
*      R4,RR5,RR6,RR7,RR8,RR9,RR10,RR11,RR12,RR13,RR14,R1,R2,R3,R4,R5,R6,R7,R
*      8,R9,R10,R11,R12,R13,R14,LRR1,LRR2,LRR3,LRR4,LRR5,LRR6,LRR7,LRR8,LRR9,
*      LRR10,LRR11,LRR12,LRR13,LRR14,LR1,LR2,LR3,LR4,LR5,LR6,LR7,LR8,LR9,LR10
*
,LR11,LR12,LR13,LR14,ERR1,ERR2,ERR3,ERR4,ERR5,ERR6,ERR7,ERR8,ERR9,ERR1
*      0,ERR11,ERR12,ERR13,ERR14,ER1,ER2,ER3,ER4,ER5,ER6,ER7,ER8,ER9,ER10,ER1
*      1,ER12,ER13,ER14 ION, GAMA1,
GAMA2,C1EQ,C2EQ,C3EQ,C4EQ,C5EQ,C6EQ,C7EQ,
*
C8EQ,C9EQ,C10EQ,C11EQ,C12EQ,C13EQ,C14EQ,H,PCO2,C1,C2,C3,C4,C5,DTANK,AT
*
ANK,VTANK,RIN,XR1,DPIPE,VREAKTOR,NCACO3,SP1,SP2,ROP1,ROP2,CTCA,W,K1,K2
*      ,KW,K4,K5,K6,K7,K8,K9,K10,K11,K12,CC4,CC5,CC7,CC10,ECC4,ECC5,ECC7,ECC1
*      0
!
!:Insert the elements of the Matrix E(NEQ)
!:Retrieve the Sensitivity Parameters
!
  Do J=1,Neq
    E(J)=1.0
  End Do
!
!:End of Subroutine EDSUB
!
  Return
  End

  Subroutine JDSUB(T, Neq, U, dF, RPAR, IPAR, Ieform, Ires)
  Implicit Real*8(A-H,O-Z)
  Integer MEQ
  Parameter (MEQ=6)
  Parameter (NCMAX=10,Zero=0.0D0,One=1.0D0,Pi=3.141592653589793D0)
  Parameter (LEQ=MEQ)
!
!:Variable Declaration Statements section
!
  Dimension U(*),dF(Neq,*),RPAR(0:*),IPAR(0:*)
  Dimension Uini(LEQ),Fini(LEQ),UFeed(LEQ)
  Return
  End

  Subroutine BDSUB(T, Neq, U, B, JSPAR, RPAR, IPAR, Ieform, Ires)
  Implicit Real*8(A-H,O-Z)
  Integer MEQ
  Parameter (MEQ=6)
  Parameter (NCMAX=10,Zero=0.0D0,One=1.0D0,Pi=3.141592653589793D0)
  Parameter (LEQ=MEQ)
!
!:Variable Declaration Statements section
!
  Dimension U(Neq),B(Neq),RPAR(0:*),IPAR(0:*)
  Dimension Uini(LEQ),Fini(LEQ),UFeed(LEQ)
  Real*8 D1,D2,D3,D4,D5,D6,D7,D8,D9,D10,D11,D12,D13,D14,KKF1,KKB1,KKF2,KKB2,KKF
*
3,KKB3,KKF4,KKB4,KKF5,KKB5,KKF6,KKB6,KKF7,KKB7,KKF8,KKB8,KKF9,KKB9,KKF
*      10,KKB10,KKF11,KKB11,KKF12,KKB12,KKF13,KKB13,KKF14,KKB14,RR1,RR2,RR3,R
*      4,RR5,RR6,RR7,RR8,RR9,RR10,RR11,RR12,RR13,RR14,R1,R2,R3,R4,R5,R6,R7,R
*      8,R9,R10,R11,R12,R13,R14,LRR1,LRR2,LRR3,LRR4,LRR5,LRR6,LRR7,LRR8,LRR9,

```

```

*   LRR10,LRR11,LRR12,LRR13,LRR14,LR1,LR2,LR3,LR4,LR5,LR6,LR7,LR8,LR9,LR10
*   ,LR11,LR12,LR13,LR14,ERR1,ERR2,ERR3,ERR4,ERR5,ERR6,ERR7,ERR8,ERR9,ERR1
*   0,ERR11,ERR12,ERR13,ERR14,ER1,ER2,ER3,ER4,ER5,ER6,ER7,ER8,ER9,ER10,ER1
*   1,ER12,ER13,ER14 ION, GAMA1, GAMA2,C1EQ,C2EQ,C3EQ,C4EQ,C5EQ,C6EQ,C7EQ,
*   C8EQ,C9EQ,C10EQ,C11EQ,C12EQ,C13EQ,C14EQ,H,PCO2,C1,C2,C3,C4,C5,DTANK,AT
*
ANK,VTANK,RIN,XR1,DPIPE,VREAKTOR,NCACO3,SP1,SP2,ROP1,ROP2,CTCA,W,K1,K2
*   ,KW,K4,K5,K6,K7,K8,K9,K10,K11,K12,CC4,CC5,CC7,CC10,ECC4,ECC5,ECC7,ECC1
*   0
!
!:Executable Code and Common Blocks Section
!
Common/USRR00D/ Fini,Uini,UFeed
Common/USRI00D/ IOFSET
Common/WEIGHTS/
PROOT(NCMAX),WQ(NCMAX),AX(NCMAX,NCMAX),BXX(NCMAX,NCMAX)
Common/USRR01D/
D1,D2,D3,D4,D5,D6,D7,D8,D9,D10,D11,D12,D13,D14,KKF1,KKB1,KKF2,KKB2,KKF
*
3,KKB3,KKF4,KKB4,KKF5,KKB5,KKF6,KKB6,KKF7,KKB7,KKF8,KKB8,KKF9,KKB9,KKF
*
10,KKB10,KKF11,KKB11,KKF12,KKB12,KKF13,KKB13,KKF14,KKB14,RR1,RR2,RR3,R
*   R4,RR5,RR6,RR7,RR8,RR9,RR10,RR11,RR12,RR13,RR14,R1,R2,R3,R4,R5,R6,R7,R
*   8,R9,R10,R11,R12,R13,R14,LRR1,LRR2,LRR3,LRR4,LRR5,LRR6,LRR7,LRR8,LRR9,
*   LRR10,LRR11,LRR12,LRR13,LRR14,LR1,LR2,LR3,LR4,LR5,LR6,LR7,LR8,LR9,LR10
*
,LR11,LR12,LR13,LR14,ERR1,ERR2,ERR3,ERR4,ERR5,ERR6,ERR7,ERR8,ERR9,ERR1
*   0,ERR11,ERR12,ERR13,ERR14,ER1,ER2,ER3,ER4,ER5,ER6,ER7,ER8,ER9,ER10,ER1
*   1,ER12,ER13,ER14 ION, GAMA1,
GAMA2,C1EQ,C2EQ,C3EQ,C4EQ,C5EQ,C6EQ,C7EQ,
*
C8EQ,C9EQ,C10EQ,C11EQ,C12EQ,C13EQ,C14EQ,H,PCO2,C1,C2,C3,C4,C5,DTANK,AT
*
ANK,VTANK,RIN,XR1,DPIPE,VREAKTOR,NCACO3,SP1,SP2,ROP1,ROP2,CTCA,W,K1,K2
*   ,KW,K4,K5,K6,K7,K8,K9,K10,K11,K12,CC4,CC5,CC7,CC10,ECC4,ECC5,ECC7,ECC1
*   0
!
!:Compute the Partial derivatives
!:Retrieve the Sensitivity Parameters
!
Ires=0
!
!:End of Subroutine BDSUB
!
Return
End

```

VITA

PERSONALITY

Date of Birth : August 21, 1978

Place of Birth: Ayvalık

EDUCATION

2004 Master of Science (M.S.) İzmir Institute of Technology, Environmental Engineering Program (Environmental Pollution and Control)

2000 Bachelor of Science (B.S.) Kocaeli University, Department of Environmental Engineering

PRESENTATIONS

Molva M., Ozdemir E. “Effect of Shear on CaCO₃ Morphology”, In Proceeding of 6th Nanoscience and Nanotechnology Conference (NanoTR-VI), İzmir, 15-18 June, 2010

Molva M., Ozdemir E. “Effect of Toluene on Nano Calcite Production by Carbonation Route” In Proceeding of 6th Nanoscience and Nanotechnology Conference (NanoTR-VI), İzmir, 15-18 June, 2010

Molva M., Ozdemir E. “Experimental Design on Nano Calcite Production” In Proceeding of 6th Nanoscience and Nanotechnology Conference (NanoTR-VI), İzmir, 15-18 June, 2010

Molva, M. and Ozdemir, E. “Calcite Production as Nano Filling Material in the Presence of Carbonic Anhydrase”, In Proceedings of 5th Nanoscience and Nanotechnology Conference (NanoTR-V), Eskişehir, 08-12 June, 2009

Ozdemir, E. and Molva, M. “Nano and Global Warming”, In Proceeding of 5th Nanoscience and Nanotechnology Conference (NanoTR-V), Eskişehir, 08-12 June, 2009